

NEAR-SURFACE MOUNTED, FIBER-REINFORCED POLYMER STRIPS FOR  
NEGATIVE-MOMENT STRENGTHENING OF CONCRETE  
BRIDGES—DESIGN METHODOLOGY

Except where reference is made to the work of others, the work described in this thesis is my own or was done in collaboration with my advisory committee. This thesis does not include proprietary or classified information.

---

Jeffrey Kyle Alexy

Certificate of Approval:

---

Anton K. Schindler  
Gottlieb Associate Professor  
Civil Engineering

---

Robert W. Barnes, Chair  
James J. Mallett Associate Professor  
Civil Engineering

---

Hassan H. Abbas  
Assistant Professor  
Civil Engineering

---

George T. Flowers  
Dean  
Graduate School

NEAR-SURFACE MOUNTED, FIBER-REINFORCED POLYMER STRIPS FOR  
NEGATIVE-MOMENT STRENGTHENING OF CONCRETE  
BRIDGES—DESIGN METHODOLOGY

Jeffrey Kyle Alexy

A Thesis

Submitted to

the Graduate Faculty of

Auburn University

in Partial Fulfillment of the

Requirements for the

Degree of

Master of Science

Auburn, Alabama  
August 10, 2009

NEAR-SURFACE MOUNTED, FIBER-REINFORCED POLYMER STRIPS FOR  
NEGATIVE-MOMENT STRENGTHENING OF CONCRETE  
BRIDGES—DESIGN METHODOLOGY

Jeffrey Kyle Alexy

Permission is granted to Auburn University to make copies of this thesis at its discretion, upon request of individuals or institutions and at their expense. The author reserves all publication rights.

---

Signature of Author

---

Date of Graduation

## VITA

Jeffrey Kyle Alexy, son of Thomas and Susan Alexy, was born January 10, 1984, in Anniston, Alabama. He graduated from Jacksonville High School as salutatorian in 2002. He attended Auburn University and graduated summa cum laude with a Bachelor of Civil Engineering degree in 2007. He entered graduate school at Auburn University in August, 2007, to seek the degree of Master of Science in Civil Engineering. On May 16, 2009, he will marry Brigitte Demasi of Swanton, Vermont, and then begin work as a structural design engineer for Hodnett Hurst Engineers, Inc., in Huntsville, Alabama.



THESIS ABSTRACT

NEAR-SURFACE MOUNTED, FIBER-REINFORCED POLYMER STRIPS FOR  
NEGATIVE-MOMENT STRENGTHENING OF CONCRETE  
BRIDGES—DESIGN METHODOLOGY

Jeffrey Kyle Alexy

Master of Science, August 10, 2009  
(B.C.E., Auburn University, 2007)

321 Typed Pages

Directed by Robert W. Barnes

A bridge near Letohatchee, Alabama, was found to be deficient for certain types of truck loadings. Fiber-reinforced polymer (FRP) strips were selected to use in the strengthening scheme. Various models and code recommendations were studied and compared against existing experimental results to determine the most effective models for FRP-strengthened members. The models were divided into three groups: plate-end (PE) debonding models for near-surface mounted (NSM) FRP, intermediate-crack (IC) debonding models for externally-bonded (EB) FRP, and IC-debonding models for NSM FRP.

None of the three PE-debonding models correlated well with the experimental results. Four of the six IC-debonding models for EB were relatively accurate for the test data. All five of the IC-debonding models for NSM produced mostly conservative results, with three models being relatively accurate. These three models—ACI 440 (2008), Standards Australia (2008), and Seracino et al. (2007a)—were used in the proposed strengthening scheme to determine the amount of NSM FRP the Letohatchee bridge needed. To verify this proposed design and to further examine the behavior of NSM-strengthened concrete members, a laboratory testing program was proposed.

One of the main reasons for a laboratory testing program is that the published experimental test configurations do not match the Letohatchee bridge very well. The reinforcement ratios for the actual bridge are lower than the tests, and the NSM test specimens were not cracked prior to FRP strengthening. In the proposed testing program, the effects of the amounts of FRP and steel, the concrete compressive strength, and the cross-sectional shape were analyzed.

## ACKNOWLEDGEMENTS

First and foremost, I want to give all glory and honor to Jesus Christ, our Savior and Lord.

I would like to thank my family—Dad, Mom, Tommy, Kristin, and Grandma—for all of the love and support they have given me throughout the years. I would also like to thank my fiancée Brigitte Demasi for her love and support as well as her caring and thoughtfulness during these last few busy semesters.

I would especially like to thank Dr. Robert Barnes for all of his wisdom and guidance throughout my college career. I would also like to thank Dr. Anton Schindler and Dr. Hassan Abbas, for their work as committee members, as well as all of the other professors at Auburn University who have helped teach and mold me into the engineer I am today.

Finally, I am grateful for the monetary support given by the Alabama Department of Transportation through the funding of this project.

Style manual used Kate L. Turabian A Manual for Writers of Term Papers, Theses, and  
Dissertations. 6<sup>th</sup> ed.

Computer software used Microsoft Word, Microsoft Excel, AutoCAD 2007

## TABLE OF CONTENTS

LIST OF TABLES.....	xvii
LIST OF FIGURES.....	xxii
Chapter 1: Introduction.....	1
1.1 Background.....	1
1.2 Research Objectives and Tasks.....	3
1.3 Organization of Thesis.....	3
Chapter 2: Behavior of Reinforced Concrete Beams Strengthened with FRP.....	5
2.1 Introduction.....	5
2.2 Components and Applications of FRP.....	6
2.2.1 Different FRP Materials and Properties.....	6
2.2.2 Externally-Bonded (EB) FRP.....	8
2.2.3 Near-Surface Mounted (NSM) FRP.....	13
2.3 Failure Modes of FRP-Strengthened Members.....	15
2.3.1 Plate-End (PE) Debonding.....	15
2.3.2 Intermediate Crack (IC) Debonding.....	16
2.3.3 FRP Rupture.....	16
2.3.4 Concrete Failure.....	17
2.3.5 Combined Failure Modes.....	17
2.4 Available Recommended Design Provisions.....	19

2.4.1 ACI Committee 440 Design Recommendations.....	20
2.4.1.1 Debonding of FRP Reinforcement.....	21
2.4.1.2 Strengthened Moment Capacity.....	22
2.4.1.3 Development Length.....	26
2.4.1.4 Serviceability Recommendations.....	26
2.4.2 <i>fib</i> Task Group 9.3.....	27
2.4.3 Standards Australia.....	29
2.4.3.1 PE-Debonding Models.....	30
2.4.3.2 IC-Debonding Models.....	31
2.4.3.2.1 Basic IC-Debonding Models.....	32
2.4.3.2.2 Beam IC-Debonding Model.....	32
2.5 Models for FRP Debonding Failure Modes.....	33
2.5.1 Plate-End (PE) Debonding Models.....	33
2.5.1.1 Blaschko (2003).....	33
2.5.1.2 Hassan and Rizkalla (2003).....	35
2.5.1.3 Vasquez (2008).....	39
2.5.2 Intermediate Crack (IC) Debonding Models.....	43
2.5.2.1 Rosenboom (2006).....	43
2.5.2.2 Seracino, Raizal Saifulnaz, and Oehlers (2007).....	48
2.5.2.3 Seracino et al. (2007a).....	50
2.5.2.4 Said and Wu (2008).....	52
2.6 FRP Spacing Recommendations for NSM Strips.....	53
2.7 Effect of Concrete Surface Roughness.....	55

2.8 Effect of Embedding NSM Strips.....	56
2.9 Previous Testing of FRP-Strengthened Members.....	56
2.9.1 Externally-Bonded (EB) FRP Flexural Tests.....	57
2.9.1.1 Reed et al. (2005).....	57
2.9.1.2 War Memorial Bridge.....	59
2.9.2 Near-Surface Mounted (NSM) FRP Flexural Tests.....	60
2.9.2.1 Yost et al. (2007).....	60
2.9.2.2 Taljsten and Nordin (2007).....	61
2.9.2.3 Teng et al. (2006).....	62
2.9.2.4 Liu, Oehlers, and Seracino (2006).....	64
2.9.3 Both EB and NSM FRP Flexural Tests.....	65
2.9.3.1 El-Hacha and Rizkalla (2004).....	66
2.9.3.2 Jung et al. (2005).....	67
2.9.4 NSM Modified-Beam Pullout Tests.....	70
2.9.4.1 De Lorenzis and Nanni (2002).....	70
2.9.4.2 Sena Cruz and Barros (2004).....	72
2.9.4.3 Sena Cruz et al. (2006).....	73
2.10 Summary.....	74
Chapter 3: Letohatchee Bridge Background.....	77
3.1 Bridge Description.....	77
3.2 Demand on Existing Bridge.....	81
3.2.1 Dead Load.....	81
3.2.2 Live Load.....	82

3.2.3 Factored Total Load.....	87
3.3 Capacity of Existing Bridge.....	90
3.4 Bridge Deficiencies.....	98
3.5 Summary.....	102
Chapter 4: Evaluation of Existing Models.....	106
4.1 Introduction.....	106
4.2 PE-Debonding Models for NSM.....	108
4.2.1 Standards Australia (2008).....	108
4.2.1.1 Comparison to Previous Testing.....	108
4.2.1.2 Discussion of Model.....	116
4.2.2 Blaschko (2003).....	116
4.2.2.1 Discussion of Model.....	116
4.2.3 Hassan and Rizkalla (2003).....	117
4.2.3.1 Comparison to Previous Testing.....	117
4.2.3.2 Discussion of Model.....	123
4.2.4 Vasquez (2008).....	124
4.2.4.1 Comparison to Previous Testing.....	124
4.2.4.2 Discussion of Model.....	129
4.3 IC-Debonding Models for EB.....	130
4.3.1 ACI 440 (2008).....	130
4.3.1.1 Comparison to Previous Testing.....	130
4.3.1.2 Discussion of Model.....	136
4.3.2 <i>fib</i> 9.3 (2001).....	136



4.3.2.1 Comparison to Previous Testing.....	136
4.3.2.2 Discussion of Model.....	141
4.3.3 Standards Australia (2008).....	142
4.3.3.1 Comparison to Previous Testing.....	142
4.3.3.2 Discussion of Model.....	148
4.3.4 Rosenboom (2006).....	148
4.3.4.1 Comparison to Previous Testing.....	149
4.3.4.2 Discussion of Model.....	154
4.3.5 Seracino, Raizal Saifulnaz, and Oehlers (2007).....	154
4.3.5.1 Comparison to Previous Testing.....	154
4.3.5.2 Discussion of Model.....	160
4.3.6 Said and Wu (2008).....	160
4.3.6.1 Comparison to Previous Testing.....	160
4.3.6.2 Discussion of Model.....	166
4.4 IC-Debonding Models for NSM.....	166
4.4.1 ACI 440 (2008).....	166
4.4.1.1 Comparison to Previous Testing.....	166
4.4.1.2 Discussion of Model.....	174
4.4.2 <i>fib</i> 9.3 (2001).....	175
4.4.2.1 Comparison to Previous Testing.....	175
4.4.2.2 Discussion of Model.....	184
4.4.3 Standards Australia (2008).....	185
4.4.3.1 Comparison to Previous Testing.....	185

4.4.3.2 Discussion of Model.....	194
4.4.4 Seracino et al. (2007a).....	194
4.4.4.1 Comparison to Previous Testing.....	194
4.4.4.2 Discussion of Model.....	204
4.4.5 Said and Wu (2008).....	205
4.4.5.1 Comparison to Previous Testing.....	205
4.4.5.2 Discussion of Model.....	214
4.5 Summary of Model Evaluations.....	214
4.5.1 PE-Debonding Models.....	214
4.5.2 IC-Debonding Models.....	216
Chapter 5: Proposed Strengthening for the Letohatchee Bridge.....	222
5.1 FRP Selection.....	222
5.2 FRP Amount Needed.....	226
5.2.1 ACI 440 (2008).....	229
5.2.2 Standards Australia (2008).....	231
5.2.3 Seracino et al. (2007a).....	233
5.2.4 Summary of Models.....	235
5.3 FRP Length and Termination Points.....	237
5.4 FRP Spacing Recommendations.....	240
5.5 Summary of Proposed Design.....	242
5.6 Further Testing.....	243
Chapter 6: Proposed Laboratory Testing Program.....	247
6.1 Overall Objectives and Scope of Testing Program.....	247

6.2 Test Procedure.....	251
6.3 Test Series 1.....	253
6.3.1 Objectives of Test Series.....	253
6.3.2 Description of Test Specimens.....	253
6.3.3 Anticipated Behavior and Failure Modes.....	256
6.3.3.1 Unstrengthened Specimens.....	257
6.3.3.2 Strengthened Specimens.....	258
6.4 Test Series 2.....	260
6.4.1 Objectives of Test Series.....	261
6.4.2 Description of Test Specimens.....	261
6.4.3 Anticipated Behavior and Failure Modes.....	264
6.4.3.1 Unstrengthened Specimens.....	264
6.4.3.2 Strengthened Specimens.....	265
6.5 Test Series 3.....	266
6.5.1 Objectives of Test Series.....	266
6.5.2 Description of Test Specimens.....	266
6.5.3 Anticipated Behavior and Failure Modes.....	268
6.5.3.1 Unstrengthened Specimens.....	268
6.5.3.2 Strengthened Specimens.....	269
6.6 Test Series 4.....	270
6.6.1 Objectives of Test Series.....	270
6.6.2 Description of Test Specimens.....	271
6.6.3 Anticipated Behavior and Failure Modes.....	272

6.6.3.1 Unstrengthened Specimens.....	273
6.6.3.2 Strengthened Specimens.....	273
Chapter 7: Summary and Conclusions.....	275
7.1 Summary.....	275
7.2 Conclusions.....	277
7.2.1 Debonding Models.....	277
7.2.2 Letohatchee Bridge.....	278
7.3 Recommendations.....	279
REFERENCES.....	281
APPENDIX A: NOTATION.....	286
APPENDIX B: SAMPLE CALCULATIONS.....	291

## LIST OF TABLES

Table 2-1: Values of Tensile Strength and Young's Modulus for FRP.....	6
Table 2-2: Typical Density Values for FRP Materials and Steel (ACI 440 2008).....	8
Table 2-3: Environment Reduction Factor Values Given by ACI 440 (2008).....	21
Table 2-4: Summary of NSM Groove Spacing and Side Cover Recommendations.....	55
Table 3-1: Vehicle Names and Load Arrangements Used for Bridge Analysis.....	83
Table 3-2: AASHTO Load Combinations.....	88
Table 3-3: Portion of Each Bar Group's Yield Stress Used for Positive Moment Capacity Calculations.....	94
Table 3-4: Portion of Each Bar Group's Yield Stress Used for Negative Moment Capacity Calculations.....	97
Table 3-5: Positive-Moment Deficiency for Posting Trucks at Critical Locations.....	101
Table 3-6: Negative-Moment Deficiencies for Posting Trucks at Critical Locations.....	102
Table 4-1: List of Experimental Test Series.....	106
Table 4-2: Comparison of the PE-Debonding Model by Standards Australia (2008) to NSM Test Results.....	110
Table 4-3: FRP Strain Predictions using the Standards Australia (2008) PE-Debonding Model and NSM Test Results.....	115
Table 4-4: Comparison of the PE-Debonding Model by Hassan and Rizkalla (2003) to NSM Test Results.....	118

Table 4-5: FRP Strain Predictions using the Hassan and Rizkalla (2003) PE-Debonding Model and NSM Test Results.....	123
Table 4-6: Comparison of the PE-Debonding Model by Vasquez (2008) to NSM Test Results.....	125
Table 4-7: FRP Strain Predictions using the Vasquez (2008) PE-Debonding Model and NSM Test Results.....	129
Table 4-8: Comparison of the IC-Debonding Model by ACI 440 (2008) to EB Test Results.....	131
Table 4-9: FRP Strain Predictions using the ACI 440 (2008) IC-Debonding Model and EB Test Results.....	135
Table 4-10: Comparison of the IC-Debonding Model by <i>fib</i> 9.3 (2001) to EB Test Results.....	137
Table 4-11: FRP Strain Predictions using the <i>fib</i> 9.3 (2001) IC-Debonding Model and EB Test Results.....	140
Table 4-12: Comparison of the IC-Debonding Model by Standards Australia (2008) to EB Test Results.....	143
Table 4-13: FRP Strain Predictions using the Standards Australia (2008) IC-Debonding Model and EB Test Results.....	147
Table 4-14: Comparison of the IC-Debonding Model by Rosenboom (2006) to EB Test Results.....	149
Table 4-15: FRP Strain Predictions using the Rosenboom (2006) IC-Debonding Model and EB Test Results.....	153
Table 4-16: Comparison of the IC-Debonding Model by Seracino, Raizal Saifulnaz, and	

Oehlers (2007) to EB Test Results.....	155
Table 4-17: FRP Strain Predictions using the Seracino, Raizal Saifulnaz, and Oehlers (2007) IC-Debonding Model and EB Test Results.....	159
Table 4-18: Comparison of the IC-Debonding Model by Said and Wu (2008) to EB Test Results.....	161
Table 4-19: FRP Strain Predictions using the Said and Wu (2008) IC-Debonding Model and EB Test Results.....	165
Table 4-20: Comparison of the IC-Debonding Model by ACI 440 (2008) to NSM Test Results.....	168
Table 4-21: FRP Strain Predictions using the ACI 440 (2008) IC-Debonding Model and NSM Test Results.....	173
Table 4-22: Comparison of the IC-Debonding Model by <i>fib</i> 9.3 (2001) to NSM Test Results.....	176
Table 4-23: FRP Strain Predictions using the <i>fib</i> 9.3 (2001) IC-Debonding Model and NSM Test Results.....	183
Table 4-24: Comparison of the IC-Debonding Model by Standards Australia (2008) to NSM Test Results.....	186
Table 4-25: FRP Strain Predictions using the Standards Australia (2008) IC-Debonding Model and NSM Test Results.....	193
Table 4-26: Comparison of the IC-Debonding Model by Seracino et al. (2007a) to NSM Test Results.....	195
Table 4-27: FRP Strain Predictions using the Seracino et al. (2007a) IC-Debonding Model and NSM Test Results.....	203

Table 4-28: Comparison of the IC-Debonding Model by Said and Wu (2008) to NSM Test Results.....	206
Table 4-29: FRP Strain Predictions using the Said and Wu (2008) IC-Debonding Model and NSM Test Results.....	213
Table 5-1: Negative Moment Deficiencies for Posting Trucks at Critical Locations.....	224
Table 5-2: Dimensions and Material Properties for Capacity Calculations.....	227
Table 5-3: FRP Strain Values for the Letohatchee Bridge using the Model by Standards Australia (2008).....	232
Table 5-4: FRP Strain Values for the Letohatchee Bridge using the Model by Seracino, Jones, et al. (2007).....	234
Table 5-5: FRP Spacing Recommendations for Letohatchee Bridge.....	240
Table 5-6: Reinforcement Ratios for the Letohatchee Bridge.....	243
Table 5-7: Reinforcement Ratios for the Experimental Tests from the Literature.....	245
Table 6-1: Properties and Dimensions of Steel and FRP for Proposed Testing Program.....	251
Table 6-2: Unstrengthened Moments for Specimens in Test Series 1.....	257
Table 6-3: Predicted Strengthened Capacities, Stresses, Strains, and Failure Modes.....	259
Table 6-4: Unstrengthened Moments for Specimens in Test Series 2.....	264
Table 6-5: Predicted Strengthened Capacities, Stresses, Strains, and Failure Modes.....	265
Table 6-6: Unstrengthened Moments for Specimens in Test Series 3.....	268
Table 6-7: Predicted Strengthened Capacities, Stresses, Strains, and Failure Modes.....	269
Table 6-8: Unstrengthened Moments for Specimens in Test Series 4.....	273
Table 6-9: Predicted Strengthened Capacities, Stresses, Strains, and Failure Modes.....	274



Table B-1: Input for Sample Calculations for All Models.....	291
Table B-2: Sample Calculations using each Model.....	291

## LIST OF FIGURES

Figure 1-1: Photo of an NSM Application (Hughes Brothers 2009).....	2
Figure 2-1: Stress-Strain Graph of Typical FRP Systems Compared to Steel (Vasquez 2008).....	7
Figure 2-2: Surface Preparation for a Wet-Layup EB System Installation.....	9
Figure 2-3: Application of FRP in a Wet-Layup EB System.....	9
Figure 2-4: Installation of a Wet-Layup System.....	10
Figure 2-5: Completed Installation of a Wet-Layup EB System.....	10
Figure 2-6: Application of FRP in a Precured System (Carmichael and Barnes 2005)....	11
Figure 2-7: Installation of a Precured System (Carmichael and Barnes 2005).....	12
Figure 2-8: Completed Installation of a Precured System (Carmichael and Barnes 2005).....	12
Figure 2-9: Installation of an NSM System (Hughes Brothers 2009).....	14
Figure 2-10: Illustration of a PE-Debonding Failure Mode (Vasquez 2008).....	15
Figure 2-11: Illustration of an IC-Debonding Failure Mode (Vasquez 2008).....	16
Figure 2-12: Illustration of a CDC Debonding Failure Mode (Vasquez 2008).....	18
Figure 2-13: Test Results of a Cover Delamination Failure (Fanning and Kelly 2001)....	19
Figure 2-14: Internal Strain and Stress Profiles for a Section in Flexure (ACI 440 2008).....	25
Figure 2-15: Elevation Views of a Pull-Off Test (Blaschko 2003).....	34

Figure 2-16: Elevation and Cross Section of Test Specimen and the Steel Reinforcement Details (Hassan and Rizkalla 2003).....	36
Figure 2-17: Mohr-Coulomb Failure Criterion (Hassan and Rizkalla 2003).....	38
Figure 2-18: Stress Distribution at the NSM Strip Cutoff Point (Vasquez 2008).....	40
Figure 2-19: Mohr’s Circle (left) and the Resultant Stress Distribution (right) (Vasquez 2008).....	42
Figure 2-20: Layout of C-Channel Girders (Rosenboom 2006).....	44
Figure 2-21: Both Cross Sections of the C-Channel Girders (Rosenboom 2006).....	44
Figure 2-22: Schematic of a Push-Pull Test for EB (Seracino, Raizal Saifulnaz, and Oehlers 2007).....	48
Figure 2-23: IC-Debonding Failure Plane for EB and NSM strips (Seracino, Raizal Saifulnaz, and Oehlers 2007).....	49
Figure 2-24: Diagram of a Push-Pull Test for NSM (Seracino et al 2007a).....	50
Figure 2-25: Cross Section of Test Specimens (Reed et al. 2005).....	57
Figure 2-26: Test Setup for Specimens (Reed et al. 2005).....	58
Figure 2-27: Picture of War Memorial Bridge (Carmichael and Barnes 2005).....	59
Figure 2-28: Test Setup with Cross Sections (Yost et al. 2007).....	61
Figure 2-29: Test Setup for Specimens (Liu, Oehlers, and Seracino 2006).....	64
Figure 2-30: Test Setup and Cross Section (El-Hacha and Rizkalla 2004).....	66
Figure 2-31: Elevation View and Cross-Sectional View of Test Setup (Jung et al. 2005).....	68
Figure 2-32: Plan View of the NSM-Strengthening Schemes (Jung et al. 2005).....	68
Figure 2-33: Plan View of the Bottom of a Specimen with Mechanical Interlocking	

Grooves (Jung et al. 2005).....	69
Figure 2-34: Test Setup and Cross Section (De Lorenzis and Nanni 2002).....	71
Figure 2-35: Test Setup and Cross Section (Sena Cruz and Barros 2004).....	72
Figure 2-36: Test Setup and Cross Section (Sena Cruz et al. 2006).....	74
Figure 3-1: Location of the Letohatchee Bridge (Google Maps 2009).....	78
Figure 3-2: Picture of the Letohatchee Bridge.....	79
Figure 3-3: Plan View of Half of the Letohatchee Bridge.....	80
Figure 3-4: Sketch of the Cross Section at an Interior Support for the Letohatchee Bridge.....	80
Figure 3-5: Moment Diagrams for Dead Load Groups for an Exterior Girder.....	82
Figure 3-6: Example of a load-posting sign (Carmichael and Barnes 2005).....	85
Figure 3-7: Positive Live Load Moment Envelopes across Girder 1.....	86
Figure 3-8: Negative Live Load Moment Envelopes across Girder 1.....	87
Figure 3-9: Factored Ultimate Moment Envelope for the H20 Loadings using the Operating Load Combination.....	89
Figure 3-10: Factored Ultimate Moment Envelope for the Posting Trucks using the Operating Load Combination.....	90
Figure 3-11: Exterior Girder Cross Section at an Interior Support Location.....	91
Figure 3-12: Exterior Girder Cross Section at Midspan.....	92
Figure 3-13: Elevation View of the Amount of Steel and the Approximate Termination Locations in Girder 1.....	93
Figure 3-14: Factored Positive Moment Capacity along Exterior Girder.....	96
Figure 3-15: Factored Negative Moment Capacity along Exterior Girder.....	98

Figure 3-16: Factored Demand Versus Factored Resistance for H20 Trucks.....	99
Figure 3-17: Factored Demand Versus Factored Resistance for Posting Trucks.....	100
Figure 3-18: Elevation View of the Locations of the Letohatchee Bridge Deficiencies.....	103
Figure 3-19: Bar Termination and Deficient Region Locations.....	104
Figure 4-1: Comparison between NSM Test Results and Standards Australia (2008) PE-Debonding Capacity Predictions.....	113
Figure 4-2: Comparison between NSM Test Results and Standards Australia (2008) PE-Debonding Change-in-Capacity Predictions.....	114
Figure 4-3: Comparison between NSM Test Results and Hassan and Rizkalla (2003) PE-Debonding Capacity Predictions.....	121
Figure 4-4: Comparison between NSM Test Results and Hassan and Rizkalla (2003) PE-Debonding Change-in-Capacity Predictions.....	122
Figure 4-5: Comparison between NSM Test Results and Vasquez (2008) PE-Debonding Capacity Predictions.....	127
Figure 4-6: Comparison between NSM Test Results and Vasquez (2008) PE-Debonding Change-in-Capacity Predictions.....	128
Figure 4-7: Comparison between EB Test Results and ACI 440 (2008) IC-Debonding Capacity Predictions.....	133
Figure 4-8: Comparison between EB Test Results and ACI 440 (2008) IC-Debonding Change-in-Capacity Predictions.....	134
Figure 4-9: Comparison between EB Test Results and <i>fib</i> 9.3 (2001) IC-Debonding Capacity Predictions.....	138

Figure 4-10: Comparison between EB Test Results and <i>fib</i> 9.3 (2001) IC-Debonding Change-in-Capacity Predictions.....	139
Figure 4-11: Comparison between EB Test Results and Standards Australia (2008) IC- Debonding Capacity Predictions.....	145
Figure 4-12: Comparison between EB Test Results and Standards Australia (2008) IC- Debonding Change-in-Capacity Predictions.....	146
Figure 4-13: Comparison between EB Test Results and Rosenboom (2006) IC- Debonding Capacity Predictions.....	151
Figure 4-14: Comparison between EB Test Results and Rosenboom (2006) IC- Debonding Change-in-Capacity Predictions.....	152
Figure 4-15: Comparison between EB Test Results and Seracino, Raizal Saifulnaz, and Oehlers (2007) IC-Debonding Capacity Predictions.....	157
Figure 4-16: Comparison between EB Test Results and Seracino, Raizal Saifulnaz, and Oehlers (2007) IC-Debonding Change-in-Capacity Predictions.....	158
Figure 4-17: Comparison between EB Test Results and Said and Wu (2008) IC- Debonding Capacity Predictions.....	163
Figure 4-18: Comparison between EB Test Results and Said and Wu (2008) IC- Debonding Change-in-Capacity Predictions.....	164
Figure 4-19: Comparison between NSM Test Results and ACI 440 (2008) IC-Debonding Capacity Predictions.....	169
Figure 4-20: Comparison between NSM Test Results and ACI 440 (2008) IC-Debonding Change-in-Capacity Predictions.....	170
Figure 4-21: Enlarged Graph of the ACI 440 (2008) NSM Capacity Comparisons.....	171

Figure 4-22: Enlarged Graph of the ACI 440 (2008) NSM Change-in-Capacity Comparisons.....	172
Figure 4-23: Comparison between NSM Test Results and <i>fib</i> 9.3 (2001) IC-Debonding Capacity Predictions.....	179
Figure 4-24: Comparison between NSM Test Results and <i>fib</i> 9.3 (2001) IC-Debonding Change-in-Capacity Predictions.....	180
Figure 4-25: Enlarged Graph of the <i>fib</i> 9.3 (2001) NSM Capacity Comparisons.....	181
Figure 4-26: Enlarged Graph of the <i>fib</i> 9.3 (2001) NSM Change-in-Capacity Comparisons.....	182
Figure 4-27: Comparison between NSM Test Results and Standards Australia (2008) IC- Debonding Capacity Predictions.....	189
Figure 4-28: Comparison between NSM Test Results and Standards Australia (2008) IC- Debonding Change-in-Capacity Predictions.....	190
Figure 4-29: Enlarged Graph of the Capacity Comparisons of the Standards Australia (2008) Model.....	191
Figure 4-30: Enlarged Graph of the Change-in-Capacity Comparisons of the Standards Australia (2008) Model.....	192
Figure 4-31: Comparison between NSM Test Results and Seracino et al. (2007a) IC- Debonding Capacity Predictions.....	199
Figure 4-32: Comparison between NSM Test Results and Seracino et al. (2007a) IC- Debonding Change-in-Capacity Predictions.....	200
Figure 4-33: Enlarged Graph of the Capacity Comparisons of the Seracino et al. (2007a) Model.....	201

Figure 4-34: Enlarged Graph of the Change-in-Capacity Comparisons of the Seracino, Jones, et al. (2007) Model.....	202
Figure 4-35: Comparison between NSM Test Results and Said and Wu (2008) IC- Debonding Capacity Predictions.....	209
Figure 4-36: Comparison between NSM Test Results and Said and Wu (2008) IC- Debonding Change-in-Capacity Predictions.....	210
Figure 4-37: Enlarged Graph of the Capacity Comparisons of the Said and Wu (2008) Model.....	211
Figure 4-38: Enlarged Graph of the Change-in-Capacity Comparisons of the Said and Wu (2008) Model.....	212
Figure 4-39: Comparison of Capacity Predictions by PE-Debonding Models to NSM Experimental Results.....	215
Figure 4-40: Comparison of Change-in-Capacity Predictions by PE-Debonding Models to NSM Experimental Results.....	216
Figure 4-41: Comparison of Capacity Predictions by IC-Debonding Models to EB Experimental Results.....	217
Figure 4-42: Comparison of Change-in-Capacity Predictions by IC-Debonding Models to EB Experimental Results.....	218
Figure 4-43: Comparison of Capacity Predictions by IC-Debonding Models to NSM Experimental Results.....	219
Figure 4-44: Comparison of Change-in-Capacity Predictions by IC-Debonding Models to NSM Experimental Results.....	220
Figure 5-1: Elevation View of the Locations of the Letohatchee Bridge Deficiencies...	223



Figure 5-2: Recommended Groove Dimensions (ACI 440 2008).....	228
Figure 5-3: Letohatchee Bridge Capacities using the Model by ACI 440 (2008).....	229
Figure 5-4: Letohatchee Bridge Capacities using the Model by Standards Australia (2008).....	231
Figure 5-5: Letohatchee Bridge Capacities using the Model by Seracino et al. (2007a).....	233
Figure 5-6: Required Amounts of Thin FRP Strips for each Model.....	235
Figure 5-7: Required Amounts of Thick FRP Strips for each Model.....	236
Figure 5-8: Factored Demand Envelope and Factored Resistance.....	238
Figure 5-9: Elevation View of the Recommended FRP Lengths for the Letohatchee Bridge (not to scale).....	239
Figure 5-10: Cross Section of a Possible Spacing Configuration for Six NSM Strips per Girder.....	241
Figure 5-11: Cross Section of a Possible Spacing Configuration for Three NSM Strips per Girder.....	241
Figure 6-1: Elevation View of the Proposed Test Setup for a Typical Specimen.....	249
Figure 6-2: Specimen Identification System.....	250
Figure 6-3: (a) Cross Section for Specimens with $\rho_s$ of 0.2% (b) Cross Section for Specimens with $\rho_s$ of 0.6%.....	254
Figure 6-4: Specimen Names and Cross Sections for Test Series 1.....	255
Figure 6-5: (a) Cross Section of Specimen 2-LS2F00 (b) Cross Section for Deeper Specimens.....	262
Figure 6-6: Specimen Names and Cross Sections for Test Series 2.....	263

Figure 6-7: Cross Section of Specimens in Test Series 3.....	267
Figure 6-8: Specimen Names and Cross Sections for Test Series 3.....	267
Figure 6-9: Cross Section of Specimens in Test Series 4.....	271
Figure 6-10: Specimen Names and Cross Sections for Test Series 4.....	272

## **Chapter 1: Introduction**

### **1.1 Background**

Fiber-reinforced polymer (FRP) laminates are being used to effectively strengthen reinforced concrete members. A flexural application for this material is for strengthening of bridges. Historically, the most widely used method of strengthening bridges for positive moment has been to bond steel plates to the underside of bridge girders. This method is labor-intensive and can become very costly due to the extensive scaffolding required to support the steel plates during bonding to the concrete surface (Rosenboom 2006).

An alternative to this process is externally-bonded (EB) FRP reinforcement. For this application, EB strips or sheets are bonded to the concrete surface with an epoxy. The EB reinforcement is light enough for workers to support by themselves, so extensive scaffolding is not needed.

If the bridge girders need negative-moment strengthening, then the FRP can be applied in a near-surface mounted (NSM) application. For NSM FRP reinforcement, a longitudinal groove is cut in the top of the concrete, epoxy is applied into the groove, and the FRP strip is placed into the epoxy-filled groove. Figure 1-1 shows a picture of an NSM application.



**Figure 1-1:** Photo of an NSM Application (Hughes Brothers 2009)

For this application, no traffic lanes need to be closed for the lanes *underneath* the bridge, and only the bridge lanes that are being worked on need to be closed. As opposed to the EB application, the NSM application does not need extensive surface preparation of the concrete. It is relatively simple compared to the other methods and can be an effective strengthening technique (El-Hacha and Rizkalla 2004).

The Alabama Department of Transportation (ALDOT) has received Federal Highway Administration (FHWA) funding to strengthen a bridge in Lowndes County, near Letohatchee, Alabama, through the TEA-21 Innovative Bridge Research and Construction (IBRC) program. This bridge has a Bridge Inventory Number (BIN) of 8847. For this type of bridge, there are concerns about girder negative-moment capacity

in portions of each span. If the strengthening scheme proves to be effective for this bridge, it could be used to strengthen other bridges that were constructed using the same ALDOT standard design.

## **1.2 Research Objectives and Tasks**

The main objectives of this research are to study the behavior of FRP-strengthened concrete beams, quantify the amount of flexural strengthening that FRP can provide, and develop recommendations for an NSM FRP strengthening scheme. To accomplish these objectives, the following tasks were completed:

1. The current models in the literature were analyzed and compared to existing experimental research to determine the most accurate models.
2. Quantify the amount of strengthening needed by determining the demand and capacity of the Letohatchee bridge.
3. Once the extent of the current knowledge was known, a strengthening scheme for the bridge was developed.
4. Finally, a testing program was proposed to further study IC-debonding behavior and to result in a more efficient strengthening scheme for the bridge.

## **1.3 Organization of Thesis**

An overview on the behavior of FRP is presented in Chapter 2. Material properties and applications for FRP are discussed. Problems associated with FRP-strengthened members are reviewed, as well as various models proposed by researchers to describe the behavior of FRP-strengthened concrete beams. Existing experimental tests on FRP behavior are then described.

A background on the existing bridge near Letohatchee, Alabama, is presented in Chapter 3. A description of the bridge is given. The demand and capacity for the existing bridge are shown along with the locations and magnitudes of the bridge's deficiencies.

An examination of the code recommendations and some of the proposed models that are available in the literature is presented in Chapter 4. Model predictions are compared to published experimental results to determine the accuracy of the models. The advantages and shortcomings of the models are also discussed.

A proposed strengthening plan for the Letohatchee bridge based on analyses of the models discussed in the previous chapter is presented in Chapter 5. The amount, length, and spacing of the FRP are all proposed.

A proposed laboratory testing program to further investigate FRP behavior is presented in Chapter 6. Four different test series are suggested, and the properties and specifications of the experimental program are given.

Chapter 7 provides a summary of the thesis and conclusions reached by the author. Some recommendations for future testing are also given.

## **Chapter 2: Behavior of Reinforced Concrete Beams Strengthened with FRP**

### **2.1 Introduction**

Because fiber-reinforced polymer (FRP) materials have been found to be stronger and lighter than steel, there has been much research into understanding FRP behavior. For FRP reinforcement to be used in the field, the designer must be able to quantify how much strengthening the FRP material will add to the in-place structure. Premature debonding has become a common observance for externally-bonded FRP reinforcement, and understanding this behavior is important for the effective implementation of FRP as a strengthening material (Vasquez 2008).

This chapter covers basic principles associated with FRP behavior. The composition, applications, and important properties of FRP materials are discussed. FRP-strengthened members are examined, and different failure modes are explained. The process of determining the capacity of strengthened members is described, including available design recommendations as well as behavioral models formulated by researchers. Also, various factors that might affect this strengthened capacity are discussed. Finally, an overview of some relevant experimental programs is presented.

## 2.2 Components and Applications of FRP

FRP reinforcement is manufactured through a variety of methods using various components and is applied to existing structures in a couple of different ways. These applications can be divided into two main categories: externally-bonded (EB) FRP systems and near-surface mounted (NSM) FRP systems (Seracino, Raizal Saifulnaz, and Oehlers 2007). This section discusses FRP materials and their different applications.

### 2.2.1 Different FRP Materials and Properties

Three fiber types are commonly used in FRP: carbon, glass, and aramid fibers. Carbon fibers were the most commonly used fibers found in the available literature, whereas aramid fibers were the least common.

FRP materials generally have higher tensile strengths than steel. Table 2-1 shows some typical values for tensile strength and Young's modulus of FRP materials that are given in the document by ACI Committee 440 titled, "Guide for the Design and Construction of Externally Bonded FRP Systems for Strengthening Concrete Structures (ACI 440.2R-08)."

**Table 2-1:** Values of Tensile Strength and Young's Modulus for FRP

FRP Fiber Type	Ultimate Tensile Strength	Young's Modulus
Carbon	1,020 to 2,080 MPa (150 to 350 ksi)	100 to 140 GPa (15,000 to 21,000 ksi)
Glass	520 to 1,400 MPa (75 to 200 ksi)	20 to 40 GPa (3,000 to 6,000 ksi)
Aramid	700 to 1,720 MPa (100 to 250 ksi)	48 to 68 GPa (7,000 to 10,000 ksi)

All of these FRP materials have a greater tensile strength than reinforcing steel's typical yield strength and ultimate strength of about 420 MPa (60 ksi) and 520 MPa (75



ksi), respectively. As shown in the table, the FRP materials have a smaller elastic modulus than steel's typical value of 200 GPa (29,000 ksi).

Unlike steel reinforcement, FRP reinforcement does not yield; it remains practically linear-elastic until failure. This property of FRP results in a brittle failure in tension. Figure 2-1 shows the strength advantage of FRP reinforcement over steel reinforcement, but it also shows the non-ductile behavior of the FRP material. The FRP ruptures at a strain of around 1 to 3%, whereas the steel ruptures at around 30%. In Figure 2-1, the average values from Table 2-1 were used for the FRP materials.

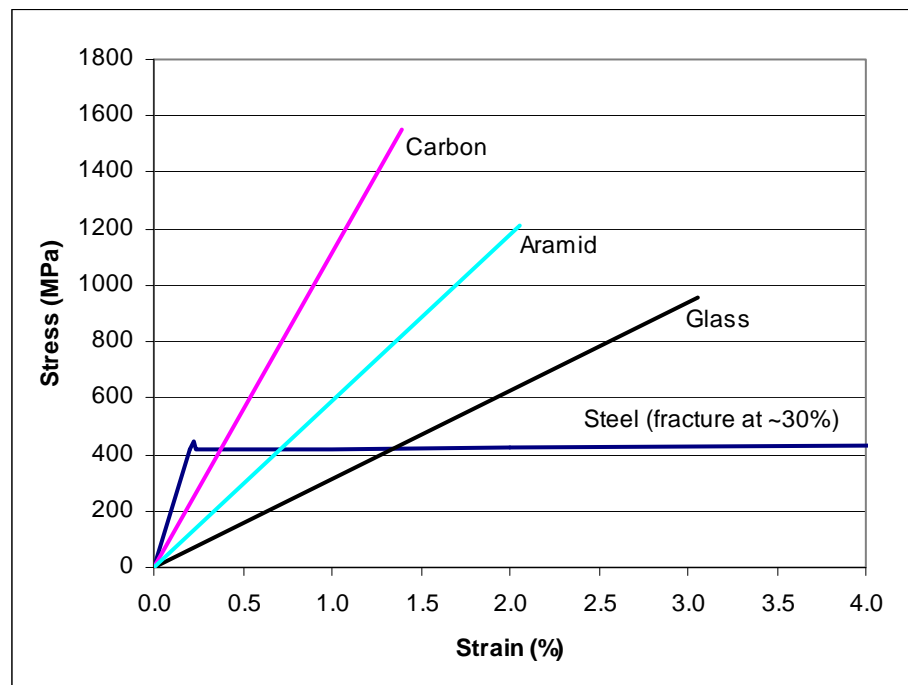


**Figure 2-1:** Stress-Strain Behavior of Typical FRP Systems Compared to Steel

(Vasquez 2008)

Another important property of FRP is its density. According to ACI 440 (2008), the typical density of FRP is approximately four to six times lower than that of steel.

Table 2-2 shows some typical density values for FRP materials and for steel.

**Table 2-2:** Typical Density Values for FRP Materials and Steel (ACI 440 2008)

Steel	CFRP	GFRP	AFRP
7.9 g/cm <sup>3</sup> (490 pcf)	1.5 to 1.6 g/cm <sup>3</sup> (90 to 100 pcf)	1.2 to 2.1 g/cm <sup>3</sup> (75 to 130 pcf)	1.2 to 1.5 g/cm <sup>3</sup> (75 to 90 pcf)

### 2.2.2 Externally-Bonded (EB) FRP

The most common application of FRP for strengthening of existing reinforced concrete structures is externally-bonded (EB) systems. In this method, the FRP sheets are bonded to the external surface of the concrete. Typical EB systems can be divided into wet-layup systems and precured systems. Wet-layup systems involve dry unidirectional or multidirectional fiber sheets that are saturated on site with a resin and then bonded to the concrete surface with the resin and a compatible primer and putty. The wet-layup systems are then cured in place, similar to cast-in-place concrete. Precured systems consist of unidirectional or multidirectional precured sheets that are applied to the concrete surface with an adhesive, primer, and putty and are cured before they arrive at the site. Both EB systems can be used to strengthen beams in flexure or shear and to strengthen columns, especially for seismic confinement (ACI 440 2008; *fib* 9.3 2001).

Figures 2-2 through 2-5 show an example of a wet-layup system installation. The pictures were taken by fellow Auburn University researchers.



**Figure 2-2:** Surface Preparation for a Wet-Layup EB System Installation



**Figure 2-3:** Application of FRP in a Wet-Layup EB System



**Figure 2-4:** Installation of a Wet-Layup EB System



**Figure 2-5:** Completed Installation of a Wet-Layup EB System

Figures 2-6 through 2-8 show the installation and application of a precured system.



**Figure 2-6:** Application of FRP in a Precured System (Carmichael and Barnes 2005)





**Figure 2-7:** Installation of a Precured System (Carmichael and Barnes 2005)



**Figure 2-8:** Completed Installation of a Precured System (Carmichael and Barnes 2005)

### **2.2.3 Near-Surface Mounted (NSM) FRP**

EB FRP systems have been found to debond at relatively low values of FRP axial strain (Seracino et al. 2007a; Liu, Oehlers, and Seracino 2006). In response to this phenomenon, near-surface mounted (NSM) reinforcement has become more appealing. In NSM systems, instead of bonding the laminate to the exterior of the concrete member, it is bonded in grooves cut into the concrete surface. First, a groove is cut in the concrete surface. After the groove is cleaned of dust and fine particles, epoxy is injected into the groove, and the NSM FRP strip or bar is placed into the epoxy-filled groove. Then, the groove is filled completely with epoxy, and the excess is scraped off so that the epoxy is flush with the concrete surface. If more than one NSM strip or bar is needed, typically another parallel groove is cut at a certain distance away from the first groove. Figure 2-9 shows the installation of an NSM system for positive-moment strengthening.

NSM reinforcement is commonly found in two types: rods and strips. The rods typically have a circular cross section and are usually deformed along the length, much like deformed steel reinforcement. The cross-sectional area of an NSM rod is typically that of a SI #10 or #13 (#3 or #4 U.S. Customary size) steel reinforcing bar. The NSM strips have a rectangular shape, with dimensions of about 2 mm (0.079 in.) thick by 16 to 20 mm (0.63 to 0.79 in.) wide (Hughes Brothers 2009).



**Figure 2-9:** Installation of an NSM System (Hughes Brothers 2009)

According to *fib* 9.3 (2001), pultrusion is “an automated, continuous process for manufacturing composite rods and structural shapes having a constant cross section. Roving and/or tows are saturated with resin and continuously pulled through a heated die, where the part is formed and cured. The cured part is then cut to length.” NSM rods are formed by this pultrusion process and typically delivered to the site in the form of a single bar. NSM strips are also formed by this pultrusion process, but are typically delivered to the site in a 1-m (3-ft) diameter roll.

One of the inherent advantages of NSM systems over EB systems is the fact that the concrete can bond to both faces of the FRP strip rather than just one face. Because EB



systems typically fail due to FRP debonding, the increased bond capacity of NSM strips should, in theory, increase the FRP debonding resistance.

### 2.3 Failure Modes of FRP-Strengthened Members

There are many different failure modes for FRP-strengthened members. The controlling failure mode depends on many parameters, such as the location of the FRP cutoff point, the concrete compressive strength, the bonded width of the FRP, and the FRP rupture stress. The strengthened member can fail due to debonding of the FRP laminate, caused by either plate-end (PE) debonding or intermediate crack (IC) debonding. It can also fail due to rupture of the FRP reinforcement, failure in the concrete, or a combination of any of these modes.

#### 2.3.1 Plate-End (PE) Debonding

Plate-end (PE) debonding occurs when the shear stresses in the FRP reinforcement at the location of the cutoff point become too high and cause the strip to peel off of the concrete. The failure can either occur in the adhesive layer or in the concrete layer (*fib* 9.3 2001). Figure 2-10 shows an illustration of this debonding mechanism.

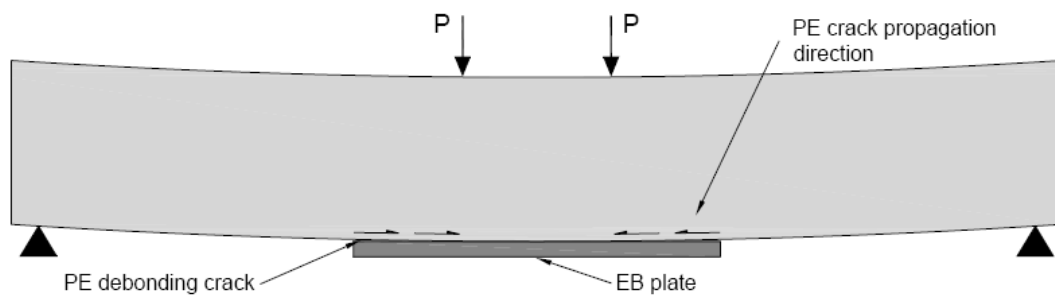


**Figure 2-10:** Illustration of a PE-Debonding Failure Mode (Vasquez 2008)

### 2.3.2 Intermediate Crack (IC) Debonding

Intermediate crack (IC) debonding occurs when a flexural crack in the concrete creates a stress concentration in the FRP reinforcement, which typically occurs in or near the region of maximum moment (Vasquez 2008). Figure 2-11 shows an illustration of this debonding mechanism.

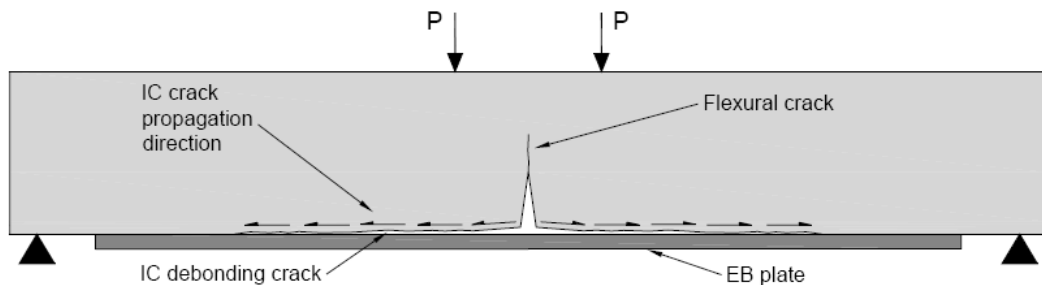


**Figure 2-11:** Illustration of an IC-Debonding Failure Mode (Vasquez 2008)

Once the stress exceeds a limiting stress at the FRP-to-concrete interface, the FRP reinforcement starts to separate from the concrete member. After this occurs, the debonding propagates from the flexural crack(s) to the end of the reinforcement until the FRP reinforcement becomes totally ineffective (Vasquez 2008).

### 2.3.3 FRP Rupture

Failure due to FRP rupture maximizes the use of the FRP material. By reaching the FRP rupture stress, the full capacity of the strengthening material is attained. Up to this rupture level, the FRP remains in the linear-elastic range. Once this rupture stress is reached, the FRP material does not yield and can no longer strengthen the concrete member. It cannot sustain any loading beyond this point, and it results in a very brittle failure of the FRP reinforcement. The concrete member may exhibit adequate curvature or displacement

ductility, but the FRP reinforcement will fail in a brittle manner, and no sustained loads beyond this rupture point can be carried by the FRP material (Rosenboom 2006).

#### **2.3.4 Concrete Failure**

If the strength of the concrete is low enough or if the member is reinforced with too much FRP reinforcement, the concrete can fail before any failure occurs in the FRP material. Concrete failure can occur due to the crushing of the concrete in the compressive region or due to a shear failure.

#### **2.3.5 Combined Failure Modes**

Frequently, FRP-strengthened members fail by a combination of failure modes, where the failure modes occur almost simultaneously. Sometimes, it is difficult to distinguish which mode caused the collapse. In a laboratory setup, if the instruments are not positioned at the critical locations, it can be very difficult to conclude which failure mode occurs first.

Some researchers have mentioned other failure modes that are not previously listed in this section. One of these is called critical diagonal crack (CDC) debonding. CDC debonding is a combination of IC and PE debonding that is caused by a diagonal shear crack (Vasquez 2008). This shear crack occurs in the shear span of the member, and if it reaches the FRP reinforcement near the end of the plate, it could cause a peel-off failure due to stress concentrations at the crack location and limited bonded length beyond the crack. CDC debonding is illustrated in Figure 2-12.

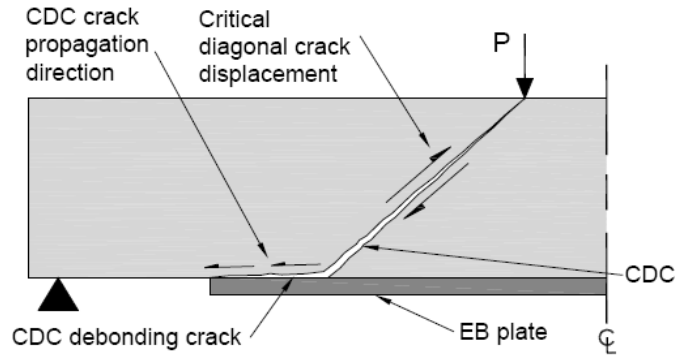


**Figure 2-12:** Illustration of a CDC Debonding Failure Mode (Vasquez 2008)

Another failure mode that has been described by researchers is cover delamination. Cover delamination involves a combination of PE debonding and a failure in the concrete. Just like PE debonding, when the shear stresses at the plate cutoff location get too high, the plate starts to peel off of the beam. However, with cover delamination, the failure plane continues into the concrete section up to the internal longitudinal tension steel. Instead of the FRP plate peeling off, the entire concrete cover, starting from the location of the plate cutoff end, peels off of the beam (Fanning and Kelly 2001). Figure 2-13 shows a laboratory test specimen that failed due to cover delamination.

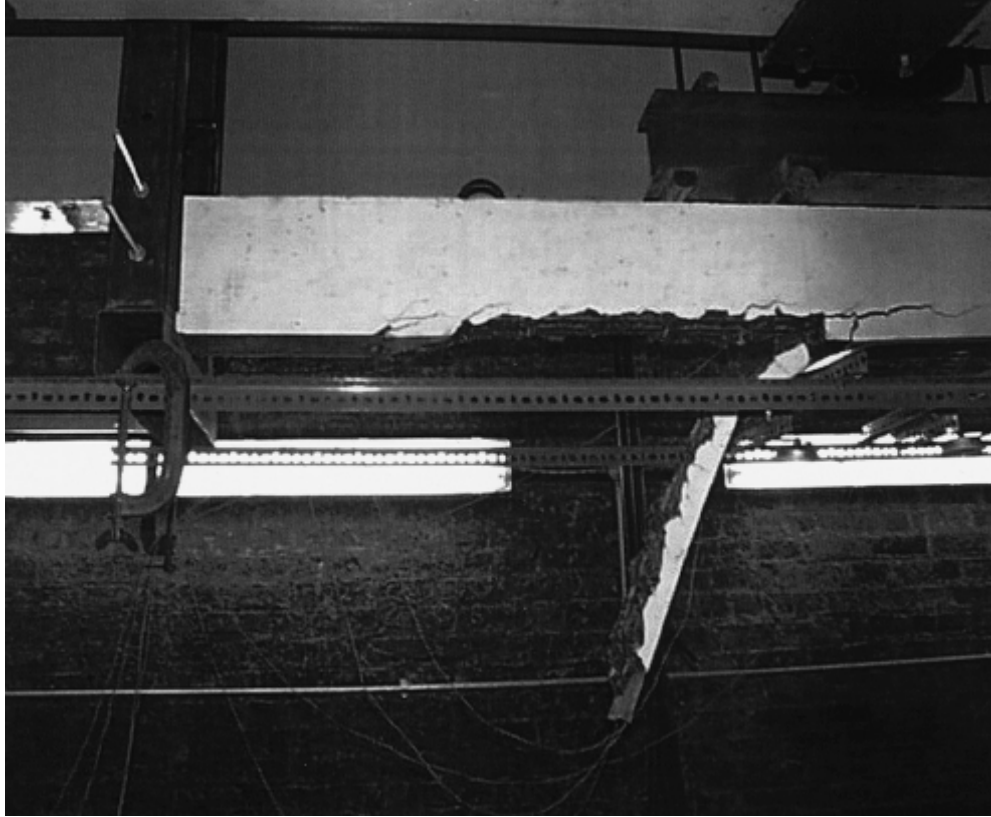


**Figure 2-13:** Test Results of a Cover Delamination Failure (Fanning and Kelly 2001)

#### **2.4 Available Recommended Design Provisions**

There are not currently any building code requirements set forth by either the American Concrete Institute (ACI), the International Federation for Structural Concrete (*fib*), or Standards Australia that specifically address FRP systems for strengthening concrete structures. However, these organizations have published guides and recommendations for the design and construction of externally-bonded (EB) FRP-strengthened concrete structures. In the Standards Australia document, both EB and near-surface mounted (NSM) systems are discussed; however, there are currently no documents published by ACI or *fib* that are specifically for NSM FRP systems.

### **2.4.1 ACI Committee 440 Design Recommendations**

The title of ACI Committee 440 is, “Fiber Reinforced Polymer Reinforcement.” This committee has published ACI 440.2R-08, titled, “Guide for the Design and Construction of Externally Bonded FRP Systems for Strengthening Concrete Structures.” In this document, the main focus is on EB FRP reinforcement, but NSM FRP reinforcement is briefly addressed. The 2008 version of ACI 440.2R has some significant changes from the earlier 2002 version; most of the changes occur in the debonding strain equations.

ACI 440.2R (2008) is divided into five parts: general, materials, recommended construction requirements, design recommendations, and design examples. Design recommendations are subdivided into six chapters: general design requirements; flexural strengthening; shear strengthening; strengthening of members subjected to axial force or combined axial and bending forces; FRP reinforcement details; and drawings, specifications, and submittals.

In the general design requirements section, the ultimate FRP rupture stress and strain are both reduced by an environmental reduction factor,  $C_E$ , to account for any degradation due to “exposure to certain environments, such as alkalinity, salt water, chemicals, ultraviolet light, high temperatures, high humidity, and freezing-and-thawing cycles.” Values for this reduction factor are shown in Table 2-3.

**Table 2-3:** Environment Reduction Factor Values Given by ACI 440 (2008)

Exposure conditions	Fiber type	Environmental reduction factor $C_E$
Interior exposure	Carbon	0.95
	Glass	0.75
	Aramid	0.85
Exterior exposure (bridges, piers, and unenclosed parking garages)	Carbon	0.85
	Glass	0.65
	Aramid	0.75
Aggressive environment (chemical plants and wastewater treatment plants)	Carbon	0.85
	Glass	0.50
	Aramid	0.70

This reduction in rupture stress and strain is shown in Equations 2-1 and 2-2,

$$f_{fu} = C_E f_{fu}^* \quad \text{Equation 2-1}$$

$$\varepsilon_{fu} = C_E \varepsilon_{fu}^* \quad \text{Equation 2-2}$$

where  $f_{fu}^*$  stands for the ultimate tensile strength of the FRP material as reported by the manufacturer;  $f_{fu}$  stands for the design ultimate tensile strength of the FRP material;  $\varepsilon_{fu}^*$  stands for the ultimate rupture strain of the FRP reinforcement; and  $\varepsilon_{fu}$  stands for the design rupture strain of the FRP reinforcement.

#### 2.4.1.1 Debonding of FRP Reinforcement

To prevent PE debonding, Section 13.1 gives three options: using anchorage near the cutoff point, minimizing the stress in the FRP by locating the cutoff point close to or beyond the region of zero moment, or both. To prevent IC debonding for EB systems, Section 10.1.1 of ACI 440.2R-08 limits the effective strain in the FRP reinforcement by Equation 2-3,

$$\varepsilon_{fd} = 0.083 \sqrt{\frac{f'_c}{nE_f t_f}} \leq 0.9\varepsilon_{fu} \text{ in in.-lb units}$$

**Equation 2-3**

$$\varepsilon_{fd} = 0.41 \sqrt{\frac{f'_c}{nE_f t_f}} \leq 0.9\varepsilon_{fu} \text{ in N-mm units}$$

where  $\varepsilon_{fd}$  is the debonding strain of the FRP;  $f'_c$  is the concrete compressive strength;  $n$  is the number of FRP plies;  $E_f$  is the FRP elastic modulus; and  $t_f$  is the FRP thickness. This debonding strain equation was calibrated using a database of IC-debonding failures. By using the average measured values of strain, the coefficient of 0.083 was attained for English units (0.41 for SI units).

To prevent IC debonding for NSM applications, Section 10.1.1 limits the effective strain in the NSM FRP reinforcement by Equation 2-4.

$$\varepsilon_{fd} = 0.7\varepsilon_{fu} \quad \text{Equation 2-4}$$

One of the biggest differences between the 2002 and 2008 versions of the ACI 440.2R document is the debonding strain equation. As shown in Equation 2-3, the 2008 version is in terms of the concrete compressive strength and the FRP axial stiffness per unit width. The 2002 version, however, is only in terms of the FRP axial stiffness per unit width. Also, the 2002 version does not have an equation for NSM, but the 2008 version does and is shown in Equation 2-4.

#### **2.4.1.2 Strengthened Moment Capacity**

To accurately calculate FRP strains, the strain in the concrete before FRP strengthening must be accurately estimated to account for any existing strain at the location of the FRP at the time of installation. This value can be determined from an elastic cracked-section



analysis of the unstrengthened section. In the analysis, only the loads on the member that will be present during strengthening need to be applied. By using this existing substrate strain and by using strain compatibility, an effective strain level in the FRP at the ultimate limit state can be found by using Equation 2-5,

$$\varepsilon_{fe} = \varepsilon_{cu} \left( \frac{d_f - c}{c} \right) - \varepsilon_{bi} \leq \varepsilon_{fd} \quad \text{Equation 2-5}$$

where  $\varepsilon_{fe}$  is the effective strain level in the FRP reinforcement at failure;  $\varepsilon_{cu}$  is the maximum usable strain of unconfined concrete, which is generally taken as 0.003 in./in.;  $d_f$  is the effective depth of the FRP flexural reinforcement;  $c$  is the distance from the extreme compression fiber to the neutral axis; and  $\varepsilon_{bi}$  is the strain level in the concrete substrate at the time of FRP installation. In Equation 2-5, if the calculated value for  $\varepsilon_{fe}$  is less than  $\varepsilon_{fd}$ , then a concrete crushing failure will control; if it is greater, then FRP debonding or FRP rupture will control.

The effective stress in the FRP can be calculated using the effective strain in the FRP with the following equation:

$$f_{fe} = E_f \varepsilon_{fe} \quad \text{Equation 2-6}$$

where  $f_{fe}$  is the effective stress in the FRP.

Based on the strain in the FRP, the strain in the steel reinforcement can be calculated as follows:

$$\varepsilon_s = \left( \varepsilon_{fe} + \varepsilon_{bi} \right) \left( \frac{d - c}{d_f - c} \right) \quad \text{Equation 2-7}$$

where  $\varepsilon_s$  is the strain in the nonprestressed steel reinforcement; and  $d$  is the distance from the extreme compression fiber to the centroid of the tension reinforcement.

Using the strain in the steel reinforcement, the stress in the steel reinforcement can be calculated with the following equation:

$$f_s = E_s \varepsilon_s \leq f_y \quad \text{Equation 2-8}$$

where  $f_s$  is the stress in the nonprestressed steel reinforcement;  $E_s$  is the modulus of elasticity of steel; and  $f_y$  is the yield strength of steel.

Once all of the strains and stresses for the cross section have been calculated using Hooke's law and strain compatibility, the neutral axis depth at failure,  $c$ , can be calculated using Equation 2-9,

$$c = \frac{A_s f_s + A_f f_{fe}}{\alpha_1 f'_c \beta_1 b} \quad \text{Equation 2-9}$$

where  $A_s$  is the area of nonprestressed steel reinforcement;  $A_f$  is the area of FRP reinforcement;  $\alpha_1$  is the multiplier on  $f'_c$  to determine the intensity of an equivalent rectangular stress distribution for concrete;  $\beta_1$  is the ratio of the depth of the equivalent rectangular stress block to the depth of the neutral axis; and  $b$  is the width of the compression face of the member. If concrete crushing is the controlling failure mode, then the Whitney stress block can be used, and  $\alpha_1$  can be taken as 0.85. If FRP rupture or debonding is the controlling failure mode, then  $\alpha_1$  can be calculated using the following equation:

$$\alpha_1 = \frac{3\varepsilon'_c \varepsilon_c - \varepsilon_c^2}{3\beta_1 \varepsilon_c'^2} \quad \text{Equation 2-10}$$

where  $\varepsilon_c$  is the strain in the concrete; and  $\varepsilon_c'$  is the maximum strain of unconfined concrete corresponding to  $f_c'$  and is usually taken as 0.002 in./in.

Figure 2-14 shows an illustration of the internal strain and stress distribution for a rectangular section under flexure at ultimate limit state.

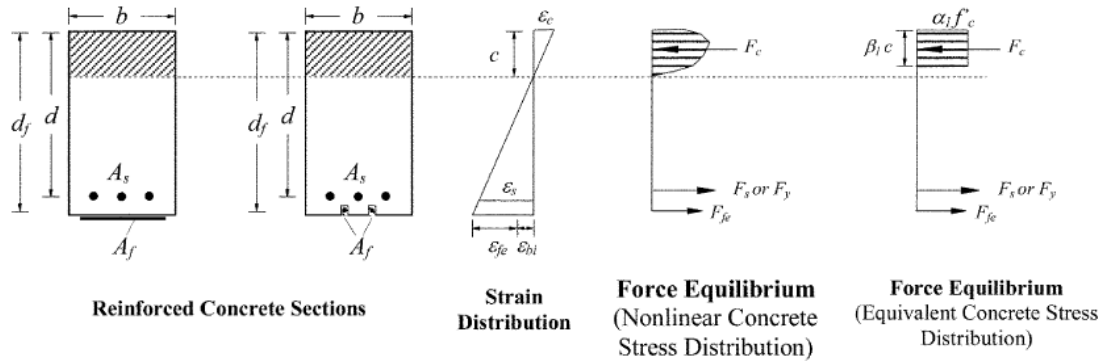


**Figure 2-14:** Internal Strain and Stress Profiles for a Section in Flexure (ACI 440 2008)

After the neutral axis depth is known, the nominal moment capacity,  $M_n$ , of the section can be determined from Equation 2-11,

$$M_n = A_s f_s \left( d - \frac{\beta_1 c}{2} \right) + \psi_f A_f f_{fe} \left( h - \frac{\beta_1 c}{2} \right) \quad \text{Equation 2-11}$$

where  $\psi_f$  is an additional strength reduction factor for the FRP reinforcement; and  $h$  is the overall height of the member. ACI 440 recommends that  $\psi_f$  be taken as 0.85 for flexure. The two minus signs shown in Equation 2-11 were erroneously omitted from the equation shown in the ACI 440 document.

### 2.4.1.3 Development Length

For EB systems, ACI 440 gives the development length of the FRP reinforcement,  $l_{df}$ , by Equation 2-12.

$$l_{df} = 0.057 \sqrt{\frac{nE_f t_f}{\sqrt{f'_c}}} \text{ in in.-lb units}$$

**Equation 2-12**

$$l_{df} = \sqrt{\frac{nE_f t_f}{\sqrt{f'_c}}} \text{ in SI units}$$

For NSM systems, ACI 440 gives the development length of the FRP reinforcement by Equation 2-13,

$$l_{df} = \frac{d_b}{4(\tau_b)} f_{fd} \quad \text{for circular bars}$$

**Equation 2-13**

$$l_{df} = \frac{a_b b_b}{2(a_b + b_b)(\tau_b)} f_{fd} \quad \text{for rectangular bars}$$

where  $d_b$  is the FRP bar diameter;  $f_{fd}$  is the design stress of the FRP reinforcement;  $\tau_b$  is the average bond stress for NSM FRP bars;  $a_b$  is the smaller cross-sectional dimension for rectangular FRP bars; and  $b_b$  is the larger cross-sectional dimension for rectangular FRP bars. ACI 440.2R-08 recommends using 1000 psi (6.9 MPa) for  $\tau_b$ .

### 2.4.1.4 Serviceability Recommendations

To avoid inelastic deformations of reinforced concrete members, ACI 440 limits the internal steel reinforcement to 80% of its yield strength and the concrete to 45% of its compressive strength under service loads.

### 2.4.2 *fib* Task Group 9.3

Task Group 9.3 of the International Federation for Structural Concrete (*fib*) prepared Bulletin 14 in 2001. The title of Task Group 9.3 is, “FRP (Fibre Reinforced Polymer) reinforcement for concrete structures.” Bulletin 14 is titled, “Externally bonded FRP reinforcement for RC structures.” The main focus of this document is on EB FRP reinforcement; NSM FRP reinforcement is mentioned only a few times.

Bulletin 14 provides recommendations on the design and use of EB FRP. The design guidelines are divided into three approaches. The first approach limits the ultimate FRP strain to a certain value and requires that the end anchorage of the EB FRP be verified. The bulletin does not give any specific equation or value for this limiting strain, but it does mention that previous tests show that the *ultimate* FRP strain can range from 0.0065 to 0.0085 mm/mm. The task group admits that a global strain limit may not be suitable to cover the entire range of FRP applications. They predict that future models will not just limit the FRP strain value but will be based on extensive testing and analytical calculations. Task Group 9.3 suggests that the other two approaches will provide a more realistic prediction of the EB FRP capacity.

The second approach involves the calculation of the change in FRP tensile stress between two subsequent cracks. Once the stress exceeds the maximum value that can be transferred by bond stresses, the FRP will debond. This debonding usually is initiated at flexural cracks. This approach consists of three steps: determination of the most unfavorable spacing of the flexural cracks; determination of the tensile force within the EB reinforcement at two subsequent cracks; and determination of the maximum possible increase in tensile stress in the FRP.

The third approach consists of two steps. In the first step, the end anchorage must be verified, as in the first approach. In the second step, the shear stress at the FRP-concrete interface is calculated and compared to a limiting shear stress value. Bulletin 14 gives the shear stress by Equation 2-14:

$$\tau_b = \frac{\Delta N_{fd}}{b_f \Delta x} \quad \text{Equation 2-14}$$

where  $\tau_b$  is the shear stress at the FRP-concrete interface;  $b_f$  is the width of the FRP;  $\Delta x$  is the distance between the two cross sections being analyzed; and  $\Delta N_{fd}$  is the change in the FRP axial force between the two cross sections. To simplify this expression, Task Group 9.3 assumed that the steel will yield before FRP debonding occurs. After making this assumption, they presented the following three expressions:

$$\Delta N_{fd} = \frac{\Delta M_d}{z_m} \quad \text{Equation 2-15}$$

$$z_m \approx 0.95d \quad \text{Equation 2-16}$$

$$\frac{\Delta M_d}{\Delta x} \approx V_d \quad \text{Equation 2-17}$$

where  $\Delta M_d$  is the change in moment across the two cross sections;  $z_m$  is the lever arm of the tensile reinforcement;  $d$  is the effective depth of the section; and  $V_d$  is the design shear force. Substituting these three equations into Equation 2-14 gives the following equation:

$$\tau_b = \frac{V_d}{0.95db_f} \quad \text{Equation 2-18}$$

To get the limiting shear stress value, Task Group 9.3 adopts the Mohr-Coulomb failure criterion where the bond strength is equal to about 1.8 times the tensile strength of the concrete. The following equation shows this limiting stress:

$$f_{cbd} = 1.8 \frac{f_{ctk}}{\gamma_c} \quad \text{Equation 2-19}$$

where  $f_{cbd}$  is the bond shear strength of concrete, in MPa;  $f_{ctk}$  is the characteristic concrete tensile strength, in MPa; and  $\gamma_c$  is a material safety factor for the concrete. To get the mean value for the bond shear strength,  $f_{ctk}$  needs to be replaced with  $f_{ctm}$ , which is given by the 1990 CEB-FIP Model Code as,

$$f_{ctm} = 1.40 \text{MPa} \left( \frac{f_{cm}}{10 \text{MPa}} \right)^{2/3} \quad \text{Equation 2-20}$$

where  $f_{ctm}$  is the concrete's mean tensile strength, in MPa, and  $f_{cm}$  is the concrete's mean compressive strength, in MPa.

In this derivation, it was assumed that the steel strain was approximately equal to the FRP strain. Task Group 9.3 noted that this assumption is conservative. Another assumption is that if this approach is used, flexural cracks will only produce micro-cracking and local debonding and will not result in bond failure (*fib* 9.3 2001).

### 2.4.3 Standards Australia

Standards Australia published a design guide titled, "Design handbook for RC structures retrofitted with FRP and metal plates: beams and slabs" in 2008. This design handbook outlines the generic and fundamental behaviors of plated beams and slabs. Some design

rules and recommendations are also given but are shown in the commentary and not in the guidelines.

Standards Australia’s design handbook on FRP uses the same environmental reduction factor as ACI 440.2R-08. It directly references ACI 440 and uses the same factors. These environmental reductions factors are shown in Table 2-3, which is located in ACI 440.

One of the main focuses of this handbook is plate debonding, specifically PE debonding and IC debonding. For these types of debonding, the guidelines state that the debonding failure will occur within the concrete because the tensile strength of the adhesive is usually an order of magnitude stronger than that of the concrete.

#### 2.4.3.1 PE-Debonding Models

The Australian handbook’s guidelines state three locations along the beam to terminate a plate in order to prevent PE debonding: at a point of contraflexure, where the curvature is low, or on a compression face in a continuous beam. If any of these guidelines cannot be met, the handbook’s commentary gives some formulas for calculating the moment at the plate end that causes PE debonding. For EB plates on the tension face of a beam, the following formula is given:

$$\left[ (M_{PE})_{t_{fp}} \right]_{ch} = \frac{K(EI)_{cr.pl} f_{cb}}{0.474 E_p t_{fp}} \quad \text{Equation 2-21}$$

where  $\left[ (M_{PE})_{t_{fp}} \right]_{ch}$  is the characteristic moment at the plate end that causes PE debonding for a tension-faced EB plate, in N-mm;  $K$  is a constant equal to 0.53 for the characteristic value and 1 for the mean value;  $(EI)_{cr.pl}$  is the flexural rigidity of the



cracked plated cross section adjacent to the plate end, in N-mm<sup>2</sup>;  $f_{cb}$  is the Brazilian or splitting tensile strength of the concrete, in MPa;  $E_p$  is the modulus of elasticity of the plate, in MPa; and  $t_{tfp}$  is the thickness of the tension-faced EB plate, in mm.

To develop an expression to describe the PE-debonding behavior of NSM plates, a model was first developed for EB plates that are bonded to the sides of a beam. These EB side plates are oriented in the same direction as NSM plates, but because the NSM plates are bonded on both sides instead of just one, the capacity for the NSM plates is taken to be twice the EB side plate capacity. For NSM plates, the following equation is given:

$$\left[ (M_{PE})_{NSM-tfp} \right]_{ch} = \frac{2K(EI)_{cr.pl} f_{cb}}{E_p (0.185t_{NSM-tfp} + 0.0185|d_{NSM-tfp}|)} \quad \text{Equation 2-22}$$

where  $\left[ (M_{PE})_{NSM-tfp} \right]_{ch}$  is the characteristic moment at the plate end that causes PE debonding for a tension-faced NSM plate, in N-mm; K is a constant equal to 0.81 for the characteristic value and 1 for the mean value;  $t_{NSM-tfp}$  is the thickness of the tension-faced NSM plate, in mm; and  $d_{NSM-tfp}$  is the distance between the centroid of the specific NSM plate and the neutral axis of the cracked plated section.

#### 2.4.3.2 IC-Debonding Models

The Australian handbook describes two types of IC-debonding models: a basic IC-debonding model and a more representative IC-debonding model for beams. The basic model is based on push-pull tests and is used as a lower bound for predicting capacities for beams. The representative model more accurately describes the behavior of a plated beam.

### 2.4.3.2.1 Basic IC-Debonding Models

There are two models given for the basic IC-debonding resistance. The first model given is a generic model that can be used for either EB or NSM plates. This model is taken from the paper by Seracino, Raizal Saifulnaz, and Oehlers (2007) and is further discussed later in this chapter. The second model was taken from a paper by Teng et al. (2002) and is shown in Equation 2-23,

$$\left[ (P_{IC})_{pp} \right]_{EB} = \alpha_{EB} \beta_p b_p \sqrt{E_p t_p \sqrt{f'_c}} \quad \text{Equation 2-23}$$

where  $\left[ (P_{IC})_{pp} \right]_{EB}$  is the IC-debonding resistance for an EB plate, in N;  $\alpha_{EB}$  is an IC-debonding coefficient and is 0.427 for the mean value and 0.315 for the characteristic value;  $b_p$  is the width of the EB plate, in mm;  $t_p$  is the thickness of the EB plate, in mm; and  $\beta_p$  is given in Equation 2-24,

$$\beta_p = \sqrt{\frac{2 - b_p / b_c}{1 + b_p / b_c}} \quad \text{Equation 2-24}$$

where  $\beta_p$  is a width factor, and  $b_c$  is the width of the concrete, in mm.

### 2.4.3.2.2 Beam IC-Debonding Model

There is just one model that is given to calculate the IC-debonding resistance for beams. According to Standards Australia, this model should only be used for EB plates and should not be used for NSM plates. No IC-debonding model for NSM plates is given by Standards Australia as of 2008. The model to calculate the mean value of the IC-debonding resistance for EB plates is shown in the following equation:

$$(P_{IC})_{EB} = 0.887 \beta_p b_p \sqrt{E_p t_p \sqrt{f'_c}} \quad \text{Equation 2-25}$$

To develop this equation, Equation 2-23 was modified by recalibrating the IC-debonding coefficient. Instead of using simple lap-shear specimens to calibrate the coefficient, FRP-strengthened beam and slab specimens were used, which resulted in a coefficient that is twice as big.

## **2.5 Models for FRP Debonding Failure Modes**

FRP-strengthened concrete members will often fail due to FRP debonding. Many models have been proposed to try to predict the capacity at which this debonding occurs. FRP debonding can be separated into plate-end (PE) debonding and intermediate crack (IC) debonding.

### **2.5.1 Plate-End (PE) Debonding Models**

The models in this section attempt to predict when PE debonding will occur. Most of the models are focused on determining the bending moment at the cutoff section when the FRP plate starts to debond. Then, this moment is used to obtain the corresponding bending moment at midspan, which is taken as the moment capacity of the strengthened cross section.

#### **2.5.1.1 Blaschko (2003)**

Blaschko (2003) conducted about one hundred pull-off tests to analyze the bond behavior between NSM FRP strips and concrete. Figure 2-15 shows a schematic of the pull-off tests conducted by Blaschko.

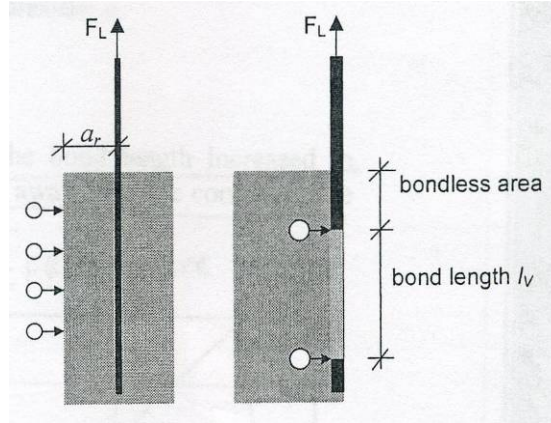


**Figure 2-15:** Elevation Views of a Pull-Off Test (Blaschko 2003)

In this test, an NSM strip was bonded to a concrete block and then pulled along its longitudinal axis until it separated from the block. The concrete blocks shown in Figure 2-15 were 300 mm (12 in.) by 300 mm (12 in.) while all other dimensions and properties were varied. He noted that in most of the tests, the failure occurred in the adhesive layer. By assuming that failure will occur in the adhesive layer and by analyzing the results of these bond tests, he proposed a design approach to calculate bond capacity at the end of the plate. The design approach consists of two equations, given as:

$$\text{for } l_v \leq 115\text{mm:} \quad F_{V,k} = b_L \tau_{K,k} \sqrt[4]{a_r} l_v (0.4 - 0.0015l_v) \quad \text{Equation 2-26}$$

$$\text{for } l_v > 115\text{mm:} \quad F_{V,k} = b_L \tau_{K,k} \sqrt[4]{a_r} \left( 26.2 + 0.065 \tanh\left(\frac{a_r}{70}\right) (l_v - 115) \right) \quad \text{Equation 2-27}$$

In Equations 2-26 and 2-27,  $F_{V,k}$  stands for the characteristic bond strength, in N;  $b_L$  is the width of the FRP strip, in mm;  $\tau_{K,k}$  is the characteristic shear strength of the adhesive, in N/mm<sup>2</sup>;  $a_r$  is the distance, in mm, no greater than 150 mm (5.9 in.), between the strip and the edge of the concrete member, in mm; and  $l_v$  is the bond length, in mm.

Blaschko gives a typical range for  $\tau_{k,k}$  as 20 to 25 N/mm<sup>2</sup> (2900 to 3600 psi).

Blaschko limits the value of  $a_r$  to a maximum value of 150 mm (5.9 in.) because, at this point, the concrete edge no longer has any influence on the FRP strip.

Two equations are needed because when the slip between the FRP strip and the concrete exceeds a certain value, the amount of bond stress that can be transferred is limited by the amount of friction between the strip and the concrete. The FRP strip's bonded length is used to determine which equation to apply. The first equation is valid in the elastic-plastic range for the adhesive, and the second equation incorporates the stresses due to friction.

#### **2.5.1.2 Hassan and Rizkalla (2003)**

In the study by Hassan and Rizkalla (2003), eight reinforced concrete beams were strengthened with NSM FRP strips and were tested under a monotonic static loading. One beam was left unstrengthened and used as a control beam. Different embedment lengths were used to investigate PE debonding. Figure 2-16 shows an elevation and cross section of a typical beam with its steel reinforcement details.

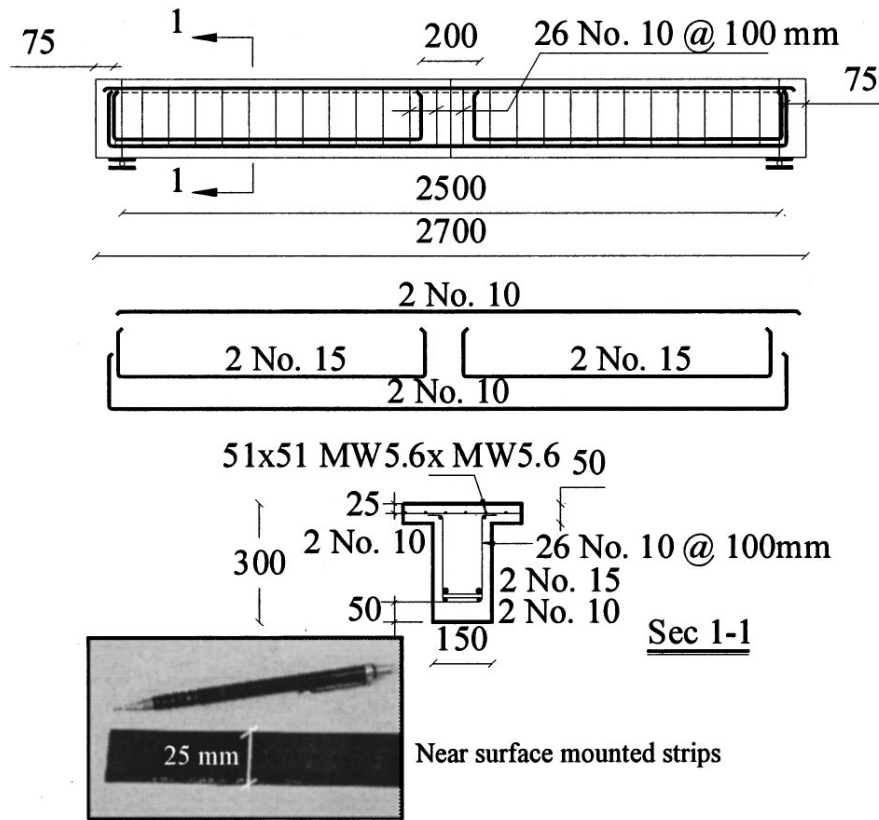


**Figure 2-16:** Elevation and Cross Section of Test Specimen and the Steel Reinforcement  
 Details (Hassan and Rizkalla 2003)

All units are in mm, and all bar sizes are SI sizes. The average concrete compressive strength after 28 days was 48 MPa (7000 psi). A closed-form analytical solution was proposed to describe the behavior at the cutoff point of an FRP strip. The authors assumed that PE debonding is a result of a concentration of high shear stresses at the FRP strip's end. Therefore, the proposed model predicts interfacial shear stresses at this point.

In this model, different closed-form solutions were derived for various loading configurations. The first loading configuration was a simply supported beam with a

concentrated load at midspan. The two boundary conditions used for this case were that the normal stress in the FRP strip was zero at its end and that the shear stress was zero at midspan. Using these boundary conditions, the following formula was derived:

$$\tau = \frac{t_f}{2} \left[ \frac{nPl_o y_{eff}}{2I_{eff}} \omega e^{-\omega x} + \frac{nPy_{eff}}{2I_{eff}} \right] \quad \text{Equation 2-28}$$

where  $\tau$  stands for the shear stress;  $t_f$  is the thickness of the FRP strip;  $n$  is the FRP's modular ratio;  $P$  is the applied concentrated load;  $l_o$  is the distance from the end of the beam to the start of the FRP strip;  $y_{eff}$  is the distance from the FRP strip to the neutral axis of the section;  $I_{eff}$  is the effective moment of inertia of the section;  $x$  is the longitudinal coordinate starting from the cutoff point of the strip; and  $\omega$  is defined by Equation 2-29.

$$\omega^2 = \frac{2G_a}{t_a t_f E_f} \quad \text{Equation 2-29}$$

In Equation 2-29,  $G_a$  is the shear modulus of the adhesive;  $t_a$  is the thickness of the adhesive; and  $E_f$  is the elastic modulus of the FRP.

The calculated shear stress from Equation 2-28 is then compared to a limiting value. The test results showed that the failure occurred in the concrete layer. Once the compressive strength and the tensile strength of concrete are known, the Mohr-Coulomb line, which is a line that is tangential to both Mohr's circles for pure tension and pure compression, can be found. Figure 2-17 shows these Mohr's circles and the Mohr-Coulomb line.

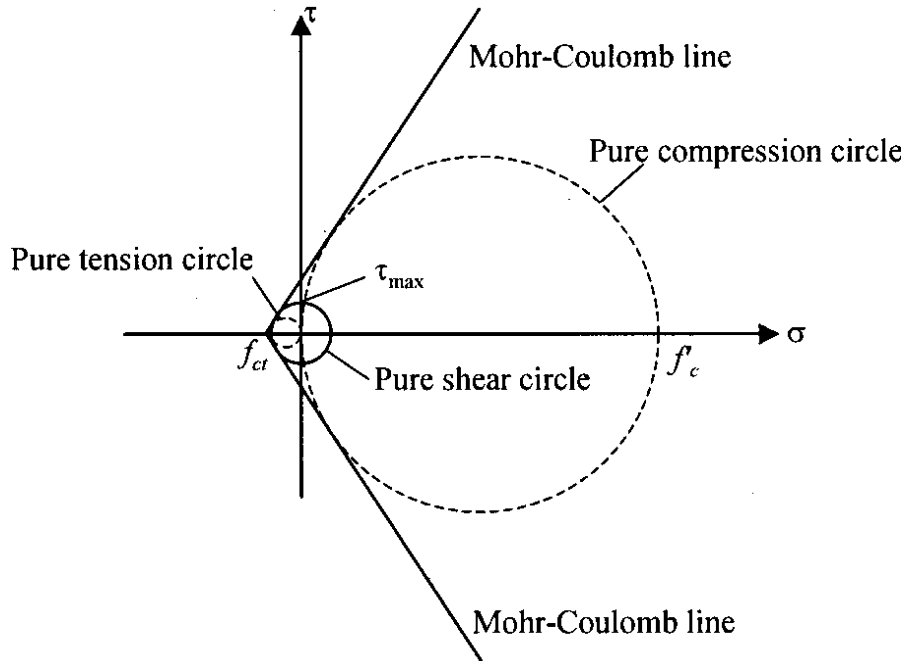


**Figure 2-17:** Mohr-Coulomb Failure Criterion (Hassan and Rizkalla 2003)

All circles tangential to the Mohr-Coulomb line represent a critical stress combination. The pure shear circle represents the critical stress combination that has its center at the origin. The authors proposed that the limiting shear stress value is equal to the maximum critical shear stress for the pure shear circle, given as follows:

$$\tau_{max} = \frac{f'_c f_{ct}}{f'_c + f_{ct}} \quad \text{Equation 2-30}$$

In Equation 2-30,  $f'_c$  equals the compressive strength of the concrete at 28 days, and  $f_{ct}$  equals the tensile strength of the concrete. By equating Equation 2-28 with Equation 2-30, the PE-debonding loads can be determined for this specific support and loading configuration. Other shear stress formulas are given in the paper for different support and loading setups.



The authors compared their predicted debonding loads to the measured debonding loads from their eight FRP-strengthened beams. They also conducted a nonlinear finite element analysis using the ANACAP program to predict shear stresses, and they compared these shear stresses to the predicted shear stresses from their analytical model. They found that their model accurately predicted the PE-debonding loads and the shear stresses when compared against the experimental results and the finite element analysis, respectively.

#### **2.5.1.3 Vasquez (2008)**

Vasquez (2008) used finite element models and previous analytical models to derive a new PE-debonding model for NSM FRP strips. In this model, the normal and shear stresses were identified, some general assumptions were made regarding reinforced concrete, and a principle-stress equation was proposed. Once the normal stresses were known, the shear stress was calculated and compared to a limiting value.

From mechanics, six different stresses can be developed at any location. These stresses, shown in Figure 2-18, are specifically for a point in the concrete that is adjacent to the cutoff point of a NSM strip.

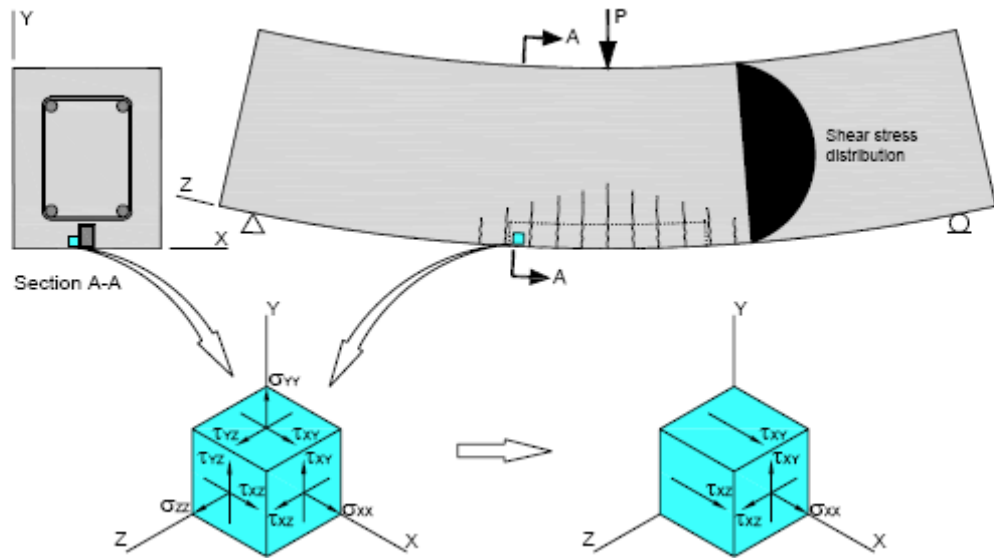


**Figure 2-18:** Stress Distribution at the NSM Strip Cutoff Point (Vasquez 2008)

Because the concrete is assumed to be cracked, the normal stress,  $\sigma_{ZZ}$ , was ignored. Also shown in Figure 2-18 is the assumed shear stress distribution. Because this point is located at the FRP cutoff location and because the shear stress approaches zero at the top and bottom of the concrete, which is near the possible locations of the NSM strip, the shear stress  $\tau_{YZ}$  was disregarded. Also, because the strip is located so close to the tension face of the concrete, the normal stress  $\sigma_{YY}$  was ignored.

After making these assumptions, the only stresses that remained were two shear stresses,  $\tau_{XZ}$ ,  $\tau_{XY}$ , and a normal stress,  $\sigma_{XX}$ . Vasquez then derived equations for these stresses by assuming linear elastic behavior, assuming that plane sections remain plane, using strain compatibility, and applying Hooke's law. Once these stresses were known, a resultant stress was derived. The principle stresses were calculated as the roots of this polynomial:

$$\sigma^3 - I_1\sigma^2 + I_2\sigma - I_3 = 0 \quad \text{Equation 2-31}$$

where  $I_1$ ,  $I_2$ , and  $I_3$  are constants.

By applying the assumptions that  $\sigma_{YY}$ ,  $\sigma_{ZZ}$ , and  $\tau_{YZ}$  are negligible, Equations 2-32 through 2-34 were then derived.

$$I_1 = \sigma_{XX} \quad \text{Equation 2-32}$$

$$I_2 = -\tau_{XY}^2 - \tau_{XZ}^2 \quad \text{Equation 2-33}$$

$$I_3 = 0 \quad \text{Equation 2-34}$$

Substituting the constants  $I_1$ ,  $I_2$ , and  $I_3$  into Equation 2-31 yields the three principle stresses,  $\sigma_1$ ,  $\sigma_2$ , and  $\sigma_3$ . Due to the previous assumptions made,  $\sigma_2$  will always equal zero,  $\sigma_1$  will be a tensile stress, and  $\sigma_3$  will be a compressive stress. For these resultant stresses, the corresponding maximum shear stress,  $\tau_{\max}$ , is calculated by Equation 2-35.

$$\tau_{\max} = \frac{|\sigma_1| + |\sigma_3|}{2} \quad \text{Equation 2-35}$$

The resulting Mohr's circle and a representation of the resultant stresses are shown in Figure 2-19.

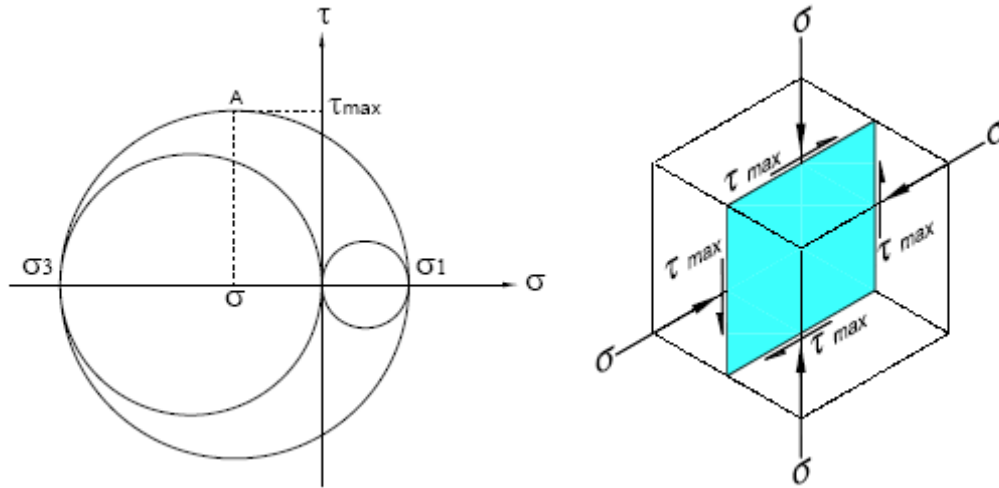


**Figure 2-19:** Mohr's Circle (left) and the Resultant Stress Distribution (right)  
(Vasquez 2008)

Once the maximum shear stress,  $\tau_{max}$ , is calculated, it can be compared to the limiting value of shear stress. Vasquez proposed that two different failure criteria be used. The first failure criterion is the same one used by Hassan and Rizkalla (2003). It is the maximum critical shear stress for the pure shear circle, given by Equation 2-30. The other limiting value comes from a paper by Mattock and Hawkins (1972). Vasquez gives the equation shown in Equation 2-36, where the only variable is  $f_{ct}$ , the tensile strength of the concrete, in MPa.

$$\tau_{max} = 1.06 f_{ct} \quad \text{Equation 2-36}$$

The process is then iterated until the maximum shear stress calculated from Equation 2-35 equilibrates the limiting shear stress value given by Equation 2-36.

This model was compared to existing experimental results of PE-debonding failures to determine the accuracy of the model. Vasquez found that his model yielded conservative yet adequately accurate results.

## **2.5.2 Intermediate Crack (IC) Debonding Models**

The models in this section attempt to predict when failure will occur due to IC debonding. Some models predict IC-debonding failure strains in the FRP reinforcement, whereas others predict the bending moment that corresponds to an IC-debonding failure.

### **2.5.2.1 Rosenboom (2006)**

In the research by Rosenboom (2006), thirty full-scale prestressed concrete bridge girders were tested under two different loading conditions: extreme loading conditions simulated by a monotonic load to failure and service loading conditions simulated by static and fatigue loading. For the first phase of the research, only the repair and strengthening of the beams was examined. For the second phase, the bond behavior of the FRP was examined, and an analytical model was proposed to describe the behavior. Rosenboom recommends that the analytical model should be used for EB reinforcement only.

For the repair and strengthening phase of the research, twenty-six bridge girders were tested using EB and NSM FRP. The girders were prestressed concrete C-channel girders with spans of 9.18 m (30.1 ft) each. All of the girders came from decommissioned bridges in North Carolina. Figure 2-20 shows a diagram of the girder layout.

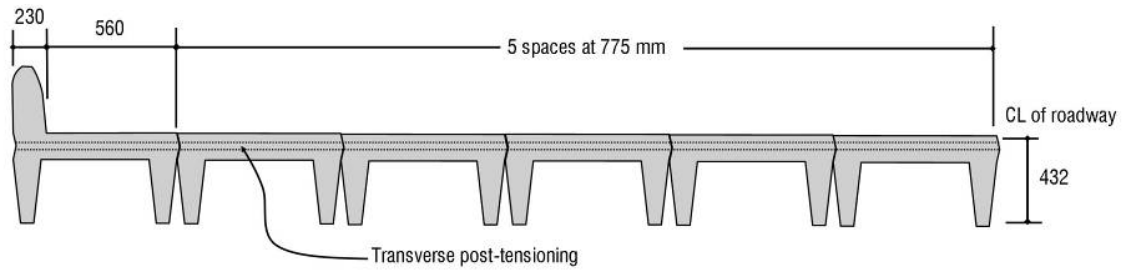


**Figure 2-20:** Layout of C-Channel Girders (Rosenboom 2006)

Figure 2-21 shows the two cross sections that were used in the tests.

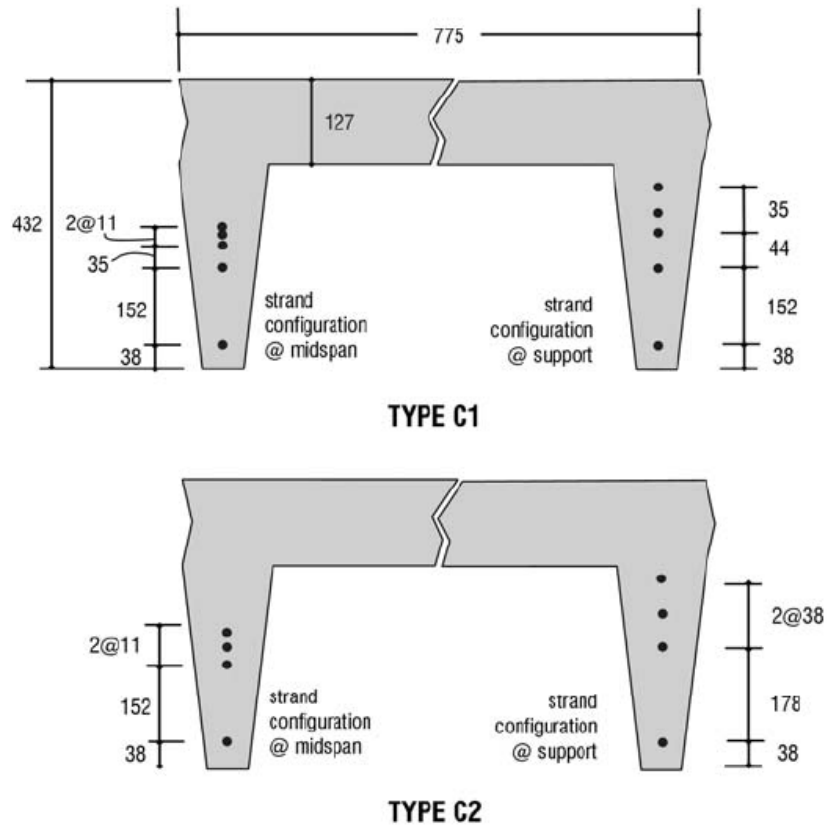


**Figure 2-21:** Both Cross Sections of the C-Channel Girders (Rosenboom 2006)

The distances shown in Figures 2-20 and 2-21 are in mm. The specified concrete compressive strength for these girders was 34.5 MPa (5000 psi). Rosenboom concluded

that NSM strips are the most structurally efficient strengthening technique, whereas EB reinforcement is the most cost-effective.

For the second phase of the research, four bridge girders were tested monotonically to failure. These girders had the same cross section as the Type C1 girder shown in Figure 2-21. Three beams failed by IC debonding, and the other beam failed due to FRP rupture. Rosenboom used twenty-eight existing models to predict the IC-debonding loads for these beams and for a database that was assembled of IC-debonding failures. Two of the models included in the analysis are Bulletin 14 by *fib* 9.3 (2001) and the 2002 version of the document by ACI 440. Most of the other models were derived or based on push-pull tests. He concluded that none of the models correlated well with the database, especially not the 2002 version of the model given by ACI Committee 440, which he concluded is actually unconservative. He also concluded that the reason most of the models were inaccurate is due to the fact that the models are based on push-pull tests rather than actual beam tests. Rosenboom then proposed a new analytical model that predicts the bond behavior at the intermediate cracks. The proposed model is based on calculating the maximum shear stress between the point at which the internal steel first yields and the debonding moment location, adding this shear stress component to the component due to stress concentrations, and then setting the total shear stress equal to a limiting value.

The proposed model is based on calculating two types of concrete shear stresses: shear stresses directly related to the load and shear stresses related to stress concentrations at the “toe” of a flexural crack. In the model, a debonding strain in the FRP is first assumed. Then, all of the strains and stresses in the cross section are

calculated using strain compatibility. Once these values are known, the moment capacity is calculated. This moment capacity is considered the moment at which debonding occurs. Then, the shear stress in the concrete related directly to the load is needed. To calculate this value, the distance from the support to the location of first yielding of the internal tensile reinforcement,  $x_y$ , needs to be computed. For three- and four-point bending, Equation 2-37 can be used.

$$x_y = s \frac{M_y}{M_{db}} \quad \text{Equation 2-37}$$

In this equation,  $s$  is the shear span;  $M_y$  is the yield moment of the strengthened section; and  $M_{db}$  is the debonding moment. Using the  $x_y$  value, the shear stress in the concrete related directly to the load, which Rosenboom assumed was the maximum shear stress and denoted as  $\tau_{wmax}$ , can be calculated by using Equation 2-38,

$$\tau_{wmax} = nE_f t_f \frac{\varepsilon_{db} - \varepsilon_{f@y}}{s - x_y} \quad \text{Equation 2-38}$$

where  $nE_f t_f$  is the axial stiffness of FRP material per unit width;  $\varepsilon_{db}$  is the FRP debonding strain; and  $\varepsilon_{f@y}$  is the tensile strain in the FRP at first yielding of the internal tensile steel at a moment of  $M_y$ . All units are in N and mm.

After computing this concrete shear stress component, the other concrete shear stress component needs to be calculated. Rosenboom assumed that the shear stress in the concrete related to stress concentrations at the “toe” of a flexural crack,  $\tau_{scmax}$ , was a function of the concrete compressive strength and the ratio of the yield moment over the



debonding moment. An equation was formulated and calibrated against a database of experimental IC-debonding failures. This expression is shown in Equation 2-39,

$$\tau_{scmax} = 2.15 \left( 1.1 - \frac{M_y}{M_{db}} \right) \sqrt{f'_c} \quad \text{Equation 2-39}$$

where  $f'_c$  is the concrete compressive strength, in MPa.

For design purposes, Equation 2-40 was proposed to give a probability of exceedance of 5%.

$$\tau_{scmax} = 3 \left( 1.1 - \frac{M_y}{M_{db}} \right) \sqrt{f'_c} \quad \text{Equation 2-40}$$

For both Equations 2-39 and 2-40, the ratio of  $M_y$  to  $M_{db}$  should be less than one because the model was not designed for debonding to occur before the internal steel yields. When both concrete shear stresses are known, the total concrete shear stress,  $\tau_i$ , can be calculated using Equation 2-41.

$$\tau_i = \tau_{vmax} + \tau_{scmax} \quad \text{Equation 2-41}$$

The failure criterion then needs to be computed. Rosenboom derives this equation as,

$$\tau_{cmax} = 1.134 f'_c \quad \text{Equation 2-42}$$

where  $\tau_{cmax}$  is the limiting shear stress in the concrete, in MPa. Once  $\tau_i$  and  $\tau_{cmax}$  are known, the debonding strain in the FRP is iterated until these two concrete shear stress values are equal. Once the debonding strain in the FRP is found, the strengthened moment capacity can then be calculated using strain compatibility.

The proposed model was compared to the database of experimental IC-debonding failures to determine its accuracy relative to the other models analyzed. Rosenboom concluded that the proposed model outperformed the other models and that most of the other models were too conservative.

### 2.5.2.2 Seracino, Raizal Saifulnaz, and Oehlers (2007)

In the study by Seracino, Raizal Saifulnaz, and Oehlers (2007), fourteen new push-pull tests using NSM FRP were conducted, and an analytical model was derived that predicts the IC-debonding resistance of FRP-strengthened reinforced concrete members. The model was used to analyze the fourteen new tests as well as existing push-pull data from the referenced literature for both NSM and EB. Figure 2-22 shows a schematic of a push-pull test for EB.

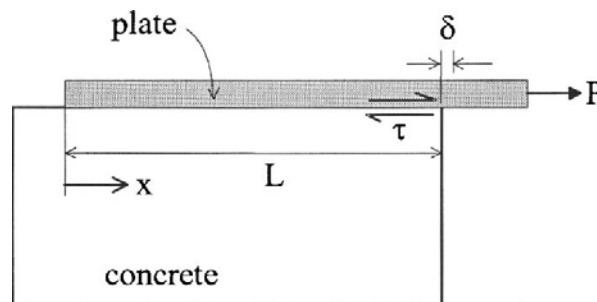


**Figure 2-22:** Schematic of a Push-Pull Test for EB (Seracino, Raizal Saifulnaz, and Oehlers 2007)

The model is based on the local interface shear stress-slip relationship ( $\tau$ - $\delta$ ) of the debonding interface. Specifically, it uses a simplified linear-softening interface bond-slip relationship and a unique confinement ratio that results in a generic model that can be used for both EB and NSM FRP and for any adhesively bonded plate cross section and

material. This unique confinement ratio is given as the aspect ratio of the IC-debonding failure surface. Figure 2-23 shows the IC-debonding failure surfaces for both EB and NSM strips.

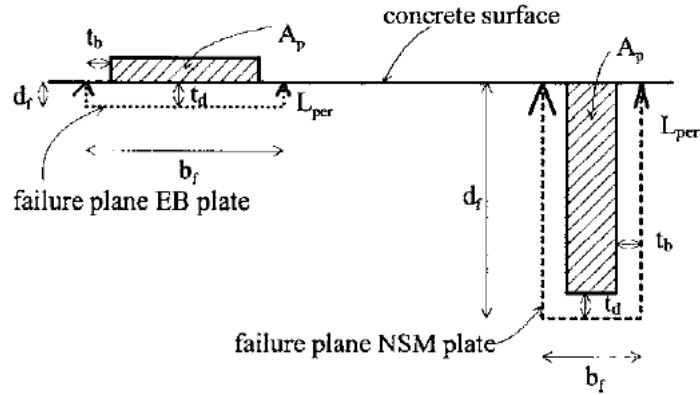


**Figure 2-23:** IC-Debonding Failure Surfaces for EB and NSM strips (Seracino, Raizal Saifulnaz, and Oehlers 2007)

Using these debonding planes, the confinement ratio,  $\phi_f$ , can be calculated using the following equation:

$$\phi_f = \frac{d_f}{b_f} \quad \text{Equation 2-43}$$

where  $d_f$  is the length of the failure plane perpendicular to the concrete surface and  $b_f$  is the length of the failure surface parallel to the concrete surface. The total length of the debonding failure surface,  $L_{per}$ , can be calculated using:

$$L_{per} = 2d_f + b_f \quad \text{Equation 2-44}$$

For these debonding surfaces, the authors conducted a parametric analysis and recommend that 1 mm (0.04 in.) be used for the values of  $t_b$  and  $t_d$ . Once these cross-sectional values are computed, the IC-debonding resistance is then given by:

$$P_{IC} = \alpha_p 0.85 \phi_f^{0.25} f_c^{0.33} \sqrt{L_{per} (EA)_p} < f_{rupt} A_p \quad \text{for N-mm units}$$

**Equation 2-45**

$$P_{IC} = \alpha_p 0.393 \phi_f^{0.25} f_c^{0.33} \sqrt{L_{per} (EA)_p} < f_{rupt} A_p \quad \text{for lb-in. units}$$

where  $P_{IC}$  is the IC-debonding resistance;  $f_c$  is the concrete cylinder compressive strength;  $(EA)_p$  is the axial rigidity of the FRP; and

$$\alpha_p = \begin{cases} 1.0 & \text{for mean} \\ 0.85 & \text{for lower 95\% confidence limit} \end{cases} \quad \text{Equation 2-46}$$

Because this model is only a function of geometric and material properties, any plate material can be used. Once the debonding resistance is calculated, the debonding stress and strain can be found, as can the moment capacity.

### 2.5.2.3 Seracino et al. (2007a)

Seracino et al. (2007a) conducted thirty-six new push-pull tests of NSM strips. Figure 2-24 shows a diagram of a push-pull test for NSM.

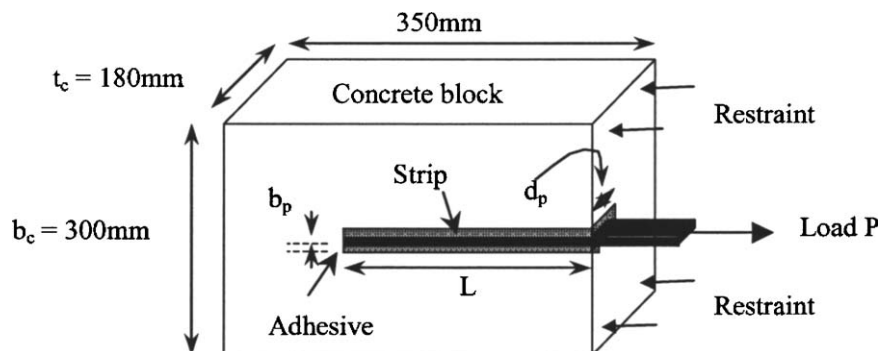


**Figure 2-24:** Diagram of a Push-Pull Test for NSM (Seracino et al. 2007a)

Using the new test results, the authors performed a nonlinear statistical analysis and proposed a model for predicting the debonding failure load for an NSM FRP-to-concrete joint. The authors determined from their analysis that the parameters necessary in determining the IC-debonding failure load are the concrete compressive strength and the FRP strip dimensions. By using these variables and conducting a nonlinear regression analysis for optimization, the following formula was reached:

$$P_{IC} = \alpha\beta\sqrt{f_c}d_p^{1.36}b_p^{0.21} \leq f_{rupt}b_p d_p \quad \text{for SI units} \quad \text{Equation 2-47}$$

$$P_{IC} = 3\alpha\beta\sqrt{f_c}d_p^{1.36}b_p^{0.21} \leq f_{rupt}b_p d_p \quad \text{for U.S. Customary units}$$

where  $P_{IC}$  is the maximum predicted IC-debonding resistance, in kN for SI units or kips for U.S. Customary units;  $\alpha$  is 0.19 or 0.16 for the mean or characteristic values, respectively;  $\beta$  is used to account for bond length;  $f_c$  is the compressive cylinder strength of concrete, in MPa or psi;  $d_p$  and  $b_p$  are the plate dimensions perpendicular and parallel to the concrete surface, respectively, in mm or in.; and  $f_{rupt}$  is the rupture stress of the FRP, in GPa or ksi. The concrete compressive strength is limited to a range of 30 to 65 MPa (4400 to 9400 psi); the FRP depth is limited to 10 mm to 20 mm (0.39 to 0.79 in.); and the FRP thickness is limited to 1.2 mm to 2.4 mm (0.047 to 0.094 in.). The  $\beta$  factor can be found using:

$$\beta = \begin{cases} 1.0 & \text{for } L \geq 200 \text{ mm} \\ L/200 & \text{for } L < 200 \text{ mm} \end{cases} \quad \text{for units of mm} \quad \text{Equation 2-48}$$

$$\beta = \begin{cases} 1.0 & \text{for } L \geq 7.9 \text{ in.} \\ L/7.9 & \text{for } L < 7.9 \text{ in.} \end{cases} \quad \text{for units of in.}$$

where  $L$  is the bonded length of the FRP.

To maximize the debonding resistance, a minimum critical FRP-bonded length of 200 mm (7.9 in.) is recommended. Efficiency further increases when the depth of the FRP into the concrete increases. The improved efficiency is attributed to the increased confinement of the interface debonding crack by the surrounding concrete cover.

#### 2.5.2.4 Said and Wu (2008)

Said and Wu (2008) reviewed two hundred previous EB test results of beams or slabs with IC-debonding failures in order to propose an IC-debonding model that would accurately predict the debonding strain value of the FRP strips. They assumed that the debonding strain,  $\varepsilon_{db}$ , is a function of the concrete compressive strength, the FRP elastic modulus, and the FRP thickness. Using these parameters, they formulated the relationship shown in Equation 2-49.

$$\varepsilon_{db} = C1(f'_c)^{C2} / (E_f t_f)^{C3} \quad \text{Equation 2-49}$$

The values of  $C1$ ,  $C2$ , and  $C3$  are constants, and the units used are N and mm. Using the two hundred previous tests from the literature, Said and Wu calibrated their model to most accurately predict the debonding strain. Using values of 0.23, 0.2, and 0.35 for constants  $C1$ ,  $C2$ , and  $C3$ , respectively, they reached a closed-form empirical solution for the debonding strain, shown in Equation 2-50.

$$\varepsilon_{db} = 0.23(f'_c)^{0.2} / (E_f t_f)^{0.35} \quad \text{Equation 2-50}$$

Said and Wu used this model to predict the debonding strains for the experimental tests. They noted that their model predicted the IC-debonding capacity more accurately than other models mentioned in the paper, including the approach by ACI Committee 440 in 2002 and the approach by *fib* 9.3 in 2001.

## 2.6 FRP Spacing Recommendations for NSM Strips

The distance between NSM FRP strips can affect the moment capacity of a strengthened member. Spacing the strips at the recommended distance from each other will result in individual failure planes. Conversely, spacing the strips too close to each other can result in one common failure plane that will make the ultimate load-carrying capacity prediction less accurate (Vasquez 2008). Also, the distance of the FRP strip from the side edge of the concrete surface is an important factor. If this distance is too small, the corner of the concrete could split off (Blaschko 2003), or premature debonding of the FRP strip could occur (ACI 440 2008).

For NSM systems, ACI 440 (2008) recommends that the clear spacing between NSM grooves be no less than twice the depth of the groove to avoid any overlapping of tensile stresses around the NSM bars. For the edge distance, their recommendation is that this distance be a minimum of four times the depth of the groove.

*fib* 9.3 (2001) does not provide any spacing limits or recommendations for NSM FRP strips.

Hassan and Rizkalla (2004) tested eight concrete beams strengthened with NSM FRP bars and developed a finite element model to describe the NSM behavior. In the model, they specifically looked at groove spacing and edge distance of the bars. The groove spacing was varied from 0.25 to 2 times the bar diameter, the groove width was varied from 1.5 to 2.5 times the bar diameter, and the edge distance was varied from 2 to 6 times the bar diameter. For the groove spacing, the authors proposed a minimum clear spacing of twice the diameter of the FRP bars, regardless of groove width. They also

recommended a minimum edge distance of four times the diameter of the FRP bars to minimize the edge effect.

Kang et al. (2005) used a finite element model to analyze the effect of FRP spacing on the capacity of four specimens strengthened with varying configurations of NSM strips. The specimens were 300 mm (12 in.) high and 200 mm (8 in.) wide, with a span of 3 m (10 ft). Once the finite element model was verified against the four test specimens, the model was used to analyze the effect of the NSM spacing. After varying the NSM spacing from 20 to 180 mm (0.8 to 7.1 in.) and the edge distance from 90 to 10 mm (3.5 to 0.4 in.) for two separate groove depths, 15 and 25 mm (0.59 and 0.98 in.), they concluded that the most efficient design should leave a minimum distance of 40 mm (1.6 in.) between NSM strips and a minimum distance of 40 mm (1.6 in.) from the strip to the concrete edge.

Rashid et al. (2008) specifically studied how the spacing of the FRP strips and the side cover distance of the FRP affects the IC-debonding resistance of the strips. They conducted twenty-two new pull tests, including seventeen tests on NSM strips. They concluded that the NSM plates have a strong effect on the adjacent plates and the concrete cover. They recommended that the lateral spacing of NSM plates be no less than 53 mm (2.1 in.), with an edge distance of no less than  $3\frac{1}{2}$  times the depth of the NSM plate.

In his thesis, Vasquez (2008) wrote that, as a general rule, the spacing between adjacent grooves should be greater than  $2\frac{1}{2}$  times the groove width, as opposed to the depth, to ensure that there will be individual failure planes. His suggestion is based on the recommendations of a document by Standards Australia while it was in the process of



being published; however, the final version of the document does not address any spacing limits for NSM.

Table 2-4 summarizes the NSM groove spacing and side cover recommendations found in the literature.

**Table 2-4:** Summary of NSM Groove Spacing and Side Cover Recommendations

	Clear spacing of strips	Side cover distance
ACI Committee 440 (2008)	2×(groove depth)	4×(groove depth)
Hassan and Rizkalla (2004)	2×(FRP bar diameter)	4×(FRP bar diameter)
Kang et al. (2005)	40 mm (1.6 in.)	40 mm (1.6 in.)
Rashid et al. (2008)	53 mm (2.1 in.)	3½×(FRP depth)
Vasquez (2008)	2½×(groove width)	-----

### 2.7 Effect of Concrete Surface Roughness

The roughness of the concrete surface has been investigated to examine the effects on an FRP-strengthened member. Yalim, Kalayci, and Mirmiran (2008) conducted research on twenty-six beams that were tested in flexure with two different EB FRP systems, three different concrete surface profiles, and six different levels of FRP anchorage. Ten additional beams were tested in double shear to investigate the bond behavior of the FRP. They concluded that the surface roughness of the concrete had no significant effect on the overall performance of the FRP system, nor did it affect the bond behavior of the FRP. However, an FRP manufacturer (Hughes Brothers 2009) and various code organizations

(ACI 440 2008; Standards Australia 2008; *fib* 9.3 2001) recommend that the concrete surface be repaired and prepared before strengthening with FRP.

### **2.8 Effect of Embedding NSM Strips**

One of the reasons that NSM strips are used instead of EB reinforcement is because of their increased confinement and increased IC-debonding strains. Embedding NSM strips farther into the concrete provides a larger, and better confined, bonded surface between the two materials. In theory, this extra embedment results in higher IC-debonding strains and, thus, greater ductility (Oehlers et al. 2008).

Oehlers et al. (2008) investigated the effects of embedding NSM strips at varying groove depths by performing twenty new pull tests. Mathematical expressions were developed to describe the effects of embedment on the IC-debonding resistance and the local bond stress-slip relationship. The authors stated that embedding the NSM strips at deeper groove depths can increase the debonding resistance by up to three times over strips embedded at shallower groove depths. Another stated benefit of embedment is that, because of better FRP bond, larger FRP cross sections can be used. The authors also suggest that embedment may improve the fire resistance of FRP.

### **2.9 Previous Testing of FRP-Strengthened Members**

This section discusses some of the previous tests that have been conducted on FRP-strengthened members. The test programs can be broken down into four different categories: flexural tests on concrete members strengthened with EB FRP strips, flexural tests on concrete members strengthened with NSM FRP strips or rods, flexural tests

including both EB and NSM types of applications, and modified-beam pullout tests strengthened with NSM strips or rods.

### 2.9.1 Externally-Bonded (EB) FRP Flexural Tests

The tests in this section include concrete members that were strengthened with EB reinforcement and tested in flexure. More EB tests were found in the literature, but because the focus of this thesis is primarily on NSM behavior, only a few EB tests were chosen to be included.

#### 2.9.1.1 Reed et al. (2005)

In the study by Reed et al. (2005), eight concrete beams were tested in four-point bending and were loaded until failure. Figure 2-25 shows the cross section that was used.

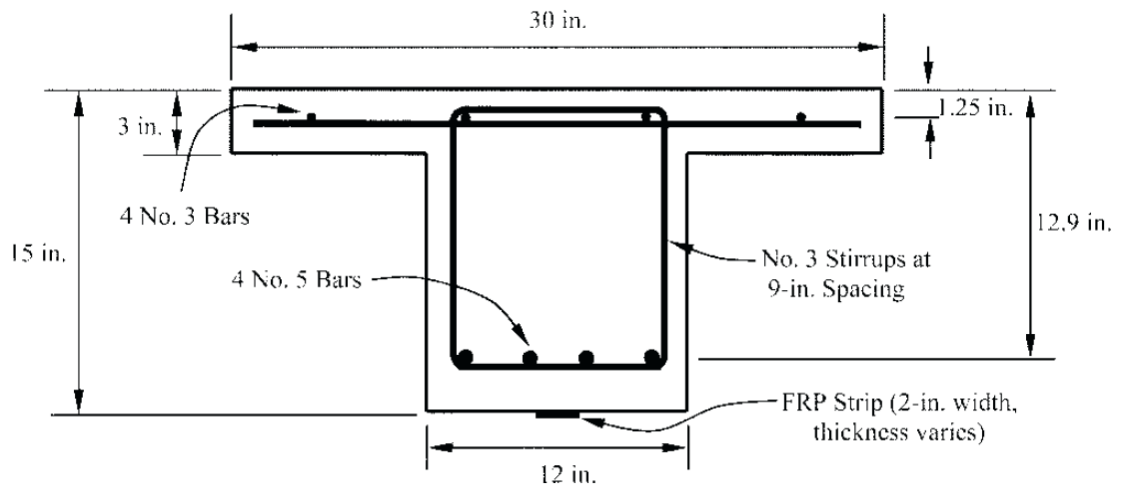


**Figure 2-25:** Cross Section of Test Specimens (Reed et al. 2005)

Figure 2-26 shows a diagram of the test setup.

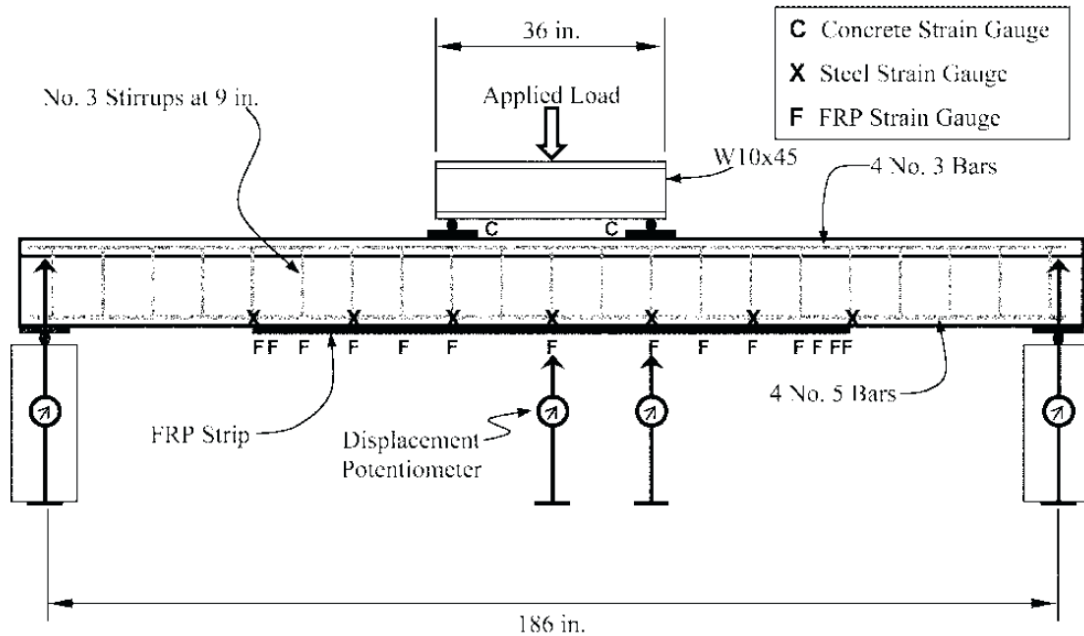


**Figure 2-26:** Test Setup for Specimens (Reed et al. 2005)

The average concrete compressive strength was 7,100 psi (49 MPa). Seven of the beams were strengthened with EB FRP strips; one was left unstrengthened and used as a control beam. The researchers varied the intensity and frequency of load cycles during the curing time of the epoxy and investigated its effect on the performance of the beams. Other variables in this study include the epoxy layer thickness and the FRP strip thickness. For all of the strengthened beams, failure was initiated by debonding initiating at the maximum moment sections. The design recommendations from the 2002 version of the ACI Committee 440 document were followed to calculate the limiting debonding strains in the FRP. This procedure was found to be unconservative for predicting capacities for six of the seven strengthened beams.

### 2.9.1.2 War Memorial Bridge

War Memorial Bridge is an eighteen-span reinforced concrete bridge that spans the Uphapee Creek in Macon County, Alabama. It consists of four variable-depth girders. In 1999, the Alabama Department of Transportation (ALDOT) selected the War Memorial Bridge for flexural strengthening because of the increased demand on the bridge. Figure 2-27 shows a picture of the bridge.

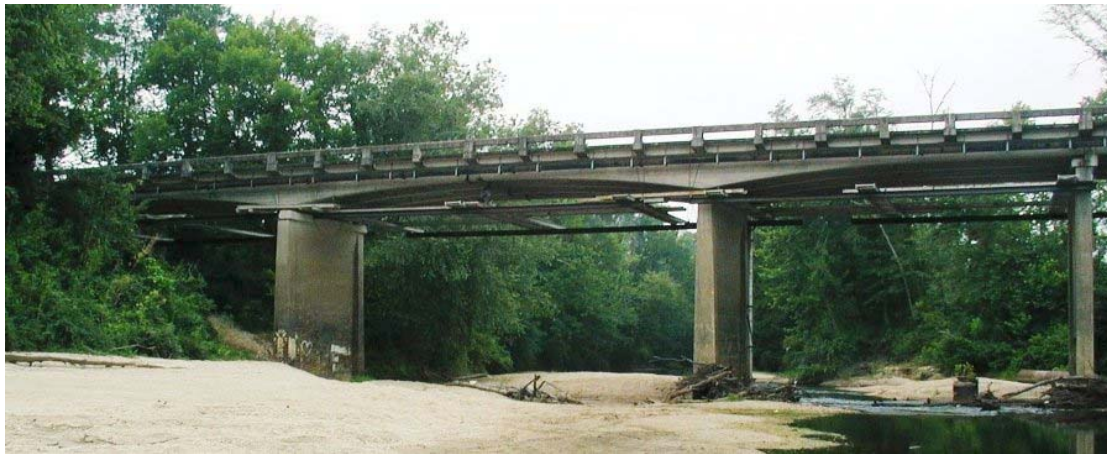


**Figure 2-27:** Picture of War Memorial Bridge (Carmichael and Barnes 2005)

The Auburn University Highway Research Center proposed an FRP-repair scheme to strengthen the bridge. Auburn University researchers focused on the three continuous spans of 161-ft length and strengthened them with EB CFRP. After strengthening, the researchers tested the girders under service loads to determine the effectiveness of the FRP-strengthened members. They concluded that no debonding of the FRP occurred under service loads and that the FRP should be able to provide additional capacity to the girder (Carmichael and Barnes 2005).

## **2.9.2 Near-Surface Mounted (NSM) FRP Flexural Tests**

The tests in this section include concrete members that were strengthened with NSM reinforcement and tested in flexure.

### **2.9.2.1 Yost et al. (2007)**

In the study by Yost et al. (2007), twelve concrete beams were strengthened with NSM strips and loaded in four-point bending until failure. Three other beams were used as control beams and, therefore, were not strengthened. Three different steel reinforcement ratios and two different FRP reinforcing ratios were used. The concrete compressive strength was measured as 37.2 MPa (5400 psi). Figure 2-28 shows the test setup and the different cross sections.

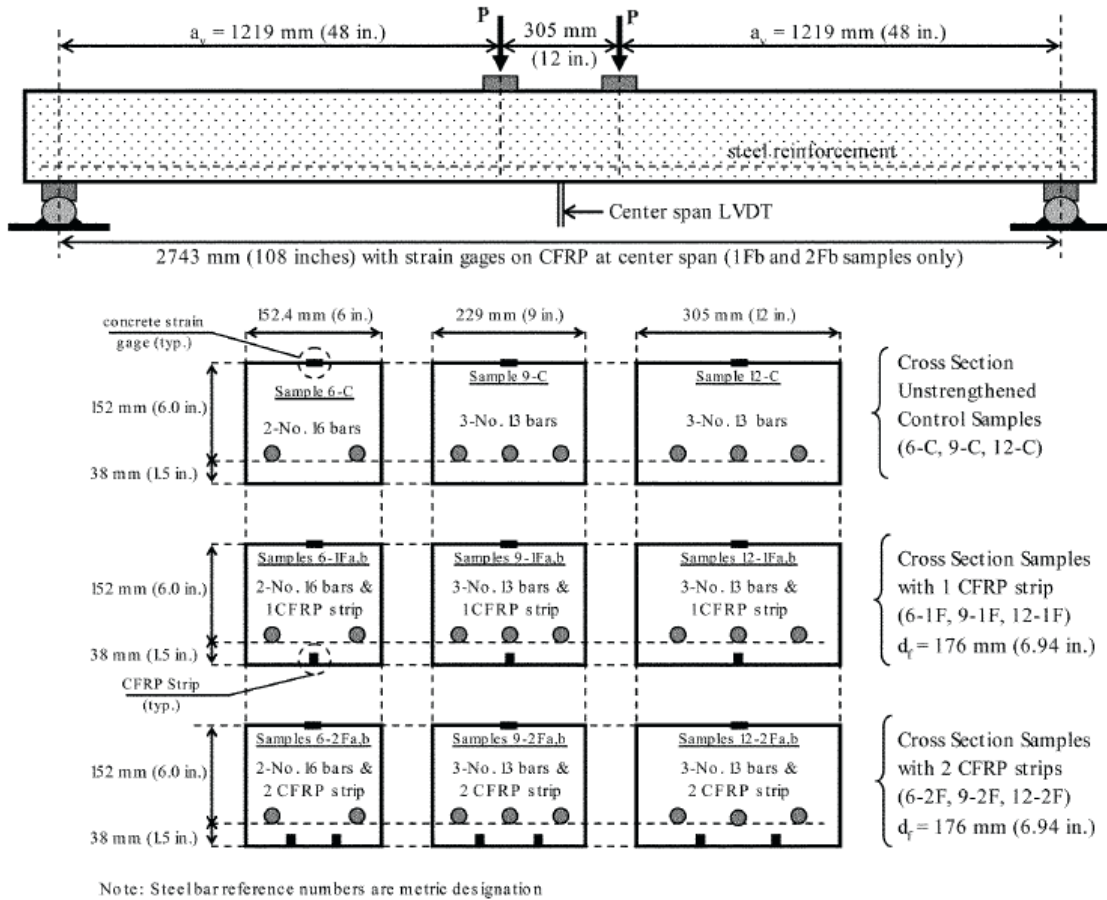


**Figure 2-28:** Test Setup with Cross Sections (Yost et al. 2007)

Two of the strengthened beams failed due to FRP rupture. The rest of the beams failed due to steel yielding followed by concrete crushing. No debonding of the NSM strips was detected.

### 2.9.2.2 Taljsten and Nordin (2007)

The tests conducted at Lulea University of Technology by Taljsten and Nordin (2007) were aimed at comparing the effects of prestressed external tendons of steel and FRP, along with prestressed and non-prestressed NSM reinforcement, on the strengthened capacity of reinforced concrete beams. All eight strengthened T-beams were 6 m (20 ft)

long and were tested in four-point bending until failure. The depth of the T-beams was 500 mm (20 in.), and the web width was 200 mm (8 in.). The flange height was 100 mm (4 in.), and the flange width was 400 mm (16 in.). For the two beams strengthened with nonprestressed NSM reinforcement, rectangular CFRP rods were used, and concrete compressive strengths of 50 and 53 MPa (7300 and 7700 psi) were used. The researchers found that the NSM reinforcement was unable to significantly contribute to the stiffness or strength of the beam in the elastic range. However, once the concrete cracked, the beam had a stiffer behavior and a higher capacity when compared to the control beam. After the NSM rods debonded from the surrounding concrete, failure in the strengthened beams occurred.

#### **2.9.2.3 Teng et al. (2006)**

Teng et al. (2006) investigated the effect of bond length on the strengthened capacity of NSM FRP-strengthened concrete beams. Five beams were loaded in four-point bending monotonically to failure. Four of the beams were strengthened with NSM strips, each with a different embedment length; the other beam was left unstrengthened and used as a control beam. The different embedment lengths used were 500, 1200, 1800, and 2900 mm (20, 47, 71, and 114 in.). All of the cross sections were 300 mm (12 in.) high by 150 mm (6 in.) wide, and all of the specimens were 3 m (10 ft) long. The concrete compressive strength was 35.2 MPa (5100 psi).

The beam with the shortest embedment length, B500, showed no improvement in strength or stiffness over the control beam, B0. Its ineffectiveness is due to the fact that the total length of the FRP strip, 500 mm, was not longer than the maximum moment



region length of 600 mm. Therefore, part of the beam was left unstrengthened in the location where the moment was greatest, and the beam behaved similarly to the control beam.

The beam with the second shortest embedment length, B1200, provided a 30% increase in capacity over the control beam. Specimen B1200 also provided a greater post-cracking stiffness than the control beam. Specimen B1800 produced a 90% increase in strength and an even greater post-cracking stiffness over the control beam. Specimens B500, B1200, and B1800 all failed due to plate-end (PE) debonding, specifically concrete cover separation starting from the cutoff section.

Specimen B2900 produced an increase in strength of 106% over the control beam. Failure for this specimen was due to concrete crushing, followed closely by IC debonding accompanied by debonding at the epoxy-concrete interface and localized splitting of the epoxy.

In this research project, Teng et al. also conducted some bond characterization tests to determine some of the bond properties of the FRP strips. These experiments consisted of pullout tests of an FRP strip embedded in a concrete block. The concrete block was 150 mm (6 in.) wide, 150 mm (6 in.) high, and 350 mm (14 in.) long. The dominant failure mode was a failure at the FRP-epoxy interface.

Teng et al. observed that the debonding failure found in the flexural tests differed greatly from the debonding failure in the bond characterization tests. They noted that debonding failure in the flexural tests was typically caused by cracking in the concrete cover region, whereas in the bond tests, pullout failure along the FRP-epoxy interface was most prevalent. The authors attributed this discrepancy to the fact that there are many

factors present in flexural tests that are not present in bond tests. These factors include the presence of flexural and flexural-shear cracks that change the bond stress distribution, the internal steel forces created by the cracking of the concrete at the FRP strip's location, and the curvature of the beam. The authors stated that the differences between the two types of tests prevent the direct application of any local bond-slip models derived from simple bond characterization tests to the flexural strengthening of reinforced concrete beams.

#### 2.9.2.4 Liu, Oehlers, and Seracino (2006)

Liu, Oehlers, and Seracino (2006) studied two-span continuous reinforced concrete members strengthened with NSM strips. They investigated the ductility and strength of the strengthened members, along with the amount of moment redistribution. Nine near-full-scale specimens were loaded at each midspan location with a concentrated load.

Figure 2-29 shows the two-span test setup.

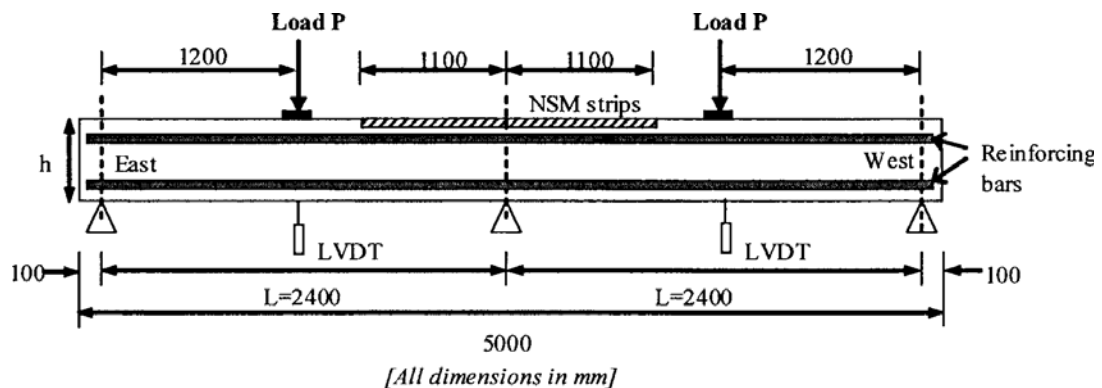


**Figure 2-29:** Test Setup for Specimens (Liu, Oehlers, and Seracino 2006)

Six of the specimens had a slab-shaped cross section, whereas the other three had beam-shaped cross sections. The slab-shaped cross sections were 120 mm (4.7 in.) high

by 375 mm (15 in.) wide with a concrete compressive strength of 37 MPa (5400 psi). The beam-shaped cross sections were 240 mm (9.4 in.) high by 220 mm (8.7 in.) wide with a concrete compressive strength of 35 MPa (5100 psi). All specimens were strengthened with NSM strips near the top of the concrete section over the middle support. To avoid PE debonding, the strips were terminated at a point of contraflexure. FRP strips were used for seven of the specimens. The other two specimens were strengthened with steel plates of approximately the same size.

Two of the NSM-strengthened beam cross sections and one of the NSM-strengthened slab cross sections failed due to IC debonding. The other specimens either failed due to a shear failure or a concrete crushing failure in the positive-moment regions. The researchers found that a significant amount of moment redistribution occurred in all nine test specimens. The NSM-strengthened specimens for the slab and beam cross sections achieved a moment redistribution of up to 35% and 39%, respectively. The authors state that the moment redistribution for the NSM-strengthened beams is much higher than the moment redistribution that previous researchers have noted for EB-strengthened beams. The researchers concluded that NSM plates are more applicable than EB plates for structures where ductility is the primary concern.

### **2.9.3 Both EB and NSM FRP Flexural Tests**

This section includes test series that consisted of EB-strengthened reinforced concrete members and NSM-strengthened reinforced concrete members. One of the main objectives of these test series was to examine the difference in capacity provided by each type of FRP application.

### 2.9.3.1 El-Hacha and Rizkalla (2004)

A total of eight reinforced concrete T-beams were tested in the research by El-Hacha and Rizkalla (2004). The beams were simply supported and loaded monotonically until failure. Seven of the beams were reinforced with different FRP systems; the other beam was left unstrengthened and used as a control beam. The concrete compressive strength was 45 MPa (6500 psi). Figure 2-30 shows the test setup and the typical cross section.

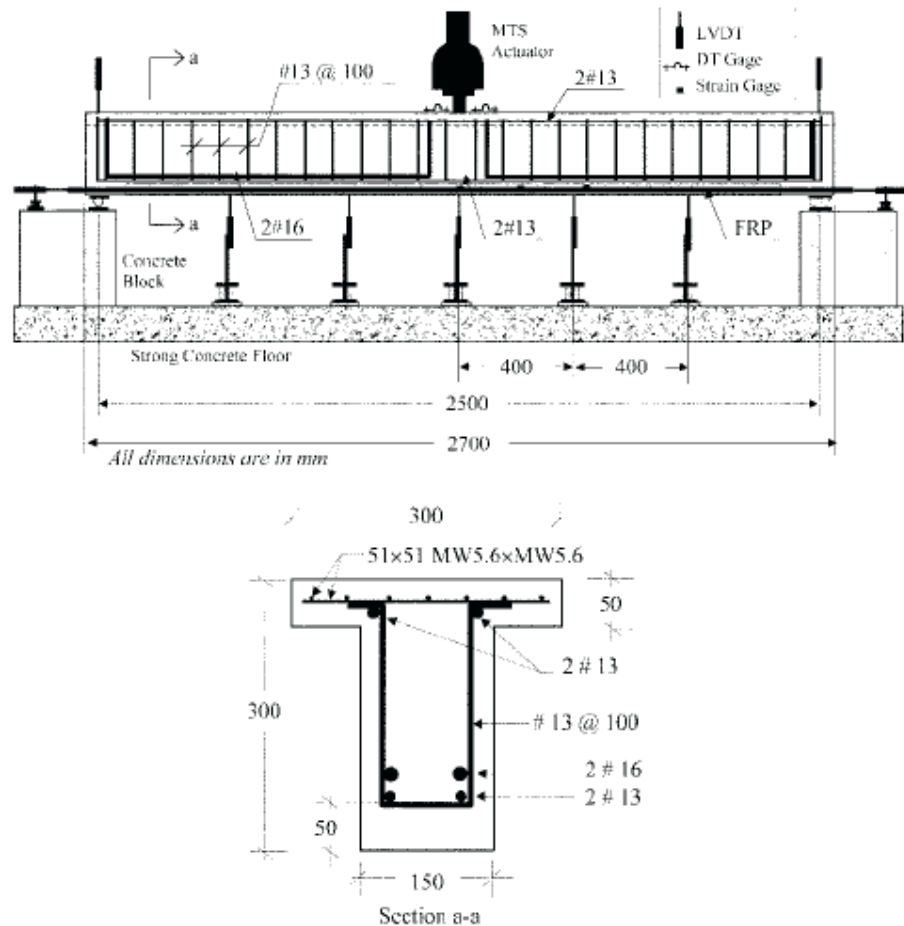


**Figure 2-30:** Test Setup and Cross Section (El-Hacha and Rizkalla 2004)

The distances in Figure 2-30 are in mm, and the bar sizes are SI sizes. The different FRP systems used were NSM strips, NSM bars, and EB strips. For the NSM

strips, two different types of FRP were used: carbon fiber-reinforced polymer (CFRP) and glass fiber-reinforced polymer (GFRP). To improve the anchorage of the EB strips, a U-shaped wrap made of CFRP was placed around the EB strips at both ends and around the web of the T-beams.

The researchers found that the NSM CFRP strips failed due to rupture of the strip. For the NSM CFRP bars, the NSM GFRP strips, and the EB strips, the mode of failure was debonding initiating from a crack either in the epoxy or in the concrete.

The NSM CFRP strips were found to have a higher capacity than the NSM CFRP bars with the same axial stiffness. The authors explain that the higher capacity is due to premature debonding of the NSM bars and to the smaller debonding surface of the bars compared to the strips. They also showed that the NSM reinforcement achieved a higher capacity than the EB reinforcement due to the increased bond area of the NSM strips.

#### **2.9.3.2 Jung et al. (2005)**

Jung et al. (2005) examined the flexural behavior of reinforced concrete beams strengthened by EB and NSM FRP reinforcement. They tested eight 3-meter-long specimens in four-point bending to failure. Two beams were strengthened with EB strips, two with NSM strips, one with an NSM rod, and two with NSM reinforcement with mechanical interlocking grooves; the other beam was left unstrengthened. The concrete compressive strength was measured as 31.3 MPa (4500 psi). Figure 2-31 shows the test setup and the cross section.

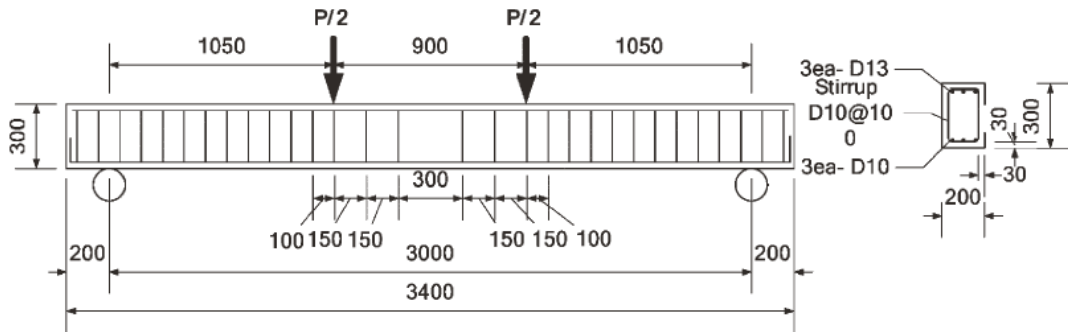


**Figure 2-31:** Elevation View and Cross-Sectional View of Test Setup (Jung et al. 2005)

For Figure 2-31, the distances are in mm, and the bar sizes are SI sizes. Figure 2-32 shows the NSM-strengthening schemes, including the mechanical interlocking grooves.

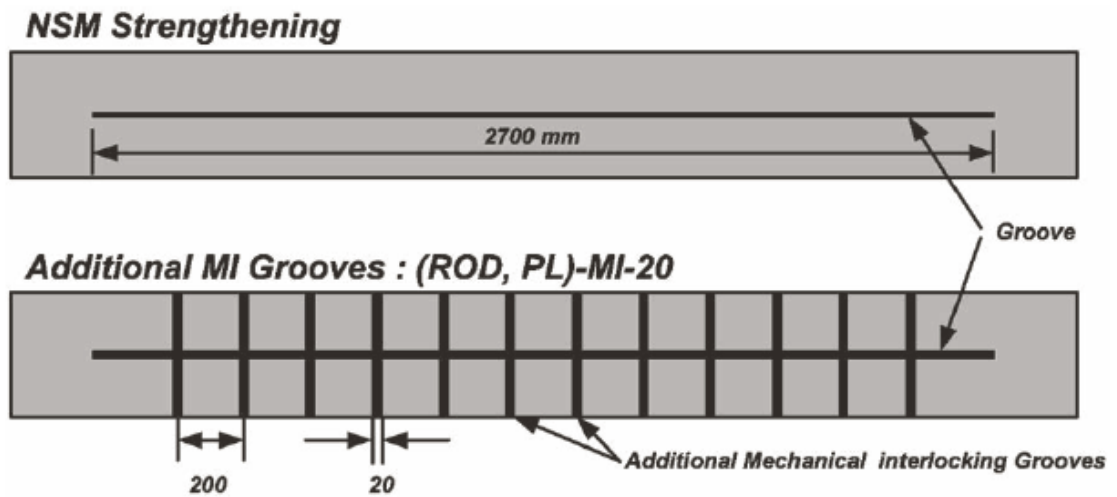


**Figure 2-32:** Plan View of the NSM-Strengthening Schemes (Jung et al. 2005)

Figure 2-32 shows a plan view of the bottom of the beams; the distances shown are in mm. Figure 2-33 shows a picture of the actual test specimen taken from the same perspective.



**Figure 2-33:** Plan View of the Bottom of a Specimen with Mechanical Interlocking Grooves (Jung et al. 2005)

Much like Taljsten and Nordin (2007), Jung et al. found that the FRP reinforcement was unable to significantly contribute to the stiffness or strength of the beam in the elastic range. However, after cracking, the EB-strengthened specimens attained a 30 to 47% increase in capacity, and the NSM-strengthened specimens attained a 39 to 65% increase in capacity. For one of the NSM strip applications and both of the mechanical interlocking groove applications, failure was due to FRP rupture. For all of the other FRP-strengthened beams, failure was due to IC debonding.

The authors concluded that beams strengthened with NSM strips had a greater moment capacity than beams strengthened with EB strips. They also concluded that mechanical interlocking grooves can improve the efficiency of NSM systems, prevent the premature debonding of the FRP, and lead to higher strengths.

## **2.9.4 NSM Modified-Beam Pullout Tests**

The tests described in this section include atypical test setups. Instead of the typical test setup where the objective is to try to produce a flexural failure, the objective of these tests is to produce a pullout failure of the FRP. Because the concrete does not undergo flexure, the concrete specimens do not have any steel reinforcement.

### **2.9.4.1 De Lorenzis and Nanni (2002)**

De Lorenzis and Nanni (2002) tested twenty-two unreinforced concrete beams strengthened with FRP rods to determine their effect on the bond behavior between NSM rods and concrete. The beams were loaded under four-point bending until failure. They analyzed the bonded length of the rod, the diameter and surface configuration of the rod, the type of FRP material, and the size of the groove for the NSM rod. They used a beam pullout test setup where a steel hinge was placed at midspan at the top of the concrete section, and a saw cut was made at midspan at the bottom of the concrete section. Figure 2-34 shows the test setup and the typical cross section.



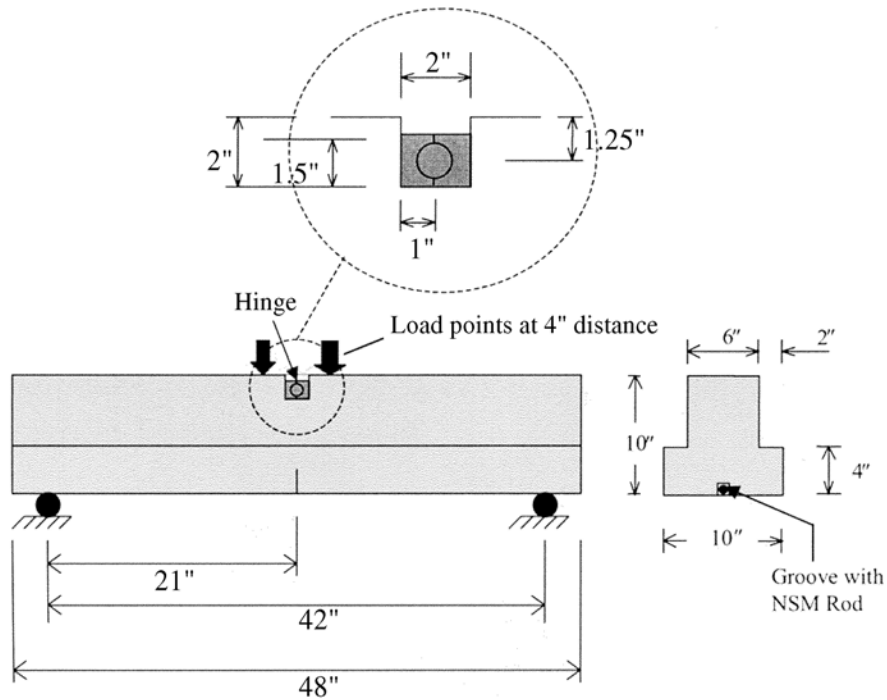


**Figure 2-34:** Test Setup and Cross Section (De Lorenzis and Nanni 2002)

The hinge and the saw cut enabled the researchers to control the internal force distribution. An inverted T-beam section was used to increase the tension area of the concrete and, thus, increase the cracking moment while minimizing the overall beam weight. Two different FRP materials and two different surface configurations for the rod were tested: carbon fiber-reinforced polymer (CFRP) and glass fiber-reinforced polymer (GFRP), and deformed rods and sandblasted rods. The average concrete compressive strength ranged from 3880 to 4100 psi (26.7 to 28.2 MPa).

Three different failure modes were observed during the tests: splitting of the epoxy cover, cracking of the concrete surrounding the groove, and pullout of the FRP bar. The researchers concluded that deformed rods have a greater bond strength than sandblasted rods. They also concluded that increasing the groove width leads to higher

bond strength when failure is controlled by splitting of the epoxy cover. However, if pullout failure controls, then increasing the groove width has no effect on bond strength.

#### 2.9.4.2 Sena Cruz and Barros (2004)

In the study by Sena Cruz and Barros (2004), they analyzed the effects that bond length and concrete strength have on the bond between NSM strips and concrete. Nine strengthened specimens were loaded to failure in a pullout-bending test. Figure 2-35 shows the setup and cross section used for this test.

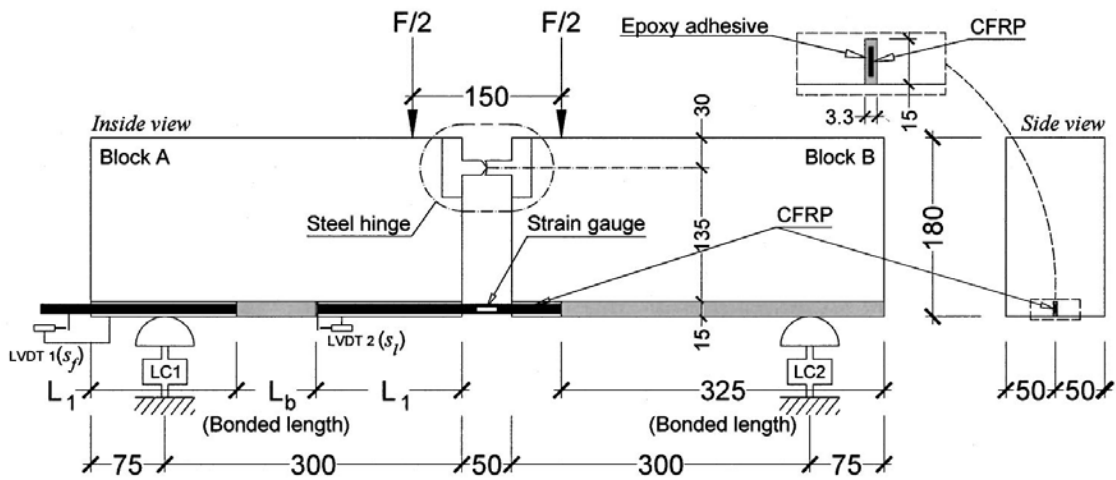


**Figure 2-35:** Test Setup and Cross Section (Sena Cruz and Barros 2004)

In this type of test, two blocks of concrete are connected by a steel hinge at the top and by an NSM strip at the bottom. The concrete blocks are then loaded near the hinge and supported at the opposite end. For this study, the NSM strip was fully bonded along the length of one of the concrete blocks. The strip embedded in the other block was only bonded in the middle section of the block for a set length. To avoid rupture of the strips, a maximum bond length of 80 mm (3.1 in.) was used. Combinations of three

different bond lengths and three different concrete strengths were analyzed. The concrete compressive strengths ranged from 33.0 to 70.3 MPa (4800 to 10200 psi).

All beams failed due to pullout of the FRP, in accordance with the design of the test setup. The researchers noted that the failure occurred in the concrete-adhesive and the adhesive-FRP interfaces and that no cracking was present in the concrete surface. Sena Cruz and Barros then concluded that the concrete's tensile and compressive strengths have little effect on the pullout behavior and that these are not important factors for this specific bond test. Conversely, they concluded that the FRP bond length had a significant influence on the bond strength.

#### **2.9.4.3 Sena Cruz et al. (2006)**

In the study by Sena Cruz et al. (2006), they repeated the same type of pullout-bending test setup that was used in the Sena Cruz and Barros (2004) paper. However, the variables this time were bond length and the type of loading, and the dimensions were slightly different than the previous test setup. Figure 2-36 shows the test setup and the cross section used by Sena Cruz et al.

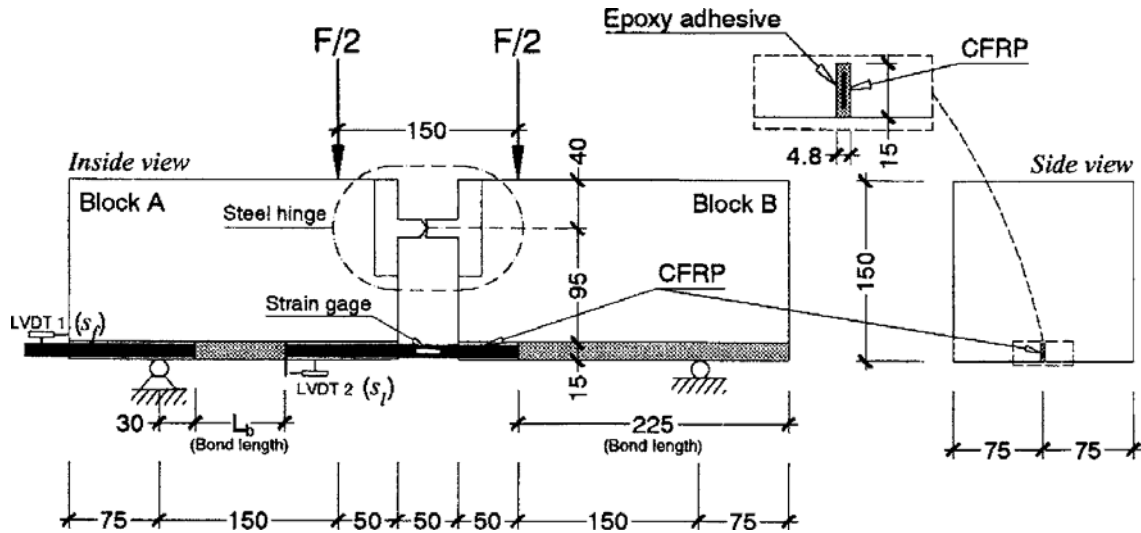


**Figure 2-36:** Test Setup and Cross Section (Sena Cruz et al. 2006)

Due to the conclusions made by Sena Cruz and Barros (2004), the concrete strength was held constant at 30 MPa (4400 psi). Three different bond lengths were used in a series of beams that were loaded monotonically until pullout failure. Three other beams with three different bond lengths were loaded cyclically for ten cycles of loading and unloading at a fixed load level. One other beam was tested with one cycle of loading and unloading at different slip levels.

As in the previous study, all the beams that were tested monotonically failed due to pullout of the FRP strips, and no cracks in the concrete surface were found. The cracking was entirely in the concrete-adhesive and the adhesive-FRP interface. The authors concluded that the peak pullout force increases with increasing bond length.

## 2.10 Summary

The following is a summary of FRP behavior and some conclusions that were reached in the studies discussed in this chapter:

1. FRP remains practically linear-elastic until failure.
2. Carbon fibers were the most commonly used fibers found in the available literature.
3. CFRP is approximately five times lighter and five times stronger than steel reinforcement (ACI 440 2008).
4. The NSM technique is very effective and practical for flexural strengthening in negative-moment regions (El-Hacha and Rizkalla 2004).
5. Two of the primary failure modes for FRP-strengthened members are plate-end (PE) debonding and intermediate crack (IC) debonding.
6. As of 2008, there are no building code requirements for ACI, *fib*, or Standards Australia that are specific to FRP-strengthened members. These code organizations have only produced recommendations on this topic.
7. There have been significant changes made to the FRP-debonding model for the ACI 440.2R document from the 2002 version to the 2008 version. One specific change was the inclusion of the concrete compressive strength in the 2008 version of the debonding model.
8. Teng et al. (2006) stated that the debonding failure found in flexural tests differs greatly from the debonding failure found in bond characterization tests, such as push-pull tests. Also, there are many factors present in flexural tests that are absent in bond characterization tests. They concluded that these differences prevent the direct application of any local bond-slip models derived from simple bond tests to a flexural application.

9. Standards Australia states that models based on push-pull tests can be used as a lower bound for flexural tests.
10. Taljsten and Nordin (2007) and Jung et al. (2005) noted that FRP reinforcement was unable to significantly contribute to the stiffness or strength of the beam in the elastic range.

## **Chapter 3: Letohatchee Bridge Background**

### **3.1 Bridge Description**

The focus of this chapter is the AL 97 bridge over Interstate 65 near Letohatchee, Alabama, in Lowndes County. It has been identified by the Alabama Department of Transportation (ALDOT) as having inadequate strength for certain truck load configurations. ALDOT's Bridge Inventory Number (BIN) for this bridge is 8847. Hereafter, the bridge will be referred to as the "Letohatchee bridge." Figure 3-1 shows its location. Figure 3-2 shows a picture of the Letohatchee bridge.

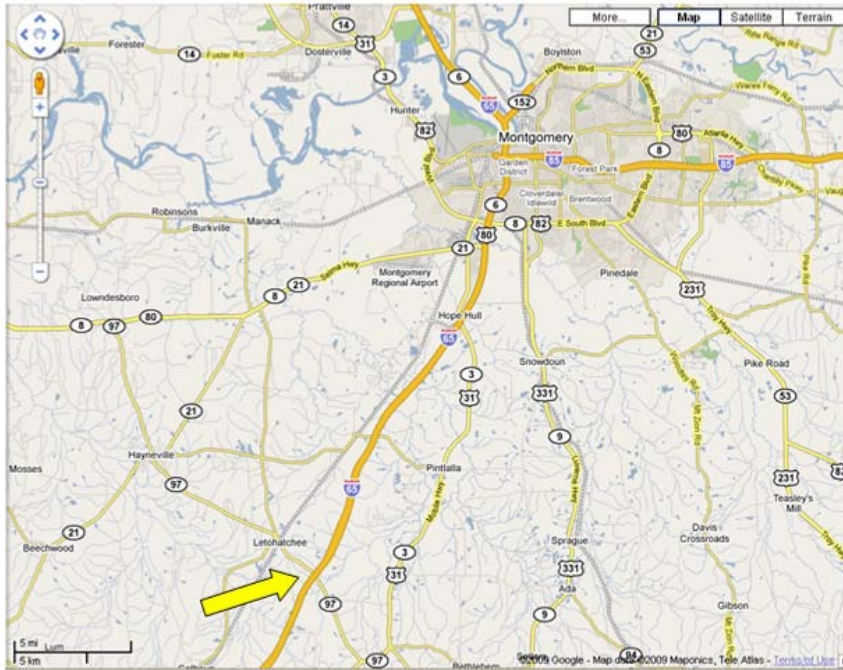


**Figure 3-1:** Location of the Letohatchee Bridge (Google Maps 2009)





**Figure 3-2:** Picture of the Letohatchee Bridge

The Letohatchee bridge is 270 feet (82.3 m) long and consists of four continuous spans with four reinforced concrete girders at a skew angle of 12 degrees. The two exterior spans are 60 feet (18.3 m), and the two interior spans are 75 feet (22.9 m). As shown in Figure 3-2, the girders have a parabolic haunch over each interior support that makes the girders have a greater height for increased negative-moment capacity. The height of the girders ranges from 43 3/8 inches (1102 mm) at midspan to 77 1/8 inches (1959 mm) over the interior supports. The girders support a 6 1/4-inch (159 mm) slab to comprise a roadway that is 28 feet (8.5 m) wide from curb to curb. In the exterior span, 6-inch (152 mm) webwalls, or diaphragms, are located between each girder at the supports and at midspan. In the interior span, the 6-inch (152 mm) diaphragms are located between

each girder at the supports and at every third point of the span. ALDOT's standard drawing for this bridge is IC-2806, and this drawing is accompanied by standard drawing I-109. Figure 3-3 shows a simplified plan view of the bridge (without the skew).

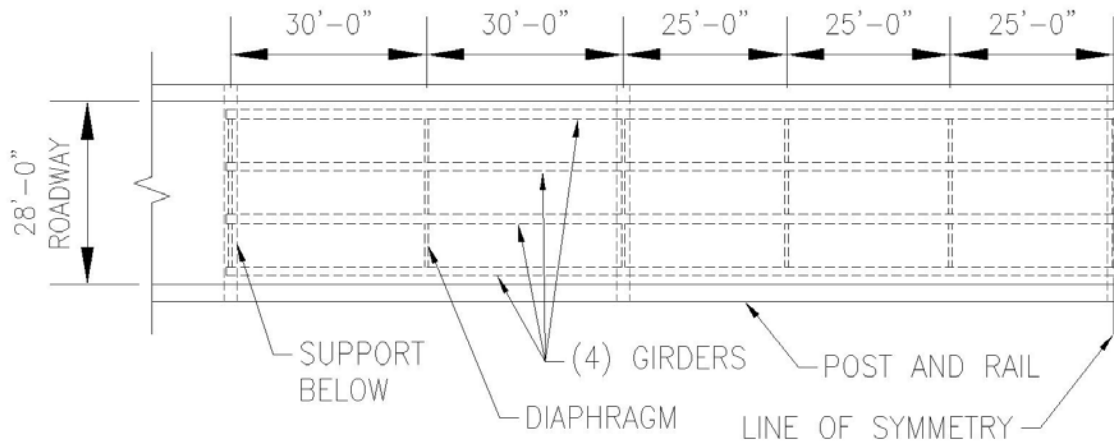


**Figure 3-3:** Plan View of Half of the Letohatchee Bridge

The bridge is symmetric, and only half of the bridge is shown. Figure 3-4 shows a sketch of the cross section of the bridge at an interior support.

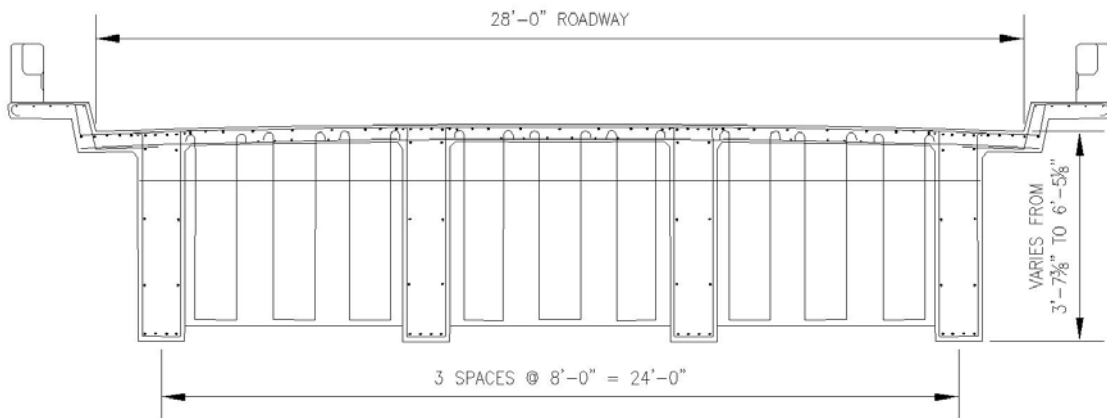


**Figure 3-4:** Sketch of the Cross Section at an Interior Support for the Letohatchee Bridge

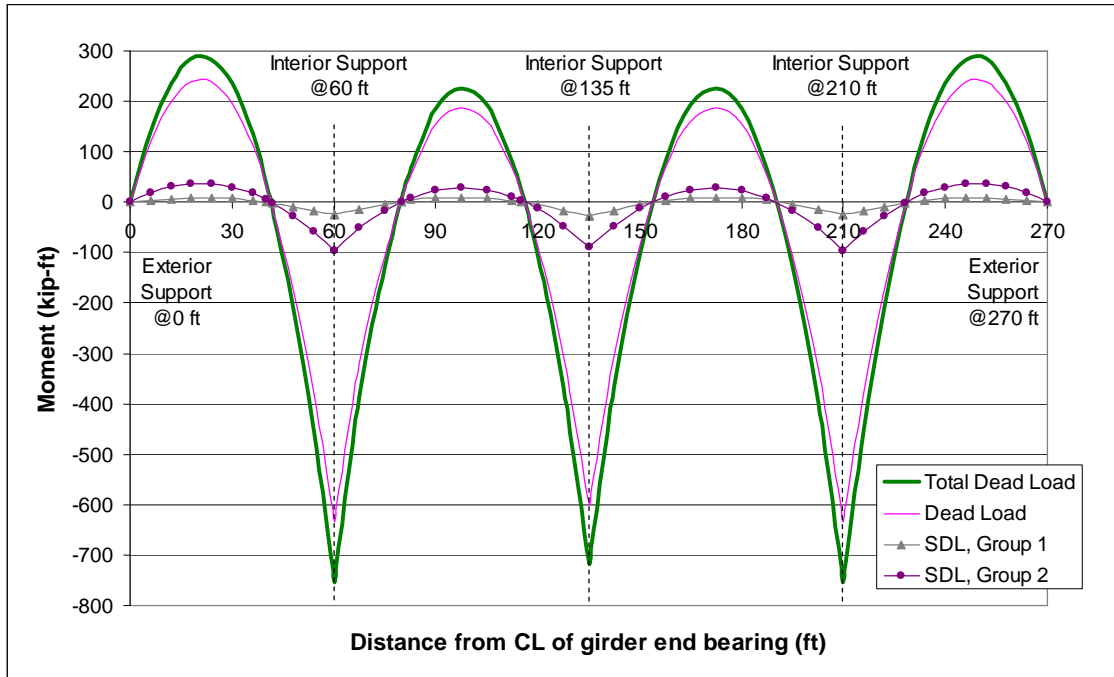
### **3.2 Demand on Existing Bridge**

The Letohatchee bridge was analyzed by ALDOT Bridge Rating and Load Testing engineers using the Bridge Rating and Analysis of Structural Systems (BRASS™) program (Wyoming DOT 2009). For this analysis and for all of the capacity calculations, *AASHTO Standard Specifications for Highway Bridges* (1996) was used. Using the results of the analysis by the ALDOT engineers, the demand on the existing bridge was determined. The loads were divided into dead loads and live loads. Once these were known, the loads were factored and combined to form the factored total load. All of the figures and calculations for this chapter are specifically for an exterior girder. Calculations were completed for an interior girder, but it was found that the exterior girder is more critical; therefore, the exterior girder will be discussed here in detail. It was determined from the BRASS™ output that shear is not critical for the Letohatchee bridge. Flexure will be the focus of the analysis in this chapter.

#### **3.2.1 Dead Load**

In the BRASS™ program, the slab was taken to be 6 inches (152 mm), rather than 6¼ inches (159 mm), due to possible degradation of the roadway surface. To account for this missing load, an extra ¼ inch (6.4 mm) of slab dead load was added into the first group of superimposed dead load (SDL), which also included the diaphragm weight. The curb and rail system was accounted for in a second SDL group. The girder weight and the slab weight were included in the group labeled, “Dead Load.” By combining these three dead load groups, the total dead load on the girder was calculated. Figure 3-5 shows the

moment diagrams for each dead load group and for the total dead load for an exterior girder, which will hereafter be called “Girder 1” or “G1.”

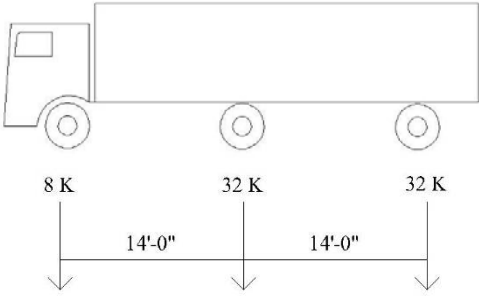
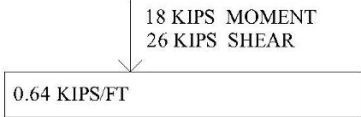
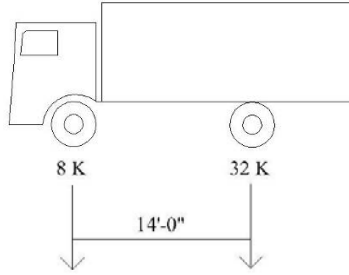
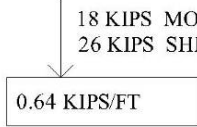
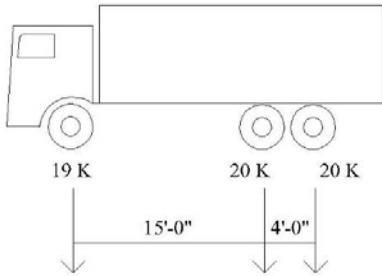
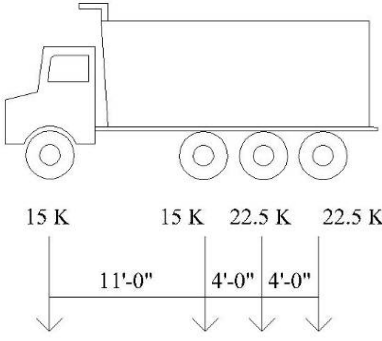


**Figure 3-5:** Moment Diagrams for Dead Load Groups for an Exterior Girder

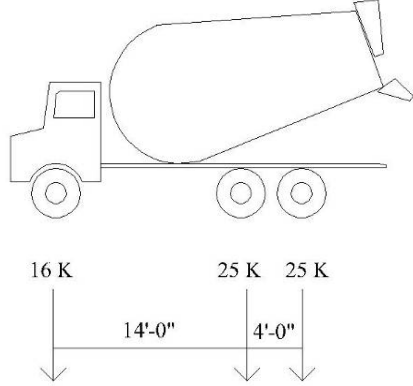
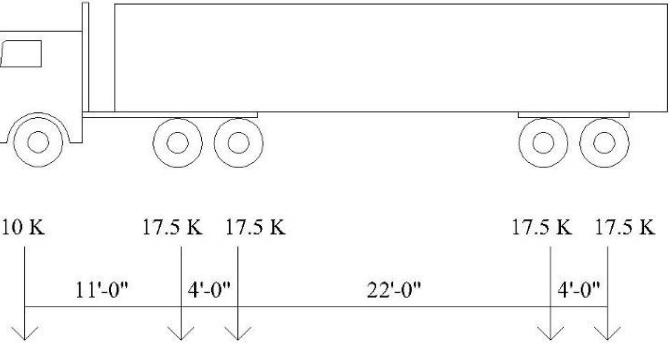
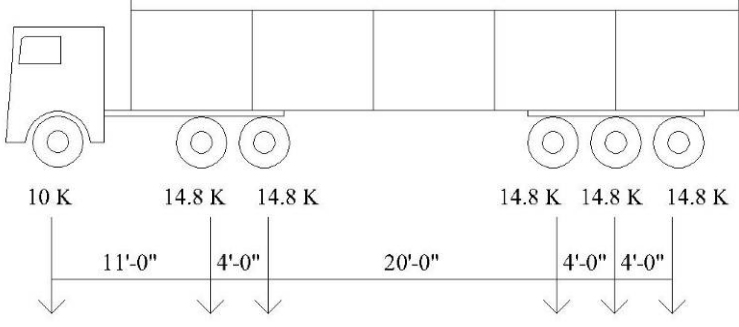
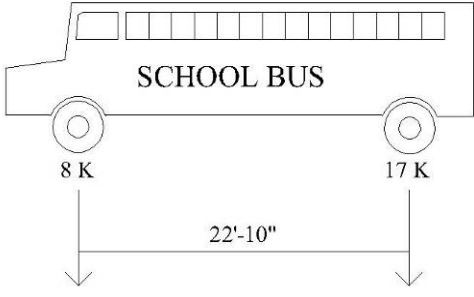
### 3.2.2 Live Load

Eight truck and two lane loadings were used in the BRASS™ program for live load calculations. An impact factor was included in these live loads. In the BRASS™ program, the live load distribution factors were used in accordance with *AASHTO Standard Specifications for Highway Bridges* (1996). The loads and their corresponding load arrangements are depicted in Table 3-1, where K stands for kips.

**Table 3-1: Vehicle Names and Load Arrangements Used for Bridge Analysis**

Vehicle ID	Picture and Load Arrangement
#1: H 20-S 16 Truck	
#2: H 20-S 16 Lane	
#3: H 20 Truck	
#4: H 20 Lane	
#5: Two-Axle Dump Truck	
#6: Three-Axle Dump Truck	

**Table 3-1: Vehicle Names and Load Arrangements Used for Bridge Analysis (continued)**

<p>#7: Concrete Truck</p>	 <p>16 K                      25 K    25 K</p> <p>                                  14'-0"    4'-0"</p>
<p>#8: 3S2 Alabama</p>	 <p>10 K            17.5 K    17.5 K                      17.5 K    17.5 K</p> <p>                  11'-0"    4'-0"                      22'-0"                      4'-0"</p>
<p>#9: 3S3 Alabama</p>	 <p>10 K            14.8 K    14.8 K                      14.8 K    14.8 K    14.8 K</p> <p>                  11'-0"    4'-0"                      20'-0"                      4'-0"    4'-0"</p>
<p>#10: School Bus</p>	 <p>SCHOOL BUS</p> <p>8 K                                      17 K</p> <p>  22'-10"</p>

Trucks 1 and 3 are standard H20 trucks. Loadings 2 and 4 are the lane loads from Trucks 1 and 3, respectively. Vehicles 5 through 10 are Alabama posting trucks, which are trucks that appear on load-posting signs. An example of a load-posting sign is shown in Figure 3-6.



**Figure 3-6:** Example of a load-posting sign (Carmichael and Barnes 2005)

For trucks heavier than those listed in Table 3-1, a special permit must be obtained from ALDOT. Permit trucks are often more critical than the trucks listed in Table 3-1. However, permit trucks do not have standard sizes, loads, or load arrangements. Therefore, only the ten standard loadings shown in the table will be used in the analysis.

The BRASS™ program applied each of the ten loadings from Table 3-1 to an exterior and an interior girder. By moving the trucks across each girder, the BRASS™ software developed a moment envelope for each loading. The moment was computed at every tenth point of each span and at critical locations. Figure 3-7 shows the positive moment envelopes, and Figure 3-8 shows the negative moment envelopes.

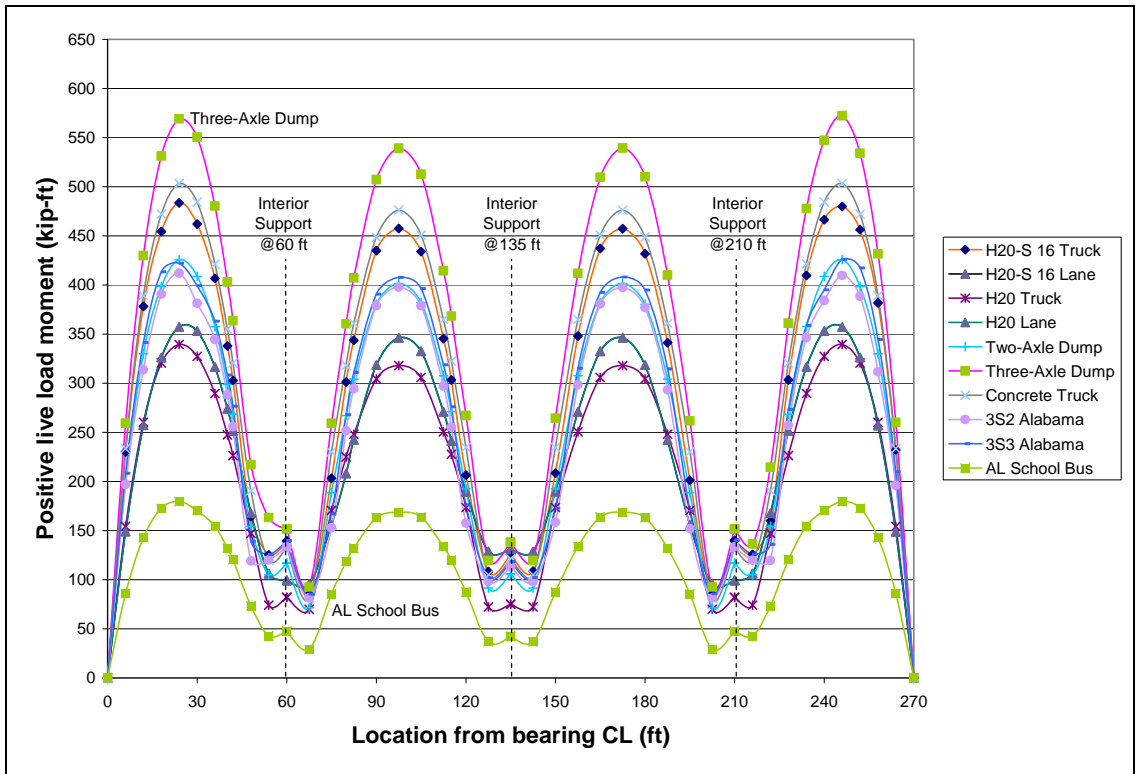
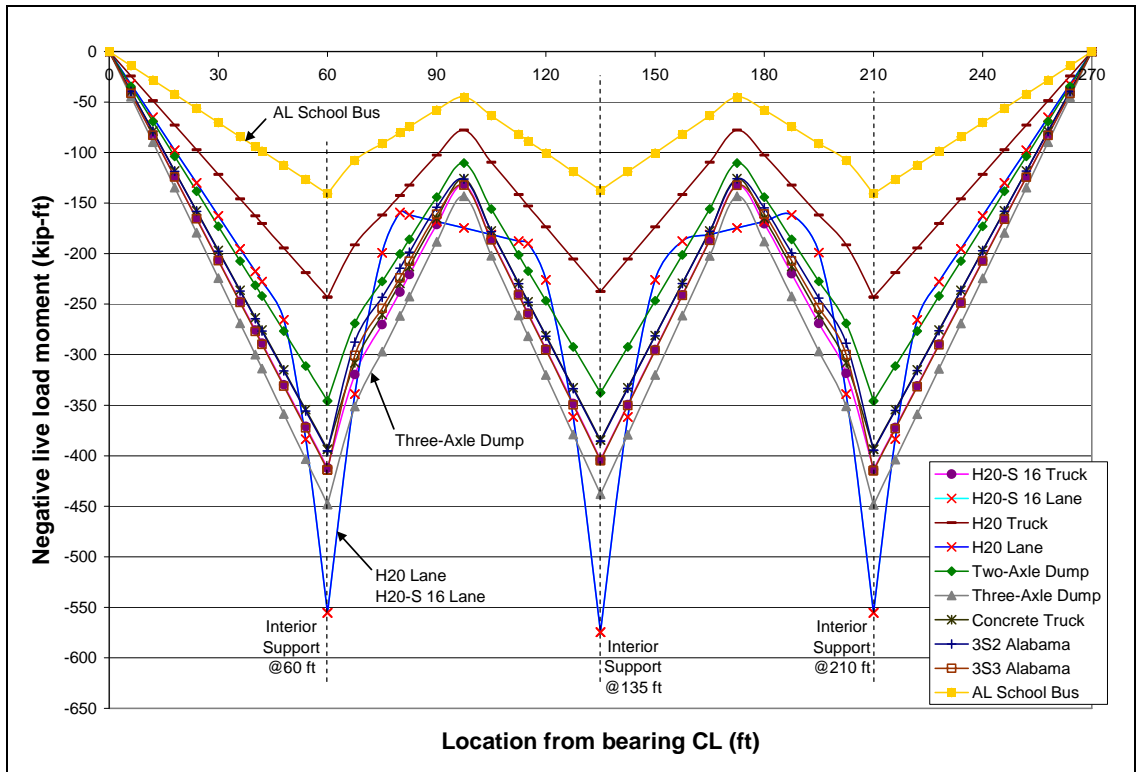


Figure 3-7: Positive Live Load Moment Envelopes across Girder 1





**Figure 3-8:** Negative Live Load Moment Envelopes across Girder 1

As shown in Figures 3-7 and 3-8, the Three-Axle Dump Truck is the worst-case loading for the majority of the moment envelopes. The lane loadings control the live load negative-moment envelope near the interior supports and near midspan of the interior spans.

### 3.2.3 Factored Total Load

After the dead load and live load moment envelopes were developed, the loads were combined and factored. The two load combinations used were operating and inventory, given by the American Association of State Highway and Transportation Officials (AASHTO) as follows:

**Table 3-2: AASHTO Load Combinations**

Load Combination	Factored Moment
Operating	$1.3(D + L)$
Inventory	$1.3(D + 1.67L)$

In Table 3-2,  $D$  stands for dead load, and  $L$  stands for live load (including impact). Because the operating load combination is typically used for bridge rating and load posting purposes, it will be the focus of this analysis, and the inventory rating will not be discussed any further.

At this point in the analysis, the four H20 loadings, numbered 1 through 4, were separated from the six load-posting trucks, numbered 5 through 10. The operating load combination was then used to calculate the factored moment envelopes for each of the loadings for positive and negative moment. Once these envelopes were found, a factored moment envelope was developed that included all four H20 loadings and both positive and negative moments. Figure 3-9 shows the factored moment envelope for positive and negative moment using the operating load combination.

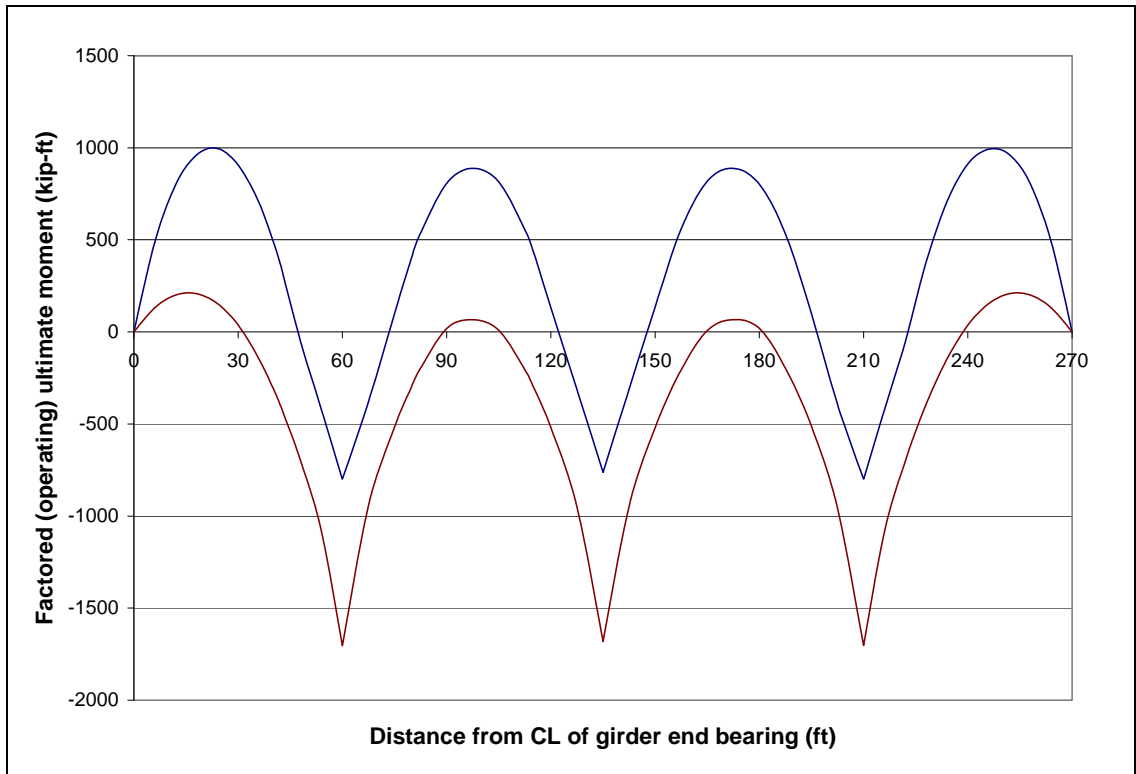


**Figure 3-9:** Factored Ultimate Moment Envelope for the H20 Loadings using the Operating Load Combination

The process was repeated for the load-posting trucks. Figure 3-10 shows the corresponding factored ultimate moment envelope for positive and negative moment using the operating load combination.

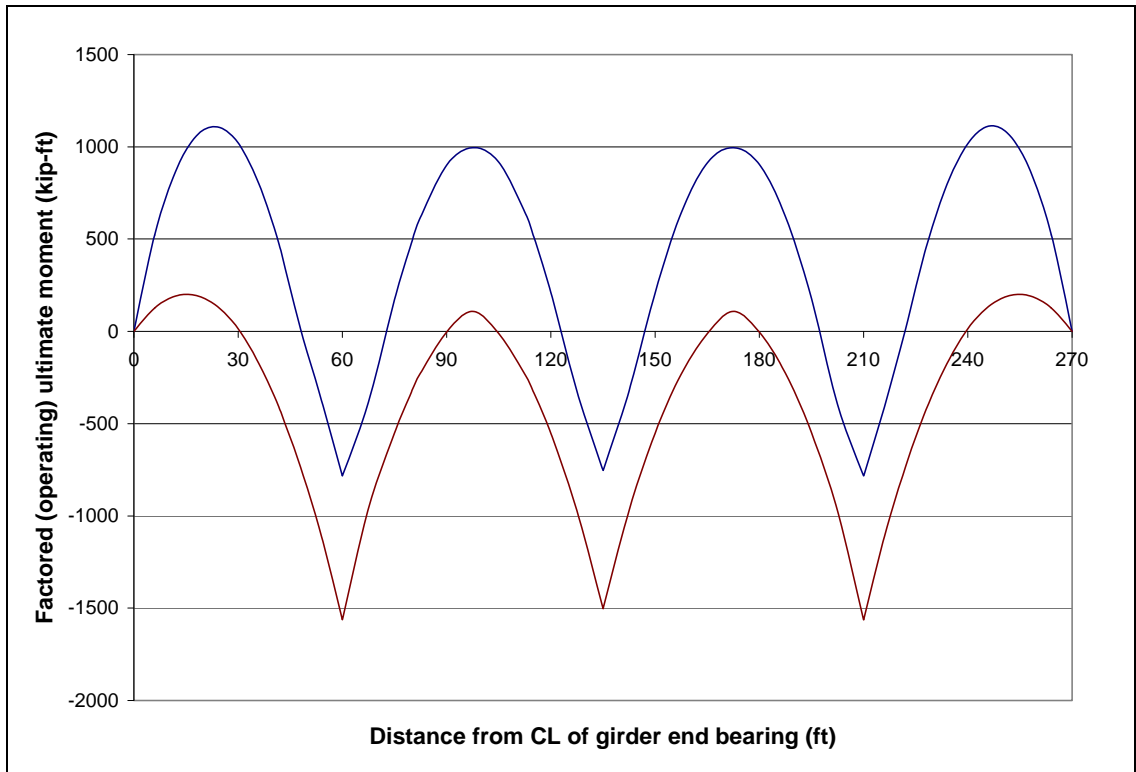


**Figure 3-10:** Factored Ultimate Moment Envelope for the Posting Trucks using the Operating Load Combination

As shown in Figures 3-9 and 3-10, some sections of Girder 1 are always subjected to positive moment and some are always subjected to negative moment. At the midspan regions and near the discontinuous girder ends, the girder is always in positive moment for the operating load combination. At the supports, the girder is always in negative moment for the operating load combination.

### 3.3 Capacity of Existing Bridge

For capacity calculations, in accordance with the age of the bridge, the concrete compressive strength was assumed to be 3000 psi (20 MPa), and the steel reinforcing

bars were assumed to have a yield strength of 40,000 psi (280 MPa). The entire 6¼ inches (159 mm) was used for the slab height. For the exterior girder, 6 feet (1.8 m) was used as the effective flange width, with 2 feet (0.6 m) as the overhang distance. The overhang distance is a conservative approximation because of the post and rail system that is connected to the slab. For all capacity calculations, except for the development length, the AASHTO Standard Specification (1996) was followed. Figure 3-11 shows the cross section used to model the resistance of an exterior girder.

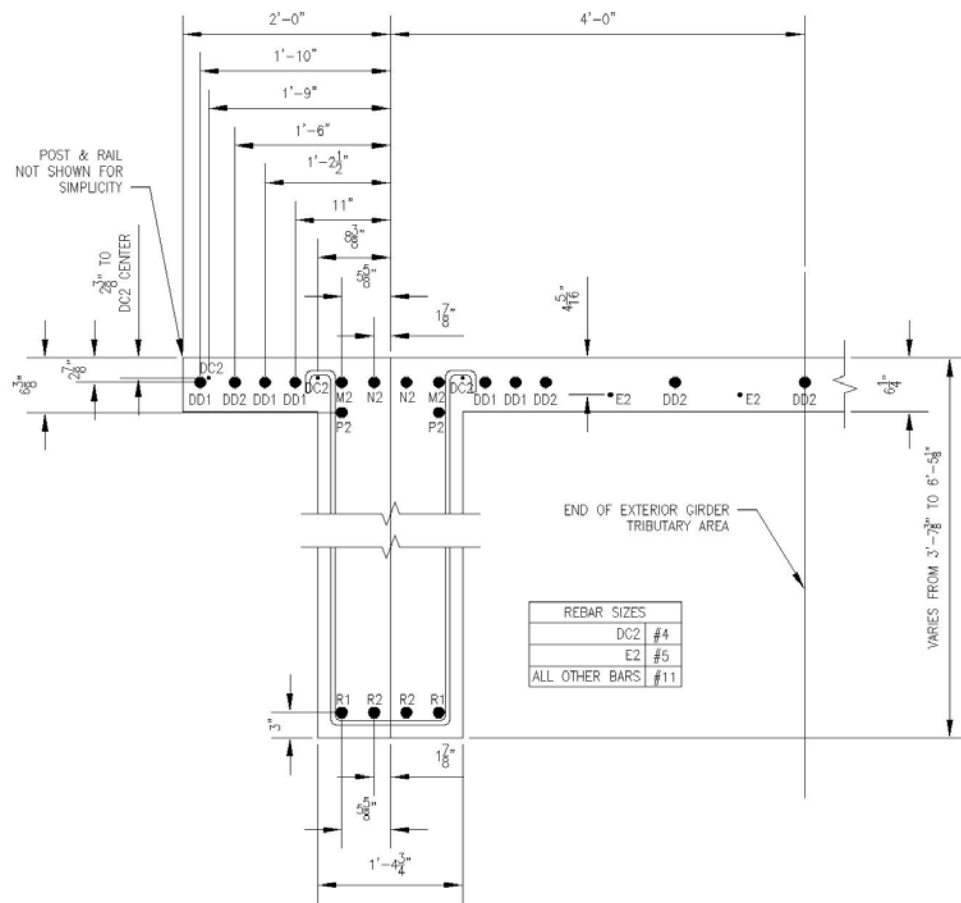


**Figure 3-11:** Exterior Girder Cross Section at an Interior Support Location

The reinforcing steel shown in Figure 3-11 is for the cross section at an interior support. For capacity calculations, the steel in the girder at approximately mid-depth and the compression steel are ignored. Figure 3-12 shows the midspan cross section used to model the resistance of the girder.

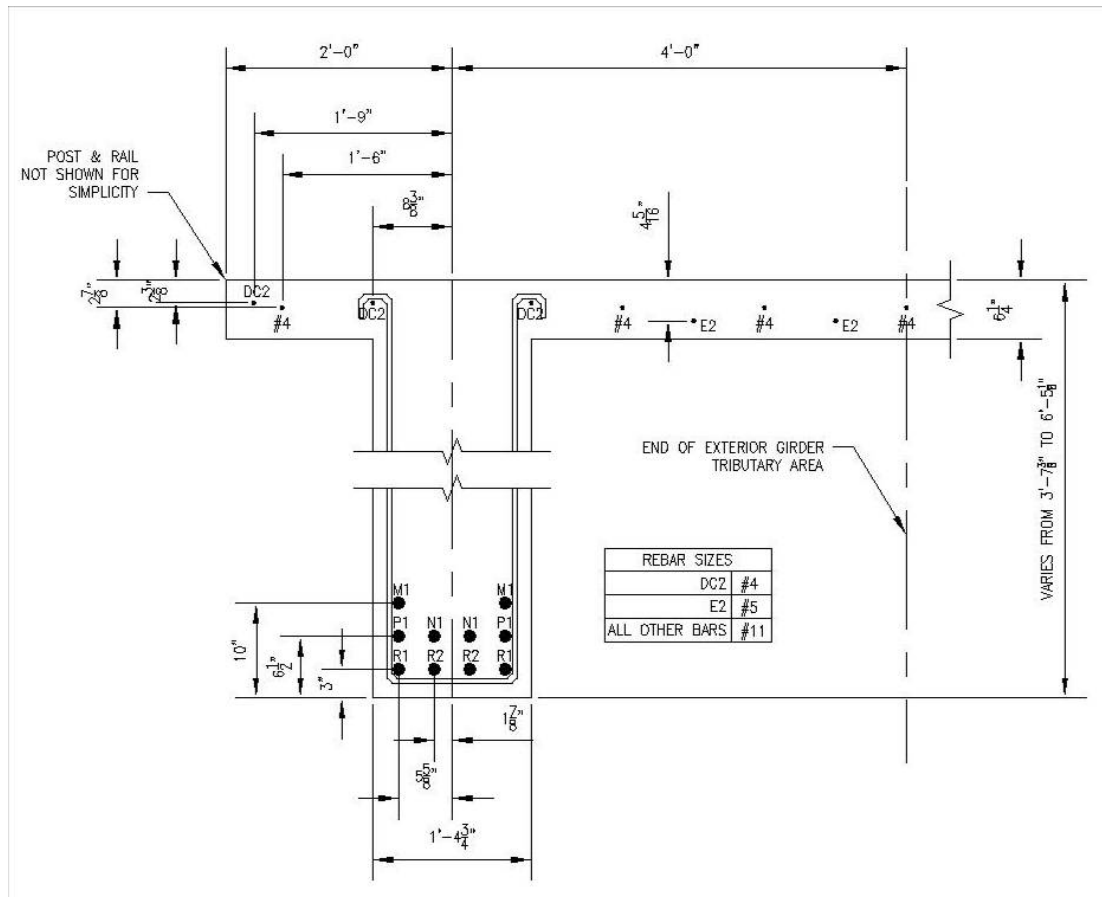


**Figure 3-12:** Exterior Girder Cross Section at Midspan

Figures 3-11 and 3-12 show the difference in steel between the support location and the midspan location. For positive moment, the bars designated M1, N1, and P1 have all been cut short of the support location. For negative moment, the bars designated DD1, M2, N2, and P2 have all been cut short of midspan. The #11 bars designated DD2 are

spliced to #4 bars between midspan and the support. Only the DC2 bars that support the stirrups, the E2 bars in the flange, and the R1 and R2 bars in the web are continued through both locations. Figure 3-13 shows the amount of positive and negative moment steel in the exterior girder and the approximate locations where the steel amount changes between the interior support centerline (CL) and the midspan CL.

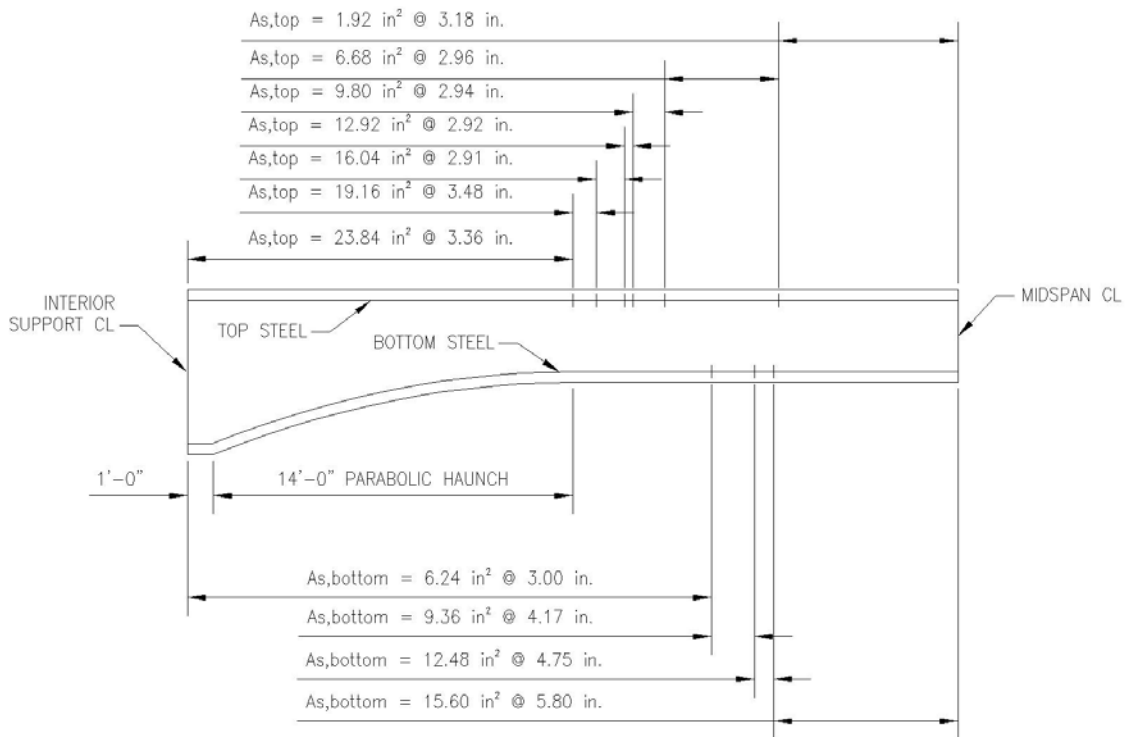


**Figure 3-13:** Elevation View of the Amount of Steel and the Approximate Termination Locations in Girder 1

Figure 3-13 also shows where the centroid of the top and bottom steel is located in relation to the top and the bottom surface of the concrete, respectively. This figure only shows where the bars are physically cut off; it does not take into account the development length of the bars.

To calculate the nominal moment capacity along Girder 1, both the amount of steel at each cross section and the amount of stress that could be developed in each terminated bar needed to be known. Due to overlapping bar development lengths, a spreadsheet was created to compute the portion of steel yield stress developed in each bar group at all of the critical locations. Table 3-3 shows part of the spreadsheet used for positive moment calculations.

**Table 3-3: Portion of Each Bar Group’s Yield Stress Used for Positive Moment Capacity Calculations**

Distance from bearing CL (ft)	Portion of yield stress used for calculations (expressed as a decimal)				
	M1 2 #11	P1 2 #11	N1 2 #11	R1 2 #11	R2 2 #11
-0.56					
-0.31				0.00	0.00
3.44				1.00	1.00
4.83		0.00	0.00	1.00	1.00
5.83	0.00	0.27	0.27	1.00	1.00
8.58	0.73	1.00	1.00	1.00	1.00
9.58	1.00	1.00	1.00	1.00	1.00
33.44	1.00	1.00	1.00	1.00	1.00
34.17	0.81	1.00	1.00	1.00	1.00
35.85	0.36	1.00	0.55	1.00	1.00
37.19	0.00	0.64	0.19	1.00	1.00
37.92		0.45	0.00	1.00	1.00
39.60		0.00		1.00	1.00
60.00				1.00	1.00
Area (in. <sup>2</sup> )	3.12	3.12	3.12	3.12	3.12
y (in.)	10.0	6.5	6.5	3.0	3.0

In Table 3-3, the distances are measured from the centerline of the bearing. Because the girder extends 6.75 inches (171 mm), or approximately 0.56 feet, past the support centerline, some of the distances calculated in the spreadsheet are negative.



In Table 3-3, the area shown at the bottom of the spreadsheet is the combined area for each bar type. The parameter labeled  $y$  is the distance from the centroid of that specific bar type to the bottom of the concrete surface. The development length for this table was calculated according to Section 5.11 of the AASHTO LRFD Bridge Design Specification (AASHTO 2006) because this document will provide more conservative results than the AASHTO Standard Specification.

Another factor accounted for was the varying depth of the cross section in the parabolic haunch region near the interior supports. The height of the girders in this section was given by the drawings at every foot. Therefore, the moment capacity was calculated at every foot of the haunch section.

Once the positive moment capacity along Girder 1 was calculated, the values were factored by multiplying by the strength-reduction factor for flexure of 0.9. The resulting factored capacity is shown in Figure 3-14.

In Figure 3-14, the supports are located at 0 feet, 60 feet, 135 feet, 210 feet, and 270 feet. The moment capacities are greatest at the midspan locations. The moment capacity then decreases from the midspan section to the start of the haunch section. At the start of the haunch section, the moment capacity increases to a peak directly over the interior supports. Because the amount of bottom steel in this region remains constant, the increased moment capacity over the supports is solely due to the increased depth of the section.

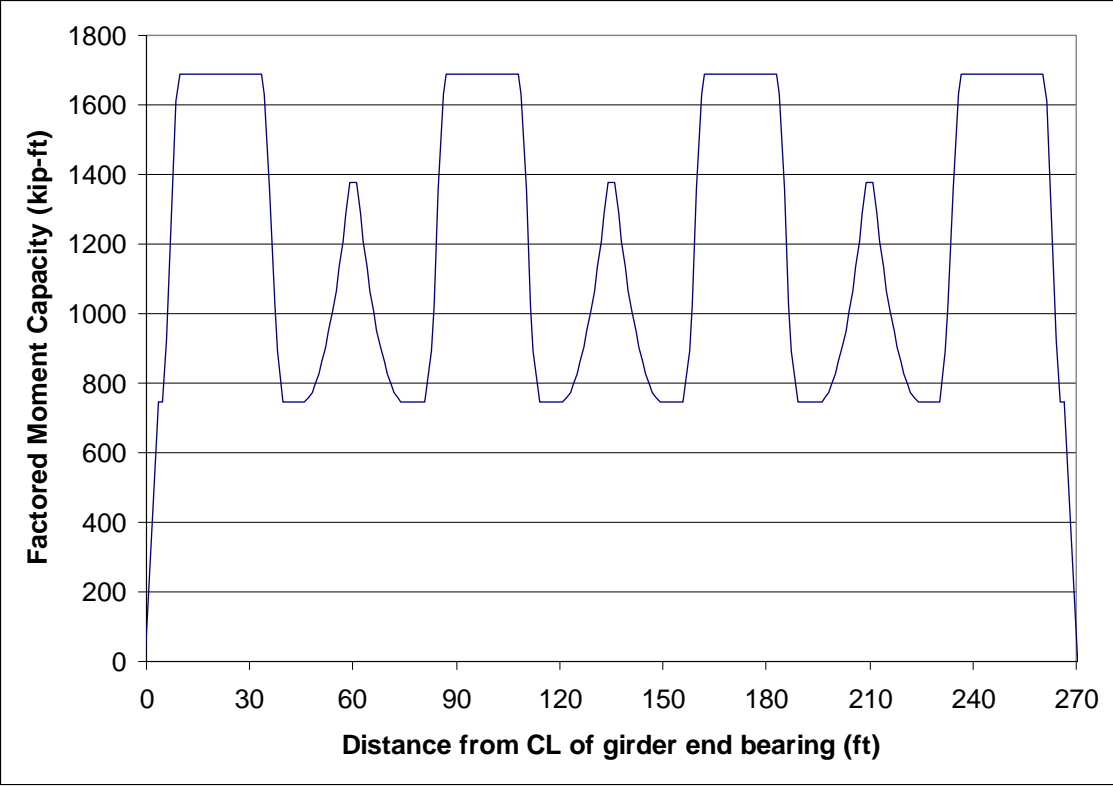


**Figure 3-14:** Factored Positive Moment Capacity along Exterior Girder

To calculate the negative moment capacity for Girder 1, the spreadsheet shown in Table 3-4 was used.

**Table 3-4: Portion of Each Bar Group’s Yield Stress Used for Negative Moment  
Capacity Calculations**

Distance from support CL (ft)	Portion of yield stress used for calculations (expressed as a decimal)								
	DD1(a) 3 #11	P2 2 #11	DD1(b) 2 #11	N2 2 #11	M2 2 #11	DD2* 3½ #11	E2 2 #5	DC2 3 #4	Spliced* 3½ #4
0.00	1.00	1.00	1.00	1.00	1.00	1.00	1.00	1.00	
10.67	1.00	1.00	1.00	1.00	1.00	1.00	1.00	1.00	
11.25	1.00	0.89	1.00	1.00	1.00	1.00	1.00	1.00	
12.08	0.78	0.73	1.00	1.00	1.00	1.00	1.00	1.00	
13.25	0.47	0.51	1.00	0.78	1.00	1.00	1.00	1.00	
13.33	0.44	0.49	0.98	0.76	1.00	1.00	1.00	1.00	
15.00	0.00	0.17	0.53	0.44	0.68	1.00	1.00	1.00	
15.92		0.00	0.29	0.27	0.51	1.00	1.00	1.00	
17.00			0.00	0.06	0.30	1.00	1.00	1.00	
17.33				0.00	0.24	1.00	1.00	1.00	
18.58					0.00	1.00	1.00	1.00	
19.00						1.00	1.00	1.00	0.00
23.00						0.00	1.00	1.00	1.00
25.00							1.00	1.00	1.00
Area (in. <sup>2</sup> )	4.68	3.12	3.12	3.12	3.12	5.46	0.62	0.60	0.70
y (in.)	2.875	6.375	2.875	2.875	2.875	2.875	4.3125	2.375	2.875

\*These bars were located directly at the halfway point between girders, so half of the bar was included in each girder cross section.

In Table 3-4, the parameter labeled y is the distance from the centroid of that specific bar type to the top of the concrete surface. For this table, three different development lengths were used: one for a #11 top bar, one for a typical #11 bar, and one for a #4 bar. The development lengths were calculated according to Section 5.11 of the AASHTO LRFD Bridge Design Specification (AASHTO 2006). Because the DD2 bars were spliced to the #4 bars, both bars were assumed to be fully developed at opposite ends of the splice.

Once the negative moment capacity along Girder 1 was calculated, the values were factored by multiplying by the strength-reduction factor of 0.9. The factored capacity is shown in Figure 3-15.

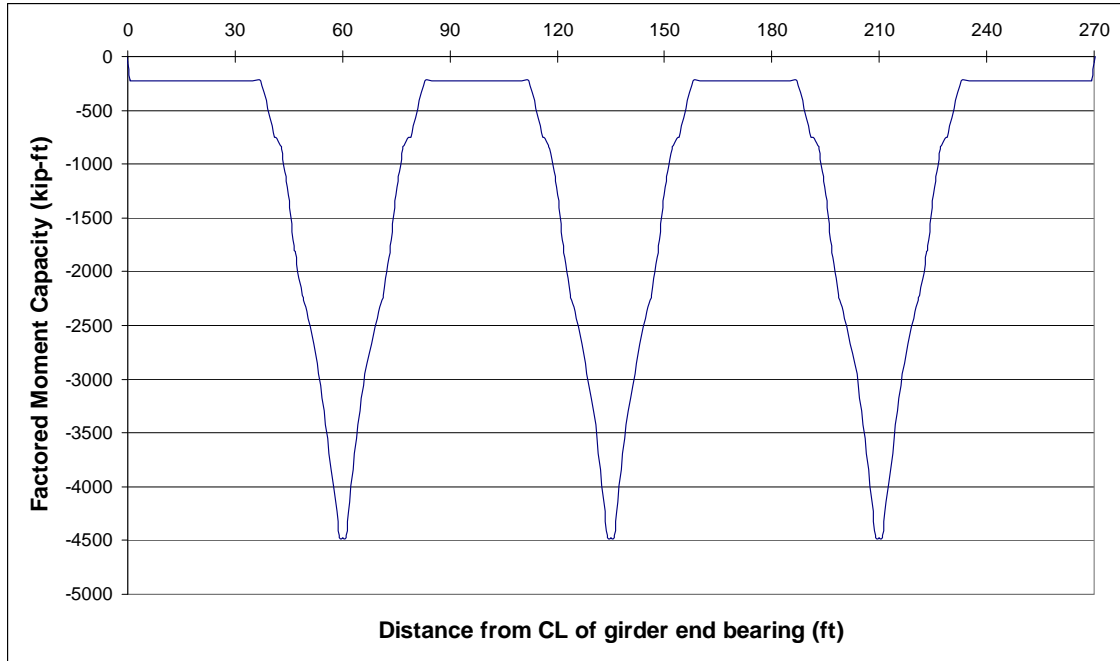


**Figure 3-15:** Factored Negative Moment Capacity along Exterior Girder

### 3.4 Bridge Deficiencies

Once the flexural demand and capacity were known for the existing Letohatchee bridge, a comparison could be made to discover any deficiencies. Before this comparison was made, the demand graph was slightly modified to account for the fact that diagonal shear cracks cause shifting of the flexural demand on the tension steel along the girder. By assuming that such a crack would occur at an angle of forty-five degrees, the demand graph was shifted a distance  $d$  out from midspan for positive moments and a distance  $d$  out from the supports for negative moments, where  $d$  is the effective depth of the reinforced concrete cross section. The effective depth of the specific section that needed strengthening was used as the shift distance. The shifting of the positive demand envelope created an irregularity in the diagram resulting in an overlap region at the

interior supports. Figure 3-16 shows the comparison between the resulting factored demand and the factored capacity of the Letohatchee bridge under H20 loadings and the operating load combination. Figure 3-17 shows the same comparison for the posting trucks.

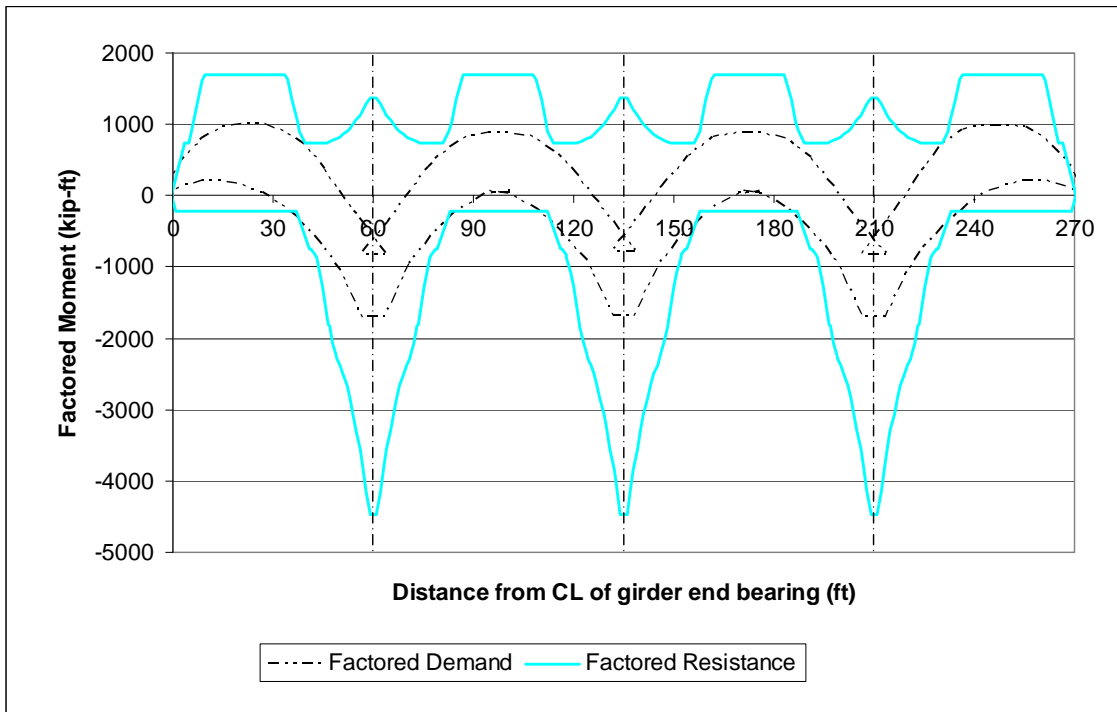


**Figure 3-16:** Factored Demand Versus Factored Resistance for H20 Trucks

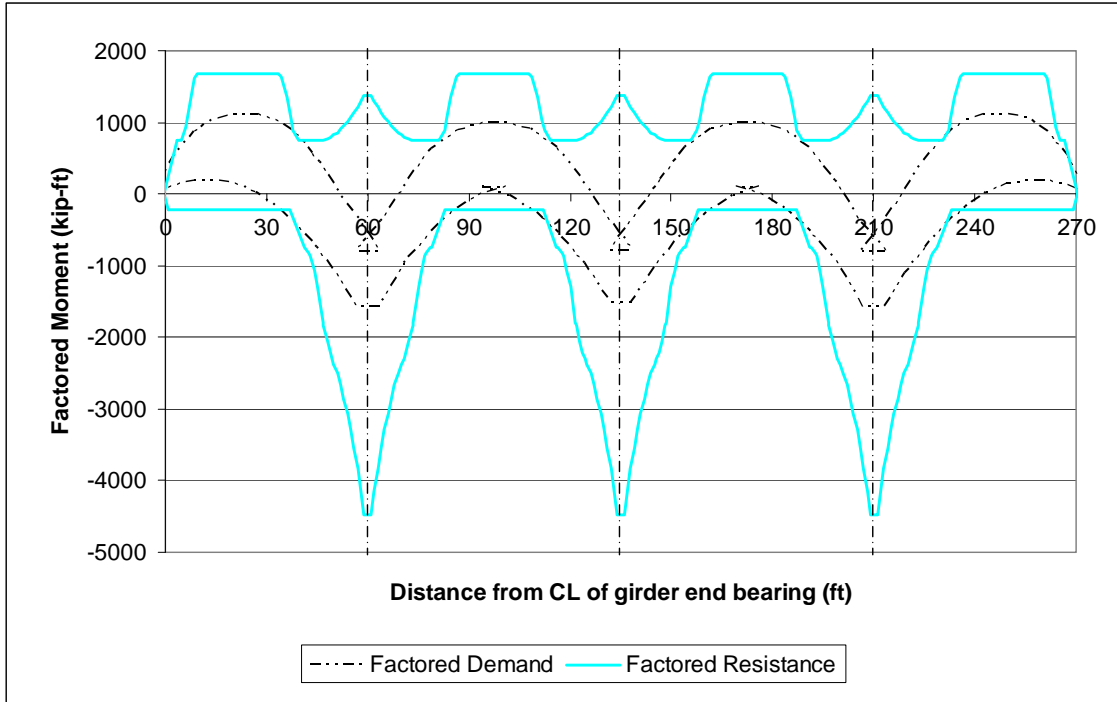


**Figure 3-17:** Factored Demand Versus Factored Resistance for Posting Trucks

Figures 3-16 and 3-17 both show deficiencies in the Letohatchee bridge. The deficiency for the posting trucks is slightly worse than for the H20 trucks. For the posting trucks, there is insufficient capacity for both positive and negative moment. For positive moment, the deficiency occurs at about 40 feet (12.2 m) from the centerline of the girder end bearing. It occurs over a length of approximately two feet (0.6 m), and the deficiency is less than 6%. Table 3-5 shows the exact location and magnitude of the deficiency.

**Table 3-5: Positive-Moment Deficiency for Posting Trucks at Critical Locations**

Location from bearing CL (ft)	$M_u$ (k-ft)	$\phi M_n$ (k-ft)	Strength Deficiency (k-ft)
38.7	825	825	----
39.6	787	745	43
40.4	744	744	----

Because the deficiency occurs over such a small region and because there is only a 6% deficiency, positive moment strengthening for the Letohatchee bridge will not be discussed further.

As shown in Figure 3-17, the negative-moment deficiencies due to the posting trucks occur at approximately 37 feet, 83 feet, and 112 feet from each end of the girder. These deficiencies occur over about a 7-foot (2.1 m) region. Table 3-6 shows the exact locations and magnitudes of the deficiencies.

**Table 3-6:** Negative-Moment Deficiencies for Posting Trucks at Critical Locations

	Distance from end bearing CL (ft)	Distance from nearest interior support (ft)	$M_u^-$ (k-ft)	$\phi M_n$ (k-ft)	Strength Deficiency (k-ft)	Strength increase needed (%)
Region 1	33	27	189	226	----	----
	34	26	229	226	2	1
	35	25	269	226	43	19
	36	24	309	226	83	37
	37	23	350	226	124	55
	38	22	396	357	39	11
	39	21	443	487	----	----
Region 2	81	21	431	487	----	----
	82	22	386	357	29	8
	83	23	341	226	114	50
	84	24	300	226	73	32
	85	25	261	226	34	15
	86	26	223	226	----	----
Region 3	108	27	198	226	----	----
	109	26	228	226	1	1
	110	25	265	226	39	17
	111	24	304	226	78	34
	112	23	344	226	118	52
	113	22	389	357	33	9
	114	21	434	487	----	----

Because the girders are symmetric, the distances shown in Table 3-6 are measured from both ends of the girder. A location on each side of the deficiency is shown to clearly define the bounds of each deficient region.

### 3.5 Summary

The Letohatchee bridge was found to be deficient in six separate regions in each girder.

Figure 3-18 shows the approximate locations of each deficient region.



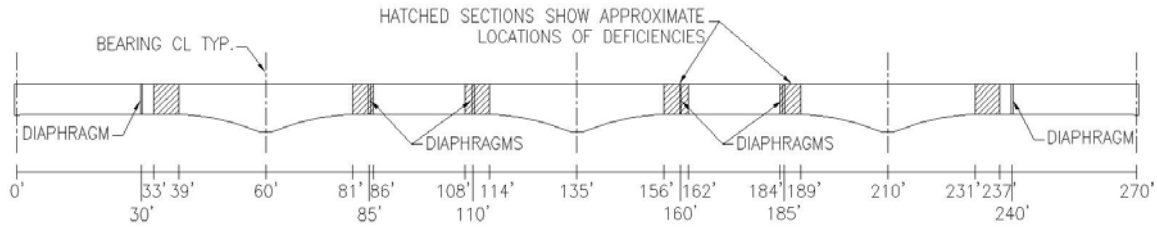


**Figure 3-18:** Elevation View of the Locations of the Letohatchee Bridge Deficiencies

In Figure 3-18, the hatched areas show the regions where the bridge is deficient. The distances shown at the bottom of the figure show the locations along the girder measured from the centerline of the girder's end bearing.

The regions where the deficiencies are the greatest occur in the exterior spans. In these regions, the moment capacity needs to be strengthened from a factored nominal moment capacity of 226 kip-feet to a required factored moment capacity of 350 kip-feet, which would be about a 55% increase in strength.

Figure 3-19 shows the bar termination locations and the approximate range of the deficiency.

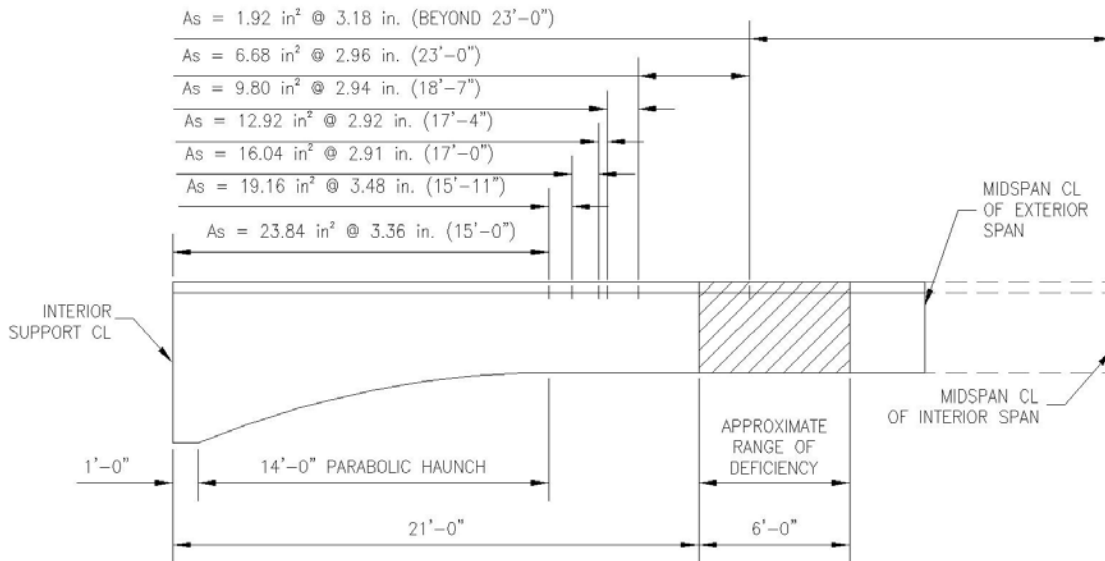


**Figure 3-19: Bar Termination and Deficient Region Locations**

The hatched region in the figure shows the deficient region. The figure is shown from the interior support centerline to the midspan centerline of the exterior span. The midspan centerline of the interior span is shown as a dashed line. The distances shown in parentheses for the bar termination locations are measured from the interior support centerline.

The cause of the negative-moment deficiencies for this bridge is not a shortage of internal steel reinforcement at the support location. As shown in Figure 3-19, the deficient region occurs at about 21 feet from interior support centerline. The cause of the negative-moment deficiencies is the premature termination of the negative-moment steel reinforcement. As shown in Figure 3-19, most of the top bars have been terminated well before the deficient region.

One of the possible strengthening techniques is to use FRP strips. Before an FRP-strengthening scheme can be proposed or implemented, however, the amount of

strengthening that FRP strips can provide needed to be investigated and quantified. In Chapter 2, several models were introduced that attempt to describe the debonding behavior of FRP. Several testing programs were also introduced. In Chapter 4, the models were compared to the experimental tests to determine the accuracy and validity of the models.

## Chapter 4: Evaluation of Existing Models

### 4.1 Introduction

In Chapter 2, several IC-debonding and PE-debonding models were introduced and explained. Some of the models are design provisions recommended by organizations, and some are models taken from published papers, theses, and dissertations. In this chapter, each of the models is evaluated by comparing it to the relevant test data from the experimental testing programs that were also introduced in Chapter 2. Table 4-1 shows the experimental tests that were used in these evaluations and the type of FRP application used in each test series.

**Table 4-1:** List of Experimental Test Series

Test Series Number	Name	EB Tests	NSM Tests
1	El-Hacha and Rizkalla (2004)	YES	YES
2	Jung et al. (2005)	YES	YES
3	Reed et al. (2005)	YES	NO
4	Carmichael and Barnes (2005)	YES	NO
5	Taljsten and Nordin (2007)	NO	YES
6	Yost et al. (2007)	NO	YES
7	Liu, Oehlers, and Seracino (2006)	NO	YES
8	Teng et al. (2006)	NO	YES
9	De Lorenzis and Nanni (2002)	NO	YES
10	Sena Cruz and Barros (2004)	NO	YES
11	Sena Cruz et al. (2006)	NO	YES
12	Hassan and Rizkalla (2003)	NO	YES

In this chapter, each test series is identified by the corresponding number shown in Table 4-1. The test series with only EB specimens, test series 3 and 4, were specifically chosen because these studies were conducted by previous Auburn University researchers and all test data were already known. The other test series were chosen because they also included specimens strengthened with NSM. Most of the tests that were chosen are flexural tests. A few of the tests, however, include modified-beam tests, with specimens that were not loaded in flexure.

As documented in this chapter, the moment capacities and the FRP strain values at flexural failure were predicted using recommended models and compared to experimental values. The experimental FRP strain values taken from the twelve test series were measured at various locations along the length of the girders. In all of the test series, the FRP strain values were measured at least at midspan and underneath the load points, which are the most likely locations for a crack. The Reed et al. (2005) study was the only test series that explicitly stated that the strain gauges were placed at crack locations. Also, the Reed et al. study and the Carmichael and Barnes (2005) study were the only test series where the specimens were cracked before strengthening.

This rest of this chapter is divided into four parts:

1. PE-debonding models for NSM,
2. IC-debonding models for EB,
3. IC-debonding models for NSM, and
4. Summary of model evaluation results.

In the section about the PE-debonding models for NSM, only one organization — Standards Australia — gives quantitative design provisions. The American Concrete

Institute (ACI) and the International Federation of Structural Concrete (*fib*) only give qualitative design provisions for both NSM and EB, which were introduced in Chapter 2. For the IC-debonding models for EB and for the IC-debonding models for NSM, three organizations give design provisions: ACI, *fib*, and Standards Australia.

## **4.2 PE-Debonding Models for NSM**

Four different PE-debonding models for NSM FRP were analyzed in this section. Each of the four models was used to predict strengthened moment capacities for different experimental specimens. The predictions of these models were compared to experimental results to determine the accuracy and level of safety of each model. The four models discussed in this section are Standards Australia (2008), Blaschko (2003), Hassan and Rizkalla (2003), and Vasquez (2008). The experimental tests used in this section are test series 8 through 12.

### **4.2.1 Standards Australia**

The PE-debonding model for NSM FRP given by Standards Australia was compared to the existing experimental NSM tests that were introduced in Chapter 2 to determine the accuracy and level of safety of the model.

#### **4.2.1.1 Comparison to Previous Testing**

The model discussed in this section was used to predict the moment at the plate end when debonding occurs. This moment was used to calculate the predicted maximum moment for the beam and then was compared to the experimental moment. The experimental tests used for this analysis were ones that involved varying embedment lengths of EB, which

included test series 8 through 12. These test series were presented in Chapter 2. Table 4-2 shows a comparison of capacities using the PE-debonding model from Standards Australia.

For test series 8, one of the four specimens was predicted to debond at a load that was less than the predicted failure load of the control beam, which is the reason the change in capacity is negative. The value shown in Table 4-2 for specimen B500 is the capacity at which PE debonding occurs. Failure for this beam would not occur until the concrete crushed, which would happen at a capacity close to the predicted capacity for the control beam of 21.5 kip-ft. The premature PE debonding of the FRP is the reason that the experimental capacity was 25% larger than the predicted capacity for this specimen.

For specimens B500 and B1200, the changes in capacity shown in Table 4-2 are misleading. For specimen B500, the experimental change in capacity was very small compared to the prediction; therefore, the ratio of changes in capacity was very small. For specimen B1200, the predicted change in capacity was very small compared to the experimental change in capacity; therefore, therefore, the ratio of changes in capacity was very large.

**Table 4-2:** Comparison of the PE-Debonding Model by Standards Australia (2008) to NSM Test Results

Test Series #	Specimen ID	Predicted			Experimental			$M_{n,exp}/M_{n,pred}$	$\Delta M_{n,exp}/\Delta M_{n,pred}$
		$M_n$ (k-ft)	$\Delta M_n$ (k-ft)	Failure Mode	$M_{exp}$ (k-ft)	$\Delta M_{exp}$ (k-ft)	Failure Mode		
8	B500	16.8	-4.7	PE	21.1	-0.4	PE	1.25	0.08
8	B1200	22.5	0.9	PE	28.0	6.5	PE	1.25	7.02
8	B1800	33.7	12.2	PE	40.6	19.1	PE	1.20	1.57
8	B2900	34.3	12.8	R	44.1	22.6	CC	1.28	1.77
9	G4D6a	9.9	N/A	PE	4.4	N/A	P	0.44	N/A
9	G4D12a	11.9	N/A	PE	6.2	N/A	P	0.52	N/A
9	G4D12b	11.9	N/A	PE	6.6	N/A	P	0.55	N/A
9	G4D12c	11.9	N/A	PE	7.6	N/A	P	0.64	N/A
9	G4D18a	14.9	N/A	PE	7.6	N/A	P	0.51	N/A
9	G4D24c	17.9	N/A	R	11.0	N/A	P	0.62	N/A
9	C3D6a	5.7	N/A	PE	2.8	N/A	P	0.49	N/A
9	C3D12a	6.5	N/A	PE	4.8	N/A	P	0.73	N/A
9	C3D12b	6.5	N/A	PE	5.4	N/A	P	0.84	N/A
9	C3D12c	6.5	N/A	PE	5.1	N/A	P	0.79	N/A
9	C3D18a	7.5	N/A	PE	7.5	N/A	P	1.00	N/A
9	C3D24b	8.9	N/A	PE	7.8	N/A	P	0.88	N/A
9	C3S6a	5.6	N/A	PE	2.3	N/A	P	0.42	N/A
9	C3S12a	6.4	N/A	PE	3.1	N/A	P	0.49	N/A
9	C3S12b	6.4	N/A	PE	2.7	N/A	P	0.43	N/A
9	C3S12c	6.4	N/A	PE	3.1	N/A	P	0.49	N/A
9	C3S18a	7.4	N/A	PE	4.4	N/A	P	0.60	N/A
9	C3S24a	8.7	N/A	PE	4.0	N/A	P	0.45	N/A
10	fcm35 Lb40	1.6	N/A	PE	1.4	N/A	P	0.88	N/A
10	fcm35 Lb60	1.7	N/A	PE	2.1	N/A	P	1.23	N/A
10	fcm35 Lb80	2.1	N/A	PE	2.1	N/A	P	0.97	N/A
10	fcm45 Lb40	1.9	N/A	PE	1.4	N/A	P	0.74	N/A
10	fcm45 Lb60	2.0	N/A	PE	1.8	N/A	P	0.91	N/A
10	fcm45 Lb80	2.5	N/A	PE	2.4	N/A	P	0.97	N/A
10	fcm70 Lb40	2.6	N/A	PE	1.4	N/A	P	0.56	N/A
10	fcm70 Lb60	2.9	N/A	PE	1.7	N/A	P	0.60	N/A
10	fcm70 Lb80	3.3	N/A	PE	2.4	N/A	P	0.72	N/A
11	Lb60 M	2.3	N/A	PE	1.0	N/A	P	0.44	N/A
11	Lb90 M	2.3	N/A	PE	1.3	N/A	P	0.57	N/A
11	Lb120 M	2.3	N/A	PE	1.5	N/A	P	0.66	N/A
12	B1	15.2	4.7	PE	24.4	0.5	PE	1.61	0.10
12	B2	16.7	6.2	PE	24.9	0.9	PE	1.49	0.15
12	B3	22.3	11.8	PE	27.7	3.7	PE	1.24	0.31
12	B4	22.7	12.2	R	34.1	10.1	PE	1.50	0.83
12	B5	22.7	12.2	R	36.4	12.4	R	1.60	1.02
12	B6	22.7	12.2	R	34.6	10.6	R	1.52	0.87
12	B7	22.7	12.2	R	36.9	12.9	R	1.62	1.06
12	B8	22.7	12.2	R	36.9	12.9	R	1.62	1.06

Notes: CC- crushing of the concrete (preceded by steel yielding); P- pullout of the FRP  
PE- plate-end debonding; R- rupture of the FRP



For specimen B1800, the failure mode was correctly predicted as PE debonding, but the experimental capacity was 20% greater than the predicted capacity. For this specimen, the experimental change in capacity was 57% larger than the predicted change in capacity. For specimen B2900, the failure mode was predicted to be FRP rupture, but the beam actually failed due to crushing of the concrete. Because of this incorrect failure mode, the experimental capacity was consequently 28% greater than the predicted capacity, and the experimental change in capacity was 77% greater than the predicted change in capacity.

For the G4 and C3S series in test series 9, the model did not predict the capacity very accurately. For these series, the experimental capacity ranged from 42 to 64% of the predicted capacity. For the C3D series, the model did not predict the capacity very accurately for the shorter bonded lengths, but as the bonded length increased, from six bar diameters to 24 bar diameters, the accuracy of the model improved. For the specimens with a bonded length of six or twelve bar diameters, C3D6 or C3D12, the experimental capacity ranged from 49 to 84% of the predicted capacity. For the specimens with a bonded length of eighteen or twenty-four bar diameters, C3D18 or C3D24, the experimental capacity was 100 and 88% of the predicted capacity, respectively.

For test series 10 and 11, the model predicted PE-debonding failures for all of the specimens, and all of the specimens failed due to pullout of the FRP. The comparison that was used for the other specimens, the ratio of the experimental capacity to the predicted capacity, is not a good measure of accuracy due to the small magnitudes of the capacities. The experimental capacities range from 1.0 to 2.4 kip-ft, and the predicted capacities

range from 1.6 to 3.3 kip-ft. The most that the capacity was overestimated is 1.3 kip-ft, and the most that it was underestimated is 0.4 kip-foot.

For specimens B1, B2, and B3 in test series 12, the failure mode was correctly predicted as PE debonding. For these specimens, the experimental strengthened moment capacities are 61, 49, and 24% higher, respectively, than the predicted strengthened moment capacities, and the experimental changes in capacity are just 10, 15, and 31% of the predicted changes in capacity. For specimens B4 through B8, the experimental capacities were well above the predicted capacities, but the experimental changes in capacity were relatively close to the predicted changes in capacity.

Figure 4-1 shows a graph of the experimental capacity versus the predicted capacity. Figure 4-2 shows a graph of the experimental change in capacity versus the predicted change in capacity.

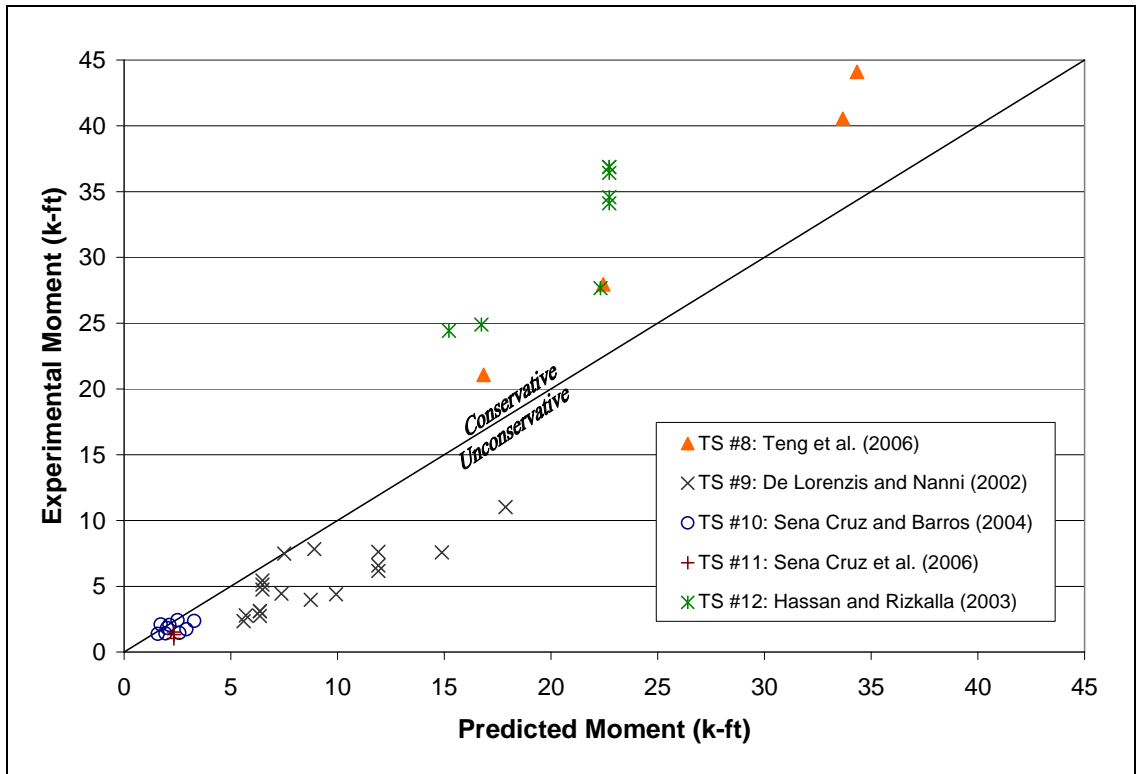


**Figure 4-1:** Comparison between NSM Test Results and Standards Australia (2008) PE-  
 Debonding Capacity Predictions

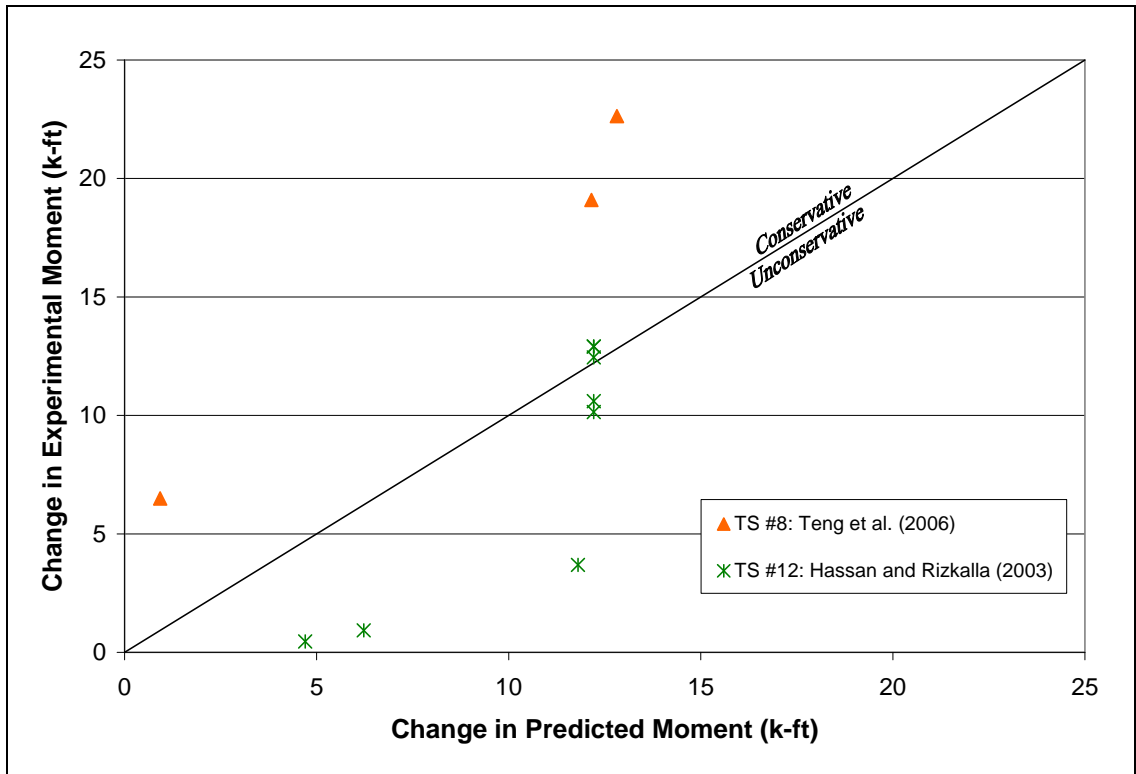


**Figure 4-2:** Comparison between NSM Test Results and Standards Australia (2008) PE-  
 Debonding Change-in-Capacity Predictions

As shown in Figures 4-1 and 4-2, there was a wide dispersion of data points with some on the conservative side and some on the unconservative side. The series that did not involve pullout failure, test series 8 and 12, all produced conservative predictions for capacity but produced mixed results for the change in capacity. Test series 9, 10, and 11 mostly produced unconservative predictions of capacity. Only test series 10 and 11 were relatively close to the line of accuracy shown in Figure 4-1. The change in capacity for specimen B500 is not shown in Figure 4-2 because it was predicted to be negative.

Table 4-3 shows the measured and predicted strain values for the FRP.

**Table 4-3: FRP Strain Predictions using the Standards Australia (2008) PE-Debonding Model and NSM Test Results**

Test Series #	Specimen ID	Predicted		Experimental		$\frac{\epsilon_{f,exp}}{\epsilon_{f,pred}}$
		$\epsilon_{f,pred}$	$\frac{\epsilon_{f,pred}}{\epsilon_{f,rupt}}$	$\epsilon_{f,exp}$	$\frac{\epsilon_{f,exp}}{\epsilon_{f,rupt}}$	
8	B500	0.21%	0.14	0.23%	0.15	1.07
8	B1200	0.29%	0.18	0.37%	0.23	1.27
8	B1800	1.30%	0.82	0.73%	0.46	0.56
8	B2900	*1.37%	*0.87	*0.97%	*0.61	0.71
12	B1	0.19%	0.56%	0.05%	0.04	0.09
12	B2	0.21%	0.72%	0.17%	0.13	0.24
12	B3	0.29%	1.32%	0.71%	0.53	0.54
12	B4	*1.33%	*1.00	1.18%	0.89	0.89
12	B5	*1.33%	*1.00	*1.27%	*0.95	0.95
12	B6	*1.33%	*1.00	*1.28%	*0.96	0.96
12	B7	*1.33%	*1.00	*1.29%	*0.97	0.97
12	B8	*1.33%	*1.00	*1.31%	*0.98	0.98

\*denotes a failure mode other than PE debonding

The FRP strain predictions for test series 8 were not very accurate. For specimens B500 and B1200, the experimental FRP strains were 107 and 127%, respectively, of the predicted FRP strains. For specimens B1800 and B2900, the experimental FRP strains were 56 and 71%, respectively, of the predicted FRP strains.

The model did not accurately predict the strain in the FRP for specimens B1, B2, and B3 in test series 12. These test specimens debonded at a relatively low strain value, and the predicted strain values were much higher. The experimental strains were 9, 24, and 54% of the predicted strains, respectively. For specimen B4, the predicted strain matched the experimental strain relatively well. The experimental strain 89% of the predicted strain. For specimens B5 through B8, the failure mode was correctly predicted as FRP rupture. Consequently, the strain in the FRP was very accurately predicted. The experimental strain ranged from 95 to 98% of the predicted strain.

#### **4.2.1.2 Discussion of Model**

The NSM PE-debonding model given by Standards Australia was not very accurate at predicting strengthened moment capacities. The commentary of the design handbook HB305-2008 states that there is not enough research at the present time to sufficiently quantify PE debonding in NSM plates. The model proposed by Standards Australia is simply the model used for EB side plates multiplied by two. It is doubled because NSM plates are bonded to the concrete on both sides as opposed to just one side. Because the model is not analytically or empirically derived and because Standards Australia even recommends that it still needs to be validated with tests, this model should be used with caution.

#### **4.2.2 Blaschko (2003)**

The model by Blaschko (2003) was one of the first models focused on NSM FRP. Most of the previous models and research had been on EB FRP only. In his NSM model, Blaschko assumed that the failure occurs in the adhesive layer. He then developed an equation to calculate the bond strength of the FRP.

##### **4.2.2.1 Discussion of Model**

The model by Blaschko is based on knowing the shear strength of the epoxy. Most epoxy manufacturers only report tensile and compressive strengths, and most researchers either do not run tests for this property of the epoxy or do not report it. Therefore, this model cannot be used for any of the experiments unless a reasonable guess is made for this value. Because the adhesive layer is the layer that is being investigated and because the shear strength of the epoxy is the only variable for the adhesive, assuming a value for the

shear strength of the epoxy would make the Blaschko equation trivial. Any assumption made, even if it is conservative, would put the equation only in terms of the FRP bonded length, the FRP width, and the FRP distance from the concrete edge. Therefore, because this value was not reported by the experimental tests in the referenced literature, it cannot be evaluated.

For IC debonding to occur, the concrete must be cracked. However, for the Blaschko model, the failure is assumed to occur in the adhesive layer, and the concrete compressive strength is not even a variable in the model. Because many of the experimental tests resulted in an IC-debonding failure and many failed in the concrete layer, the Blaschko model is not compared with these tests.

#### **4.2.3 Hassan and Rizkalla (2003)**

The model by Hassan and Rizkalla (2003) that was introduced in Chapter 2 was used to evaluate the PE-debonding resistance of the NSM experimental tests that were also introduced in Chapter 2.

##### **4.2.3.1 Comparison to Previous Testing**

Table 4-4 shows a comparison between the predicted strengthened moment capacity and the experimental strengthened moment capacity.

**Table 4-4:** Comparison of the PE-Debonding Model by Hassan and Rizkalla (2003) to  
NSM Test Results

Test Series #	Specimen ID	Predicted			Experimental			$M_{n,exp}/M_{n,pred}$	$\Delta M_{n,exp}/\Delta M_{n,pred}$
		$M_n$ (k-ft)	$\Delta M_n$ (k-ft)	Failure Mode	$M_{exp}$ (k-ft)	$\Delta M_{exp}$ (k-ft)	Failure Mode		
8	B500	8.1	-13.5	PE	21.1	-0.4	PE	2.61	0.03
8	B1200	11.1	-10.4	PE	28.0	6.5	PE	2.51	-0.63
8	B1800	16.5	-5.0	PE	40.6	19.1	PE	2.46	-3.80
8	B2900	34.3	12.8	R	44.1	22.6	CC	1.28	1.77
9	G4D6a	6.0	N/A	PE	4.4	N/A	P	0.73	N/A
9	G4D12a	7.0	N/A	PE	6.2	N/A	P	0.88	N/A
9	G4D12b	7.1	N/A	PE	6.6	N/A	P	0.92	N/A
9	G4D12c	7.2	N/A	PE	7.6	N/A	P	1.05	N/A
9	G4D18a	8.4	N/A	PE	7.6	N/A	P	0.90	N/A
9	G4D24c	10.5	N/A	PE	11.0	N/A	P	1.05	N/A
9	C3D6a	5.2	N/A	PE	2.8	N/A	P	0.54	N/A
9	C3D12a	5.8	N/A	PE	4.8	N/A	P	0.82	N/A
9	C3D12b	5.8	N/A	PE	5.4	N/A	P	0.93	N/A
9	C3D12c	5.8	N/A	PE	5.1	N/A	P	0.88	N/A
9	C3D18a	6.5	N/A	PE	7.5	N/A	P	1.15	N/A
9	C3D24b	7.4	N/A	PE	7.8	N/A	P	1.06	N/A
9	C3S6a	4.8	N/A	PE	2.3	N/A	P	0.49	N/A
9	C3S12a	5.3	N/A	PE	3.1	N/A	P	0.58	N/A
9	C3S12b	5.3	N/A	PE	2.7	N/A	P	0.52	N/A
9	C3S12c	5.3	N/A	PE	3.1	N/A	P	0.59	N/A
9	C3S18a	6.0	N/A	PE	4.4	N/A	P	0.74	N/A
9	C3S24a	6.4	N/A	PE	4.0	N/A	P	0.62	N/A
10	fcm35 Lb40	3.9	N/A	PE	1.4	N/A	P	0.36	N/A
10	fcm35 Lb60	4.2	N/A	PE	2.1	N/A	P	0.50	N/A
10	fcm35 Lb80	4.4	N/A	R	2.1	N/A	P	0.47	N/A
10	fcm45 Lb40	4.5	N/A	R	1.4	N/A	P	0.32	N/A
10	fcm45 Lb60	4.5	N/A	R	1.8	N/A	P	0.41	N/A
10	fcm45 Lb80	4.5	N/A	R	2.4	N/A	P	0.54	N/A
10	fcm70 Lb40	4.5	N/A	R	1.4	N/A	P	0.32	N/A
10	fcm70 Lb60	4.5	N/A	R	1.7	N/A	P	0.39	N/A
10	fcm70 Lb80	4.5	N/A	R	2.4	N/A	P	0.53	N/A
11	Lb60 M	3.3	N/A	PE	1.0	N/A	P	0.31	N/A
11	Lb90 M	4.1	N/A	R	1.3	N/A	P	0.33	N/A
11	Lb120 M	4.1	N/A	R	1.5	N/A	P	0.37	N/A
12	B1	12.8	2.3	PE	24.4	0.5	PE	1.91	0.20
12	B2	14.1	3.6	PE	24.9	0.9	PE	1.77	0.26
12	B3	18.7	8.2	PE	27.7	3.7	PE	1.48	0.45
12	B4	22.7	12.2	R	34.1	10.1	PE	1.50	0.83
12	B5	22.7	12.2	R	36.4	12.4	R	1.60	1.02
12	B6	22.7	12.2	R	34.6	10.6	R	1.52	0.87
12	B7	22.7	12.2	R	36.9	12.9	R	1.62	1.06
12	B8	22.7	12.2	R	36.9	12.9	R	1.62	1.06

Notes: CC- crushing of the concrete (preceded by steel yielding); P- pullout of the FRP  
PE- plate-end debonding; R- rupture of the FRP



For test series 8, three of the four specimens were predicted to debond at a load that was less than the predicted failure load for the control beam. The values shown in Table 4-4 are the capacities at which PE debonding occurs. Failure for these beams would not occur until the concrete crushed, which would happen at a capacity close to the predicted capacity for the control beam of 21.5 kip-ft. The premature PE debonding of the FRP is the reason that the experimental capacity was about one and a half times larger than the predicted capacity. The premature debonding is also the reason that the changes in moment for these specimens are negative.

For specimen B500, the experimental capacity was actually less than the capacity of the control beam. This premature failure was due to the fact that the FRP strip was only bonded for 500 mm, and the constant moment region was 600 mm long. Therefore, part of the beam in the maximum moment region was left unstrengthened, and the FRP was rendered useless. For specimen B2900, the experimental capacity was 28% larger than the predicted capacity.

In test series 9, the specimen names that end with “a” have the smallest groove size at 5/8 inch; the specimen names that end with “b” have a groove size of 3/4 inch; and the specimen names that end with “c” have the largest groove size at 1 inch. As shown in Table 4-4, as the groove size increases, the predictions of the model become more accurate.

All of the specimens in test series 9 failed due to pullout of the FRP. For the No. 4 deformed rods, denoted G4D, the predicted capacities matched the experimental results relatively well except for the shortest bonded length, denoted G4D6a. For the other five

specimens in the G4D series, the experimental strengthened moment capacities were in the range of 88 to 105% of the predicted capacities.

For the No. 3 deformed rods, denoted C3D in test series 9, the experimental capacity was in the range of 82 to 115% of the predicted capacity, except for the shortest bonded length and the smallest groove width, denoted C3D6a.

The model did not predict the strengthened moment capacity very well for the No. 3 sandblasted rods, denoted C3S. The experimental capacities for the C3S series ranged from 49 to 74% of the predicted capacities.

In tests series 10 and 11, the ratio of experimental capacity to predicted capacity was very poor and ranged from 0.31 to 0.54. The fact that these moment capacities were very small might be the reason that these ratios were very low. For example, in specimen fcm35\_Lb60, the difference between the predicted and the experimental capacity was only 2.1 kip-ft, but because the experimental capacity was only 2.1 kip-ft, this resulted in an experimental to predicted capacity ratio of 0.50. Another possible reason for the big discrepancy in moment ratios is the fact that all of the tests in test series 9, 10, and 11 failed due to a pullout failure; however, the model by Hassan and Rizkalla does not anticipate a pullout failure. The failure mode was never predicted correctly, which most likely resulted in an erroneous prediction of capacity.

In test series 12, the failure mode was correctly predicted in seven out of the eight specimens; however, the experimental capacity ranged from 48 to 91% larger than the predicted capacity. For the specimens where PE debonding was predicted, the ratios of experimental change in capacity to predicted change in capacity showed a poor relationship, ranging from 0.20 to 0.45. This poor relationship could be due to the small

magnitude of the changes in moment. For the specimens where FRP rupture was predicted, the change-in-moment ratios ranged from 0.83 to 1.06.

Figure 4-3 shows a graph of the experimental capacity versus the predicted capacity. Figure 4-4 shows a comparison between the experimental change in capacity and the predicted change in capacity.

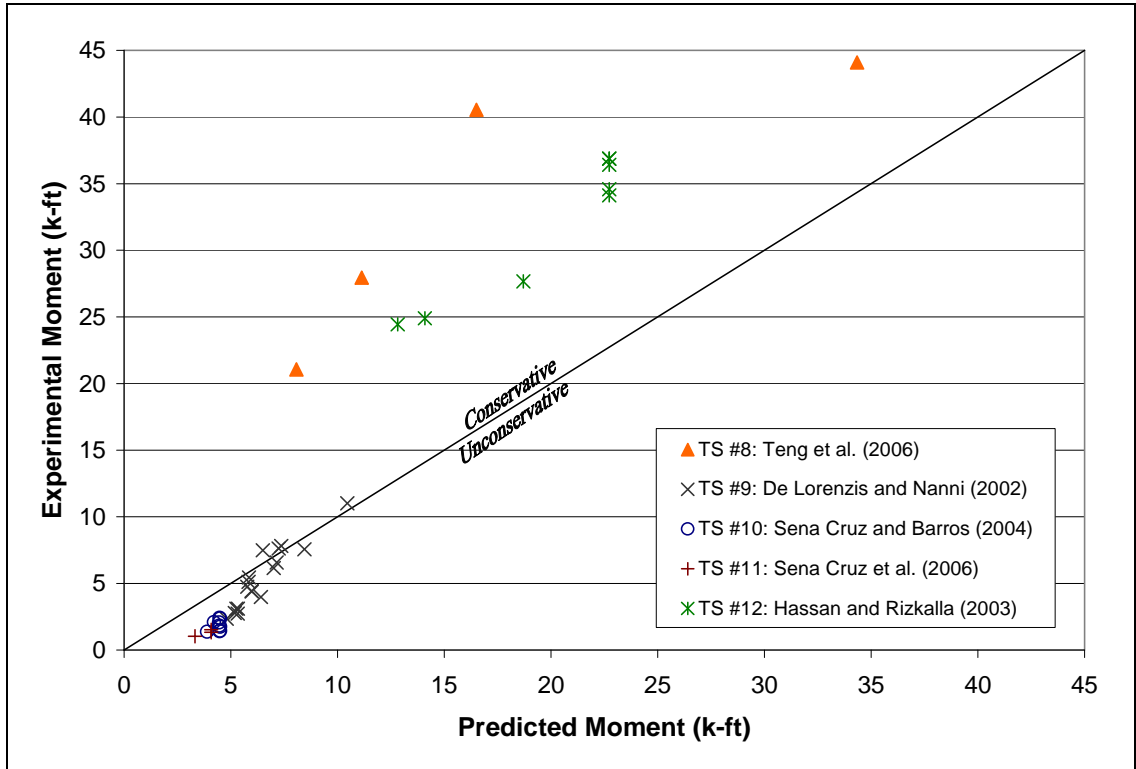


**Figure 4-3:** Comparison between NSM Test Results and Hassan and Rizkalla (2003) PE-Debonding Capacity Predictions

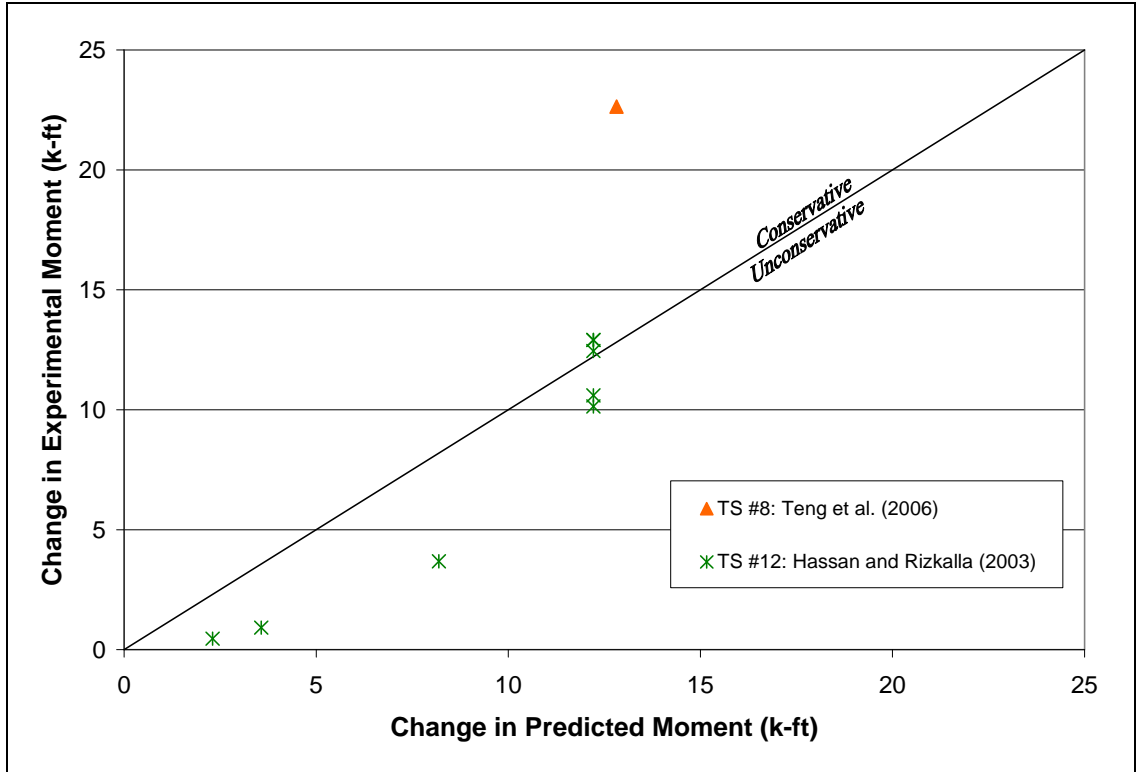


**Figure 4-4:** Comparison between NSM Test Results and Hassan and Rizkalla (2003) PE-  
 Debonding Change-in-Capacity Predictions

As seen in Figure 4-3, most of the data points are not very close to the line that separates the conservative from the unconservative. In Figure 4-4, very few of the data points are close to the line shown. The changes in capacity for three of the specimens in test series 8 are not shown in Figure 4-4 because the predicted capacities for the FRP-strengthened specimens were less than the predicted capacities for the control beams, which resulted in negative changes in capacity.

Table 4-5 shows the measured and predicted strain values for the FRP.

**Table 4-5:** FRP Strain Predictions using the Hassan and Rizkalla (2003) PE-Debonding Model and NSM Test Results

Test Series #	Specimen ID	Predicted		Experimental		$\frac{\epsilon_{f,exp}}{\epsilon_{f,pred}}$
		$\epsilon_{f,pred}$	$\frac{\epsilon_{f,pred}}{\epsilon_{f,rupt}}$	$\epsilon_{f,exp}$	$\frac{\epsilon_{f,exp}}{\epsilon_{f,rupt}}$	
8	B500	0.10%	0.06	0.23%	0.15	2.24
8	B1200	0.14%	0.09	0.37%	0.23	2.59
8	B1800	0.21%	0.13	0.73%	0.46	3.48
8	B2900	*1.37%	*0.87	*0.97%	*0.61	0.71
12	B1	0.31%	0.23	0.05%	0.04	0.16
12	B2	0.44%	0.33	0.17%	0.13	0.39
12	B3	0.93%	0.70	0.71%	0.53	0.76
12	B4	*1.33%	*1.00	1.18%	0.89	0.89
12	B5	*1.33%	*1.00	*1.27%	*0.95	0.95
12	B6	*1.33%	*1.00	*1.28%	*0.96	0.96
12	B7	*1.33%	*1.00	*1.29%	*0.97	0.97
12	B8	*1.33%	*1.00	*1.31%	*0.98	0.98

\*denotes a failure mode other than PE debonding

For test series 8, the FRP strain predictions were not very accurate. For specimens B500, B1200, and B1800, the predicted FRP strains were 6, 9, and 13%, respectively, of the rupture strain; the experimental strains were 15, 23, and 46%, respectively. For specimen B2900, the experimental strain was 71% of the predicted strain.

For the specimens where PE debonding was predicted in test series 12, the experimental strains were much lower than the predicted strains, with the ratios of the experimental to the predicted strain ranging from 0.16 to 0.76. For the five specimens where FRP rupture was predicted, the experimental strains matched the predicted strains much better, with the experimental FRP strains being 89 to 98% of the predicted strains.

#### 4.2.3.2 Discussion of Model

The model by Hassan and Rizkalla did not correlate well with the three test series that failed due to pullout of the FRP. Pullout failure was not anticipated by the model and occurred before PE debonding was predicted to occur. Due to the relatively small

moment capacities, the ratios of experimental capacity to predicted capacity are not close to 1.0. Therefore, a comparison between the test results and the predictions is difficult to make.

The Hassan and Rizkalla model predicted the failure mode fairly well for test series 8 and 12; the model correctly predicted the failure mode in ten out of the twelve specimens. The capacities predictions were not very accurate for these test series, but the changes in moment capacity for test series 12 were relatively accurate.

The model used for this analysis was specifically derived for a simply-supported beam with a concentrated load at midspan. A different form of the model must be derived for test setups that include other loading conditions or support configurations.

#### **4.2.4 Vasquez (2008)**

The model by Vasquez (2008) that was introduced in Chapter 2 was used to evaluate the PE-debonding resistance of experimental tests using NSM FRP.

##### **4.2.4.1 Comparison to Previous Testing**

Table 4-6 shows a comparison between the predicted strengthened moment capacity and the experimental strengthened moment capacity.

**Table 4-6:** Comparison of the PE-Debonding Model by Vasquez (2008) to NSM Test Results

Test Series #	Specimen ID	Predicted			Experimental			$M_{n,exp}/M_{n,pred}$	$\Delta M_{n,exp}/\Delta M_{n,pred}$
		$M_n$ (k-ft)	$\Delta M_n$ (k-ft)	Failure Mode	$M_{exp}$ (k-ft)	$\Delta M_{exp}$ (k-ft)	Failure Mode		
8	B500	15.0	-6.6	PE	21.1	-0.4	PE	1.41	0.06
8	B1200	19.9	-1.6	PE	28.0	6.5	PE	1.40	-4.11
8	B1800	29.9	8.4	PE	40.6	19.1	PE	1.36	2.28
8	B2900	34.3	12.8	R	44.1	22.6	CC	1.28	1.77
9	G4D6a	17.9	N/A	R	4.4	N/A	P	0.25	N/A
9	G4D12a	17.9	N/A	R	6.2	N/A	P	0.34	N/A
9	G4D12b	17.9	N/A	R	6.6	N/A	P	0.37	N/A
9	G4D12c	17.9	N/A	R	7.6	N/A	P	0.43	N/A
9	G4D18a	17.9	N/A	R	7.6	N/A	P	0.42	N/A
9	G4D24c	17.9	N/A	R	11.0	N/A	P	0.62	N/A
9	C3D6a	17.4	N/A	PE	2.8	N/A	P	0.16	N/A
9	C3D12a	19.8	N/A	PE	4.8	N/A	P	0.24	N/A
9	C3D12b	19.8	N/A	PE	5.4	N/A	P	0.27	N/A
9	C3D12c	19.8	N/A	PE	5.1	N/A	P	0.26	N/A
9	C3D18a	21.0	N/A	R	7.5	N/A	P	0.36	N/A
9	C3D24b	21.0	N/A	R	7.8	N/A	P	0.37	N/A
9	C3S6a	16.0	N/A	PE	2.3	N/A	P	0.15	N/A
9	C3S12a	18.2	N/A	PE	3.1	N/A	P	0.17	N/A
9	C3S12b	18.2	N/A	PE	2.7	N/A	P	0.15	N/A
9	C3S12c	18.2	N/A	PE	3.1	N/A	P	0.17	N/A
9	C3S18a	19.1	N/A	R	4.4	N/A	P	0.23	N/A
9	C3S24a	19.1	N/A	R	4.0	N/A	P	0.21	N/A
10	fcm35 Lb40	4.4	N/A	R	1.4	N/A	P	0.31	N/A
10	fcm35 Lb60	4.4	N/A	R	2.1	N/A	P	0.47	N/A
10	fcm35 Lb80	4.4	N/A	R	2.1	N/A	P	0.47	N/A
10	fcm45 Lb40	4.5	N/A	R	1.4	N/A	P	0.32	N/A
10	fcm45 Lb60	4.5	N/A	R	1.8	N/A	P	0.41	N/A
10	fcm45 Lb80	4.5	N/A	R	2.4	N/A	P	0.54	N/A
10	fcm70 Lb40	4.5	N/A	R	1.4	N/A	P	0.32	N/A
10	fcm70 Lb60	4.5	N/A	R	1.7	N/A	P	0.39	N/A
10	fcm70 Lb80	4.5	N/A	R	2.4	N/A	P	0.53	N/A
11	Lb60 M	4.1	N/A	R	1.0	N/A	P	0.25	N/A
11	Lb90 M	4.1	N/A	R	1.3	N/A	P	0.33	N/A
11	Lb120 M	4.1	N/A	R	1.5	N/A	P	0.37	N/A
12	B1	20.3	9.8	PE	24.4	0.5	PE	1.20	0.05
12	B2	22.3	11.8	PE	24.9	0.9	PE	1.11	0.08
12	B3	22.7	12.2	R	27.7	3.7	PE	1.22	0.30
12	B4	22.7	12.2	R	34.1	10.1	PE	1.50	0.83
12	B5	22.7	12.2	R	36.4	12.4	R	1.60	1.02
12	B6	22.7	12.2	R	34.6	10.6	R	1.52	0.87
12	B7	22.7	12.2	R	36.9	12.9	R	1.62	1.06
12	B8	22.7	12.2	R	36.9	12.9	R	1.62	1.06

Notes: CC- crushing of the concrete (preceded by steel yielding); P- pullout of the FRP  
PE- plate-end debonding; R- rupture of the FRP

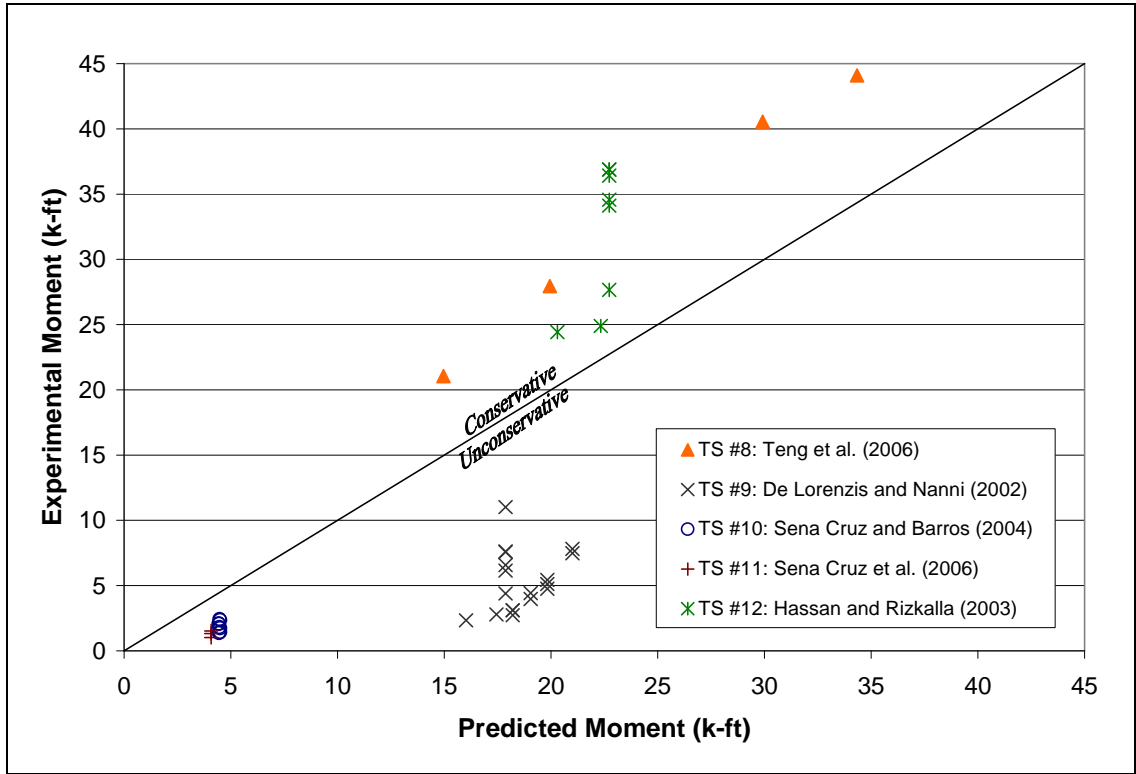
As in the results of the Hassan and Rizkalla model, the Vasquez model predicted PE debonding would occur in two of the specimens at a capacity less than the predicted capacity of the control beam. The values shown in Table 4-6 are the capacities at which PE debonding was predicted to occur. Because these capacities are less than the predicted capacities of the control beam, the test specimens, once the FRP debonds, were expected to achieve a capacity about equal to the capacity of the control beam. The Vasquez model predicted higher PE-debonding capacities for test series 8 than the Hassan and Rizkalla model, which resulted in a more accurate prediction. The experimental capacities for specimens B500 and B1200 were 41 and 40% higher, respectively, than the predicted capacities using the Vasquez model.

For test series 9, 10, and 11, pullout failure controls for all of the specimens. The Vasquez model does not, however, anticipate this failure mode and, therefore, does not accurately predict the strengthened moment capacities. For these three test series, the experimental capacities ranged from 15 to 62% of the predicted capacities, with an average of 33%.

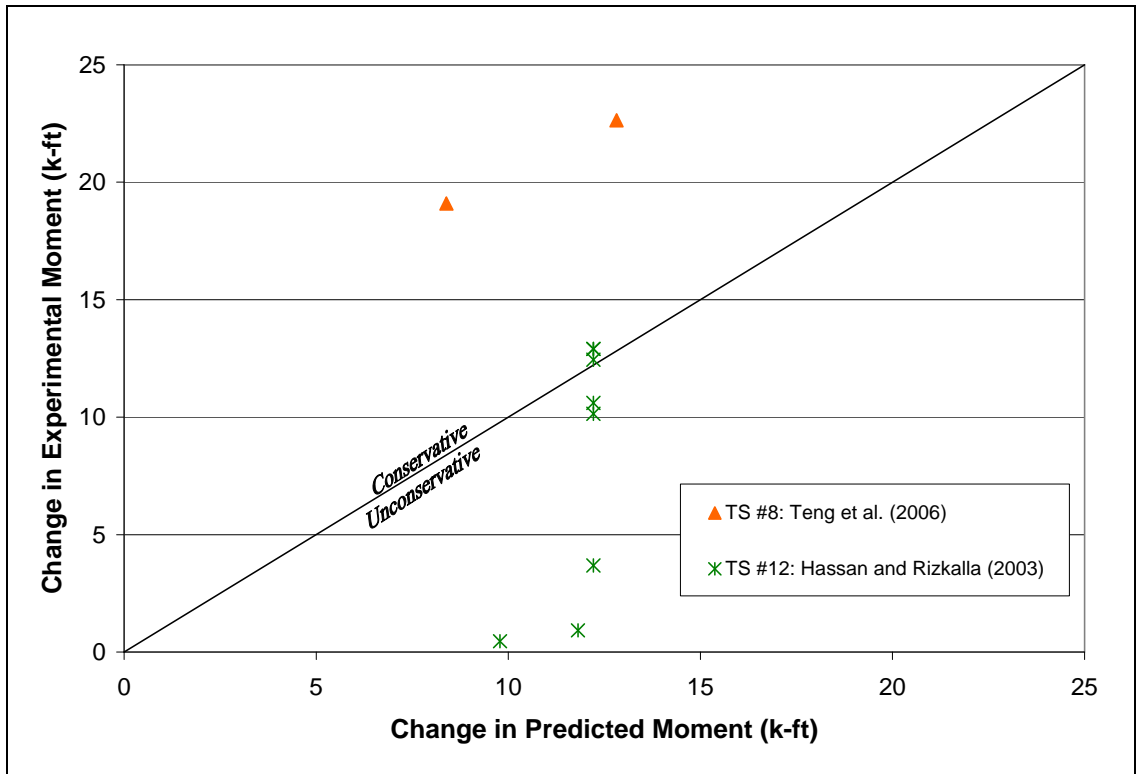
For specimens B1, B2, and B3 in test series 12, the experimental strengthened moment capacities were only 20, 11, and 22% higher, respectively, than the predicted strengthened moment capacities; however, the experimental changes in capacity were 5, 8, and 30% of the predicted changes in capacity. For specimens B4 through B8, the experimental capacities were well above the predicted capacities, but the experimental changes in capacity were very close to the predicted changes in capacity. The model by Hassan and Rizkalla produced similar results.



Figure 4-5 shows a graph of the experimental capacity versus the predicted capacity. Figure 4-6 shows a comparison between the experimental change in capacity and the predicted change in capacity.



**Figure 4-5:** Comparison between NSM Test Results and Vasquez (2008) PE-Debonding Capacity Predictions



**Figure 4-6:** Comparison between NSM Test Results and Vasquez (2008) PE-Debonding Change-in-Capacity Predictions

As shown in Figures 4-5 and 4-6, there was a wide dispersion of data points with some on the conservative side and some on the unconservative side. The series that did not involve pullout failure, test series 8 and 12, all produced conservative predictions of capacity. Test series 9, 10, and 11 all produced unconservative predictions. Few of the predictions of capacity were very close to the line of equality shown in Figure 4-5, and very few of the predictions of the change in capacity were close to the line of equality shown in Figure 4-6. The changes in capacity for two of the specimens in test series 8 are not shown in Figure 4-6 because they were predicted to be negative.

Table 4-7 shows the measured and predicted strain values for the FRP.

**Table 4-7: FRP Strain Predictions using the Vasquez (2008) PE-Debonding Model and NSM Test Results**

Test Series #	Specimen ID	Predicted		Experimental		$\frac{\epsilon_{f,exp}}{\epsilon_{f,pred}}$
		$\epsilon_{f,pred}$	$\frac{\epsilon_{f,pred}}{\epsilon_{f,rupt}}$	$\epsilon_{f,exp}$	$\frac{\epsilon_{f,exp}}{\epsilon_{f,rupt}}$	
8	B500	0.19%	0.12	0.23%	0.15	1.20
8	B1200	0.25%	0.16	0.37%	0.23	1.44
8	B1800	0.90%	0.57	0.73%	0.46	0.81
8	B2900	*1.37%	*0.87	*0.97%	*0.61	0.71
12	B1	1.10%	0.83	0.05%	0.04	0.04
12	B2	1.32%	0.99	0.17%	0.13	0.13
12	B3	*1.33%	*1.00	0.71%	0.53	0.53
12	B4	*1.33%	*1.00	1.18%	0.89	0.89
12	B5	*1.33%	*1.00	*1.27%	*0.95	0.95
12	B6	*1.33%	*1.00	*1.28%	*0.96	0.96
12	B7	*1.33%	*1.00	*1.29%	*0.97	0.97
12	B8	*1.33%	*1.00	*1.31%	*0.98	0.98

\*denotes a failure mode other than PE debonding

The FRP strain predictions for test series 8 were not very accurate. For specimens B500 and B1200, the experimental FRP strains were 120 and 144%, respectively, of the predicted FRP strains. For specimens B1800 and B2900, the experimental FRP strains were 81 and 71%, respectively, of the predicted FRP strains.

The Vasquez model did accurately predict the strain in the FRP for specimens B1, B2, and B3 in test series 12. These test specimens debonded at a relatively low strain value. The experimental strains were 4, 13, and 53% of the predicted strains, respectively. For the other five specimens in test series 12, the predicted strains matched the experimental strain very well.

#### 4.2.4.2 Discussion of Model

As in the Hassan and Rizkalla model, the Vasquez model did not anticipate a pullout failure for the FRP and, consequently, did not predict the capacities very well for test series 9, 10, and 11.

For test series 8 and 12, the predictions by the Vasquez model were conservative but not very accurate. However, the capacity predictions from the Vasquez model were more accurate than the predictions by the Hassan and Rizkalla model.

### **4.3 IC-Debonding Models for EB**

Six different IC-debonding models for EB are analyzed in this section. Each model was used to predict strengthened moment capacities for different experimental specimens. The predictions of the models were compared to experimental results of EB tests to determine the accuracy and level of safety of each model. The six models discussed in this section are ACI 440 (2008), *fib* 9.3 (2001), Standards Australia (2008), Rosenboom (2006), Seracino, Raizal Saifulnaz, and Oehlers (2007), and Said and Wu (2008). The experimental tests used in this section are test series 1 through 4.

#### **4.3.1 ACI 440 (2008)**

The EB IC-debonding model given by ACI 440 (2008) was compared to the existing experimental EB tests that were introduced in Chapter 2. These tests include test series 1–4: El-Hacha and Rizkalla (2004), Jung et al. (2005), Reed et al. (2005), and the tests conducted on War Memorial Bridge by Carmichael and Barnes (2005).

##### **4.3.1.1 Comparison to Previous Testing**

Using the ACI 440 model, nominal moment capacities were predicted for each strengthened test specimen and compared to previous testing. The objective of this capacity calculation was to predict the actual capacity at which failure occurs, rather than conservatively predicting a capacity to use in design. Therefore, the strength reduction

factor,  $\phi$ , was not applied to the total moment capacity; the reduction factor,  $\psi_f$ , was not applied to the FRP contribution to the moment capacity; and the environmental reduction factor,  $C_E$ , was not applied to the ultimate FRP stress or strain. Table 4-8 shows the predicted capacities, the experimental results, and comparisons between the two.

**Table 4-8:** Comparison of the IC-Debonding Model by ACI 440 (2008) to EB Test Results

Test Series #	Specimen ID	Predicted			Experimental			$M_{exp}/M_{n,pred}$	$\Delta M_{exp}/\Delta M_{n,pred}$
		$M_n$ (k-ft)	$\Delta M_n$ (k-ft)	Failure Mode	$M_{exp}$ (k-ft)	$\Delta M_{exp}$ (k-ft)	Failure Mode		
1	B2a	24.9	6.7	IC	29.7	4.1	IC	1.19	0.61
1	B2b				29.7	4.1	IC	1.19	0.61
1	B4a	25.7	7.5	IC	32.6	7.0	IC	1.27	0.93
2	CPL-50-BOND	26.6	10.0	IC	28.4	6.7	IC	1.07	0.67
2	SH-BOND	26.7	10.2	IC	31.9	10.2	IC	1.19	1.00
3	B1	80.9	16.5	IC	82.4	13.3	IC	1.02	0.81
3	B2				85.2	16.1	IC	1.05	0.98
3	B3				82.7	13.6	IC	1.02	0.82
3	B4				85.4	16.3	IC	1.06	0.99
3	B5				82.7	13.6	IC	1.02	0.82
3	B6				84.2	15.1	IC	1.04	0.92
3	B7	83.7	19.2	IC	88.3	19.3	IC	1.06	1.00
4	G3S9	787	N/A	IC	320	N/A	no failure	0.41	N/A
4	G3S10	787	N/A	IC	280	N/A	no failure	0.36	N/A
4	G4S9	776	N/A	IC	300	N/A	no failure	0.39	N/A
4	G4S10	924	N/A	IC	300	N/A	no failure	0.32	N/A

Notes: IC- intermediate crack debonding

In the study conducted by Carmichael and Barnes (2005), test series 4, the War Memorial Bridge was only loaded in the service level range. Because no failure occurred in the tests, the high capacity predictions relative to the experimental applied moments

were expected. Also, because there was no control beam, no change-in-moment calculations could be made.

The specimen ID used in this table and in the following tables is the specimen label that was used by the original researchers. The change in the moment predicted by ACI 440 was calculated by subtracting the predicted capacity of the control beam from the predicted capacity of the strengthened beam. The experimental change in moment was calculated by subtracting the measured capacity at failure for the control beam from the measured capacity at failure for the strengthened beam. By incorporating the predicted capacity of the control beam and the measured capacity of the control beam, the actual contribution of the FRP was more accurately assessed. The capacity of unstrengthened reinforced concrete is typically underestimated due to a couple of reasons, such as ignoring strain hardening of the internal steel and assuming a conservative concrete compressive stress distribution at failure (i.e. the Whitney stress block). By including the predicted and measured capacities of the control beam in the change-in-moment calculations, the FRP contribution can be measured more directly.

To create a normalized comparison, the experimental moment capacity was divided by the predicted moment capacity. A ratio of 1.0 is ideal, a ratio greater than 1.0 indicates a conservative prediction, and a ratio less than 1.0 indicates an unconservative prediction. The same rules apply to the change-in-moment comparisons. Figure 4-7 shows the relationship between the experimental and the predicted strengthened moment capacities. Figure 4-8 shows a comparison between the experimental change in capacity and the predicted change in capacity.

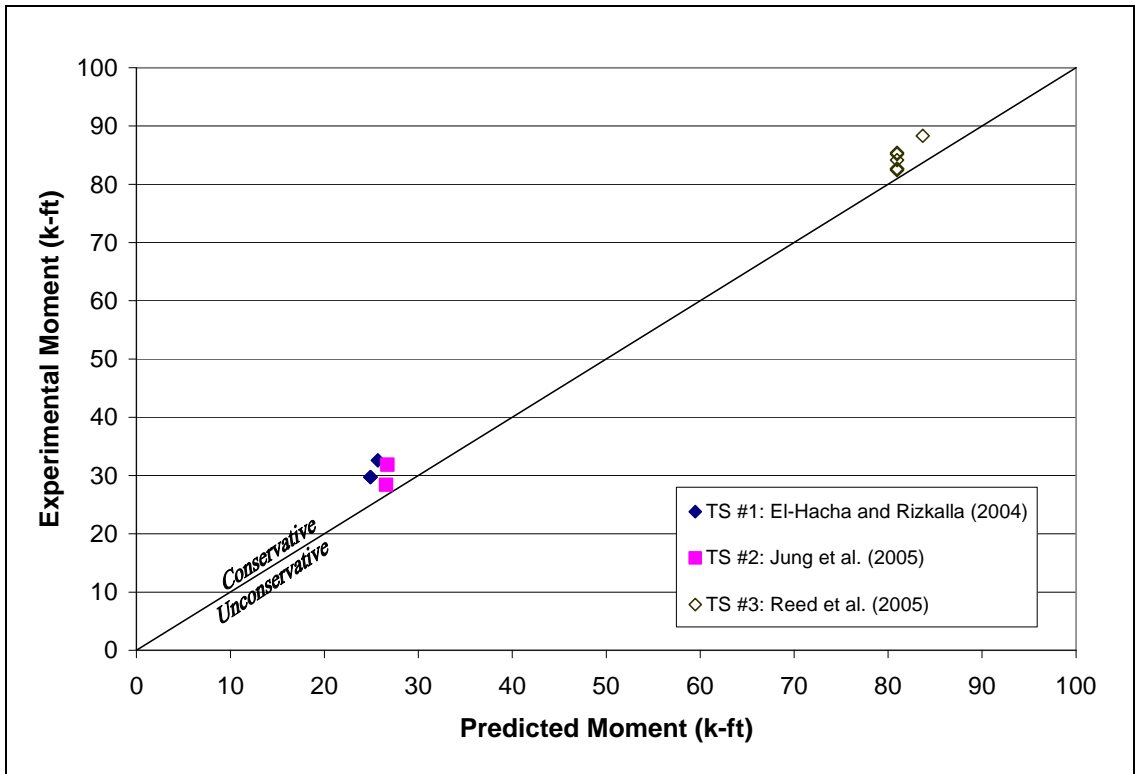


**Figure 4-7:** Comparison between EB Test Results and ACI 440 (2008) IC-Debonding Capacity Predictions

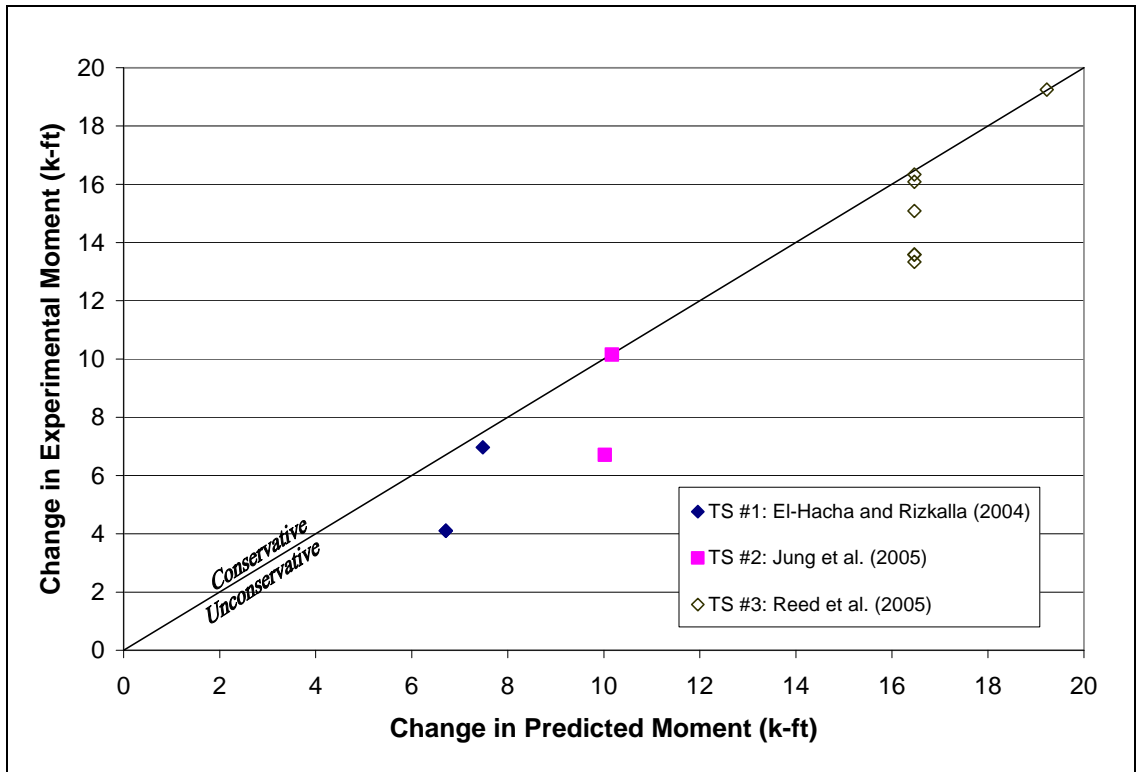


**Figure 4-8:** Comparison between EB Test Results and ACI 440 (2008) IC-Debonding Change-in-Capacity Predictions

In test series 1, specimens B2a and B2b were identical to each other. Likewise, in test series 3, specimens B1 through B6 had identical cross sections, except for varying thicknesses of epoxy, which is not a variable in the ACI 440 model. For these reasons, multiple experimental results are shown for these specimens, but only one prediction corresponds to each type of specimen.

For test series 1, 2, and 3, the predictions made by the ACI 440 model were all conservative for the strengthened moment capacity but unconservative for the change in moment capacity. As shown in Table 4-8, the ratio of the experimental moment capacity to the predicted moment capacity ranges from 1.02 to 1.27, but the ratio of the



experimental change in moment to the predicted change in moment ranges from 0.61 to 1.00. The model correctly predicted an IC-debonding failure for all of the test specimens that were loaded to failure.

The ultimate strain in the FRP was measured at failure for each of the specimens in the first three test series. Table 4-9 shows these FRP strain values.

**Table 4-9:** FRP Strain Predictions using the ACI 440 (2008) IC-Debonding Model and EB Test Results

Test Series #	Specimen ID	Predicted		Experimental		$\frac{\epsilon_{f,exp}}{\epsilon_{f,pred}}$
		$\epsilon_{f,pred}$	$\frac{\epsilon_{f,pred}}{\epsilon_{f,rupt}}$	$\epsilon_{f,exp}$	$\frac{\epsilon_{f,exp}}{\epsilon_{f,rupt}}$	
1	B2a	0.37%	0.35	0.48%	0.44	1.28
1	B2b			0.44%	0.41	1.18
1	B4a	0.42%	0.19	0.62%	0.28	1.49
2	CPL-50-BOND	0.49%	0.33	0.44%	0.30	0.91
2	SH-BOND	1.04%	0.69	0.85%	0.56	0.81
3	B1	0.67%	0.33	0.44%	0.22	0.66
3	B2			0.51%	0.25	0.77
3	B3			0.49%	0.24	0.74
3	B4			0.53%	0.26	0.80
3	B5			0.51%	0.25	0.77
3	B6			0.56%	0.28	0.84
3	B7			0.57%	0.28	0.47%

Note: All predicted and experimental failure modes were IC debonding.

In Table 4-9,  $\epsilon_{f,pred}$  is the predicted failure strain in the FRP;  $\epsilon_{f,exp}$  is the experimental failure strain in the FRP; and  $\epsilon_{f,rupt}$  is the rupture strain in the FRP. The ratio of the experimental FRP strain to the predicted FRP strain at failure is shown in the far right column. For this ratio, a value greater than 1.0 would be conservative, and a value less than 1.0 would be unconservative.

For the tests conducted by El-Hacha and Rizkalla (2004), test series 1, the ACI 440 model underestimates the IC-debonding strain. For the other two test series, the model overestimates the IC-debonding strain for all specimens.

#### **4.3.1.2 Discussion of Model**

The ACI 440 (2008) model does not predict very accurately the amount of strengthening the FRP provides. As shown in Table 4-8, it frequently overestimates the change in moment. However, the amount that the ACI 440 model overestimates the FRP contribution is balanced by the amount that is underestimated in the actual strength of the unstrengthened reinforced concrete member, which results in a fairly accurate and slightly conservative prediction of the strengthened moment capacity. Even though the FRP overestimation was balanced by the underestimation of strength of the unstrengthened specimens in these laboratory specimens, the beneficial excess strength could be smaller in full-scale bridge girders with older steel reinforcing bar types. Therefore, a more conservative estimate of the true amount of strengthening due to FRP is desirable.

#### **4.3.2 *fib* 9.3 (2001)**

The EB IC-debonding model given by *fib* 9.3 (2001) was compared to the existing experimental EB tests that were introduced in Chapter 2 to determine the accuracy and level of safety of the model.

##### **4.3.2.1 Comparison to Previous Testing**

Table 4-10 shows a comparison of capacities for EB FRP using Bulletin 14 of the *fib*.

**Table 4-10:** Comparison of the IC-Debonding Model by *fib* 9.3 (2001) to EB Test

## Results

Test Series #	Specimen ID	Predicted			Experimental			$M_{exp}/M_{n,pred}$	$\Delta M_{exp}/\Delta M_{n,pred}$
		$M_n$ (k-ft)	$\Delta M_n$ (k-ft)	Failure Mode	$M_{exp}$ (k-ft)	$\Delta M_{exp}$ (k-ft)	Failure Mode		
1	B2a	23.8	5.6	IC	29.7	4.1	IC	1.25	0.73
1	B2b				29.7	4.1	IC	1.25	0.73
1	B4a	29.8	11.6	IC	32.6	7.0	IC	1.10	0.60
2	CPL-50-BOND	43.9	27.4	CC	28.4	6.7	IC	0.65	0.25
2	SH-BOND	31.2	14.7	R	31.9	10.2	IC	1.02	0.69
3	B1	118.1	53.7	R	82.4	13.3	IC	0.70	0.25
3	B2				85.2	16.1	IC	0.72	0.30
3	B3				82.7	13.6	IC	0.70	0.25
3	B4				85.4	16.3	IC	0.72	0.30
3	B5				82.7	13.6	IC	0.70	0.25
3	B6				84.2	15.1	IC	0.71	0.28
3	B7	137.7	73.2	R	88.3	19.3	IC	0.64	0.26
4	G3S9	1122	N/A	R	320	N/A	no failure	0.29	N/A
4	G3S10	1122	N/A	R	280	N/A	no failure	0.25	N/A
4	G4S9	1173	N/A	R	300	N/A	no failure	0.26	N/A
4	G4S10	1322	N/A	R	300	N/A	no failure	0.23	N/A

Notes: CC- crushing of the concrete (preceded by steel yielding)  
 IC- intermediate crack debonding  
 R- rupture of the FRP

As in the results of the ACI 440 model, Bulletin 14 of Task Group 9.3 predicted very high strengthened moment capacities for test series 4 relative to the experimental loads. Because these specimens were only tested under service loads and the predicted capacities were calculated using ultimate loads, the relatively high ratios of predicted capacity to applied bending moment were expected. Once again, these specimens will be excluded from further discussion.

Figure 4-9 shows a comparison between the experimental capacity and the predicted capacity. Figure 4-10 shows a comparison between the experimental change in capacity and the predicted change in capacity.

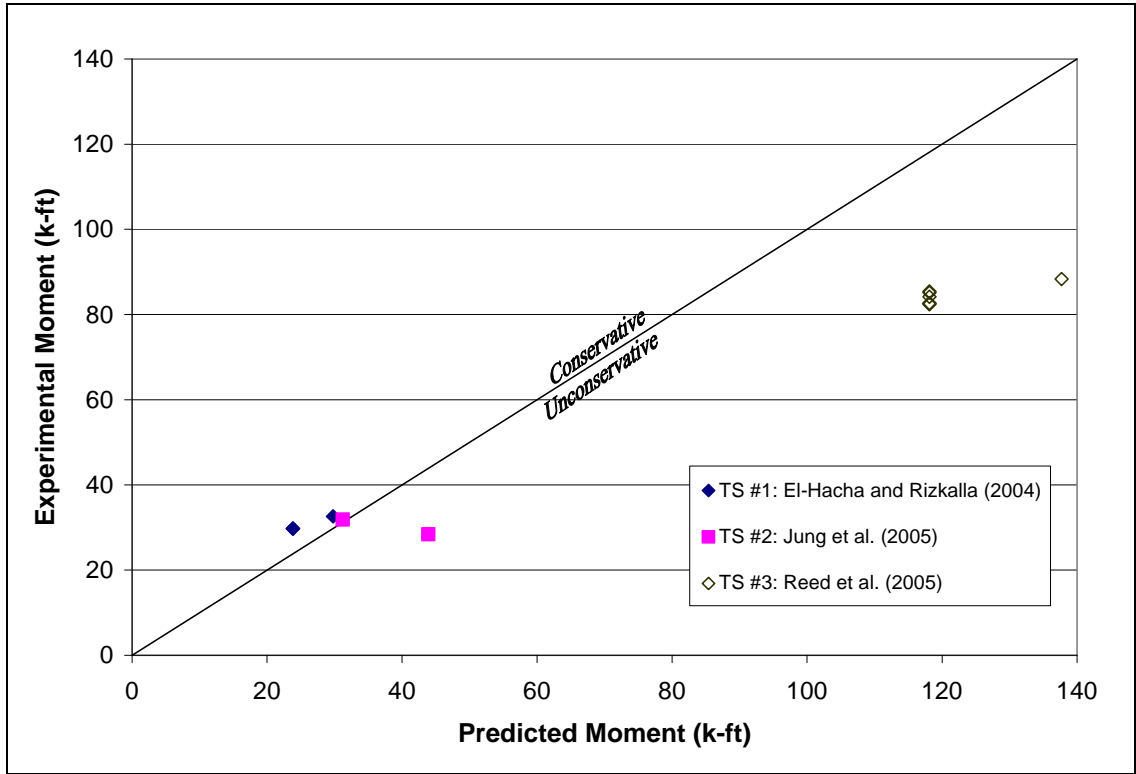


**Figure 4-9:** Comparison between EB Test Results and *fib* 9.3 (2001) IC-Debonding Capacity Predictions

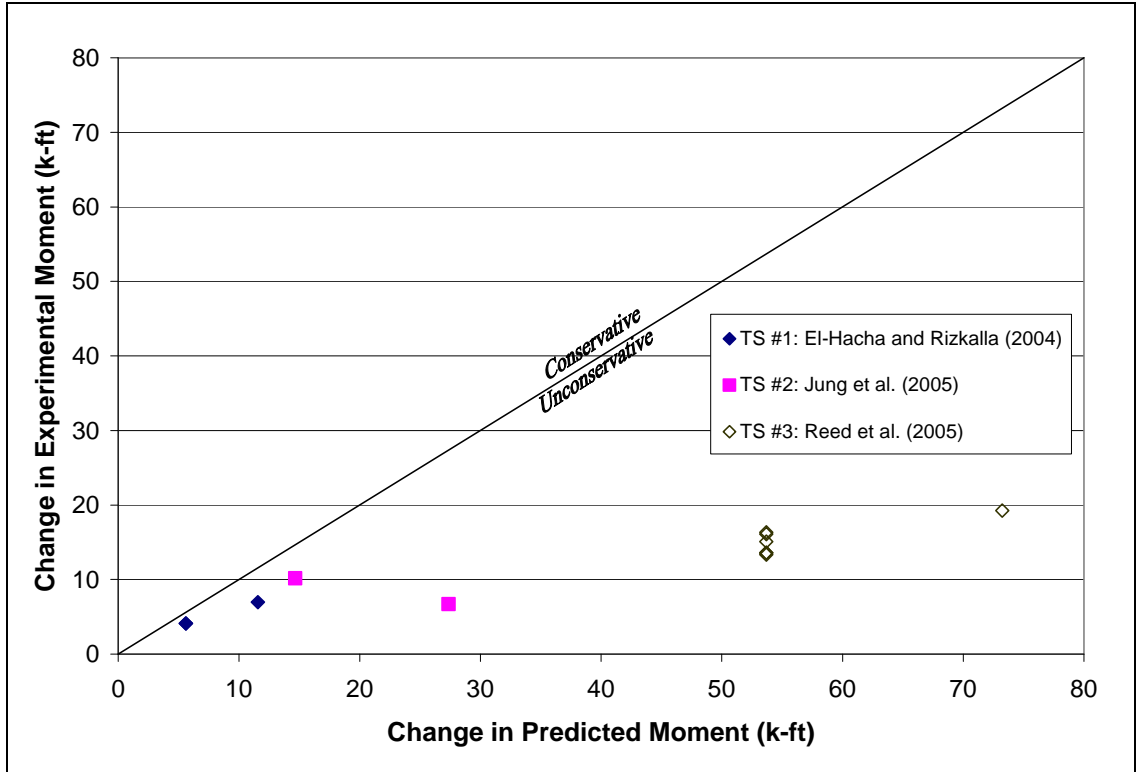


**Figure 4-10:** Comparison between EB Test Results and *fib* 9.3 (2001) IC-Debonding Change-in-Capacity Predictions

For test series 1, the failure mode was predicted correctly, and the predicted strengthened moment capacity was slightly underestimated when compared to the experimental results. Conversely, the changes in moment were overestimated.

For test series 2 and 3, the failure mode (actually IC-debonding for all) was not predicted correctly for any of the specimens. Consequently, the strengthened moment capacities were overestimated for all but one specimen, and the changes in moment capacity were extremely inaccurate, with the experimental change in moment capacity ranging from 25 to 69% of the predicted change in moment capacity.

The predicted FRP strains and the comparisons to the experimental strains are shown in Table 4-11.

**Table 4-11:** FRP Strain Predictions using the *fib* 9.3 (2001) IC-Debonding Model and EB

Test Results

Test Series #	Specimen ID	Predicted		Experimental		$\frac{\epsilon_{f,exp}}{\epsilon_{f,pred}}$
		$\epsilon_{f,pred}$	$\frac{\epsilon_{f,pred}}{\epsilon_{f,rupt}}$	$\epsilon_{f,exp}$	$\frac{\epsilon_{f,exp}}{\epsilon_{f,rupt}}$	
1	B2a	0.27%	0.25	0.48%	0.44	1.79
1	B2b			0.44%	0.41	1.64
1	B4a	0.58%	0.26	0.62%	0.28	1.07
2	CPL-50-BOND	*1.30%	*0.88	0.44%	0.30	0.34
2	SH-BOND	*1.51%	*1.00	0.85%	0.56	0.56
3	B1	*2.03%	*1.00	0.44%	0.22	0.22
3	B2			0.51%	0.25	0.25
3	B3			0.49%	0.24	0.24
3	B4			0.53%	0.26	0.26
3	B5			0.51%	0.25	0.25
3	B6			0.56%	0.28	0.28
3	B7			*2.03%	*1.00	0.47%

\*denotes a failure mode other than IC debonding

Like Table 4-10, Table 4-11 shows an underestimation of the predicted FRP strain for test series 1 and an overestimation of the predicted FRP strain for test series 2 and 3. For specimens B2a and B2b of test series 1, the *fib* model predicted an FRP strain of 0.0027, but the experimental FRP strains were 0.0048 and 0.0044, respectively. For specimen B4a, the predicted FRP strain matched the experimental value much better. The predicted strain was 0.0058, and the experimental strain was 0.0062, which resulted in an experimental strain only 7% higher than the predicted strain.

Because the model does not predict IC-debonding failure modes for any of the specimens in test series 2 or 3, the corresponding predicted FRP strain values at failure were very high compared to the experimental strain values. As shown in Table 4-11, the

ratios of the predicted strain to the rupture strain for test series 2 were predicted to be 88 and 100% of the rupture strain, which is much greater than the experimental FRP strains of 30 and 56% of the rupture strain, respectively. For the ratio of 0.88, the predicted failure mode was crushing of the concrete; for the ratio of 1.00, the predicted failure mode was FRP rupture. Test series 3 has experimental FRP strains ranging from 22 to 28% of the rupture strain when IC debonding occurred, which is much less than the predicted FRP rupture failure of 100% of the rupture strain.

#### **4.3.2.2 Discussion of Model**

When compared to the EB tests, the model by Task Group 9.3 of *fib* did not correlate well with the experimental results. Out of the twelve laboratory specimens, the model only correctly predicted the failure mode three times. For most of the specimens, the model overestimated the strengthened moment capacities and was not very accurate.

Task Group 9.3 also reported two other approaches for calculating the IC-debonding resistance of reinforced concrete members. Approach 1 is a simplified method that provides a global strain limit on the FRP, which ranges from 0.0065 to 0.0085 mm/mm. This approach is very similar to the approach by ACI 440 where the strain is limited to 70% of the ultimate strain. Both limit the maximum strain value that can be used, but the strain limit of ACI 440 depends on the ultimate strain of the FRP whereas the strain limit of Task Group 9.3 is fixed at a constant value. Task Group 9.3 does not recommend Approach 1 and even states that the other two approaches will provide a more realistic prediction of IC-debonding resistance. Approach 2 is more detailed and is based on computation of the maximum possible increase in tensile stress within the FRP

that can be transferred by means of bond stresses between two adjacent flexural cracks. Said and Wu (2008) examined this approach and concluded that it has wide ranges of prediction ratios and high levels of dispersion; however, future work should involve a more detailed investigation of Approach 2. Approach 3, the approach used in this chapter, did not prove to be very accurate or precise. One cause of its inadequacy could be that Bulletin 14 was last published in 2001. Since then, new research has been conducted and newer models have been proposed that more accurately predict FRP-strengthened capacity. Another possible reason for its inaccuracies could be because the model is based on the assumption that IC-debonding can only occur in the presence of sectional shear force (i.e. moment changing along member). Thus, the local “in and out” bond stresses that transmit forces from the FRP to concrete adjacent to cracked sections are not considered.

### **4.3.3 Standards Australia (2008)**

The IC-debonding model for EB FRP given by Standards Australia was compared to the existing experimental EB tests introduced in Chapter 2 to determine the accuracy and level of safety of the model.

#### **4.3.3.1 Comparison to Previous Testing**

Table 4-12 shows a comparison of capacities using the IC-debonding model from Standards Australia.



**Table 4-12:** Comparison of the IC-Debonding Model by Standards Australia (2008) to  
EB Test Results

Test Series #	Specimen ID	Predicted			Experimental			$M_{exp}/M_{n,pred}$	$\Delta M_{exp}/\Delta M_{n,pred}$
		$M_n$ (k-ft)	$\Delta M_n$ (k-ft)	Failure Mode	$M_{exp}$ (k-ft)	$\Delta M_{exp}$ (k-ft)	Failure Mode		
1	B2a	28.6	10.4	IC	29.7	4.1	IC	1.04	0.39
1	B2b				29.7	4.1	IC	1.04	0.39
1	B4a	36.3	18.1	IC	32.6	7.0	IC	0.90	0.38
2	CPL-50-BOND	27.2	10.7	IC	28.4	6.7	IC	1.04	0.63
2	SH-BOND	25.0	8.5	IC	31.9	10.2	IC	1.27	1.20
3	B1	79.9	15.4	IC	82.4	13.3	IC	1.03	0.87
3	B2				85.2	16.1	IC	1.07	1.05
3	B3				82.7	13.6	IC	1.04	0.88
3	B4				85.4	16.3	IC	1.07	1.06
3	B5				82.7	13.6	IC	1.04	0.88
3	B6				84.2	15.1	IC	1.05	0.98
3	B7				82.4	17.9	IC	88.3	19.3
4	G3S9	757	N/A	IC	320	N/A	no failure	0.42	N/A
4	G3S10	757	N/A	IC	280	N/A	no failure	0.37	N/A
4	G4S9	726	N/A	IC	300	N/A	no failure	0.42	N/A
4	G4S10	874	N/A	IC	300	N/A	no failure	0.34	N/A

Notes: IC- intermediate crack debonding

As shown in Table 4-12, the failure mode was correctly predicted as IC debonding for test series 1, 2, and 3. For the B2 specimens in test series 1, the experimental moment capacities were both 4% greater than the predicted moment capacities. For the B4a specimen, the experimental capacity was 80% of the predicted capacity. The changes in capacity for all three specimens were overestimated. The predicted changes in moment capacity were about 2.5 times the experimental changes in moment capacity.

For test series 2, the experimental capacities were 4 and 27% greater than the predicted capacities. The changes in capacity predictions were both underestimated and

overestimated. The experimental changes in capacity were 63 and 120% of the predicted changes in capacity.

For test series 3, the capacity predictions were very accurate, with the experimental capacities ranging from 103 to 107% of the predicted capacities. The changes in capacity were relatively accurate, with the experimental changes in moment ranging from 87 to 107% of predicted changes in capacity.

Once again, the high capacity predictions for test series 4 relative to the applied moments were expected as the War Memorial Bridge was only loaded in the service level range.

Figure 4-11 shows a comparison between the experimental moment capacity and the predicted moment capacity. Figure 4-12 shows a comparison between the experimental change in capacity and the predicted change in capacity.

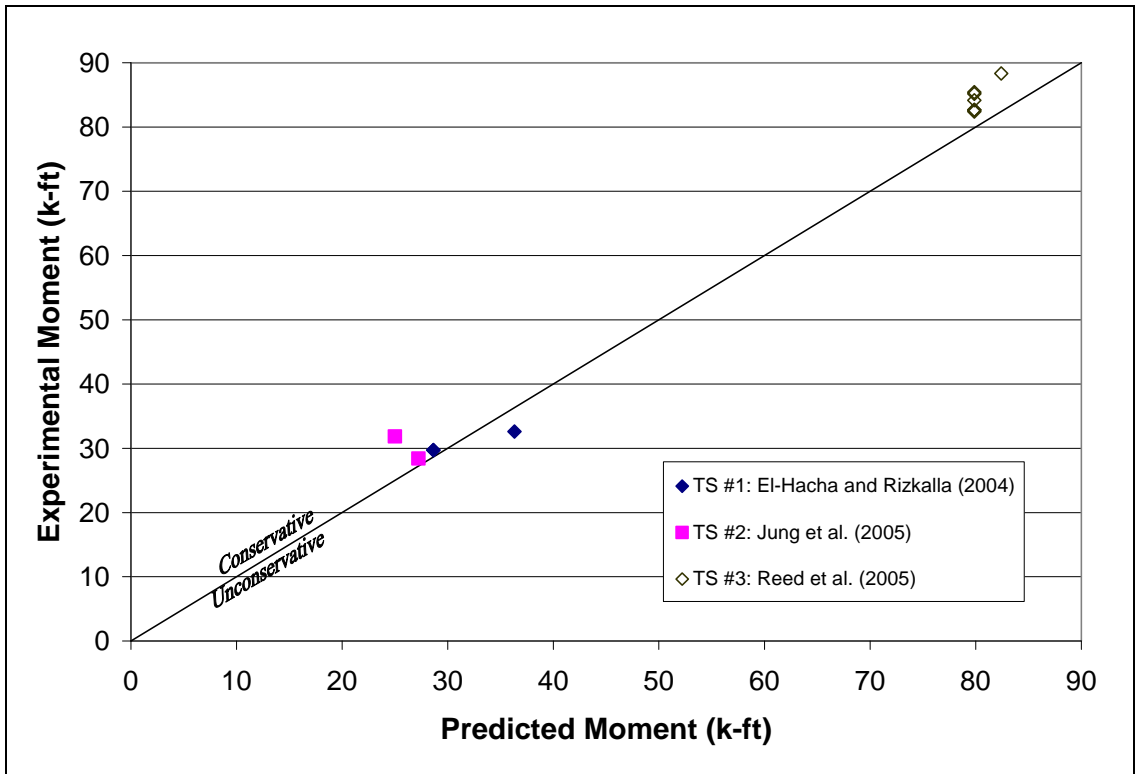


**Figure 4-11:** Comparison between EB Test Results and Standards Australia (2008) IC-  
 Debonding Capacity Predictions

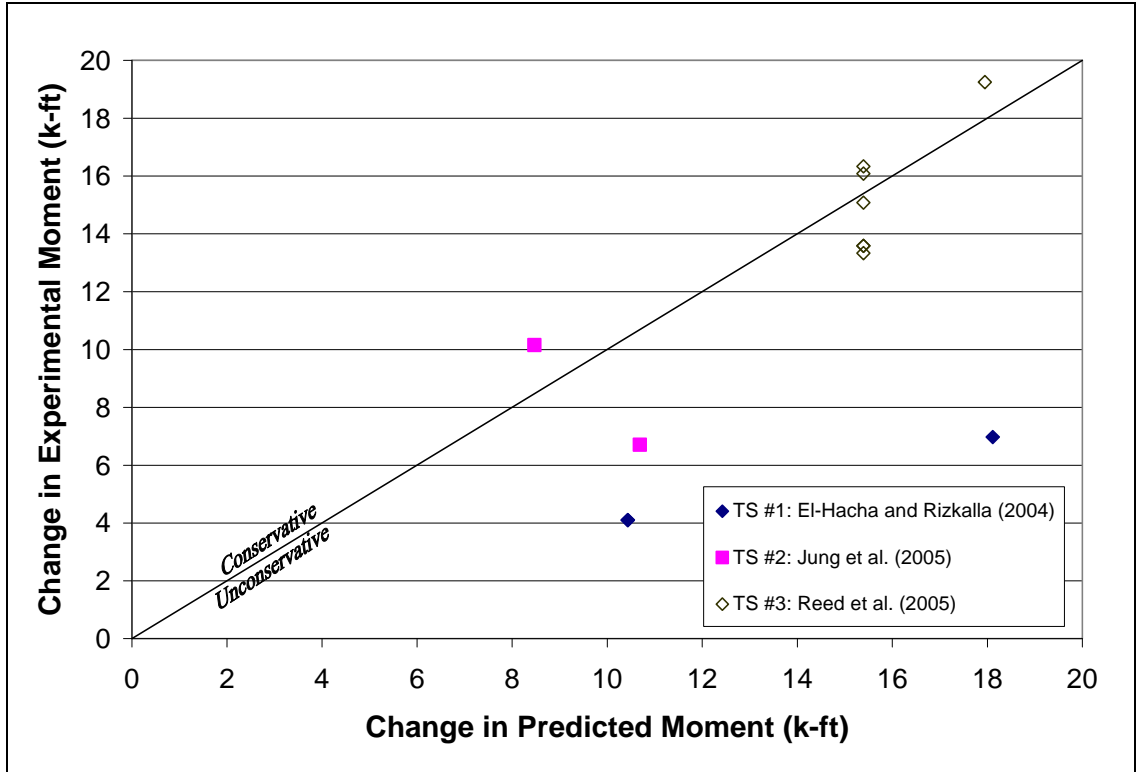


**Figure 4-12:** Comparison between EB Test Results and Standards Australia (2008) IC-Debonding Change-in-Capacity Predictions

As shown in Figure 4-11, the data points are fairly close to the line shown, which means that the model is fairly accurate. Most of the points are above and to the left of the line, which means that the model is typically conservative in its predictions of capacity. In Figure 4-12, most of the data points are relatively close the line shown, but three of the points are very inaccurate and unconservative.

Table 4-13 shows the FRP strain predictions and experimental results.

**Table 4-13: FRP Strain Predictions using the Standards Australia (2008) IC-Debonding Model and EB Test Results**

Test Series #	Specimen ID	Predicted		Experimental		$\frac{\epsilon_{f,exp}}{\epsilon_{f,pred}}$
		$\epsilon_{f,pred}$	$\frac{\epsilon_{f,pred}}{\epsilon_{f,rupt}}$	$\epsilon_{f,exp}$	$\frac{\epsilon_{f,exp}}{\epsilon_{f,rupt}}$	
1	B2a	0.57%	0.52	0.48%	0.44	0.85
1	B2b			0.44%	0.41	0.78
1	B4a	0.98%	0.44	0.62%	0.28	0.63
2	CPL-50-BOND	0.52%	0.35	0.44%	0.30	0.86
2	SH-BOND	0.87%	0.58	0.85%	0.56	0.97
3	B1	0.67%	0.33	0.44%	0.22	0.66
3	B2			0.51%	0.25	0.76
3	B3			0.49%	0.24	0.73
3	B4			0.53%	0.26	0.80
3	B5			0.51%	0.25	0.77
3	B6			0.56%	0.28	0.84
3	B7	0.57%	0.28	0.47%	0.23	0.82

Note: All predicted and experimental failure modes were IC debonding.

In test series 1, the predicted strain values were 44 and 52% of the rupture strain, while the experimental strains ranged from 28 to 44% of the rupture strain. The ratio of experimental FRP strain to predicted FRP strain ranged from 0.63 to 0.85 for the specimens in this test series.

In test series 2, the predicted strains were slightly greater than the experimental strains. For specimens CPL-50-BOND and SH-BOND, the predicted FRP strains were 0.0052 and 0.0087, respectively, and the experimental failure strains in the FRP were 0.0044 and 0.0085, respectively. The ratios of experimental strain to predicted strain were 0.86 and 0.97.

In test series 3, the predicted strains were greater than the experimental strains. For specimens B1 through B6, the model predicted an FRP strain of 33% of the rupture strain. The experimental FRP strains at failure for these specimens ranged from 22 to 28% of the rupture strain, which resulted in ratios of experimental strain to predicted

strain of 0.66 to 0.84. For specimen B7, the ratio of experimental strain to predicted strain was 0.82.

#### **4.3.3.2 Discussion of Model**

When compared to the experimental tests of EB FRP, the IC-debonding model given by Standards Australia was very accurate for predicting strengthened moment capacities. All but two of the specimens had experimental capacities that were in the range of 3 to 7% greater than the predicted capacities. The two specimens that were outside of this range had experimental capacities that were 90 and 127% of the predicted capacities.

The changes in capacity predictions for test series 1 and 2 were not very accurate, but the changes in capacity predictions for test series 3 were relatively accurate. For test series 3, the difference in the changes in capacity for each specimen was about 2 kip-ft or less.

When compared to the results of the other EB IC-debonding models, the model given by Standards Australia was very accurate at predicting FRP strain values. The strains were overestimated but not as severely as the other models.

#### **4.3.4 Rosenboom (2006)**

The model by Rosenboom (2006) was used to evaluate the IC-debonding resistance of experimental tests using EB FRP.

#### 4.3.4.1 Comparison to Previous Testing

Using the Rosenboom model, nominal moment capacities were predicted for each strengthened test specimen and compared to previous testing. Table 4-14 shows the predicted capacities, the experimental results, and comparisons between the two.

**Table 4-14:** Comparison of the IC-Debonding Model by Rosenboom (2006) to EB Test Results

Test Series #	Specimen ID	Predicted			Experimental			$M_{exp}/M_{n,pred}$	$\Delta M_{exp}/\Delta M_{n,pred}$
		$M_n$ (k-ft)	$\Delta M_n$ (k-ft)	Failure Mode	$M_{exp}$ (k-ft)	$\Delta M_{exp}$ (k-ft)	Failure Mode		
1	B2a	39.6	21.4	R	29.7	4.1	IC	0.75	0.19
1	B2b				29.7	4.1	IC	0.75	0.19
1	B4a	24.1	5.9	IC	32.6	7.0	IC	1.35	1.18
2	CPL-50-BOND	25.6	9.1	IC	28.4	6.7	IC	1.11	0.74
2	SH-BOND	24.6	8.0	IC	31.9	10.2	IC	1.30	1.26
3	B1	85.4	20.9	IC	82.4	13.3	IC	0.97	0.64
3	B2				85.2	16.1	IC	1.00	0.77
3	B3				82.7	13.6	IC	0.97	0.65
3	B4				85.4	16.3	IC	1.00	0.78
3	B5				82.7	13.6	IC	0.97	0.65
3	B6				84.2	15.1	IC	0.99	0.72
3	B7	87.5	23.0	IC	88.3	19.3	IC	1.01	0.84
4	G3S9	866	N/A	IC	320	N/A	no failure	0.37	N/A
4	G3S10	880	N/A	IC	280	N/A	no failure	0.32	N/A
4	G4S9	830	N/A	IC	300	N/A	no failure	0.37	N/A
4	G4S10	1008	N/A	IC	300	N/A	no failure	0.30	N/A

Notes: IC- intermediate crack debonding  
R- rupture of the FRP

For the B2 specimens in test series 1, the model incorrectly predicted an FRP rupture failure model. For all other specimens in test series 1, 2, and 3, the model correctly predicted the failure mode as IC debonding. For test series 1, the model was not

very precise; it both underestimated and overestimated the capacity and the change in capacity.

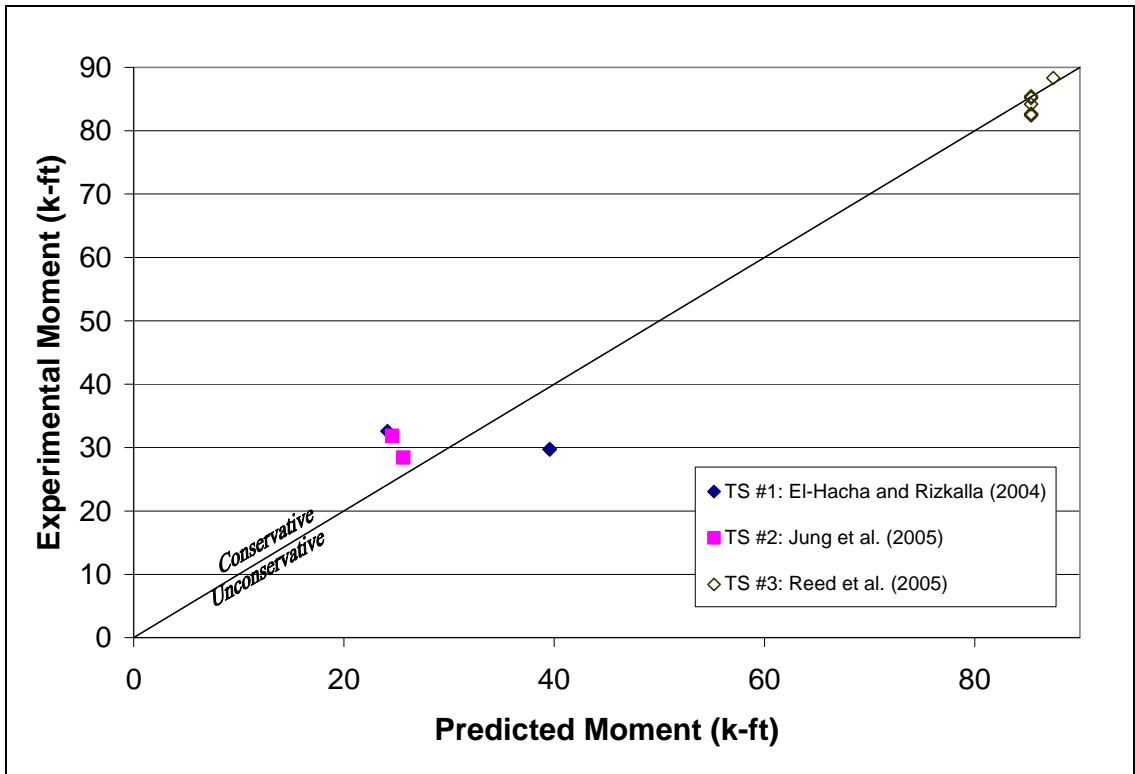
The model more accurately predicted the capacities in test series 2 than in test series 1. Both predictions for the specimens in test series 2 were conservatively underestimated. The experimental capacities were 11 and 30% of the predicted capacities. For the changes in capacity, however, the model overestimated it for one specimen and underestimated it for the other.

The model was extremely accurate when compared to test series 3. The experimental capacities ranged from 97 to 101% of the predicted capacities. The changes in moment capacities, however, were not very accurate. The experimental changes in capacity ranged from 64 to 84% of the predicted changes in capacity.

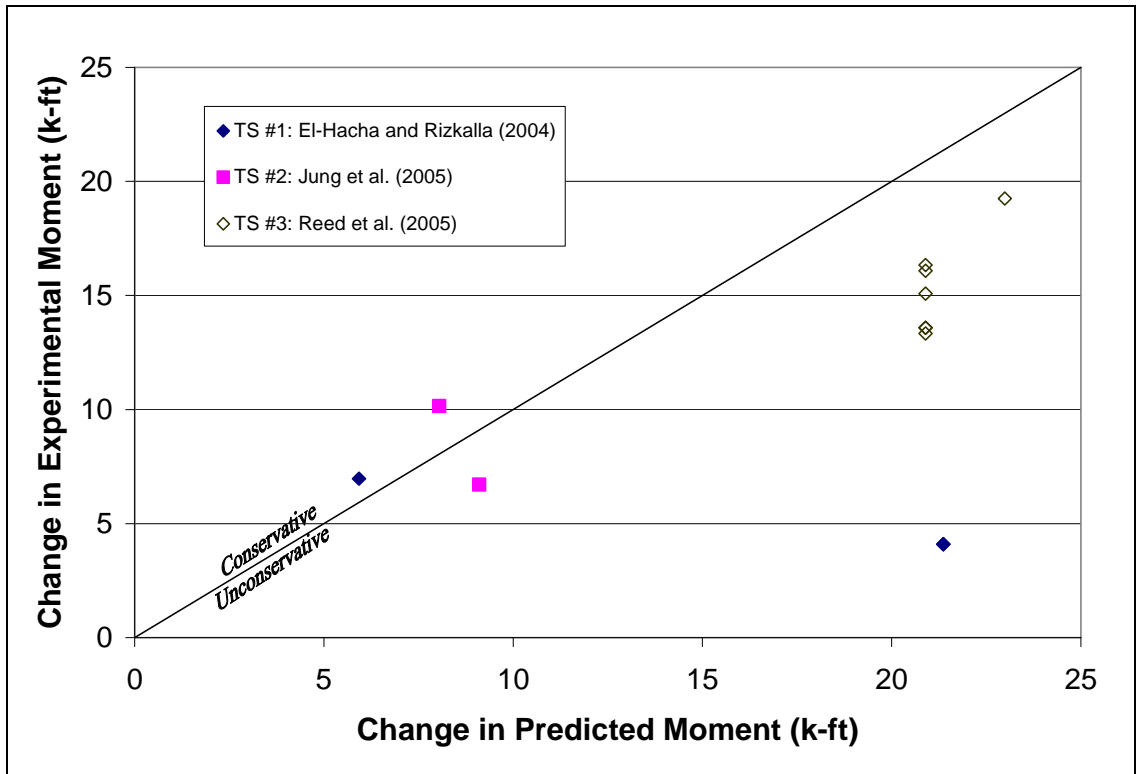
In test series 4, the War Memorial Bridge was only loaded in the service level range; therefore, the high capacity predictions relative to the experimental moments were expected.

Figure 4-13 shows a comparison between the experimental capacity and the predicted capacity. Figure 4-14 shows a comparison between the experimental change in capacity and the predicted change in capacity.





**Figure 4-13:** Comparison between EB Test Results and Rosenboom (2006) IC-  
 Debonding Capacity Predictions



**Figure 4-14:** Comparison between EB Test Results and Rosenboom (2006) IC-  
 Debonding Change-in-Capacity Predictions

As shown in Figure 4-13, most of the data points lie fairly close to the line that separates a conservative and an unconservative prediction. In Figure 4-14, however, very few of the data points lie close to the line.

Table 4-15 shows the FRP strain values that were measured for each test specimen and that were predicted by the Rosenboom model.

**Table 4-15: FRP Strain Predictions using the Rosenboom (2006) IC-Debonding Model and EB Test Results**

Test Series #	Specimen ID	Predicted		Experimental		$\frac{\epsilon_{f,exp}}{\epsilon_{f,pred}}$
		$\epsilon_{f,pred}$	$\frac{\epsilon_{f,pred}}{\epsilon_{f,rupt}}$	$\epsilon_{f,exp}$	$\frac{\epsilon_{f,exp}}{\epsilon_{f,rupt}}$	
1	B2a	*1.08%	*1.00	0.48%	0.44	0.44
1	B2b			0.44%	0.41	0.41
1	B4a	0.33%	0.15	0.62%	0.28	1.88
2	CPL-50-BOND	0.41%	0.28	0.44%	0.30	1.09
2	SH-BOND	0.67%	0.44	0.85%	0.56	1.27
3	B1	0.83%	0.41	0.44%	0.22	0.53
3	B2			0.51%	0.25	0.62
3	B3			0.49%	0.24	0.60
3	B4			0.53%	0.26	0.65
3	B5			0.51%	0.25	0.62
3	B6			0.56%	0.28	0.68
3	B7			0.67%	0.33	0.47%

\*denotes a failure mode other than IC debonding

The predicted FRP strains shown in Table 4-15 do not correlate well with the experimental strains. Except for specimen CPL-50-BOND, which has a ratio of experimental strain to predicted strain of 1.09, none of the specimens have a ratio of experimental to predicted FRP strain between 0.75 and 1.25.

For the B2 specimens in test series 1, the model predicts a rupture failure, but the experimental strains only reach 44 and 41% of the rupture strain. For specimen B4a, the model underestimates the FRP strain by nearly two times.

For test series 2, the model had the most accurate predictions. The experimental strains were 9 and 27% higher than the predicted FRP strains.

For test series 3, the model overestimated the FRP strains. The ratio of experimental to predicted strains ranged from 0.53 to 0.70.

#### **4.3.4.2 Discussion of Model**

The Rosenboom model was fairly accurate at predicting strengthened moment capacities. As shown in Figure 4-13, most of the data points were close to the line that corresponds to an experimental to predicted capacity ratio of 1.0. However, the model did not predict the changes in capacity or the FRP strains very well. Most of the FRP strains were overestimated, which resulted in overestimations for most of the changes in capacity. Because the strengthened moment capacities were fairly accurate and the FRP contribution was overestimated, other factors must have affected the strengthened capacity. One possible explanation is that the reinforced concrete was stronger and had a greater contribution to the strengthened capacity than was predicted, which may have been due to inaccuracies in the concrete compressive strength, assuming the Whitney stress block, or possible overstrength or strain hardening of the reinforcing steel.

#### **4.3.5 Seracino, Raizal Saifulnaz, and Oehlers (2007)**

The model by Seracino, Raizal Saifulnaz, and Oehlers (2007) is a generic IC-debonding model that was designed to be used for both EB and NSM. Standards Australia has accepted the model in their design provisions but has recommended a different model for EB that is specific to beams, which was evaluated in Section 4.3.3.

In this section, the Seracino, Raizal Saifulnaz, and Oehlers model is compared to EB tests to determine the accuracy of the model.

##### **4.3.5.1 Comparison to Previous Testing**

Using the generic IC-debonding model, nominal moment capacities were predicted for each EB-strengthened test specimen and compared to previous testing. Table 4-16 shows

the predicted capacities, the experimental results, and comparisons between the two for specimens with EB FRP.

**Table 4-16:** Comparison of the IC-Debonding Model by Seracino, Raizal Saifulnaz, and Oehlers (2007) to EB Test Results

Test Series #	Specimen ID	Predicted			Experimental			$M_{exp}/M_{n,pred}$	$\Delta M_{exp}/\Delta M_{n,pred}$
		$M_n$ (k-ft)	$\Delta M_n$ (k-ft)	Failure Mode	$M_{exp}$ (k-ft)	$\Delta M_{exp}$ (k-ft)	Failure Mode		
1	B2a	39.6	21.4	R	29.7	4.1	IC	0.75	0.19
1	B2b				29.7	4.1	IC	0.75	0.19
1	B4a				62.0	43.8	R	32.6	7.0
2	CPL-50-BOND	22.1	5.6	IC	28.4	6.7	IC	1.28	1.20
2	SH-BOND	20.7	4.1	IC	31.9	10.2	IC	1.54	2.45
3	B1	117.6	53.2	IC	82.4	13.3	IC	0.70	0.25
3	B2				85.2	16.1	IC	0.72	0.30
3	B3				82.7	13.6	IC	0.70	0.26
3	B4				85.4	16.3	IC	0.73	0.31
3	B5				82.7	13.6	IC	0.70	0.26
3	B6				84.2	15.1	IC	0.72	0.28
3	B7				124.4	59.9	IC	88.3	19.3
4	G3S9	1122	N/A	R	320	N/A	no failure	0.29	N/A
4	G3S10	1122	N/A	R	280	N/A	no failure	0.25	N/A
4	G4S9	1173	N/A	R	300	N/A	no failure	0.26	N/A
4	G4S10	1322	N/A	R	300	N/A	no failure	0.23	N/A

Notes: IC- intermediate crack debonding  
R- rupture of the FRP

As shown in Table 4-16, the failure mode was correctly predicted as IC debonding for test series 2 and 3, but the failure mode was incorrectly predicted as FRP rupture for test series 1. Because the model predicted that the FRP would reach higher FRP strains in test series 1, the capacities were overestimated. For the three specimens in test series 1, the experimental moment capacities ranged from 53 to 75% of the predicted moment capacities. The changes in capacity, however, were extremely overestimated.

The experimental changes in moment capacity ranged from 16 to 19% of the predicted changes in moment capacity.

For test series 2, the predicted capacities and the predicted changes in capacity were actually underestimated. The experimental capacities were 28 and 54% greater than the predicted capacities, and the experimental changes in capacity were 20 and 145% greater than the predicted changes in capacity.

For test series 3, the capacity predictions were very inaccurate, with the experimental capacities ranging from 70 to 73% of the predicted capacities. The changes in capacity were even more inaccurate, with the predicted changes in moment ranging from three to four times as large as the experimental changes in capacity.

Once again, the high capacity predictions for test series 4 relative to the experimental moments were expected as the War Memorial Bridge was only loaded in the service level range.

Figure 4-15 shows a comparison between the experimental moment capacity and the predicted moment capacity. Figure 4-16 shows a comparison between the experimental change in capacity and the predicted change in capacity.

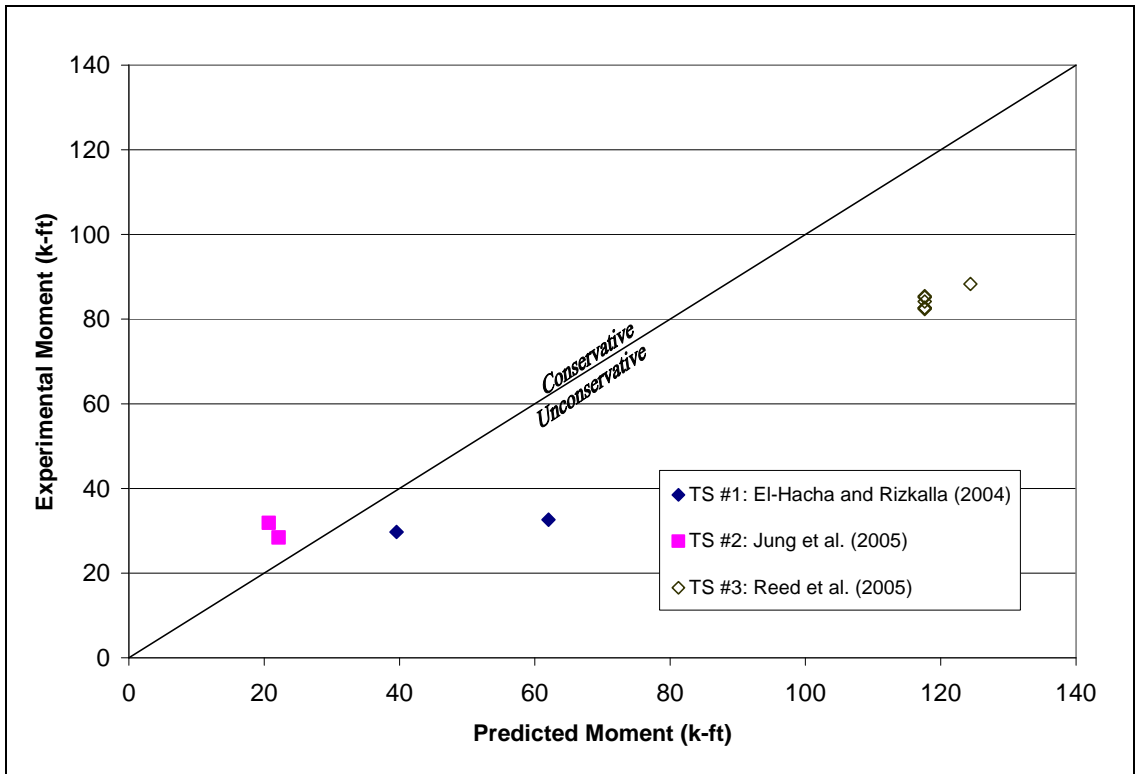


**Figure 4-15:** Comparison between EB Test Results and Seracino, Raizal Saifulnaz, and Oehlers (2007) IC-Debonding Capacity Predictions

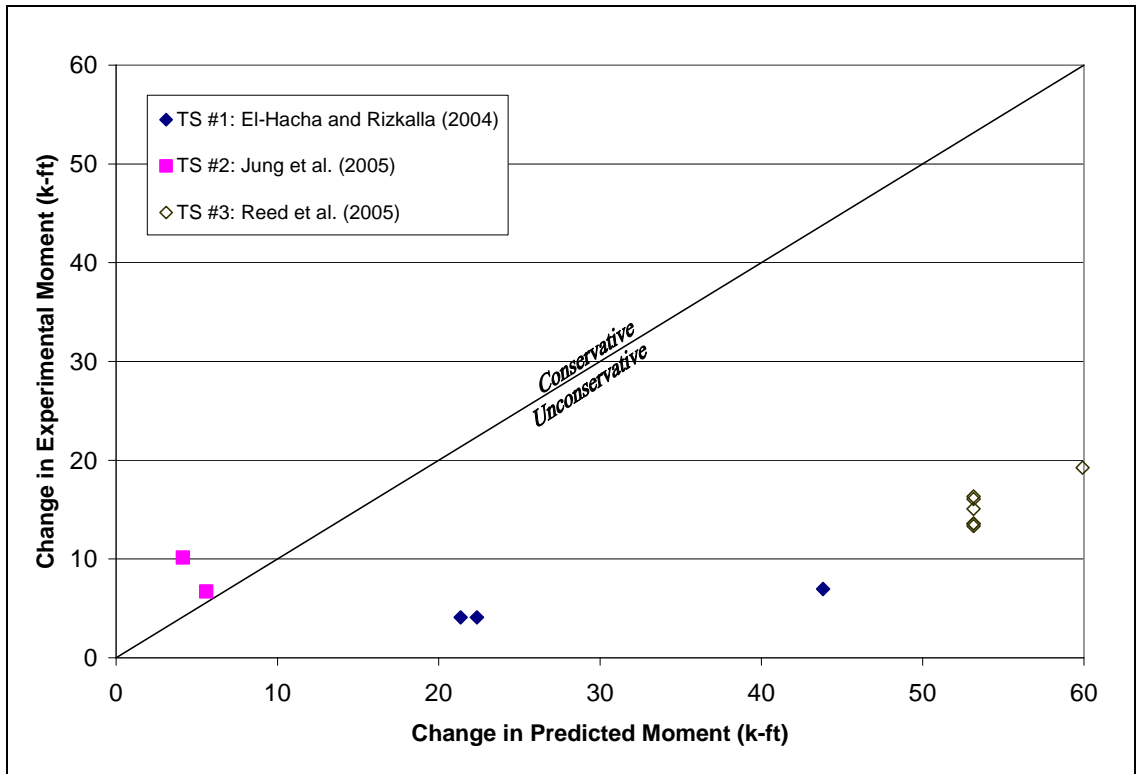


**Figure 4-16:** Comparison between EB Test Results and Seracino, Raizal Saifulnaz, and Oehlers (2007) IC-Debonding Change-in-Capacity Predictions

As shown in Figures 4-15 and 4-16, the data points are not very close to the lines shown, which means that the model is not very accurate. Most of the points are below and to the right of the lines, which means that the model was unconservative in its predictions.

Table 4-17 shows the FRP strain predictions and experimental results.



**Table 4-17:** FRP Strain Predictions using the Seracino, Raizal Saifulnaz, and Oehlers (2007) IC-Debonding Model and EB Test Results

Test Series #	Specimen ID	Predicted		Experimental		$\frac{\epsilon_{f,exp}}{\epsilon_{f,pred}}$
		$\epsilon_{f,pred}$	$\frac{\epsilon_{f,pred}}{\epsilon_{f,rupt}}$	$\epsilon_{f,exp}$	$\frac{\epsilon_{f,exp}}{\epsilon_{f,rupt}}$	
1	B2a	*1.08%	*1.00	0.48%	0.44	0.44
1	B2b			0.44%	0.41	0.41
1	B4a	*2.22%	*1.00	0.62%	0.28	0.28
2	CPL-50-BOND	0.27%	0.18	0.44%	0.30	1.64
2	SH-BOND	0.38%	0.25	0.85%	0.56	2.24
3	B1	2.01%	0.99	0.44%	0.22	0.22
3	B2			0.51%	0.25	0.25
3	B3			0.49%	0.24	0.25
3	B4			0.53%	0.26	0.27
3	B5			0.51%	0.25	0.26
3	B6			0.56%	0.28	0.28
3	B7			1.66%	0.82	0.47%

\*denotes a failure mode other than IC debonding

As shown in Table 4-17, the predicted FRP strains do not match the experimental FRP strains very well. In test series 1 and 3, the predicted strains were very high, with predicted strain values ranging from 82 to 100% of the rupture strain. The experimental strains for test series 1 and 3, however, only ranged from 22 to 44% of the rupture strain, which is about one quarter to one half of the predicted strain for most cases. For the two specimens in test series 2, the predicted strains were 18 and 25% of the rupture strain, while the experimental strains were 30 and 56% of the rupture strain.

Even though the model correctly predicted IC debonding as the failure mode for the specimens in test series 3, the predicted FRP strains were very close to the rupture strain value. For specimens B1 through B6, the predicted strain was 99% of the rupture strain, which almost resulted in a predicted failure mode of FRP rupture. However, the strains in the actual test specimens never approached this level prior to IC debonding.

#### **4.3.5.2 Discussion of Model**

The model given by Seracino, Raizal Saifulnaz, and Oehlers (2007) did not accurately predict the strengthened moment capacities for EB tests. Most of the specimens had experimental capacities that were 75% or less of the predicted capacities, which resulted in a very unconservative model.

Because it was based on push-pull tests, this model should give a lower bound for the moment capacity (Standards Australia 2008). For the EB tests, this model produced unconservative results; therefore, this model should not be used as a lower bound for any predictions for EB FRP

#### **4.3.6 Said and Wu (2008)**

The model by Said and Wu (2008) was used to evaluate the IC-debonding resistance of experimental tests using EB FRP.

##### **4.3.6.1 Comparison to Previous Testing**

Using the IC-debonding model by Said and Wu (2008), nominal moment capacities were predicted for each strengthened test specimen and compared to previous testing. Table 4-18 shows the predicted capacities, the experimental results, and comparisons between the two for specimens with EB FRP.

**Table 4-18:** Comparison of the IC-Debonding Model by Said and Wu (2008) to EB Test Results

Test Series #	Specimen ID	Predicted			Experimental			$M_{exp}/M_{n,pred}$	$\Delta M_{exp}/\Delta M_{n,pred}$
		$M_n$ (k-ft)	$\Delta M_n$ (k-ft)	Failure Mode	$M_{exp}$ (k-ft)	$\Delta M_{exp}$ (k-ft)	Failure Mode		
1	B2a	23.5	5.3	IC	29.7	4.1	IC	1.27	0.78
1	B2b				29.7	4.1	IC	1.27	0.78
1	B4a	25.7	7.5	IC	32.6	7.0	IC	1.27	0.93
2	CPL-50-BOND	22.8	6.3	IC	28.4	6.7	IC	1.25	1.07
2	SH-BOND	29.9	13.3	IC	31.9	10.2	IC	1.07	0.76
3	B1	82.1	17.6	IC	82.4	13.3	IC	1.00	0.76
3	B2				85.2	16.1	IC	1.04	0.91
3	B3				82.7	13.6	IC	1.01	0.77
3	B4				85.4	16.3	IC	1.04	0.93
3	B5				82.7	13.6	IC	1.01	0.77
3	B6				84.2	15.1	IC	1.03	0.86
3	B7				86.1	21.7	IC	88.3	19.3
4	G3S9	816	N/A	IC	320	N/A	no failure	0.39	N/A
4	G3S10	816	N/A	IC	280	N/A	no failure	0.34	N/A
4	G4S9	810	N/A	IC	300	N/A	no failure	0.38	N/A
4	G4S10	959	N/A	IC	300	N/A	no failure	0.31	N/A

Notes: IC- intermediate crack debonding  
R- rupture of the FRP

As shown in Table 4-18, the failure mode was correctly predicted as IC debonding for test series 1, 2, and 3. For the three specimens in test series 1, the experimental moment capacities were all 27% greater than the predicted moment capacities. The changes in capacity, however, were slightly overestimated. The predicted changes in moment capacity ranged from 0.5 to 1.2 kip-ft greater than the experimental changes in moment capacity.

For test series 2, the predicted capacities and the predicted changes in capacity were underestimated. The experimental capacities were 7 and 25% greater than the

predicted capacities, respectively, and the experimental changes in capacity were 76 and 107% of the predicted changes in capacity, respectively.

For test series 3, the capacity predictions were very accurate, with the experimental capacities ranging from 100 to 104% of the predicted capacities. The changes in capacity were less accurate, with the experimental changes in moment ranging from 76 to 93% of predicted changes in capacity.

Once again, the high capacity predictions for test series 4 relative to the experimental moments were expected as the War Memorial Bridge was only loaded in the service level range.

Figure 4-17 shows a comparison between the experimental moment capacity and the predicted moment capacity. Figure 4-18 shows a comparison between the experimental change in capacity and the predicted change in capacity.

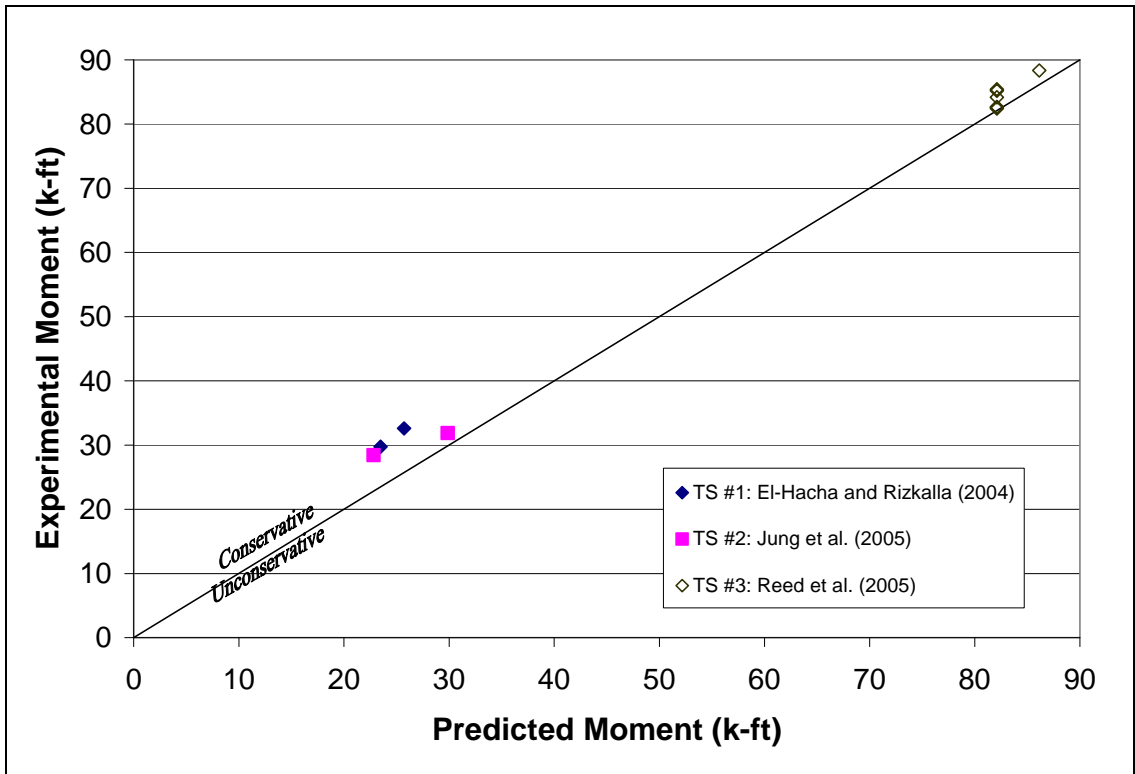


**Figure 4-17:** Comparison between EB Test Results and Said and Wu (2008) IC-  
 Debonding Capacity Predictions

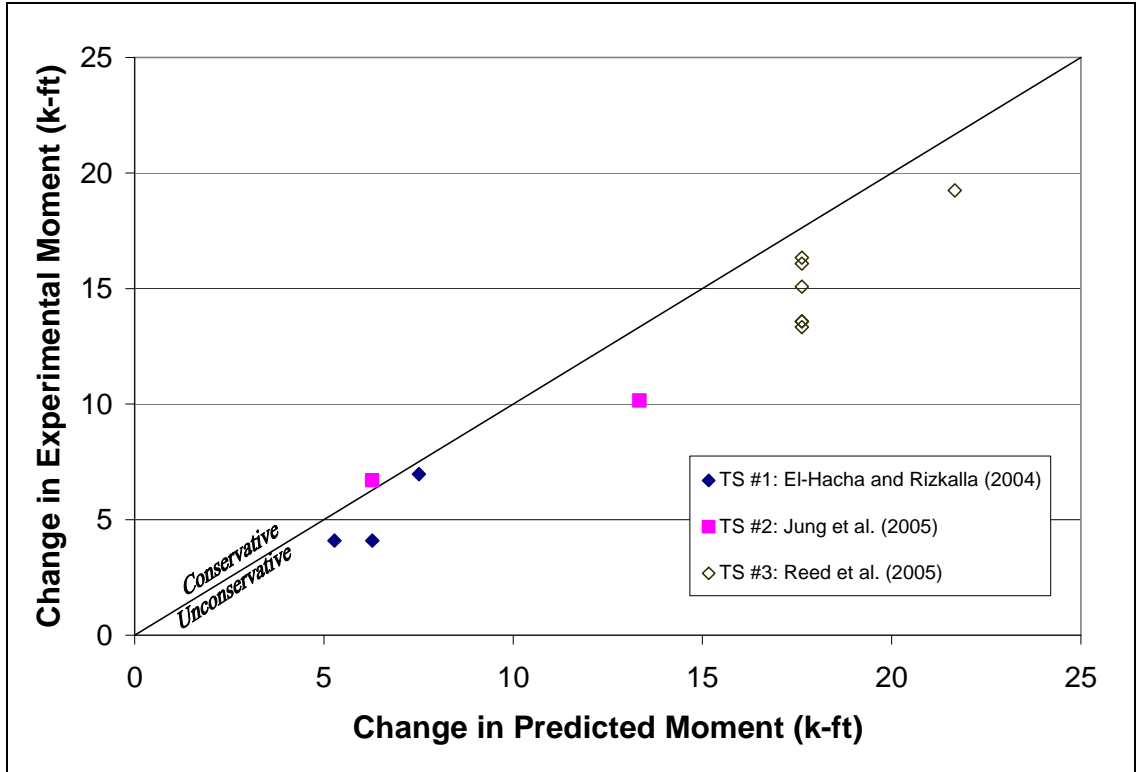


**Figure 4-18:** Comparison between EB Test Results and Said and Wu (2008) IC-  
 Debonding Change-in-Capacity Predictions

As shown in Figure 4-17, the data points are fairly close to the line shown, which means that the model is fairly accurate for predicting the strengthened moment capacity. All of the points are above and to the left of the line, which means that the model was conservative in its predictions. In Figure 4-18, the data points are relatively close to the line of equality, which means that the model is relatively accurate at predicting the change in capacity.

Table 4-19 shows the FRP strain predictions and experimental results.

**Table 4-19: FRP Strain Predictions using the Said and Wu (2008) IC-Debonding Model and EB Test Results**

Test Series #	Specimen ID	Predicted		Experimental		$\frac{\epsilon_{f,exp}}{\epsilon_{f,pred}}$
		$\epsilon_{f,pred}$	$\frac{\epsilon_{f,pred}}{\epsilon_{f,rupt}}$	$\epsilon_{f,exp}$	$\frac{\epsilon_{f,exp}}{\epsilon_{f,rupt}}$	
1	B2a	0.29%	0.27	0.48%	0.44	1.63
1	B2b			0.44%	0.41	1.49
1	B4a	0.41%	0.18	0.62%	0.28	1.52
2	CPL-50-BOND	0.61%	0.41	0.44%	0.30	0.73
2	SH-BOND	1.03%	0.68	0.85%	0.56	0.82
3	B1	0.06%	0.03	0.44%	0.22	6.84
3	B2			0.51%	0.25	7.96
3	B3			0.49%	0.24	7.67
3	B4			0.53%	0.26	8.31
3	B5			0.51%	0.25	8.02
3	B6			0.56%	0.28	8.77
3	B7			0.06%	0.03	0.47%

Note: All predicted and experimental failure modes were IC debonding.

As shown in Table 4-19, the predicted FRP strains do not match the experimental FRP strains very well. In test series 1, the predicted strain values were 18 and 27% of the rupture strain, while the experimental strains ranged from 28 to 44% of the rupture strain. The ratio of experimental FRP strain to predicted FRP strain was around 1.5 for the specimens in this test series.

In test series 2, the predicted strains were greater than the experimental strains. The ratios of experimental strain to predicted strain were 0.73 and 0.82.

In test series 3, the predicted strains were extremely low compared to the experimental strains. For all of the specimens, the model predicted an FRP strain of 3% of the rupture strain. The experimental strains at failure were 22 to 28% of the rupture strain, which resulted in ratios of experimental strain to predicted strain of 6.84 to 8.77.

#### **4.3.6.2 Discussion of Model**

When compared to EB tests from the referenced literature, the Said and Wu model was very accurate. For test series 1 and 2, the model was slightly conservative. For test series 3, the model was extremely accurate. For the changes in capacity predictions, the model was relatively accurate. The predicted FRP strains, however, were not accurate at all, with some of the experimental strains being more than seven times greater than the predicted strains.

#### **4.4 IC-Debonding Models for NSM**

Five different IC-debonding models for NSM are analyzed in this section. Each model was used to predict strengthened moment capacities for different experimental specimens. The predictions of the models were compared to experimental results of NSM tests to determine the accuracy and level of safety of each model. The five models discussed in this section are ACI 440 (2008), *fib* 9.3 (2001), Standards Australia (2008), Seracino et al. (2007a), and Said and Wu (2008). The experimental tests used in this section are test series 1, 2, and 5 through 11.

##### **4.4.1 ACI 440 (2008)**

The NSM IC-debonding model given by ACI Committee 440 was compared to existing experimental tests to determine the accuracy of the model.

##### **4.4.1.1 Comparison to Previous Testing**

Using the NSM model given by ACI 440, nominal moment capacities were predicted for each test specimen and compared to experimental results. Like the predictions by the ACI



440 EB model, the NSM model predictions do not include any reduction factors. Table 4-20 shows the capacity predictions and comparisons to the test results.

For test series 9, 10, and 11, the embedment length of the FRP was the main variable in each test, and the only failure mode that occurred was pullout of the FRP. For each test series, only the specimens with the longest embedment lengths were included in the database of IC-debonding tests used in the analysis of the IC-debonding models. Because these tests incorporated an unusual test setup and because the ACI 440 model is based on an assumed long bonded length (i.e. no pullout failure), these tests will be ignored in the determination of the accuracy of the model.

**Table 4-20:** Comparison of the IC-Debonding Model by ACI 440 (2008) to NSM Test

## Results

Test Series #	Specimen ID	Predicted			Experimental			$M_{exp}/M_{n,pred}$	$\Delta M_{exp}/\Delta M_{n,pred}$
		$M_n$ (k-ft)	$\Delta M_n$ (k-ft)	Failure Mode	$M_{exp}$ (k-ft)	$\Delta M_{exp}$ (k-ft)	Failure Mode		
1	B1	32.9	14.7	IC	43.1	17.4	IC	1.31	1.19
1	B2	32.4	14.2	IC	45.7	20.1	R	1.41	1.42
1	B3	35.5	17.3	IC	50.6	25.0	R	1.43	1.45
1	B4	46.9	28.7	IC	47.4	21.7	IC	1.01	0.76
2	NSM-PL-15	23.5	7.0	IC	30.3	8.6	R	1.29	1.23
2	NSM-PL-25	28.2	11.7	IC	33.4	11.7	IC	1.18	1.00
2	CRD-NSM	32.8	16.2	IC	35.8	14.1	IC	1.09	0.87
5	NSMR 1	284.2	186.6	IC	278.4	180.9	IC	0.98	0.97
5	NSMR 2	283.6	186.0	IC	274.7	177.2	IC	0.97	0.95
6	6-1Fa	21.4	3.5	CC	22.3	5.3	CC	1.04	1.53
6	6-1Fb				20.9	3.9	CC	0.98	1.13
6	6-2Fa	23.7	5.8	CC	22.5	5.5	CC	0.95	0.94
6	6-2Fb				24.2	7.2	CC	1.02	1.25
6	9-1Fa	23.7	4.4	IC	25.4	6.8	CC	1.07	1.56
6	9-1Fb				25.1	6.6	CC	1.06	1.51
6	9-2Fa	27.8	8.5	IC	33.3	14.8	CC	1.20	1.74
6	9-2Fb				32.2	13.7	CC	1.16	1.61
6	12-1Fa	24.2	4.4	IC	26.6	7.6	R	1.10	1.72
6	12-1Fb				27.9	8.9	R	1.15	2.01
6	12-2Fa	28.6	8.8	IC	30.4	11.4	CC	1.06	1.29
6	12-2Fb				37.6	18.5	CC	1.31	2.11
7	NS F1	19.6	N/A	CC	18.7	N/A	S	0.96	N/A
7	NS F2	12.9	N/A	IC	14.6	N/A	CC	1.13	N/A
7	NS F3	10.1	N/A	IC	14.0	N/A	CC	1.38	N/A
7	NS F4	12.7	N/A	IC	12.8	N/A	IC	1.00	N/A
7	NB F2	29.5	N/A	IC	49.6	N/A	IC	1.68	N/A
7	NB F3	38.6	N/A	IC	54.0	N/A	IC	1.40	N/A
8	B2900	30.5	8.9	IC	44.1	22.6	CC	1.45	2.53
9	G4D24c	12.7	N/A	IC	11.0	N/A	P	0.87	N/A
9	C3D24b	16.3	N/A	IC	7.8	N/A	P	0.48	N/A
9	C3S24a	13.4	N/A	IC	4.0	N/A	P	0.30	N/A
10	fcm35 Lb80	3.1	N/A	IC	2.1	N/A	P	0.66	N/A
10	fcm45 Lb80	3.1	N/A	IC	2.4	N/A	P	0.78	N/A
10	fcm70 Lb80	3.1	N/A	IC	2.4	N/A	P	0.75	N/A
11	Lb120 M	2.9	N/A	IC	1.5	N/A	P	0.53	N/A

Notes: CC- crushing of the concrete (preceded by steel yielding)

IC- intermediate crack debonding

P- pullout of the FRP

R- rupture of the FRP

S- shear failure in the concrete

Figure 4-19 shows a comparison between the experimental strengthened moment capacity and the predicted strengthened moment capacity. Figure 4-20 shows a comparison between the experimental change in capacity and the predicted change in capacity.

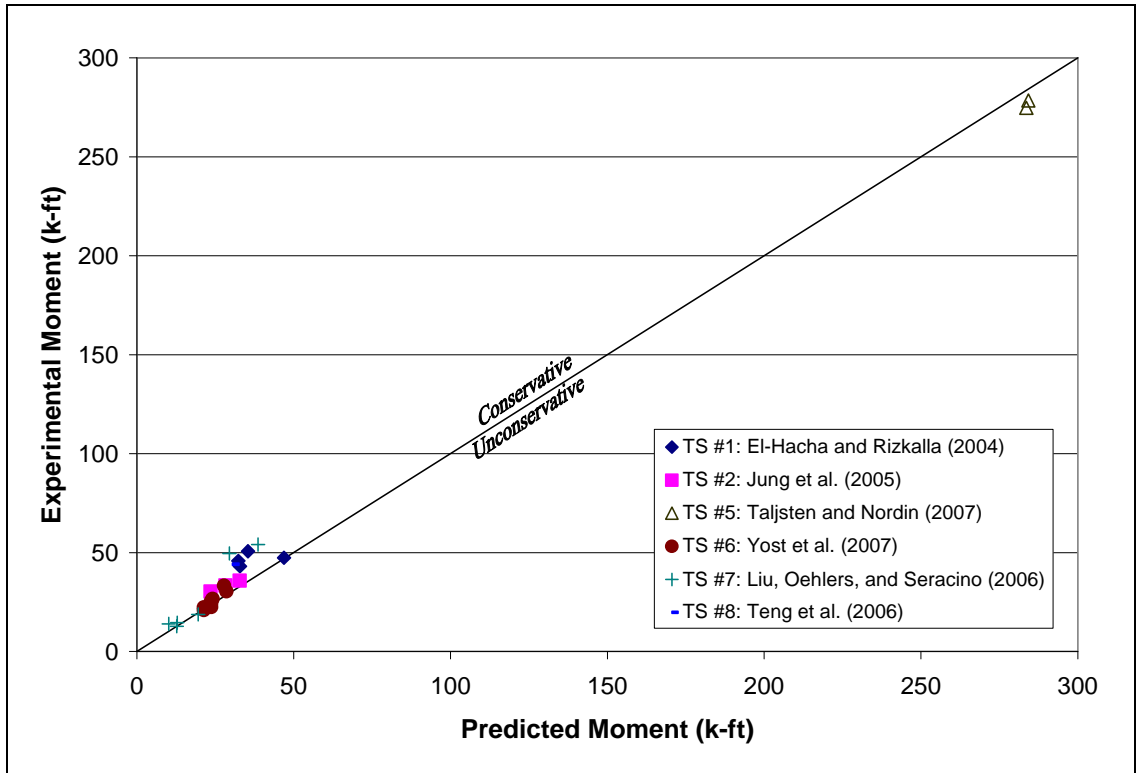


**Figure 4-19:** Comparison between NSM Test Results and ACI 440 (2008) IC-Debonding Capacity Predictions

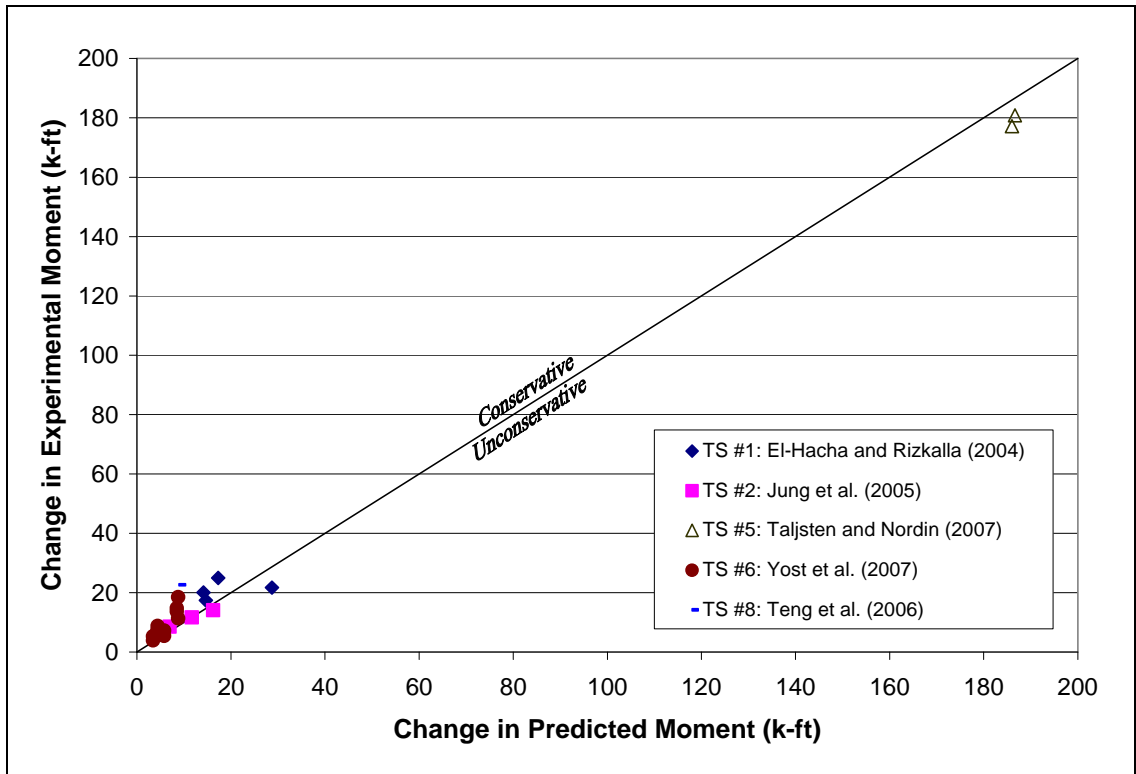


**Figure 4-20:** Comparison between NSM Test Results and ACI 440 (2008) IC-Debonding Change-in-Capacity Predictions

To more closely examine the dispersion of the data points, test series 5 will be excluded; the relatively large moments greatly change the scale of the graph. Figures 4-21 and 4-22 show these enlarged regions of the graphs.

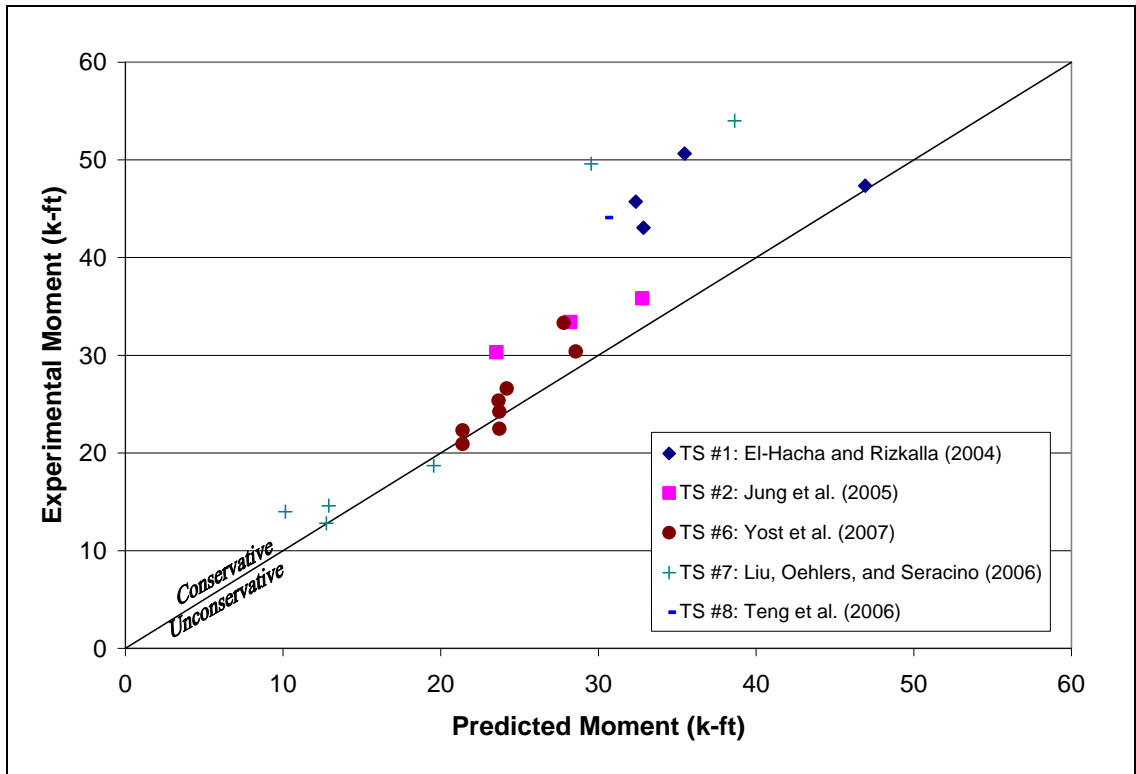


**Figure 4-21:** Enlarged Graph of the ACI 440 (2008) NSM Capacity Comparisons

For test series 1 and 2, the ACI 440 NSM model was mostly conservative, with the experimental strengthened capacities up to 43% greater than the predicted strengthened capacities. For three of the specimens, the failure mode was incorrectly predicted as IC debonding, while the actual failure mode was FRP rupture. The change-in-moment comparisons for these test series were conservative for four of the specimens, but two of the comparisons were actually unconservative. The two unconservative predictions corresponded to the two specimens that had the largest area of FRP reinforcement. Specimen B4 had five NSM strips; the other NSM specimens in test series 1 had one or two strips. Specimen CRD-NSM had an FRP area of  $63.6 \text{ mm}^2$ ; the other two NSM specimens in test series 2 had much smaller FRP areas of 21 and  $35 \text{ mm}^2$ .

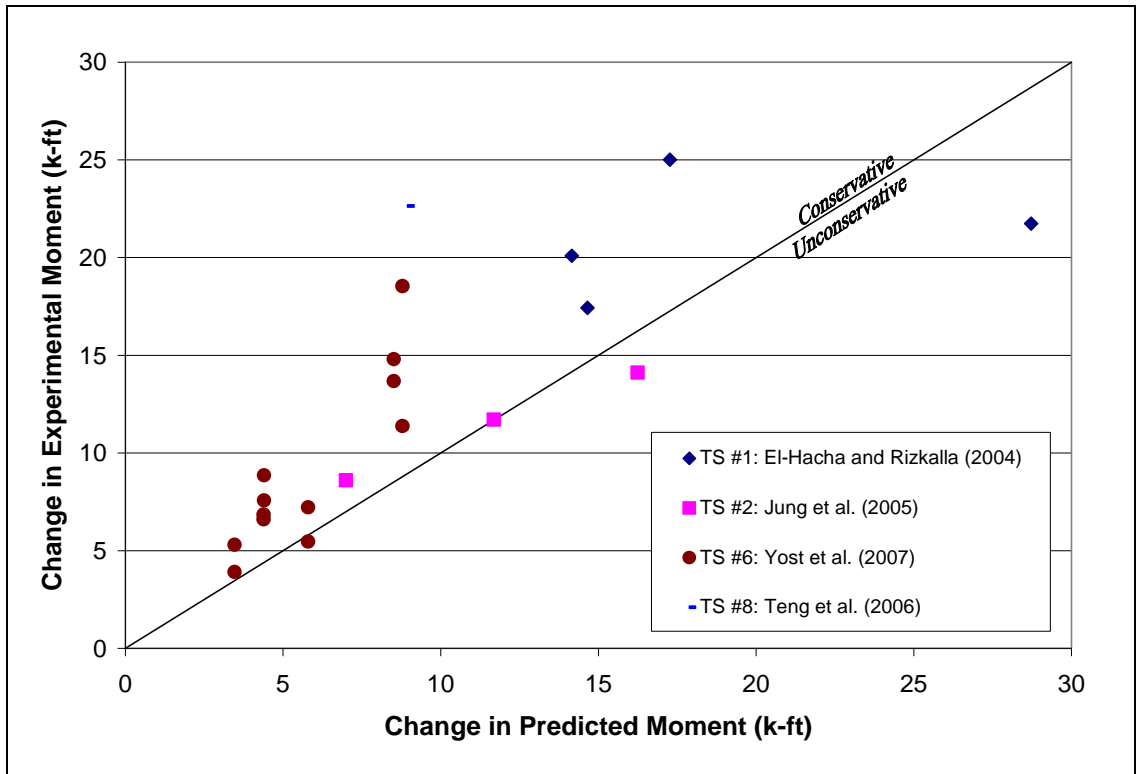


**Figure 4-22:** Enlarged Graph of the ACI 440 (2008) NSM Change-in-Capacity Comparisons

For the tests conducted by Taljsten and Nordin (2007) and Yost et al. (2007), test series 5 and 6, respectively, the ACI model was relatively accurate. However, for eight of the twelve specimens in the Yost et al. test series, the failure mode was incorrectly predicted, which resulted in very conservative estimates of the change in moment in all but three specimens.

The tests conducted by Liu, Oehlers, and Seracino (2006), test series 7, had mixed results when compared to the ACI 440 model. The predicted failure mode only matched the experimental failure mode in half of the specimens. Three of the specimens had an experimental strengthened capacity of 38% or greater than the predicted strengthened

capacity. This test series did not have a control beam so no change-in-moment comparisons could be made.

Table 4-21 shows the experimental and predicted FRP strains using the ACI 440 NSM model.

**Table 4-21: FRP Strain Predictions using the ACI 440 (2008) IC-Debonding Model and NSM Test Results**

Test Series #	Specimen ID	Predicted		Experimental		$\frac{\epsilon_{f,exp}}{\epsilon_{f,pred}}$
		$\epsilon_{f,pred}$	$\frac{\epsilon_{f,pred}}{\epsilon_{f,rupt}}$	$\epsilon_{f,exp}$	$\frac{\epsilon_{f,exp}}{\epsilon_{f,rupt}}$	
1	B1	0.80%	0.70	0.88%	0.77	1.10
1	B2	0.76%	0.70	*1.34%	*1.24	1.76
1	B3	0.93%	0.70	*1.38%	*1.04	1.48
1	B4	1.55%	0.70	1.35%	0.61	0.87
2	NSM-PL-15	1.04%	0.70	*1.54%	*1.04	1.49
2	NSM-PL-25	1.04%	0.70	1.24%	0.83	1.19
2	CRD-NSM	1.08%	0.70	1.31%	0.84	1.21
5	NSMR 1	1.21%	0.70	0.92%	0.53	0.76
5	NSMR 2	1.21%	0.70	0.92%	0.53	0.76
7	NS F1	*0.82%	*0.51	*0.72%	*0.45	0.88
7	NS F2	1.13%	0.70	*1.30%	*0.81	1.15
7	NS F3	1.13%	0.70	*1.50%	*0.93	1.33
7	NS F4	1.17%	0.70	0.84%	0.50	0.72
7	NB F2	1.13%	0.70	1.02%	0.63	0.91
7	NB F3	1.17%	0.70	0.83%	0.50	0.71
8	B2900	0.96%	0.70	*0.97%	*0.71	1.01

\*denotes a failure mode other than IC debonding

Only test series 1, 2, 5, 7, and 8 are shown in Table 4-21 because these are the only series that provided experimental strain values for the FRP.

The ACI model limits the FRP strain to 70% of the rupture strain for all test specimens except one in Table 4-21. For this one specimen, the predicted failure mode was not IC debonding but rather crushing of the concrete prior to IC debonding. As shown in Table 4-21, the predicted FRP debonding strains did not match the experimental failure strains very well. Most of the strain values were either less than 65% of the FRP

rupture strain or greater than 75% of the FRP rupture strain. Only one specimen's experimental failure strain was within this range. A possible source of error could be due to the fact that it is not clear whether these strains were measured at crack sections. If they were not, tension stiffening would reduce the strains relative to the cracked-section values.

Specimens B2, B3, and NSM-PL-15 all failed due to FRP rupture at a measured strain higher than the reported *rupture* strain of the FRP. Specimen B3 attained a strain that was 24% higher than the reported rupture strain, while the other two specimens failed at a strain that was 4% higher than the reported rupture strain. A possible explanation for the incorrect rupture strain value that was reported could be due to some level of safety and conservatism built into the rupture strain value given by the manufacturer. Another explanation could be due to material irregularities that increased the strength of the FRP.

The ratios of experimental FRP strains to predicted FRP strains are also shown in Table 4-21. These ratios show a poor correlation between the predicted versus the experimental results; only three of the specimens resulted in an experimental FRP strain that was within the range of 90 to 110% of the predicted strain. The other thirteen specimens fell outside of this range.

#### **4.4.1.2 Discussion of Model**

By taking the FRP strain as 70% of the rupture strain, the ACI 440 (2008) NSM model makes a rough approximation of the IC-debonding failure strain in the FRP. This method only works if the failure strain is close to this value. For the tests analyzed, only one



specimen fell within the range of 65 to 75% of the rupture strain. By using this simplistic method, the strengthened moment capacities were accurate for some of the test series and overly conservative for other test series. The precision of the model was poor for the change-in-moment comparisons; for some of the specimens, it greatly underestimated the capacity, while for others it overestimated it. These inaccuracies might be related to the amount of FRP reinforcement that was provided.

For three of the specimens, the measured FRP strain at failure was higher than the reported rupture strain. This overestimation of the rupture strain is partly why the model was conservative for some of the specimens.

#### **4.4.2 *fib* 9.3 (2001)**

In Bulletin 14, Task Group 9.3 does not report the procedure for an NSM application of FRP. NSM is briefly mentioned in the bulletin, but no NSM-specific model was given; however, because the IC-debonding model for EB is generic in nature, it was compared to NSM test results to determine the accuracy and level of safety of the model for NSM.

##### **4.4.2.1 Comparison to Previous Testing**

Table 4-22 shows the comparison between the *fib* 9.3 (2001) model and NSM test results.

**Table 4-22:** Comparison of the IC-Debonding Model by *fib* 9.3 (2001) to NSM Test

## Results

Test Series #	Specimen ID	Predicted			Experimental			$M_{exp}/M_{n,pred}$	$\Delta M_{exp}/\Delta M_{n,pred}$
		$M_n$ (k-ft)	$\Delta M_n$ (k-ft)	Failure Mode	$M_{exp}$ (k-ft)	$\Delta M_{exp}$ (k-ft)	Failure Mode		
1	B1	39.2	21.0	R	43.1	17.4	IC	1.10	0.83
1	B2	24.0	5.8	IC	45.7	20.1	R	1.91	3.46
1	B3	38.1	19.9	IC	50.6	25.0	R	1.33	1.26
1	B4	29.8	11.6	IC	47.4	21.7	IC	1.59	1.88
2	NSM-PL-15	26.9	10.3	R	30.3	8.6	R	1.13	0.83
2	NSM-PL-25	25.4	8.8	IC	33.4	11.7	IC	1.32	1.33
2	CRD-NSM	40.4	23.8	R	35.8	14.1	IC	0.89	0.59
5	NSMR 1	362.2	264.6	R	278.4	180.9	IC	0.77	0.68
5	NSMR 2	360.5	262.9	R	274.7	177.2	IC	0.76	0.67
6	6-1Fa	21.4	3.5	CC	22.3	5.3	CC	1.04	1.53
6	6-1Fb				20.9	3.9	CC	0.98	1.13
6	6-2Fa	23.7	5.8	CC	22.5	5.5	CC	0.95	0.94
6	6-2Fb				24.2	7.2	CC	1.02	1.25
6	9-1Fa	24.9	5.7	CC	25.4	6.8	CC	1.02	1.21
6	9-1Fb				25.1	6.6	CC	1.01	1.17
6	9-2Fa	28.6	9.4	CC	33.3	14.8	CC	1.16	1.58
6	9-2Fb				32.2	13.7	CC	1.12	1.46
6	12-1Fa	26.2	6.4	R	26.6	7.6	R	1.02	1.18
6	12-1Fb				27.9	8.9	R	1.06	1.38
6	12-2Fa	32.2	12.4	R	30.4	11.4	CC	0.94	0.91
6	12-2Fb				37.6	18.5	CC	1.17	1.49
7	NS F1	17.5	N/A	IC	18.7	N/A	S	1.07	N/A
7	NS F2	13.2	N/A	IC	14.6	N/A	CC	1.11	N/A
7	NS F3	22.5	N/A	R	14.0	N/A	CC	0.62	N/A
7	NS F4	12.9	N/A	IC	12.8	N/A	IC	0.99	N/A
7	NB F2	30.3	N/A	IC	49.6	N/A	IC	1.64	N/A
7	NB F3	29.9	N/A	IC	54.0	N/A	IC	1.81	N/A
8	B2900	34.3	12.8	R	44.1	22.6	CC	1.28	1.77
9	G4D24c	3.9	N/A	IC	11.0	N/A	P	2.85	N/A
9	C3D24b	2.9	N/A	IC	7.8	N/A	P	2.73	N/A
9	C3S24a	2.9	N/A	IC	4.0	N/A	P	1.39	N/A
10	fcm35 Lb80	1.0	N/A	IC	2.1	N/A	P	2.06	N/A
10	fcm45 Lb80	1.2	N/A	IC	2.4	N/A	P	2.07	N/A
10	fcm70 Lb80	1.5	N/A	IC	2.4	N/A	P	1.55	N/A
11	Lb120 M	0.6	N/A	IC	1.5	N/A	P	2.73	N/A

Notes: CC- crushing of the concrete (preceded by steel yielding)

IC- intermediate crack debonding

P- pullout of the FRP

R- rupture of the FRP

S- shear failure in the concrete

For test series 1, the failure mode was only predicted correctly for one of the four test specimens. For specimen B1, *fib* 9.3 predicted that the FRP would rupture before debonding. In the experiment, however, the FRP debonded before it ruptured. Even though the failure mode was incorrectly predicted, the strengthened moment capacity prediction was relatively accurate. For specimens B2 and B3, the model predicted an IC-debonding failure, but the actual failure was rupture of the FRP, which resulted in very low estimations of capacity. The failure mode was correctly predicted for specimen B4, but the strengthened capacity prediction was well below the experimental capacity.

For test series 2 and 5, the failure mode was predicted correctly for two of the five specimens. For these two specimens, the strengthened capacity was conservatively predicted as lower than the experimental capacity. For the other three specimens, however, the capacity was unconservatively predicted as higher than the experimental capacity.

For test series 6, the failure mode was correctly predicted for five of the six types of specimens, which resulted in relatively accurate predictions of capacity. All of the experimental capacities in test series 6 fell within the range of 94 to 117% of the predicted capacity, with seven of the twelve specimens within 5% of the predicted capacity. No IC-debonding failures were reported or predicted for this test series.

For three of the four slab specimens in test series 7, denoted “NS,” the predicted capacity matched the experimental capacity relatively well. These three experimental capacities were within 11% of the predicted capacities. For the other slab specimen and the two beam specimens, the predictions were not very accurate. The experimental

moments were not within 35% of the predicted moments. Only three of the six specimens had a correctly predicted failure mode.

In test series 8, the experimental moment was 28% larger than the predicted moment, and the failure mode was incorrectly predicted.

The changes in moment for all of the specimens showed a wide dispersion of results. Some experimental changes in moment were as low as 59% of the predicted change in moment, and some were as high as 346% of the predicted change in moment.

Figure 4-23 shows a comparison between the experimental strengthened moment capacity and the predicted strengthened moment capacity. Figure 4-24 shows a comparison between the experimental change in capacity and the predicted change in capacity.

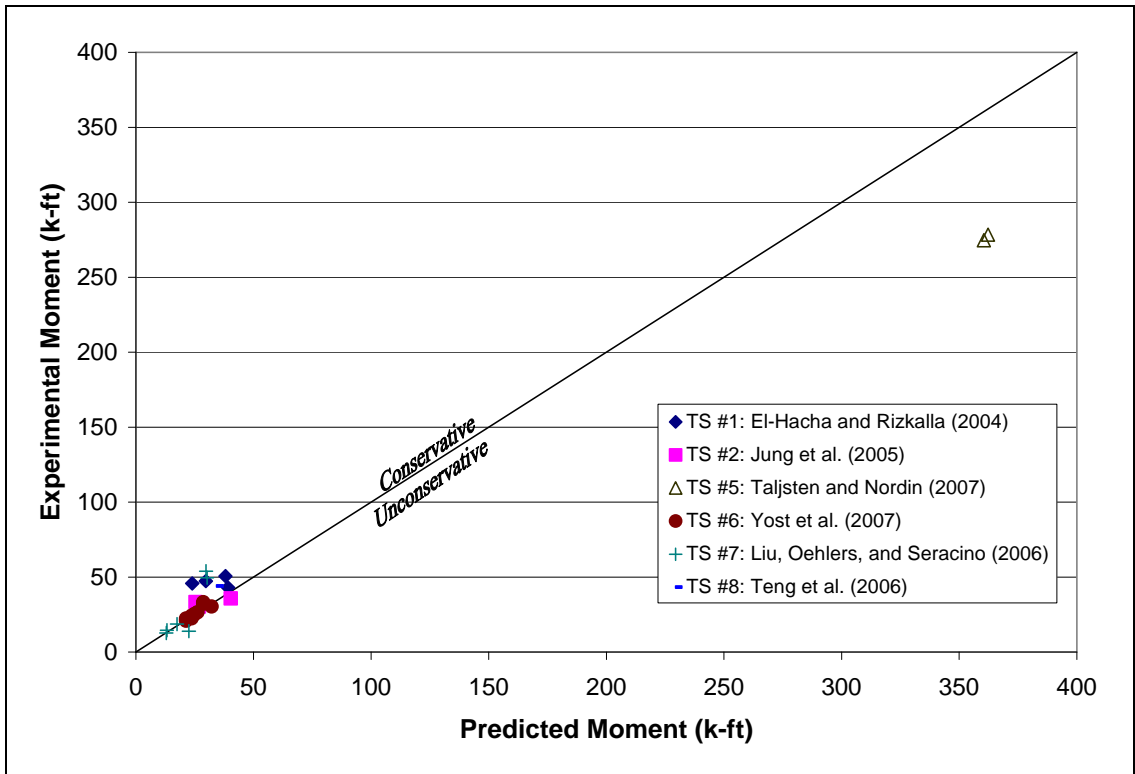


**Figure 4-23:** Comparison between NSM Test Results and *fib* 9.3 (2001) IC-Debonding Capacity Predictions

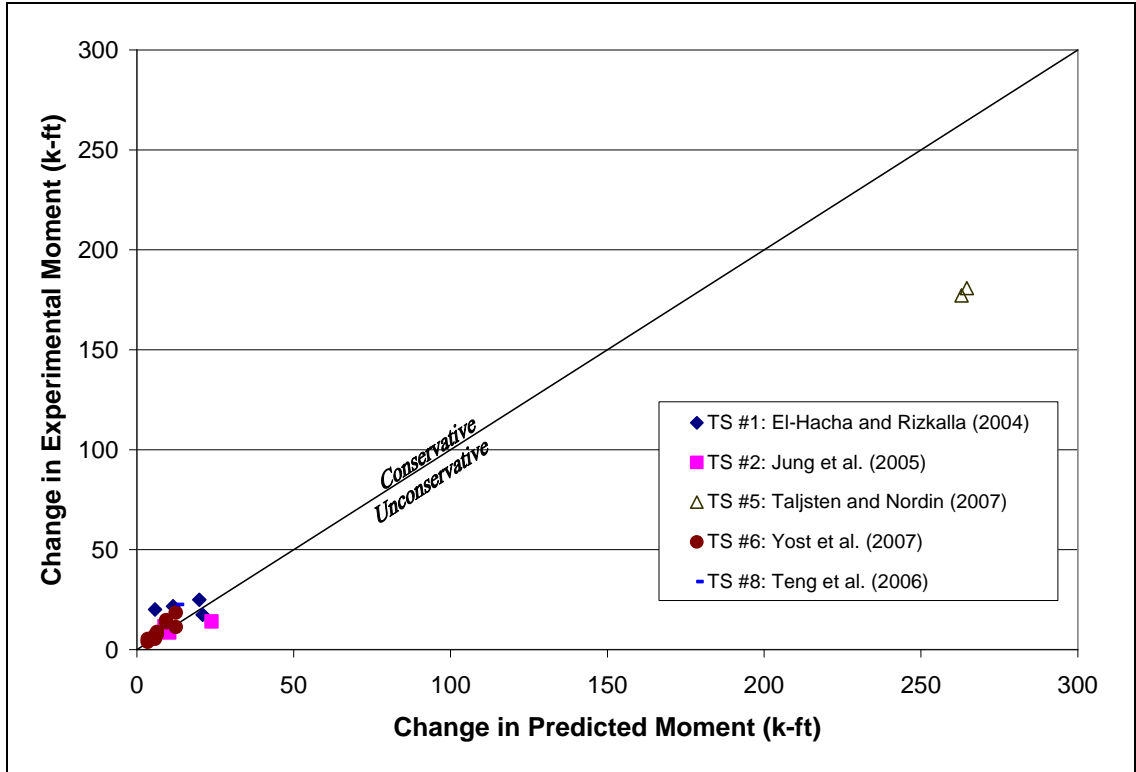


**Figure 4-24:** Comparison between NSM Test Results and *fib* 9.3 (2001) IC-Debonding Change-in-Capacity Predictions

Because the Taljsten and Nordin (2007) test series includes specimens with relatively high moments, they were excluded from the enlarged graphs shown in Figures 4-25 and 4-26.

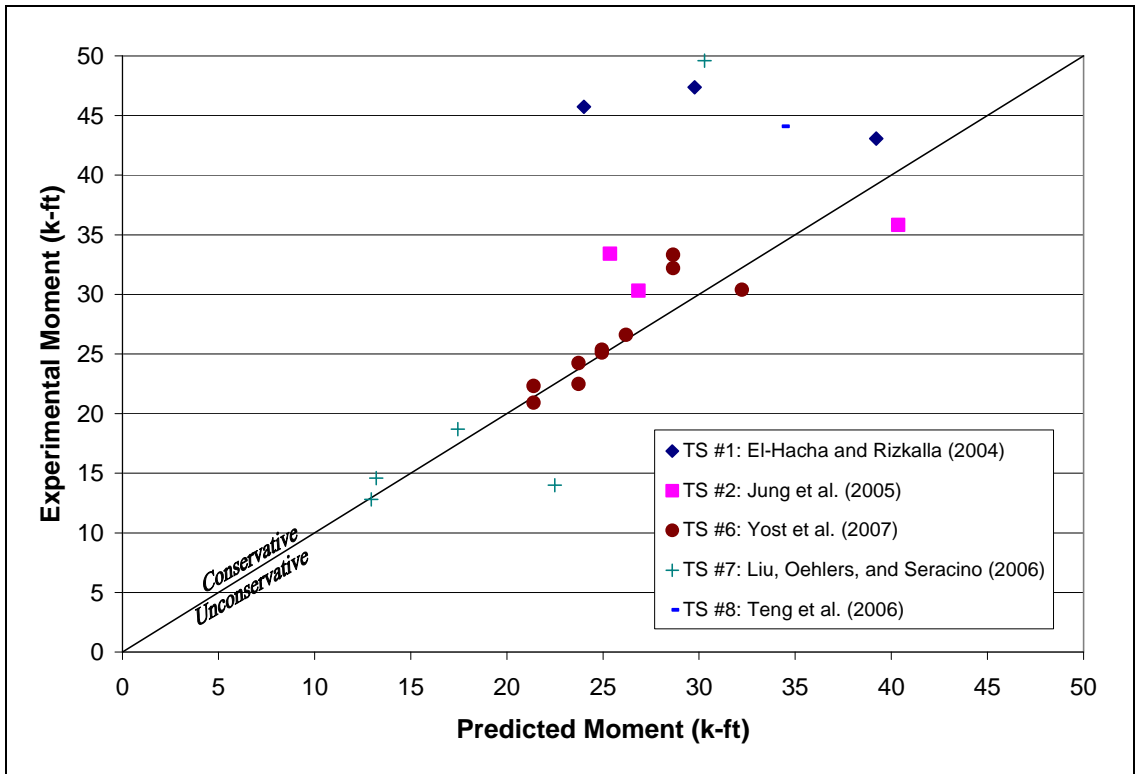


**Figure 4-25:** Enlarged Graph of the *fib* 9.3 (2001) NSM Capacity Comparisons

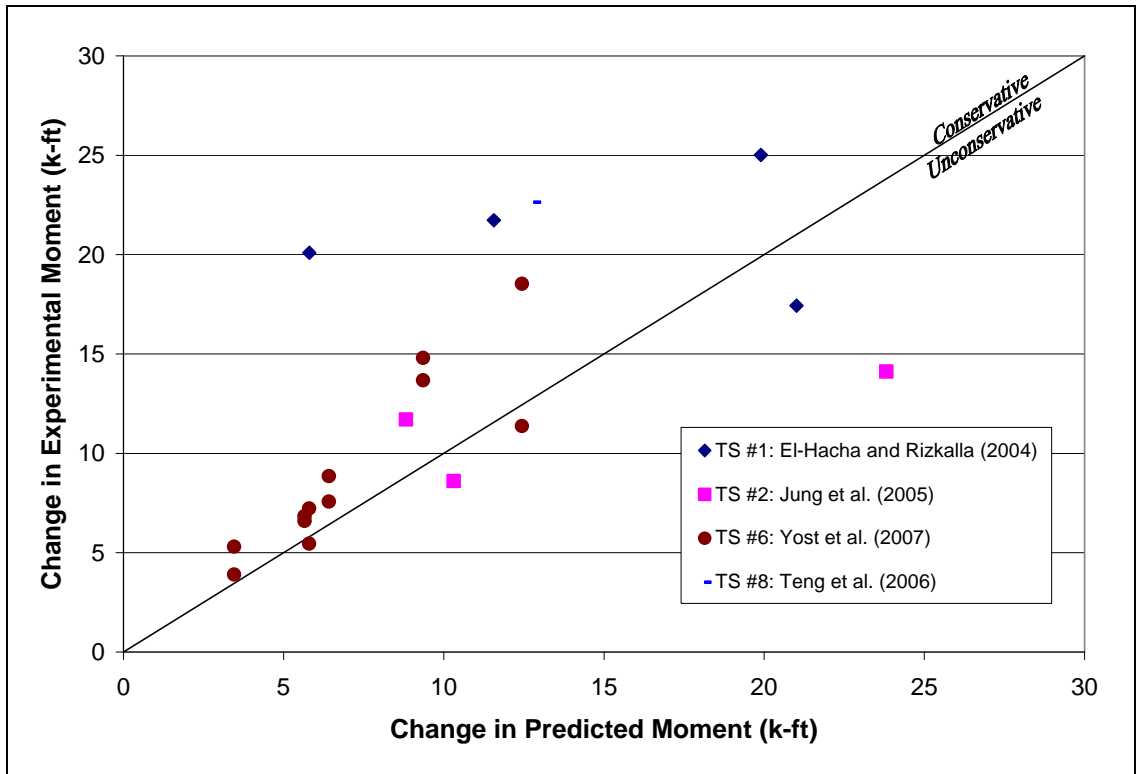


**Figure 4-26:** Enlarged Graph of the *fib* 9.3 (2001) NSM Change-in-Capacity Comparisons

A data point to the left and above the line is a conservative prediction. A data point below and to the right of the line is an unconservative prediction. An ideal prediction would result in a data point that falls directly on the line.

Table 4-23 shows the experimental failure strains in the FRP, the predicted failure strains in the FRP, and comparisons between the two.



**Table 4-23:** FRP Strain Predictions using the *fib* 9.3 (2001) IC-Debonding Model and NSM Test Results

Test Series #	Specimen ID	Predicted		Experimental		$\frac{\epsilon_{f,exp}}{\epsilon_{f,pred}}$
		$\epsilon_{f,pred}$	$\frac{\epsilon_{f,pred}}{\epsilon_{f,rupt}}$	$\epsilon_{f,exp}$	$\frac{\epsilon_{f,exp}}{\epsilon_{f,rupt}}$	
1	B1	*1.14%	*1.00	0.88%	0.77	0.77
1	B2	0.28%	0.26	*1.34%	*1.24	4.71
1	B3	1.06%	0.80	*1.38%	*1.04	1.30
1	B4	0.60%	0.27	1.35%	0.61	2.24
2	NSM-PL-15	*1.48%	*1.00	*1.54%	*1.04	1.04
2	NSM-PL-25	0.78%	0.53	1.24%	0.83	1.59
2	CRD-NSM	*1.55%	*1.00	1.31%	0.85	0.85
5	NSMR 1	*1.73%	*1.00	0.92%	0.53	0.53
5	NSMR 2	*1.73%	*1.00	0.92%	0.53	0.53
7	NS F1	0.68%	0.42	*0.72%	*0.45	1.06
7	NS F2	1.22%	0.76	*1.30%	*0.81	1.07
7	NS F3	*1.61%	*1.00	*1.50%	*0.93	0.93
7	NS F4	1.23%	0.74	0.84%	0.50	0.68
7	NB F2	1.22%	0.76	1.02%	0.63	0.84
7	NB F3	0.66%	0.40	0.83%	0.50	1.25
8	B2900	*1.37%	*1.00	*0.97%	*0.71	0.71

\*denotes a failure mode other than IC debonding

For two of the specimens in test series 1, the FRP strain was only predicted to be about a quarter of the rupture strain. The corresponding experimental strains were more than two and four times these predicted values. For the other two specimens in test series 1, the experimental FRP strains were 77 and 130% of the predicted strains.

For specimen NSM-PL-15, *fib* 9.3 correctly predicted the failure mode as FRP rupture and also made a very accurate prediction of the debonding strain. For specimen NSM-PL-25, however, the failure mode was correctly predicted as IC debonding, but the experimental FRP strain was 59% higher than the predicted strain.

For test series 5, FRP rupture was predicted for both specimens, but failure occurred due to IC debonding instead, resulting in an experimental strain that was about half of the predicted strain.

In test series 7, the failure mode was correctly predicted for specimen NS\_F4 and for both beam specimens, denoted “NB.” The failure mode was incorrectly predicted for the other three slab specimens, denoted NS\_F1, NS\_F2, and NS\_F3. However, the predicted strains for the three slab specimens had a better correlation with the experimental strains than the three specimens where the failure mode was correctly predicted.

In test series 8, the failure mode was incorrectly predicted, and the experimental FRP strain was 71% of the predicted strain.

#### **4.4.2.2 Discussion of Model**

The *fib* model did not correlate well with the NSM tests. Out of the twenty-eight specimens, not including the pullout failures, the model correctly predicted the failure mode sixteen times. If the Yost et al. series is removed because of a lack of IC-debonding failures in this test series, then only six of the sixteen specimens had a correctly predicted failure mode. Also, only five of the nine IC-debonding failures were correctly predicted. These incorrect failure modes led to incorrect FRP strain predictions and, consequently, incorrect strengthened moment capacities. As shown in Figures 4-25 and 4-26, the data were widely dispersed.

In Bulletin 14, Task Group 9.3 does not report the procedure for an NSM application of FRP. NSM is briefly mentioned in the bulletin, but no NSM-specific model was given, which is most likely the reason that the NSM test results did not match the predicted values very well.

### **4.4.3 Standards Australia (2008)**

The IC-debonding model for NSM given by Standards Australia (2008) is the same model given by Seracino, Raizal Saifulnaz, and Oehlers (2007). This model is a generic IC-debonding model designed to be used for both EB and NSM. In this section, the model by Standards Australia is compared to NSM tests to determine the accuracy of the model.

#### **4.4.3.1 Comparison to Previous Testing**

The model given by Standards Australia (2008) was used to predict capacities for NSM test specimens. Table 4-24 shows the predicted capacities, the experimental results, and comparisons between the two.

In test series 1, the failure mode was correctly predicted in three of the four specimens. In these three specimens, the capacity was underestimated. For specimen B1, which failed due to IC debonding, the experimental capacity was 55% greater than the predicted capacity. For specimens B2 and B3, which failed due to FRP rupture, the experimental capacity was just 19% greater than the predicted capacity. Specimen B4 failed due to IC debonding but was predicted to fail due to FRP rupture. The experimental capacity was 80% of the predicted capacity.

For test series 1, the changes in moment capacity were underestimated by about two times for specimen B1 and overestimated by about two times for specimen B4. For specimens B2 and B3, the changes in moment capacity were extremely accurate.

**Table 4-24:** Comparison of the IC-Debonding Model by Standards Australia (2008) to  
NSM Test Results

Test Series #	Specimen ID	Predicted			Experimental			$M_{exp}/M_{n,pred}$	$\Delta M_{exp}/\Delta M_{n,pred}$
		$M_n$ (k-ft)	$\Delta M_n$ (k-ft)	Failure Mode	$M_{exp}$ (k-ft)	$\Delta M_{exp}$ (k-ft)	Failure Mode		
1	B1	27.8	9.6	IC	43.1	17.4	IC	1.55	1.81
1	B2	38.4	20.2	R	45.7	20.1	R	1.19	0.99
1	B3	42.7	24.5	R	50.6	25.0	R	1.19	1.02
1	B4	59.1	40.9	R	47.4	21.7	IC	0.80	0.53
2	NSM-PL-15	25.2	8.6	IC	30.3	8.6	R	1.20	1.00
2	NSM-PL-25	32.0	15.4	IC	33.4	11.7	IC	1.04	0.76
2	CRD-NSM	23.7	7.2	IC	35.8	14.1	IC	1.51	1.96
5	NSMR 1	166.6	69.0	IC	278.4	180.9	IC	1.67	2.62
5	NSMR 2	164.9	67.3	IC	274.7	177.2	IC	1.67	2.63
6	6-1Fa	21.4	3.5	CC	22.3	5.3	CC	1.04	1.53
6	6-1Fb				20.9	3.9	CC	0.98	1.13
6	6-2Fa	23.7	5.8	CC	22.5	5.5	CC	0.95	0.94
6	6-2Fb				24.2	7.2	CC	1.02	1.25
6	9-1Fa	24.9	5.7	CC	25.4	6.8	CC	1.02	1.21
6	9-1Fb				25.1	6.6	CC	1.01	1.17
6	9-2Fa	28.6	9.4	CC	33.3	14.8	CC	1.16	1.58
6	9-2Fb				32.2	13.7	CC	1.12	1.46
6	12-1Fa	26.1	6.3	IC	26.6	7.6	R	1.02	1.20
6	12-1Fb				27.9	8.9	R	1.07	1.41
6	12-2Fa	32.0	12.2	IC	30.4	11.4	CC	0.95	0.93
6	12-2Fb				37.6	18.5	CC	1.17	1.51
7	NS F1	19.6	N/A	CC	18.7	N/A	S	0.96	N/A
7	NS F2	13.8	N/A	CC	14.6	N/A	CC	1.06	N/A
7	NS F3	10.8	N/A	IC	14.0	N/A	CC	1.30	N/A
7	NS F4	11.6	N/A	IC	12.8	N/A	IC	1.11	N/A
7	NB F2	31.8	N/A	IC	49.6	N/A	IC	1.56	N/A
7	NB F3	34.7	N/A	IC	54.0	N/A	IC	1.55	N/A
8	B2900	31.9	10.4	IC	44.1	22.6	CC	1.38	2.18
9	G4D24c	6.3	N/A	IC	11.0	N/A	P	1.76	N/A
9	C3D24b	6.5	N/A	IC	7.8	N/A	P	1.21	N/A
9	C3S24a	8.0	N/A	IC	4.0	N/A	P	0.50	N/A
10	fcm35 Lb80	3.3	N/A	IC	2.1	N/A	P	0.63	N/A
10	fcm45 Lb80	3.5	N/A	IC	2.4	N/A	P	0.69	N/A
10	fcm70 Lb80	4.0	N/A	IC	2.4	N/A	P	0.58	N/A
11	Lb120 M	2.8	N/A	IC	1.5	N/A	P	0.54	N/A

Notes: CC- crushing of the concrete (preceded by steel yielding)  
 IC- intermediate crack debonding  
 P- pullout of the FRP  
 R- rupture of the FRP  
 S- shear failure in the concrete

The failure mode was correctly predicted in two of the three specimens in test series 2. For specimen NSM-PL-15, the model predicted a capacity of 25.2 kip-ft and a failure mode of IC debonding. The experimental specimen failed due to FRP rupture at a capacity of 30.3 kip-ft, which was 20% higher than the predicted capacity. The change in moment for this specimen was perfectly predicted to be 8.6 kip-ft. For specimen NSM-PL-25, the predicted capacity was 32.0 kip-ft, and the experimental capacity was 33.4 kip-ft, which is only 4% higher than the prediction. The experimental change in moment capacity, however, was 76% of the predicted change in moment capacity. For specimen CRD-NSM, the predicted capacity was 51% greater than the experimental capacity, and the predicted change in capacity was nearly half as large as the experimental change in capacity.

For test series 5, the model was very conservative in its estimation of capacity. The experimental capacity was 67% of the predicted capacity for both specimens. The experimental changes in capacity were more than 1.5 times larger than the predicted changes in capacity.

In test series 6, the failure mode was correctly predicted as crushing of the concrete for the 6-inch and the 9-inch wide specimens. For the 12-inch wide specimens, the failure mode was predicted as IC debonding, but the specimens failed due to FRP rupture and due to crushing of the concrete. The model was relatively accurate for all of the specimens. The experimental capacities ranged from 95 to 117% of the predicted capacities. The changes in capacity, however, were not as accurate. The experimental changes in capacity ranged from 93 to 158% of the predicted changes in capacity, with most of the experimental values being greater than the predictions.

For the slab specimens in test series 7, the model was relatively accurate at predicting strengthened moment capacities. The capacity for slab specimen NS\_F1 was slightly overestimated. The capacities for the other three slab specimens were underestimated. The experimental capacities for these three specimens were 6, 30, and 11% higher, respectively, than the corresponding predicted capacities. The failure mode was only correctly predicted for two of the four slab specimens.

For the beam specimens in test series 7, the failure mode was correctly predicted as IC debonding; however, the experimental capacities were 56 and 55% greater, respectively, than the predicted capacities.

The capacity and failure mode for specimen B2900 in test series 8 were not accurately predicted. The experimental capacity was 38% greater than the predicted capacity, and the experimental change in capacity was more than two times the predicted change in capacity. The predicted failure mode was IC debonding, but the beam failed due to crushing of the concrete.

In test series 9, 10, and 11, the failure mode was pullout of the FRP. The predicted failure mode for all of these specimens was IC debonding. Consequently, the capacity predictions were not very accurate. These specimens are not shown in the following comparison graphs.

Figure 4-27 shows a comparison between the experimental moment capacity and the predicted moment capacity. Figure 4-28 shows a comparison between the experimental change in capacity and the predicted change in capacity.

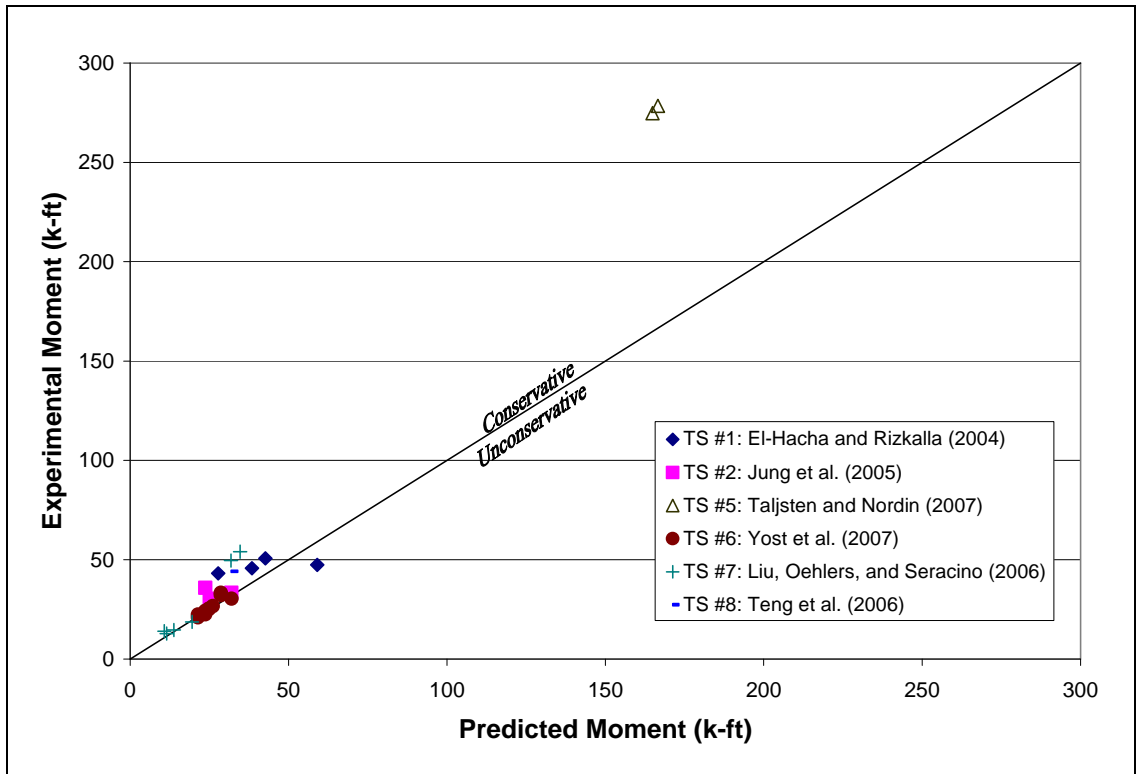


**Figure 4-27:** Comparison between NSM Test Results and Standards Australia (2008) IC-  
 Debonding Capacity Predictions

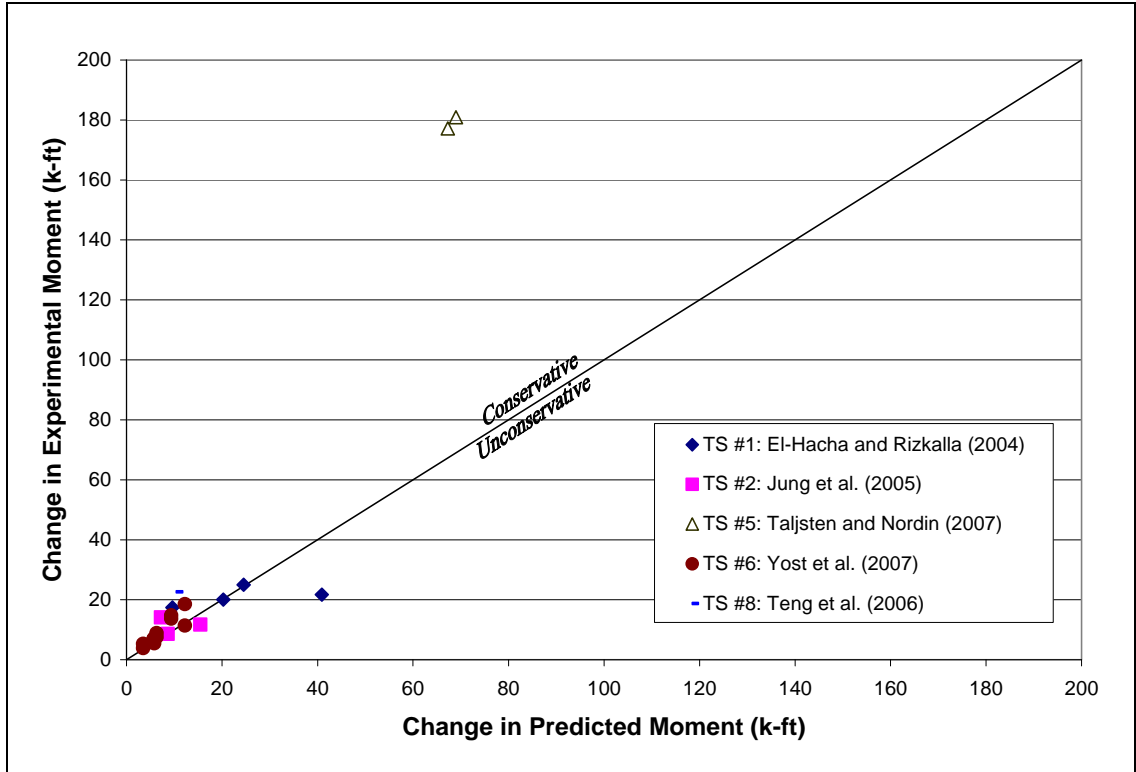


**Figure 4-28:** Comparison between NSM Test Results and Standards Australia (2008) IC-  
 Debonding Change-in-Capacity Predictions

Because the Taljsten and Nordin (2007) test series includes specimens with relatively high moments, they were excluded from the enlarged graphs shown in Figures 4-29 and 4-30.



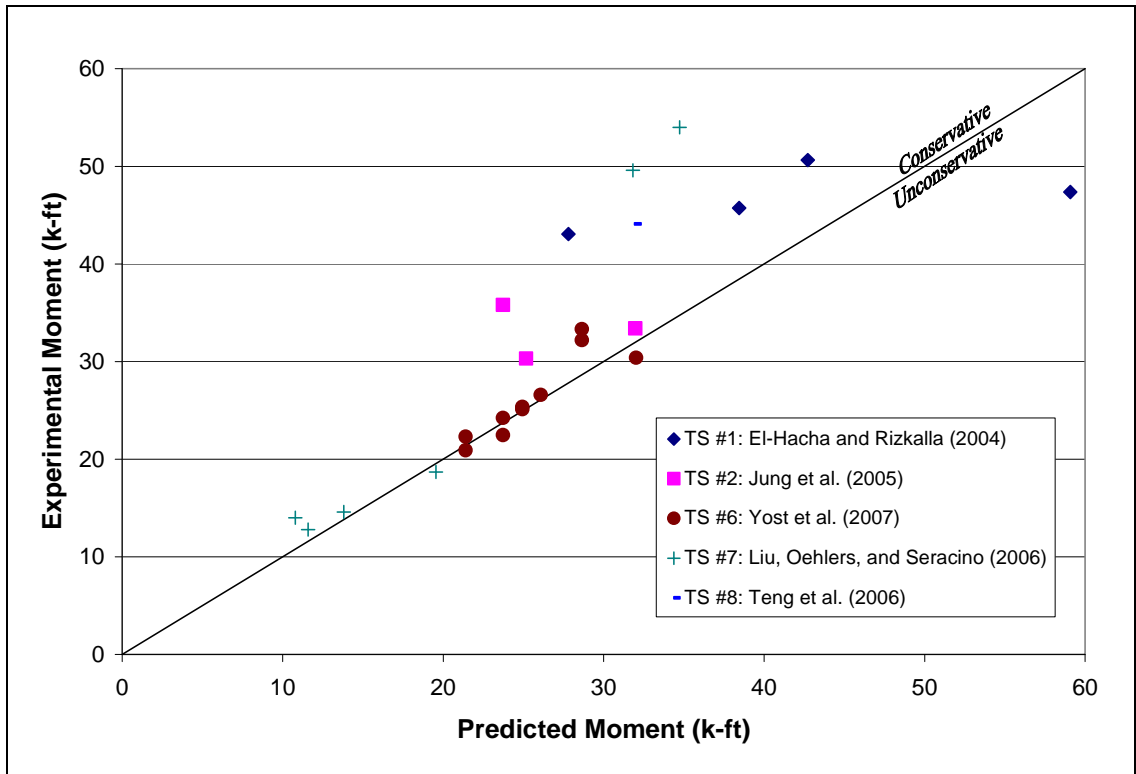


**Figure 4-29:** Enlarged Graph of the Capacity Comparisons of the Standards Australia (2008) Model

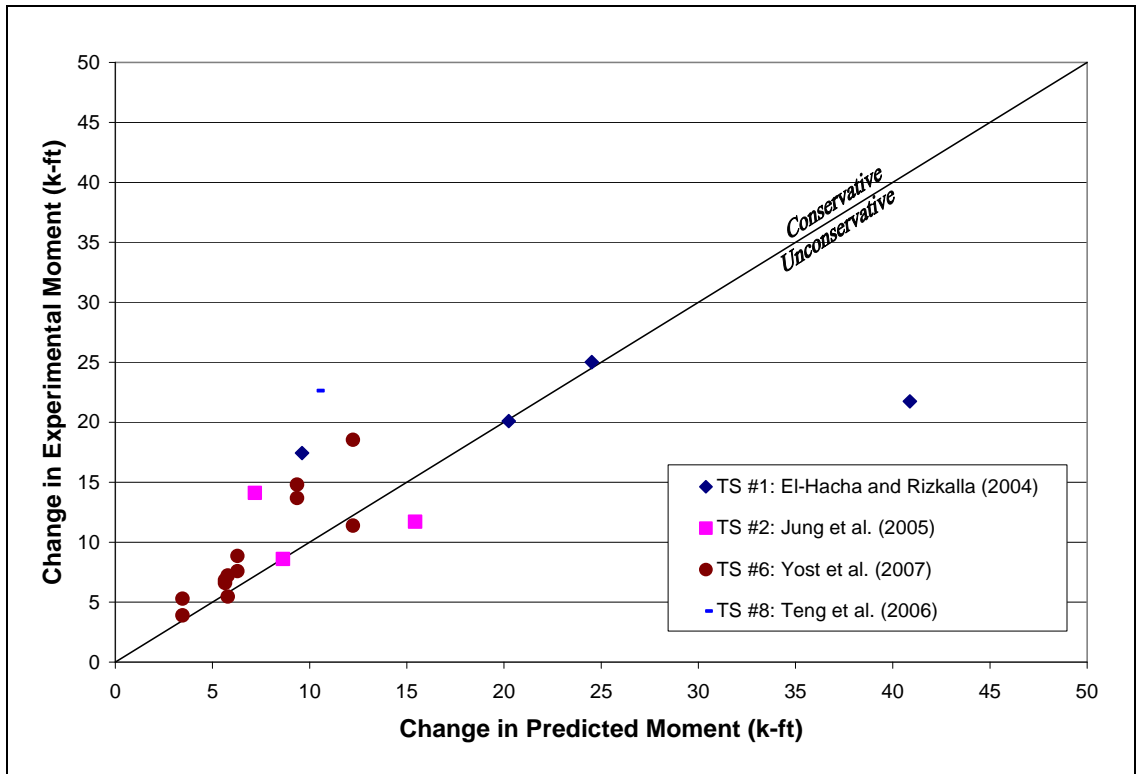


**Figure 4-30:** Enlarged Graph of the Change-in-Capacity Comparisons of the Standards Australia (2008) Model

Figures 4-29 and 4-30 show that the model was relatively accurate for most of the specimens in test series 6 and 7; however, for test series 1, 2, and 8, the model was not as accurate or as precise.

Table 4-25 shows the measured and predicted strain values for the FRP.

**Table 4-25: FRP Strain Predictions using the Standards Australia (2008) IC-Debonding Model and NSM Test Results**

Test Series #	Specimen ID	Predicted		Experimental		$\frac{\epsilon_{f,exp}}{\epsilon_{f,pred}}$
		$\epsilon_{f,pred}$	$\frac{\epsilon_{f,pred}}{\epsilon_{f,rupt}}$	$\epsilon_{f,exp}$	$\frac{\epsilon_{f,exp}}{\epsilon_{f,rupt}}$	
1	B1	0.53%	0.47	0.88%	0.77	1.65
1	B2	*1.08%	*1.00	*1.34%	*1.24	1.24
1	B3	*1.33%	*1.00	*1.38%	*1.04	1.04
1	B4	*2.22%	*1.00	1.35%	0.61	0.61
2	NSM-PL-15	1.24%	0.84	*1.54%	*1.04	1.24
2	NSM-PL-25	1.36%	0.92	1.24%	0.83	0.91
2	CRD-NSM	0.49%	0.32	1.31%	0.84	2.66
5	NSMR 1	0.46%	0.27	0.92%	0.53	1.98
5	NSMR 2	0.46%	0.26	0.92%	0.53	2.02
7	NS F1	*0.82%	*0.51	*0.72%	*0.45	0.88
7	NS F2	*1.33%	*0.83	*1.30%	*0.81	0.98
7	NS F3	1.38%	0.86	*1.50%	*0.93	1.09
7	NS F4	0.92%	0.55	0.84%	0.50	0.91
7	NB F2	1.35%	0.84	1.02%	0.63	0.75
7	NB F3	0.93%	0.56	0.83%	0.50	0.89
8	B2900	1.11%	0.81	*0.97%	*0.71	0.88

\*denotes a failure mode other than IC debonding

As shown in Table 4-25, the FRP strain for specimen B1 was underestimated, the strain for specimen B4 was overestimated, and the strains for specimens B2 and B3 were relatively accurate. These strain values correspond to the pattern already shown in Table 4-24, where the capacity for specimen B1 was underestimated, the capacity for specimen B4 was overestimated, and the capacities for specimens B2 and B3 were relatively accurate.

For specimen NSM-PL-15, the FRP strain was predicted to be 84% of the rupture strain. In the experimental specimen, the failure mode was FRP rupture, but the FRP strain was 4% greater than the rupture strain. For specimen NSM-PL-25, the FRP strain was slightly overestimated, with the ratio of experimental to predicted strain being 0.91. For specimen CRD-NSM, the experimental FRP strain was 166% greater than the predicted strain.

In test series 7 and 8, the predicted FRP strains were relatively accurate for most of the specimens. Most of the experimental strains ranged from 88 to 109% of the predicted strains, except for specimen NB\_F2, which had an experimental strain that was 75% of the predicted strain.

#### **4.4.3.2 Discussion of Model**

The majority of the capacity predictions for the NSM specimens were on the conservative side. Most of the specimens were relatively accurate, but there were some specimens that had very inaccurate predictions, especially in test series 1, 2, 5, and 8.

Because it was based on push-pull tests, this model should give a lower bound for the moment capacity (Standards Australia 2008). For the NSM tests, the model was conservative for most of the tests, but unconservative for some of the tests, which would not be possible if this model were accurate and a true lower bound to the capacity.

#### **4.4.4 Seracino et al. (2007a)**

The model by Seracino et al. (2007a) is an IC-debonding model that was used to evaluate the moment capacities for experimental tests using NSM FRP.

##### **4.4.4.1 Comparison to Previous Testing**

The IC-debonding model by Seracino et al. (2007a) was used to predict strengthened moment capacities for NSM test specimens. Table 4-26 shows the predicted capacities, the experimental results, and comparisons between the two.

**Table 4-26:** Comparison of the IC-Debonding Model by Seracino et al. (2007a) to NSM

## Test Results

Test Series #	Specimen ID	Predicted			Experimental			$M_{exp}/M_{n,pred}$	$\Delta M_{exp}/\Delta M_{n,pred}$
		$M_n$ (k-ft)	$\Delta M_n$ (k-ft)	Failure Mode	$M_{exp}$ (k-ft)	$\Delta M_{exp}$ (k-ft)	Failure Mode		
1	B1	25.6	7.4	IC	43.1	17.4	IC	1.68	2.36
1	B2	38.4	20.2	R	45.7	20.1	R	1.19	0.99
1	B3	42.7	24.5	R	50.6	25.0	R	1.19	1.02
1	B4	59.1	40.9	R	47.4	21.7	IC	0.80	0.53
2	NSM-PL-15	25.6	9.1	IC	30.3	8.6	R	1.18	0.95
2	NSM-PL-25	33.3	16.8	R	33.4	11.7	IC	1.00	0.70
2	CRD-NSM	21.5	5.0	IC	35.8	14.1	IC	1.66	2.84
5	NSMR 1	147.0	49.5	IC	278.4	180.9	IC	1.89	3.66
5	NSMR 2	145.2	47.6	IC	274.7	177.2	IC	1.89	3.72
6	6-1Fa	21.4	3.5	CC	22.3	5.3	CC	1.04	1.53
6	6-1Fb				20.9	3.9	CC	0.98	1.13
6	6-2Fa	23.7	5.8	CC	22.5	5.5	CC	0.95	0.94
6	6-2Fb				24.2	7.2	CC	1.02	1.25
6	9-1Fa	24.9	5.7	CC	25.4	6.8	CC	1.02	1.21
6	9-1Fb				25.1	6.6	CC	1.01	1.17
6	9-2Fa	28.6	9.4	CC	33.3	14.8	CC	1.16	1.58
6	9-2Fb				32.2	13.7	CC	1.12	1.46
6	12-1Fa	26.2	6.4	R	26.6	7.6	R	1.02	1.18
6	12-1Fb				27.9	8.9	R	1.06	1.38
6	12-2Fa	32.2	12.4	R	30.4	11.4	CC	0.94	0.91
6	12-2Fb				37.6	18.5	CC	1.17	1.49
7	NS F1	19.6	N/A	CC	18.7	N/A	S	0.96	N/A
7	NS F2	13.8	N/A	CC	14.6	N/A	CC	1.06	N/A
7	NS F3	11.1	N/A	IC	14.0	N/A	CC	1.27	N/A
7	NS F4	11.7	N/A	IC	12.8	N/A	IC	1.10	N/A
7	NB F2	32.7	N/A	IC	49.6	N/A	IC	1.52	N/A
7	NB F3	35.0	N/A	IC	54.0	N/A	IC	1.54	N/A
8	B2900	32.5	10.4	IC	44.1	22.6	CC	1.36	2.06
9	G4D24c	8.0	N/A	IC	11.0	N/A	P	1.38	N/A
9	C3D24b	5.0	N/A	IC	7.8	N/A	P	1.56	N/A
9	C3S24a	5.0	N/A	IC	4.0	N/A	P	0.80	N/A
10	fcm35 Lb80	3.3	N/A	IC	2.1	N/A	P	0.64	N/A
10	fcm45 Lb80	3.7	N/A	IC	2.4	N/A	P	0.66	N/A
10	fcm70 Lb80	4.5	N/A	IC	2.4	N/A	P	0.53	N/A
11	Lb120 M	2.6	N/A	IC	1.5	N/A	P	0.58	N/A

Notes: CC- crushing of the concrete (preceded by steel yielding)

IC- intermediate crack debonding

P- pullout of the FRP

R- rupture of the FRP

S- shear failure in the concrete

In test series 1, the failure mode was correctly predicted in three of the four specimens. In these three specimens, the capacity was underestimated. For specimen B1, which failed due to IC debonding, the experimental capacity was 68% greater than the predicted capacity. For specimens B2 and B3, which failed due to FRP rupture, the experimental capacities were just 19% greater than the predicted capacities. Specimen B4 failed due to IC debonding but was predicted to fail due to FRP rupture. The experimental capacity was 80% of the predicted capacity.

For specimen B1, the changes in moment capacity were underestimated by more than two times. For specimen B4, it was overestimated by about two times. For specimens B2 and B3, the changes in moment capacity were extremely accurate.

The failure mode was correctly predicted in one of the three specimens in test series 2. For specimen NSM-PL-15, the model predicted a capacity of 25.6 kip-ft and a failure mode of IC debonding. The experimental specimen failed due to FRP rupture at a capacity of 30.3 kip-ft, which was 18% higher than the predicted capacity. The change in moment for this specimen was slightly overestimated as 9.1 kip-ft. The experimental change in moment was actually 8.6 kip-ft. For specimen NSM-PL-25, the model's prediction was extremely accurate. The predicted capacity was 33.3 kip-ft, and the experimental capacity was 33.4 kip-ft. The experimental change in moment capacity, however, was 70% of the predicted change in moment capacity. For specimen CRD-NSM, the predicted capacity was 66% greater than the experimental capacity, and the predicted change in capacity was nearly one third as large as the experimental change in capacity.

For test series 5, the model was very conservative in its estimation of capacity. The experimental capacity was 89% of the predicted capacity for both specimens. The experimental changes in capacity were over 2.5 times larger than the predicted changes in capacity.

In test series 6, the failure mode was correctly predicted as crushing of the concrete for the 6-inch and the 9-inch wide specimens. For specimens 12-1Fa and 12-1Fb, the failure was correctly predicted as FRP rupture. For specimens 12-2Fa and 12-2Fb, the failure mode was predicted as FRP rupture, but the specimens failed due to crushing of the concrete. The model was relatively accurate for all of the specimens in test series 6. The experimental capacities ranged from 94 to 117% of the predicted capacities. The changes in capacity, however, were not as accurate. The experimental changes in capacity ranged from 91 to 158% of the predicted changes in capacity, with most of the experimental values being greater than the predictions.

For the slab specimens in test series 7, the model was relatively accurate at predicting strengthened moment capacities. The capacity for slab specimen NS\_F1 was slightly overestimated. The capacities for the other three slab specimens were underestimated. The experimental capacities for these three specimens were 6, 27, and 10% higher, respectively, than the corresponding predicted capacities. The failure mode was only correctly predicted for two of the four slab specimens.

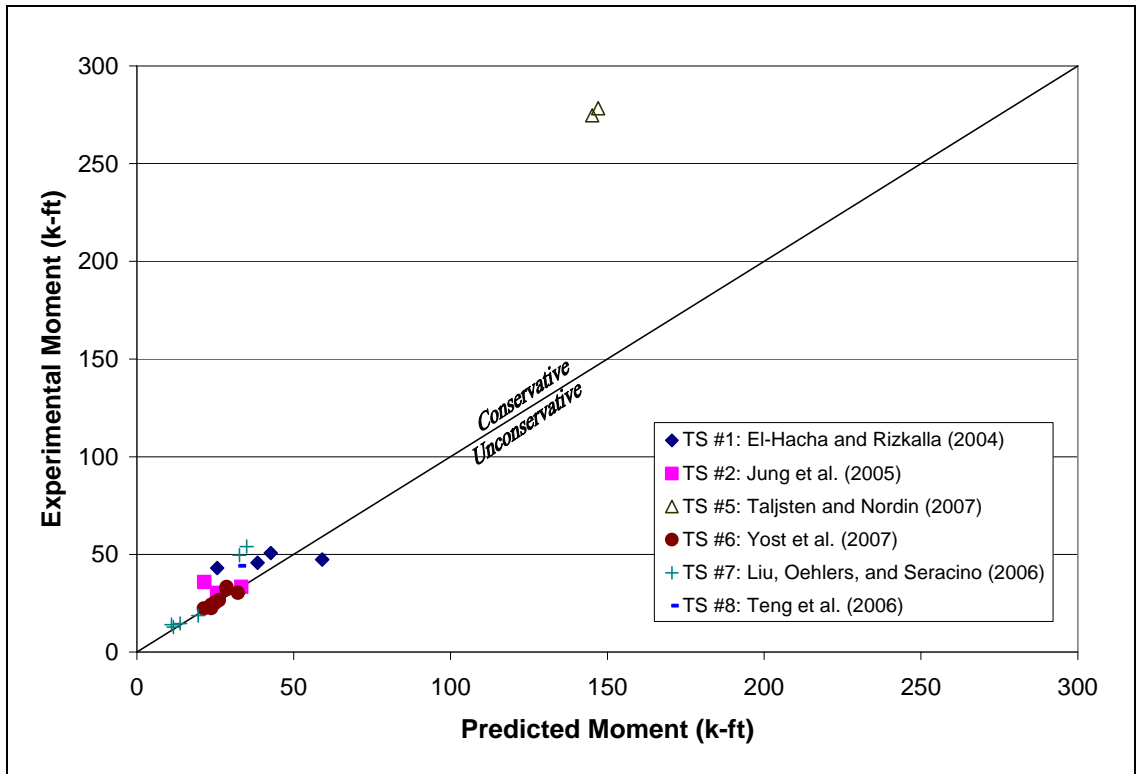
For the beam specimens in test series 7, the failure mode was correctly predicted as IC debonding; however, the experimental capacities were 52 and 54% greater than the predicted capacities, respectively.

The capacity and failure mode for specimen B2900 in test series 8 were not accurately predicted. The experimental capacity was 36% greater than the predicted capacity, and the experimental change in capacity was more than two times the predicted change in capacity. The predicted failure mode was IC debonding, but the beam failed due to crushing of the concrete.

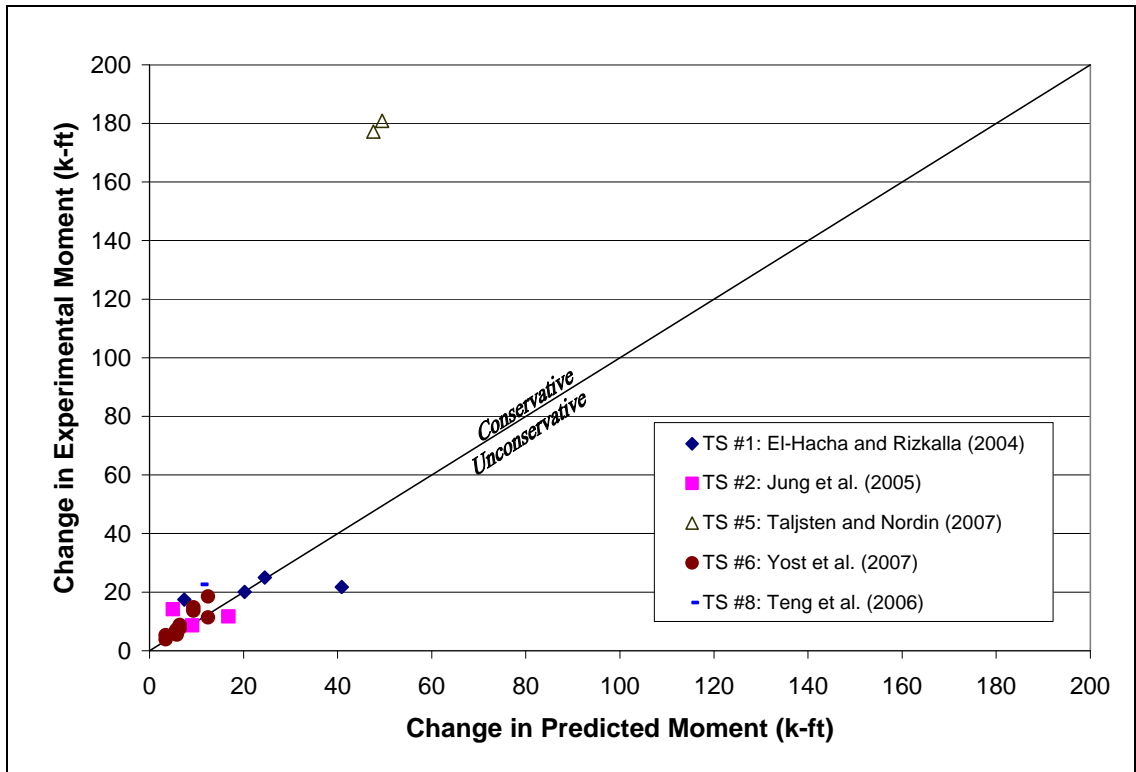
In test series 9, 10, and 11, the failure mode was pullout of the FRP. The predicted failure mode for all of these specimens was IC debonding. Consequently, the capacity predictions were not very accurate and are not shown in the following comparison graphs.

Figure 4-31 shows a comparison between the experimental moment capacity and the predicted moment capacity. Figure 4-32 shows a comparison between the experimental change in capacity and the predicted change in capacity.





**Figure 4-31:** Comparison between NSM Test Results and Seracino et al. (2007a) IC-  
 Debonding Capacity Predictions



**Figure 4-32:** Comparison between NSM Test Results and Seracino et al. (2007a) IC-  
 Debonding Change-in-Capacity Predictions

Because the Taljsten and Nordin (2007) test series includes specimens with relatively high moments, they were excluded from the enlarged graphs shown in Figures 4-33 and 4-34.

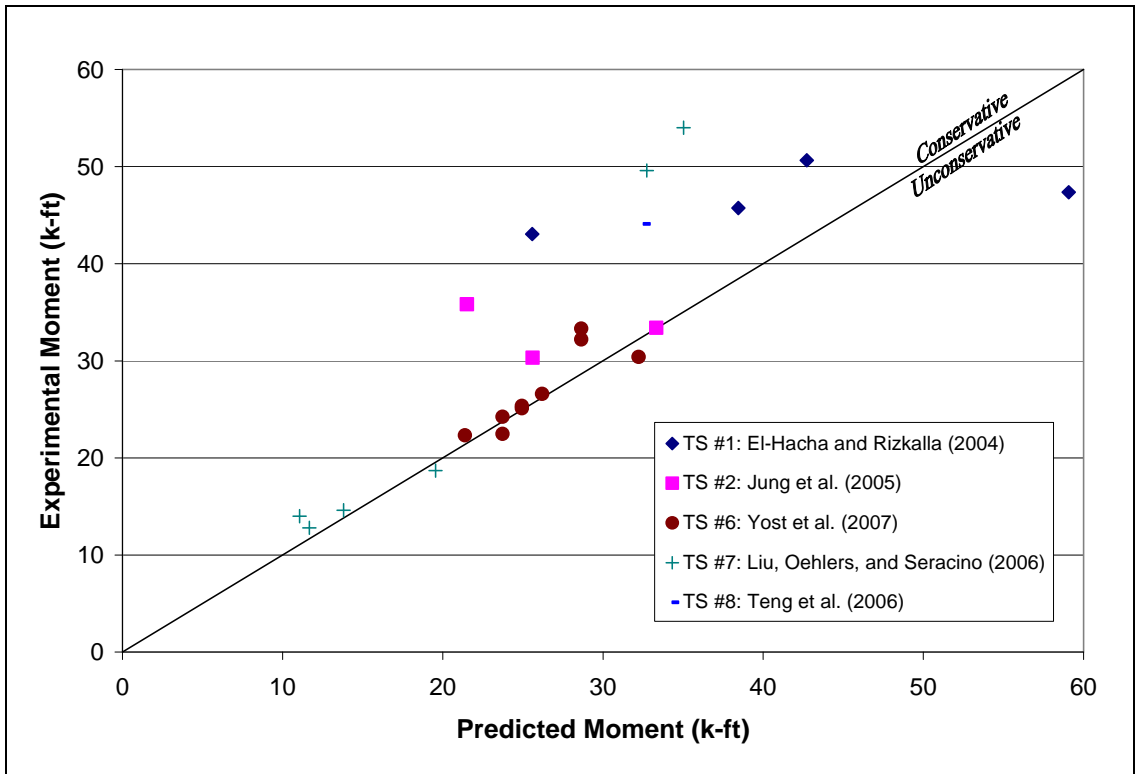


**Figure 4-33:** Enlarged Graph of the Capacity Comparisons of the Seracino et al. (2007a) Model

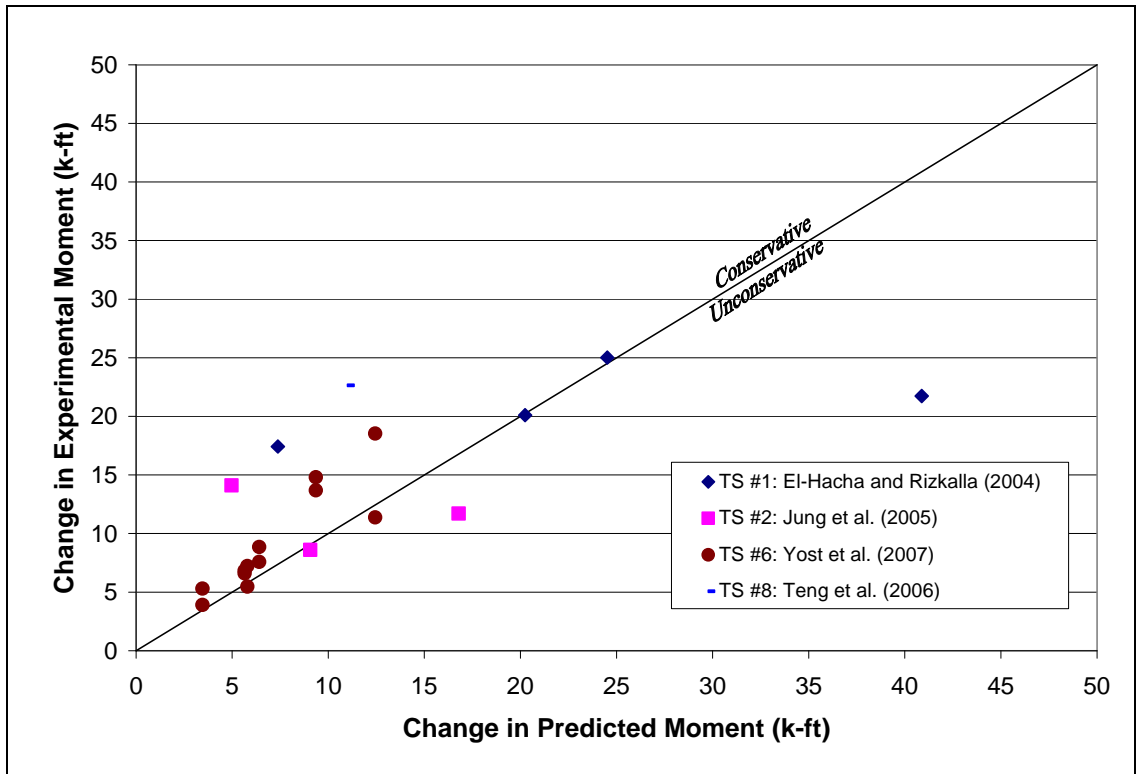


**Figure 4-34:** Enlarged Graph of the Change-in-Capacity Comparisons of the Seracino et al. (2007a) Model

Figures 4-33 and 4-34 show that the model was relatively accurate for most of the specimens in test series 6 and 7; however, for test series 1, 2, and 8, the model was not as accurate or as precise.

Table 4-27 shows the measured and predicted strain values for the FRP.

**Table 4-27:** FRP Strain Predictions using the Seracino et al. (2007a) IC-Debonding Model and NSM Test Results

Test Series #	Specimen ID	Predicted		Experimental		$\frac{\epsilon_{f,exp}}{\epsilon_{f,pred}}$
		$\epsilon_{f,pred}$	$\frac{\epsilon_{f,pred}}{\epsilon_{f,rupt}}$	$\epsilon_{f,exp}$	$\frac{\epsilon_{f,exp}}{\epsilon_{f,rupt}}$	
1	B1	0.42%	0.36	0.88%	0.77	2.12
1	B2	*1.08%	*1.00	*1.34%	*1.24	1.24
1	B3	*1.33%	*1.00	*1.38%	*1.04	1.04
1	B4	*2.22%	*1.00	1.35%	0.61	0.61
2	NSM-PL-15	1.31%	0.88	*1.54%	*1.04	1.18
2	NSM-PL-25	*1.48%	*1.00	1.24%	0.83	0.83
2	CRD-NSM	0.36%	0.23	1.31%	0.84	3.64
5	NSMR 1	0.34%	0.20	0.92%	0.53	2.68
5	NSMR 2	0.33%	0.19	0.92%	0.53	2.76
7	NS F1	*0.82%	*0.51	*0.72%	*0.45	0.88
7	NS F2	*1.33%	*0.83	*1.30%	*0.81	0.98
7	NS F3	1.49%	0.93	*1.50%	*0.93	1.01
7	NS F4	0.94%	0.56	0.84%	0.50	0.90
7	NB F2	1.45%	0.90	1.02%	0.63	0.70
7	NB F3	0.95%	0.57	0.83%	0.50	0.87
8	B2900	1.17%	0.86	*0.97%	*0.71	0.83

\*denotes a failure mode other than IC debonding

As shown in Table 4-27, the FRP strain for specimen B1 was underestimated, the strain for specimen B4 was overestimated, and the strains for specimens B2 and B3 were relatively accurate. These strain values correspond to the pattern already shown in Table 4-26, where the capacity for specimen B1 was underestimated, the capacity for specimen B4 was overestimated, and the capacities for specimens B2 and B3 were relatively accurate.

For specimen NSM-PL-15, the FRP strain was predicted to be 88% of the rupture strain. In the experimental specimen, the failure mode was FRP rupture, but the FRP strain was 4% greater than the rupture strain. For specimen NSM-PL-25, the FRP strain was slightly overestimated, with the ratio of experimental to predicted strain being 0.83. For specimen CRD-NSM, the experimental FRP strain was more than 2.5 times larger than the predicted strain.

In test series 7 and 8, the predicted FRP strains were relatively accurate for most of the specimens. Most of the experimental strains ranged from 83 to 101% of the predicted strains, except for specimen NB\_F2, which had an experimental strain that was 70% of the predicted strain.

#### **4.4.4.2 Discussion of Model**

The model given by Seracino et al. was compared to experimental tests of NSM FRP. The majority of the capacity predictions for the specimens were on the conservative side, but some of the data points were on the unconservative side. Because this model was based on push-pull tests, the model should theoretically give a lower bound to the capacity (Standards Australia 2008); however, the model should not be used as a lower bound because of the unconservative predictions. Most of the specimens were relatively accurate, but there were some specimens that had very inaccurate predictions, especially in test series 1, 2, 5, and 8.

The Seracino et al. model and the Standards Australia model produced very similar results for many reasons. First, the Standards Australia model was based on the model by Seracino, Raizal Saifulnaz, and Oehlers (2007), and both of the referenced papers were co-authored by two of the same people— Seracino and Oehlers. Secondly, both models are based on push-pull tests. Finally, both models are statistical models that are based solely on the dimensions of the FRP and the compressive strength of the concrete.

#### **4.4.5 Said and Wu (2008)**

The model by Said and Wu (2008) is an IC-debonding model that was calibrated using a database of IC-debonding failures of EB FRP. Because the model is empirical, however, and is not derived for an EB type of application, the model was also used to evaluate capacities for experimental tests using NSM FRP. In this section, the model was compared to NSM test results to determine the accuracy of the model.

##### **4.4.5.1 Comparison to Previous Testing**

The IC-debonding model by Said and Wu was used to predict strengthened moment capacities for NSM test specimens. Table 4-28 shows the predicted capacities, the experimental results, and comparisons between the two.

In test series 1, the failure mode was correctly predicted for two of the four specimens; however, the strengthened moment capacity was underestimated for all four specimens. The experimental capacities ranged from 36 to 72% greater than the predicted capacities. The predictions for the changes in capacity were even more conservative. The experimental changes in capacity ranged from 30 to 155% greater than the predicted changes in capacity.

**Table 4-28:** Comparison of the IC-Debonding Model by Said and Wu (2008) to NSM

## Test Results

Test Series #	Specimen ID	Predicted			Experimental			$M_{exp}/M_{n,pred}$	$\Delta M_{exp}/\Delta M_{n,pred}$
		$M_n$ (k-ft)	$\Delta M_n$ (k-ft)	Failure Mode	$M_{exp}$ (k-ft)	$\Delta M_{exp}$ (k-ft)	Failure Mode		
1	B1	25.0	6.8	IC	43.1	17.4	IC	1.72	2.55
1	B2	29.5	11.3	IC	45.7	20.1	R	1.55	1.78
1	B3	31.4	13.2	IC	50.6	25.0	R	1.61	1.90
1	B4	34.9	16.7	IC	47.4	21.7	IC	1.36	1.30
2	NSM-PL-15	23.1	6.6	IC	30.3	8.6	R	1.31	1.31
2	NSM-PL-25	23.1	6.6	IC	33.4	11.7	IC	1.45	1.78
2	CRD-NSM	19.1	2.5	IC	35.8	14.1	IC	1.88	5.59
5	NSMR 1	148.3	50.8	IC	278.4	180.9	IC	1.88	3.56
5	NSMR 2	147.4	49.8	IC	274.7	177.2	IC	1.86	3.56
6	6-1Fa	20.9	3.0	IC	22.3	5.3	CC	1.07	1.78
6	6-1Fb				20.9	3.9	CC	1.00	1.31
6	6-2Fa	23.5	5.6	IC	22.5	5.5	CC	0.96	0.98
6	6-2Fb				24.2	7.2	CC	1.03	1.29
6	9-1Fa	22.2	2.9	IC	25.4	6.8	CC	1.14	2.34
6	9-1Fb				25.1	6.6	CC	1.13	2.25
6	9-2Fa	25.2	5.9	IC	33.3	14.8	CC	1.32	2.51
6	9-2Fb				32.2	13.7	CC	1.28	2.32
6	12-1Fa	22.6	2.9	IC	26.6	7.6	R	1.17	2.65
6	12-1Fb				27.9	8.9	R	1.23	3.10
6	12-2Fa	25.7	5.9	IC	30.4	11.4	CC	1.18	1.92
6	12-2Fb				37.6	18.5	CC	1.46	3.12
7	NS F1	17.1	N/A	IC	18.7	N/A	S	1.09	N/A
7	NS F2	10.4	N/A	IC	14.6	N/A	CC	1.40	N/A
7	NS F3	8.8	N/A	IC	14.0	N/A	CC	1.59	N/A
7	NS F4	9.5	N/A	IC	12.8	N/A	IC	1.34	N/A
7	NB F2	24.3	N/A	IC	49.6	N/A	IC	2.04	N/A
7	NB F3	27.0	N/A	IC	54.0	N/A	IC	2.00	N/A
8	B2900	26.5	10.4	IC	44.1	22.6	CC	1.67	4.57
9	G4D24c	4.4	N/A	IC	11.0	N/A	P	2.53	N/A
9	C3D24b	4.9	N/A	IC	7.8	N/A	P	1.60	N/A
9	C3S24a	6.5	N/A	IC	4.0	N/A	P	0.61	N/A
10	fcm35 Lb80	1.7	N/A	IC	2.1	N/A	P	1.25	N/A
10	fcm45 Lb80	1.7	N/A	IC	2.4	N/A	P	1.40	N/A
10	fcm70 Lb80	1.9	N/A	IC	2.4	N/A	P	1.25	N/A
11	Lb120 M	1.5	N/A	IC	1.5	N/A	P	1.03	N/A

Notes: CC- crushing of the concrete (preceded by steel yielding)

IC- intermediate crack debonding

P- pullout of the FRP

R- rupture of the FRP

S- shear failure in the concrete



The Said and Wu model was very conservative in its predictions of capacity in test series 2. Despite correctly predicting the failure mode in two of the three specimens, the experimental capacities ranged from 31 to 88% greater than the predicted capacities. For the changes in capacity predictions for specimens NSM-PL-15 and NSM-PL-25, the model was conservative. The experimental changes in capacity were 31 and 78% greater than the predicted changes in capacity. For specimen CRD-NSM, the model was extremely conservative; it predicted a change in capacity of 2.5 kip-ft, and the experimental change in capacity was 14.1 kip-ft, which is more than 5.5 times the prediction.

For the two specimens in test series 5, the model was very conservative in its estimations of capacity. The experimental capacities were 88 and 86% of the predicted capacities, respectively. The experimental changes in capacity were over 2.5 times larger than the predicted changes in capacity.

In test series 6, the model predicted an IC-debonding failure for all of the specimens, but none of the specimens failed due to an anchorage failure. Consequently, the model underestimated the capacity and the change in capacity for most of the specimens. For the 6-inch specimens, the model was relatively accurate. The experimental capacities ranged from 96 to 107% of the predicted capacities, and the experimental changes in capacity ranged from 98 to 178% of the predicted changes in capacity.

The predictions for the 9-inch and 12-inch specimens were more conservative than the predictions for the 6-inch specimens. The experimental capacities ranged from 13 to 46% greater than the predicted capacities. The changes in capacity were much more

conservative, with the experimental changes in capacity ranging from 92 to 212% greater than the predicted changes in capacity.

For the slab specimens in test series 7, denoted NS, the model was conservative at predicting strengthened moment capacities. The experimental capacities for these four specimens were 9, 40, 59, and 34% higher, respectively, than the corresponding predicted capacities. The failure mode was only correctly predicted for one of the four slab specimens.

For the two beam specimens in test series 7, denoted NB, the failure mode was correctly predicted as IC debonding; however, the experimental capacities were about twice as large as the predicted capacities.

The capacity and failure mode for specimen B2900 in test series 8 were not accurately predicted. The experimental capacity was 67% greater than the predicted capacity, and the experimental change in capacity was more than three times greater than the predicted change in capacity. The predicted failure mode was IC debonding, but the beam failed due to crushing of the concrete.

In test series 9, 10, and 11, the failure mode was pullout of the FRP. The predicted failure mode for all of these specimens was IC debonding. Consequently, the capacity predictions were not very accurate and are not shown in the following comparison graphs.

Figure 4-35 shows a comparison between the experimental moment capacity and the predicted moment capacity. Figure 4-36 shows a comparison between the experimental change in capacity and the predicted change in capacity.

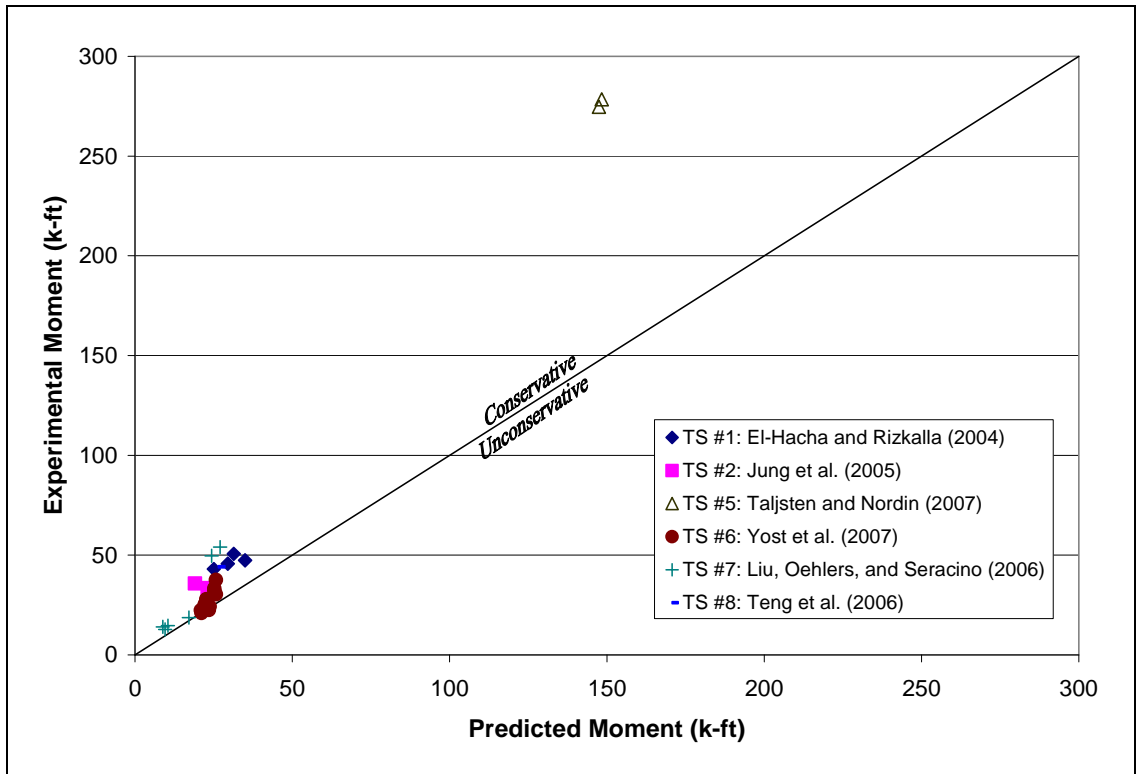


**Figure 4-35:** Comparison between NSM Test Results and Said and Wu (2008) IC-  
 Debonding Capacity Predictions

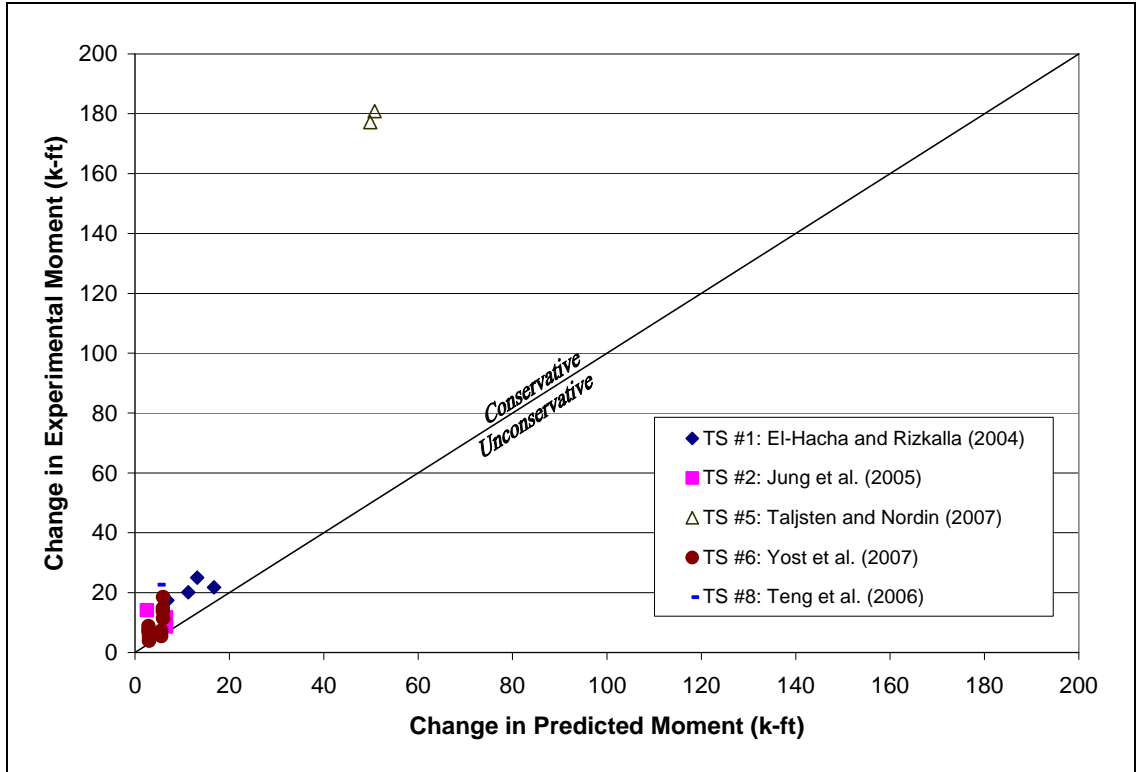


**Figure 4-36:** Comparison between NSM Test Results and Said and Wu (2008) IC-  
 Debonding Change-in-Capacity Predictions

Because the Taljsten and Nordin (2007) test series includes specimens with relatively high moments, they were excluded from the enlarged graphs shown in Figures 4-37 and 4-38.

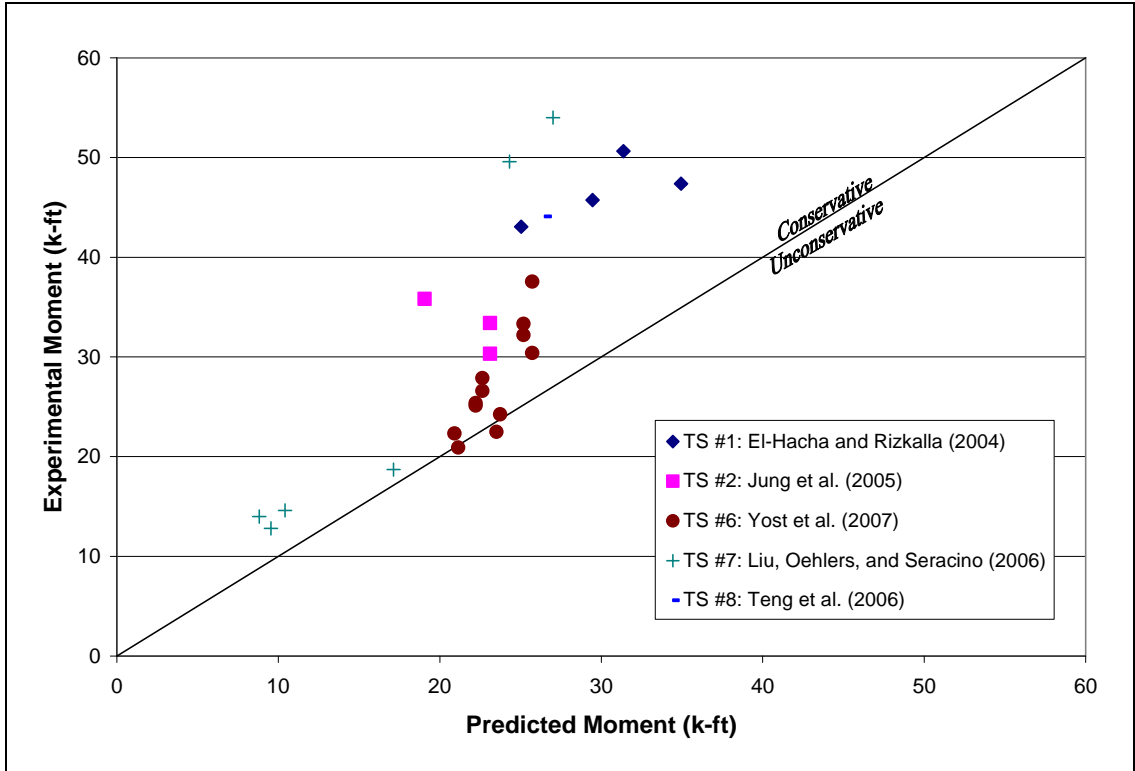


**Figure 4-37:** Enlarged Graph of the Capacity Comparisons of the Said and Wu (2008)

Model

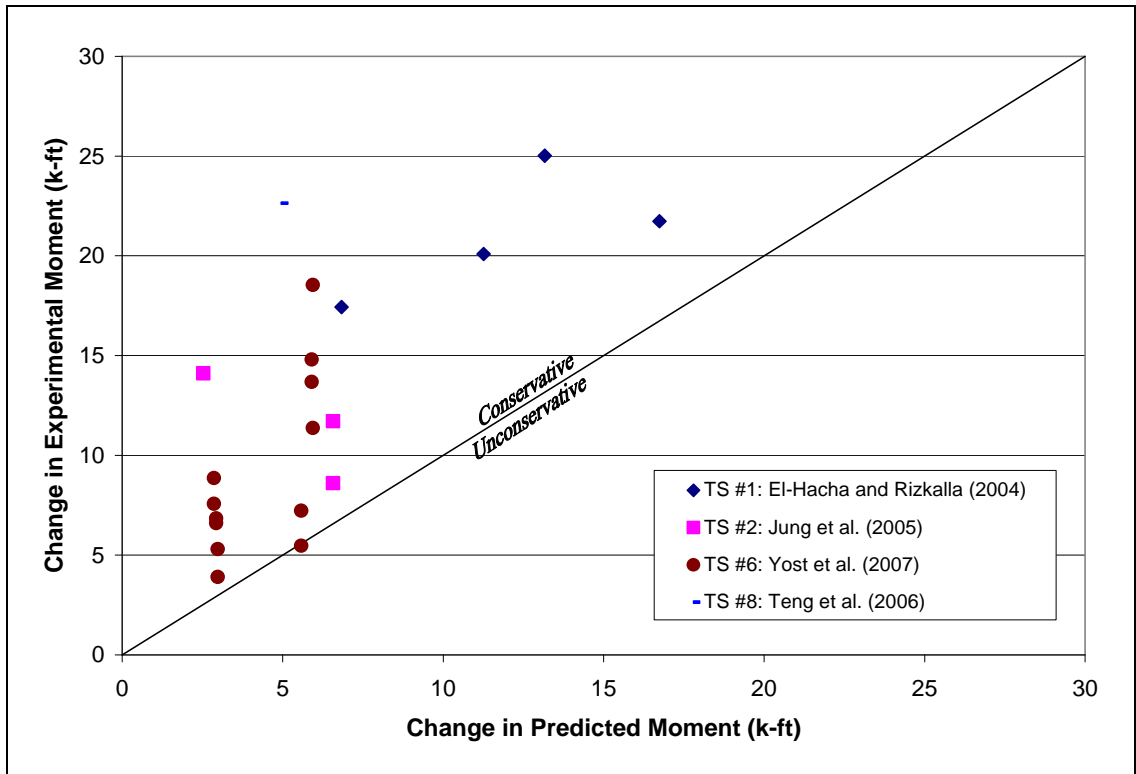


**Figure 4-38:** Enlarged Graph of the Change-in-Capacity Comparisons of the Said and Wu (2008) Model

Figure 4-37 shows that the model was conservative for capacity predictions for test series 6 and 7 and extremely conservative for test series 1, 2, and 8. Most of the data points in Figure 4-38 are well above and to the left of the line shown; therefore, the model is conservative for most of the test specimens for change-in-capacity predictions.

Table 4-29 shows the measured and predicted strain values for the FRP.

**Table 4-29: FRP Strain Predictions using the Said and Wu (2008) IC-Debonding Model and NSM Test Results**

Test Series #	Specimen ID	Predicted		Experimental		$\frac{\epsilon_{f,exp}}{\epsilon_{f,pred}}$
		$\epsilon_{f,pred}$	$\frac{\epsilon_{f,pred}}{\epsilon_{f,rupt}}$	$\epsilon_{f,exp}$	$\frac{\epsilon_{f,exp}}{\epsilon_{f,rupt}}$	
1	B1	0.39%	0.34	0.88%	0.77	2.28
1	B2	0.61%	0.56	*1.34%	*1.24	2.20
1	B3	0.71%	0.54	*1.38%	*1.04	1.93
1	B4	0.91%	0.41	1.35%	0.61	1.49
2	NSM-PL-15	0.61%	0.41	*1.54%	*1.04	2.54
2	NSM-PL-25	0.61%	0.41	1.24%	0.83	2.03
2	CRD-NSM	0.37%	0.24	1.31%	0.84	3.55
5	NSMR 1	0.35%	0.20	0.92%	0.53	2.62
5	NSMR 2	0.35%	0.20	0.92%	0.53	2.65
7	NS F1	0.65%	0.40	*0.72%	*0.45	1.11
7	NS F2	0.64%	0.40	*1.30%	*0.81	2.02
7	NS F3	0.64%	0.40	*1.50%	*0.93	2.34
7	NS F4	0.51%	0.31	0.84%	0.50	1.64
7	NB F2	0.64%	0.40	1.02%	0.63	1.60
7	NB F3	0.52%	0.31	0.83%	0.50	1.60
8	B2900	0.57%	0.41	*0.97%	*0.71	1.71

\*denotes a failure mode other than IC debonding

As shown in Table 4-29, the FRP strains for test series 1 were all underestimated. The ratios of experimental strain to predicted strain range from 1.49 to 2.28.

For specimen NSM-PL-15, the FRP strain was predicted to be 41% of the rupture strain. In the experimental specimen, the failure mode was FRP rupture, but the FRP strain was 4% greater than the rupture strain. For specimen NSM-PL-25, the FRP strain was predicted to be about half of the experimental strain. For specimen CRD-NSM, the experimental FRP strain was 255% greater than the predicted strain.

The predicted FRP strains for test series 7 and 8 were also very conservative. For specimen NS\_F1, the ratio of experimental FRP strain to predicted FRP strain was 1.11. For the other specimens in test series 7 and 8, the ratios ranged from 1.60 to 2.34.

#### **4.4.5.2 Discussion of Model**

The Said and Wu model was very conservative in its predictions of capacity, change in capacity, and FRP strain for practically all of the NSM specimens. The inaccuracy of the model for NSM FRP was expected. The model by Said and Wu was not intended to be used for NSM, and the results in this chapter verify that.

### **4.5 Summary of Model Evaluations**

In this section, a summary of all of the models analyzed in this chapter is presented. For this discussion, the models are divided into PE-debonding models and IC-debonding models. The IC-debonding models are subdivided into models for EB FRP and models for NSM FRP.

#### **4.5.1 PE-Debonding Models**

There are three PE-debonding models that were analyzed: those recommended by Standards Australia (2008), Hassan and Rizkalla (2003), and Vasquez (2008) Figure 4-39 shows a graph that compares the accuracy and level of safety of the capacity predictions of each model against the experimental tests from the referenced literature. Figure 4-40 shows the same comparison for the experimental change in capacity versus the predicted change in capacity.



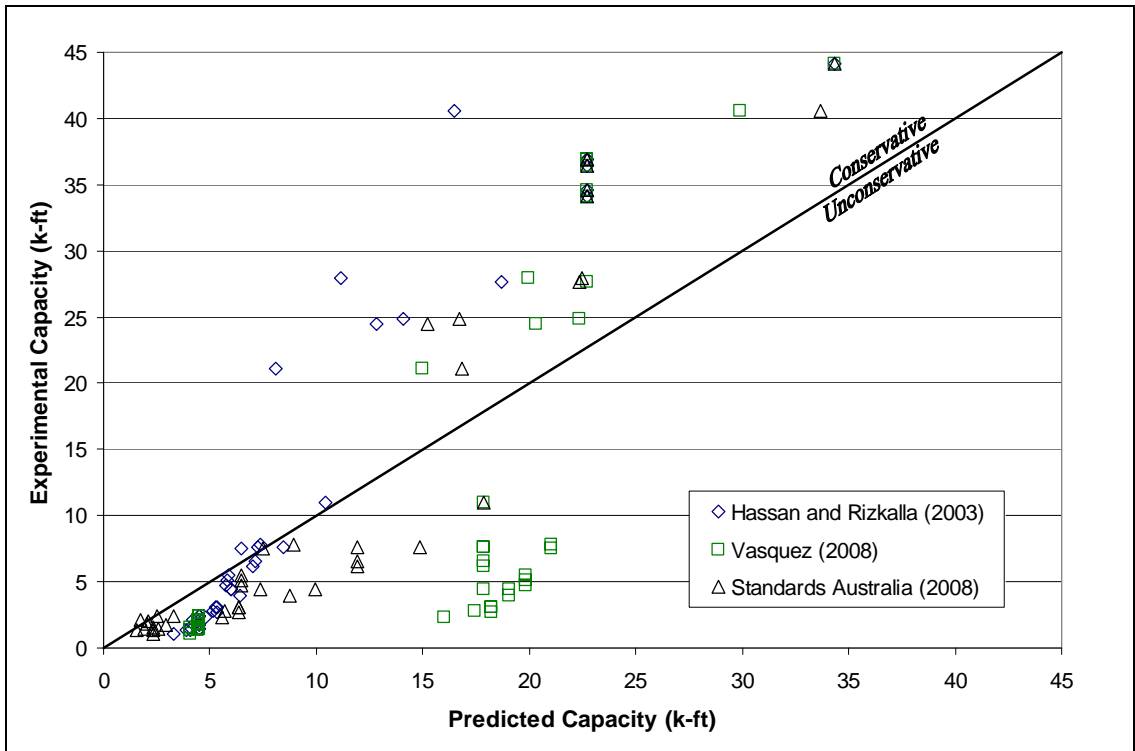


**Figure 4-39:** Comparison of Capacity Predictions by PE-Debonding Models to NSM Experimental Results

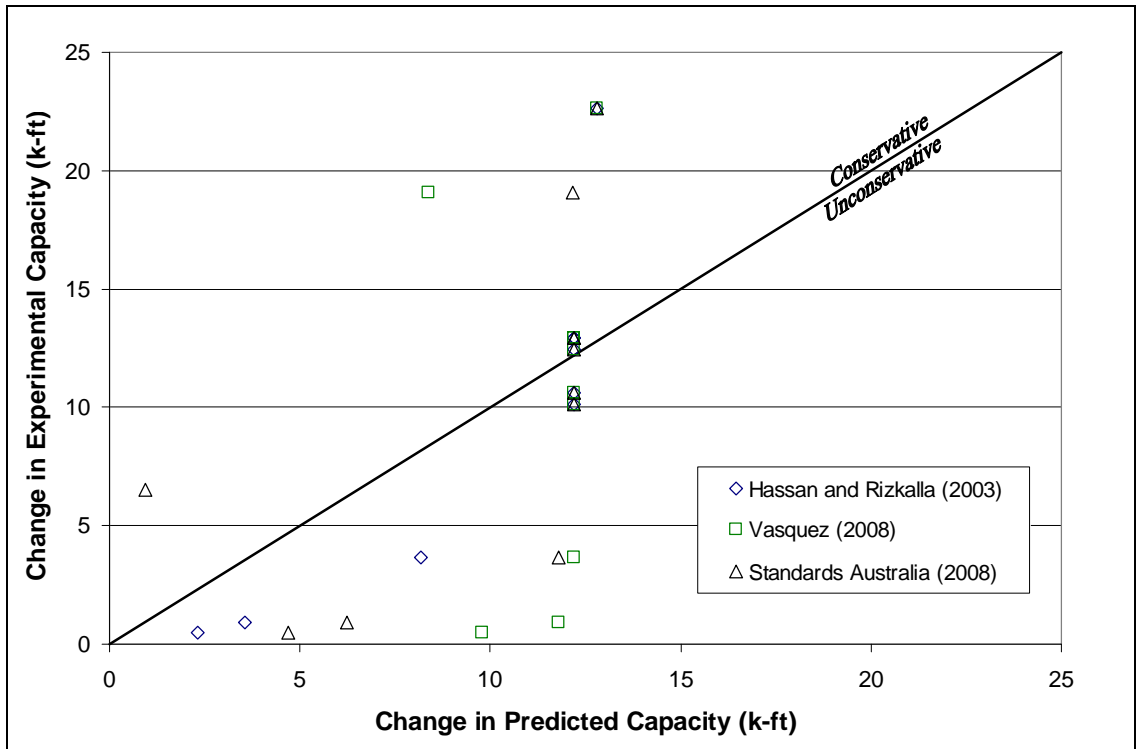


**Figure 4-40:** Comparison of Change-in-Capacity Predictions by PE-Debonding Models to NSM Experimental Results

As shown in Figures 4-39 and 4-40, none of the models accurately predicts the strengthened moment capacity for all of the experimental tests. There is a wide dispersion of data points on the graphs, with some points on the conservative side of the line and some on the unconservative side.

#### 4.5.2 IC-Debonding Models

There are six IC-debonding models for EB FRP that were analyzed: ACI 440 (2008), *fib* 9.3 (2001), Standards Australia (2008), Rosenboom (2006), Seracino, Raizal Saifulnaz, and Oehlers (2007), and Said and Wu (2008). Figure 4-41 shows a graph that compares the accuracy and level of safety of the capacity predictions of each model against the

experimental tests from the referenced literature. Figure 4-42 shows the same comparison for the experimental change in capacity versus the predicted change in capacity.

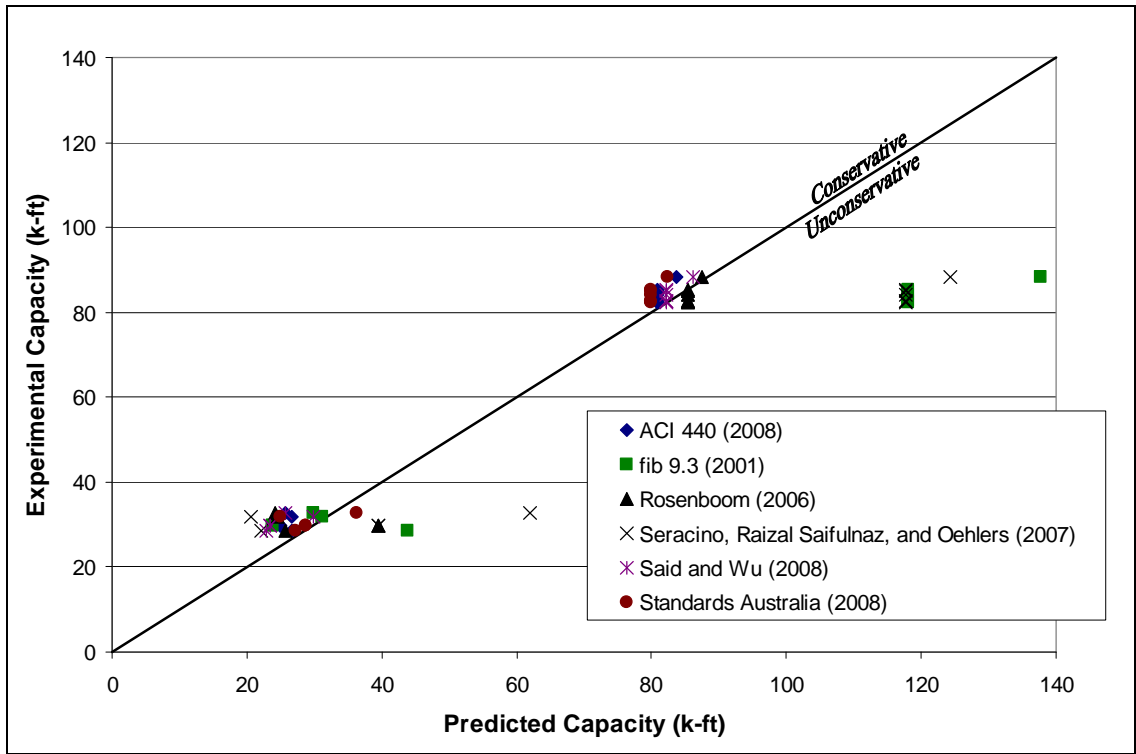


**Figure 4-41:** Comparison of Capacity Predictions by IC-Debonding Models to EB Experimental Results

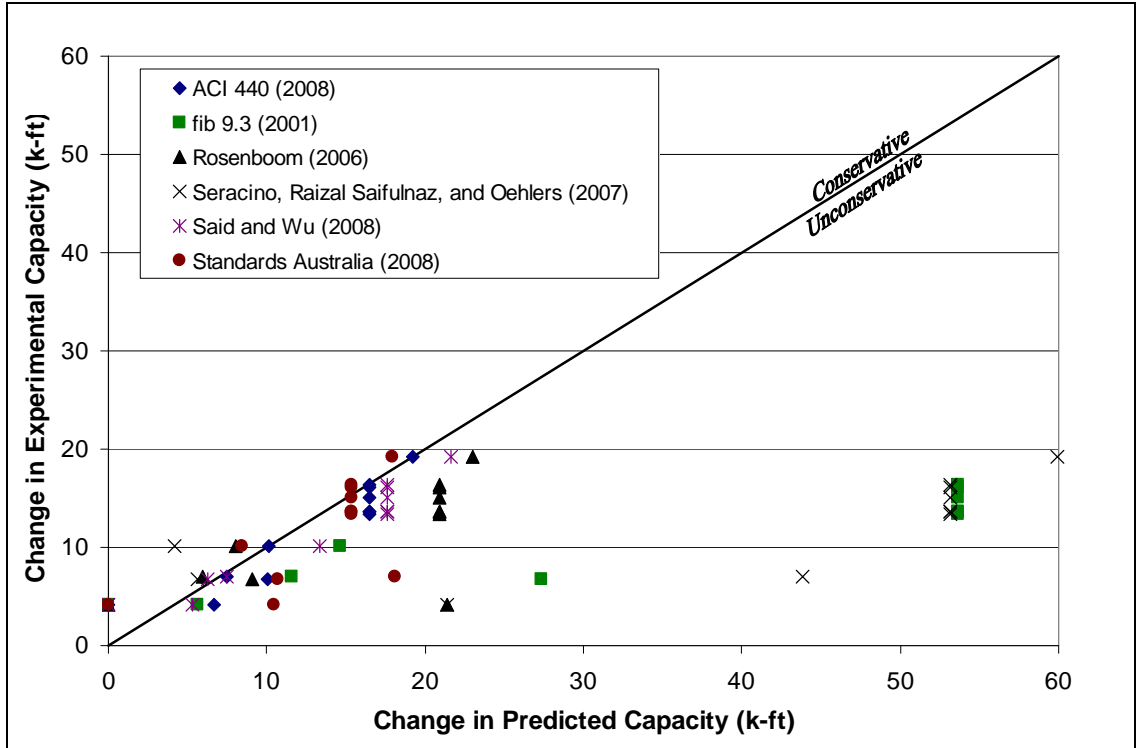


**Figure 4-42:** Comparison of Change-in-Capacity Predictions by IC-Debonding Models to EB Experimental Results

From Figures 4-41 and 4-42, the *fib* 9.3 (2001) model is shown to be mainly unconservative and not very accurate. The *fib* model did not include variables for the concrete compressive strength, the FRP modulus of elasticity, or the thickness of the FRP. A possible reason why this model was not very accurate could be due to the absence of these variables in the model. The model by Seracino, Raizal Saifulnaz, and Oehlers (2007) also had mostly unconservative results, but it included the previously mentioned variables; no conclusions could be made why this model did not perform well. The other four models were relatively accurate at predicting the strengthened moment

capacities for the experimental tests but slightly unconservative at predicting changes in capacity.

For the models related to NSM FRP, there are five IC-debonding models that were examined: ACI 440 (2008), *fib* 9.3 (2001), Standards Australia (2008), Seracino et al. (2007a), and Said and Wu (2008). Figure 4-43 shows a graph that compares the accuracy and level of safety of the capacity predictions of each model against the experimental tests from the referenced literature. Figure 4-44 shows the same comparison for the experimental change in capacity versus the predicted change in capacity.

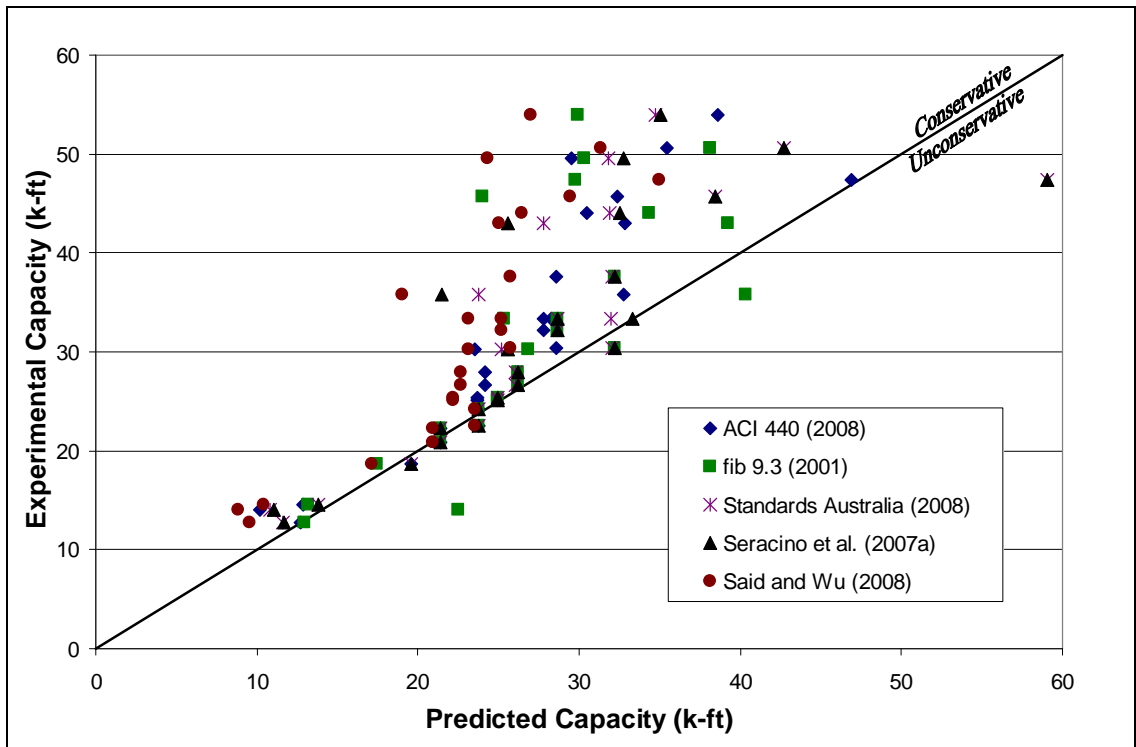


**Figure 4-43:** Comparison of Capacity Predictions by IC-Debonding Models to NSM Experimental Results

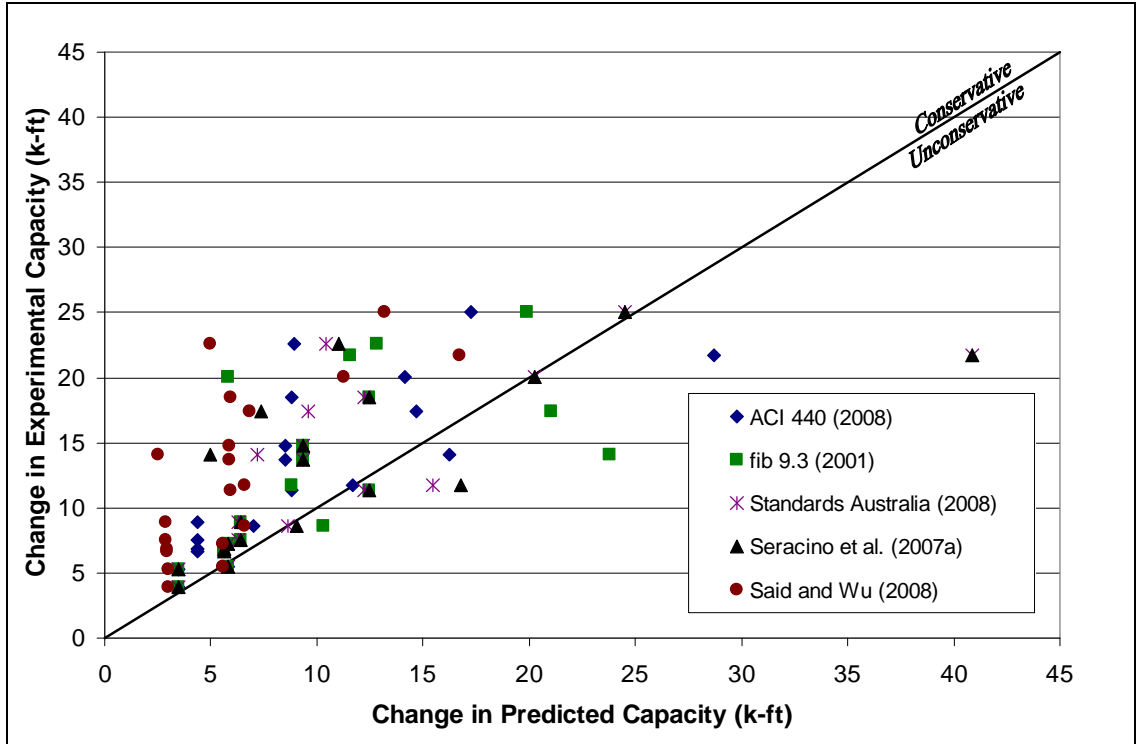


**Figure 4-44:** Comparison of Change-in-Capacity Predictions by IC-Debonding Models to NSM Experimental Results

As shown in Figure 4-43, the model by Said and Wu (2008) was very conservative for most of its predictions of capacity. The main cause of this conservatism is most likely due to the fact that this model was not calibrated using NSM tests. The model by *fib* 9.3 (2001) was also conservative for most of its capacity predictions but was unconservative for a few of the test specimens. The main cause of the inaccuracy of the model is probably due to the fact that the model was only intended for EB and not NSM. Also, this model did not include variables for the concrete compressive strength, the FRP modulus of elasticity, or the thickness of the FRP. The models by Seracino et al. (2007a)

and Standards Australia (2008) are very similar to each other; these two models were relatively accurate and usually on the conservative side of the line. These two models both included variables for the concrete compressive strength, the depth of the FRP, and the thickness of the FRP. The model by Seracino et al. did not include the FRP modulus of elasticity directly, but it used this variable for strain compatibility to determine the moment capacity. The model given by ACI 440 (2008) was also relatively accurate and typically on the conservative side. This model was only based on the FRP rupture strain; no conclusions could be made regarding why this model outperformed some of the other models. None of the models shown in Figure 4-44 was determined to be more accurate than the others, and no conclusions could be drawn from the figure. Standards Australia does not give an IC-debonding model for NSM-strengthened beam specimens; it only gives an NSM model for push-pull specimens, which Standards Australia says is a lower bound for beam tests. This NSM model for push-pull specimens is the exact same model given by Seracino, Raizal Saifulnaz, and Oehlers (2007).

The data points that were the most unconservative in Figures 4-43 and 4-44 correspond to specimens B4 and CRD-NSM from the studies by El-Hacha and Rizkalla (2004) and Jung et al. (2005), respectively. The FRP reinforcement ratios for these specimens were 0.27 and 0.12%, respectively, which are higher than all of the other FRP reinforcement ratios in these test series.

Because the models by Seracino et al. (2007a), Standards Australia (2008), and ACI 440 (2008) were relatively accurate compared to the other models, they were used to propose an NSM FRP strengthening scheme for the Letohatchee bridge in Chapter 5 and to propose a laboratory testing scheme in Chapter 6.

## **Chapter 5: Proposed Strengthening for the Letohatchee Bridge**

### **5.1 FRP Selection**

To develop a strengthening scheme for the Letohatchee bridge, the FRP type and application first needed to be chosen. Out of the three most common types of fibers used in the literature – carbon, glass, and aramid – carbon fibers were found to be the most common and the most readily available. Also, carbon fibers are typically stronger, as shown in Table 5-1, than glass or aramid fibers. For these reasons, carbon fibers were chosen for the FRP used in the Letohatchee bridge.

The two choices for the type of FRP application were externally-bonded (EB) and near-surface mounted (NSM). The focus of the strengthening of the Letohatchee bridge is negative-moment strengthening over the interior supports of the continuous structure. For an EB type of application, the EB strips would need to be located near the top of the concrete cross section. If the strips were bonded to the top of the concrete slab, the FRP would be exposed to vehicular traffic, and continual traffic loads could cause degradation or debonding. An alternative to bonding the strips to the top of the slab is to bond them to the bottom of the slab. The main disadvantage of this type of application is the discontinuity that would be caused by the diaphragms. The diaphragms, or webwalls, are located at every support and at midspan of both 60-foot exterior spans and at every third point of both 75-foot interior spans. As shown in Figure 5-1, which is a reproduction of



Figure 3-18, the biggest deficiencies occur at the approximate locations of the diaphragms.

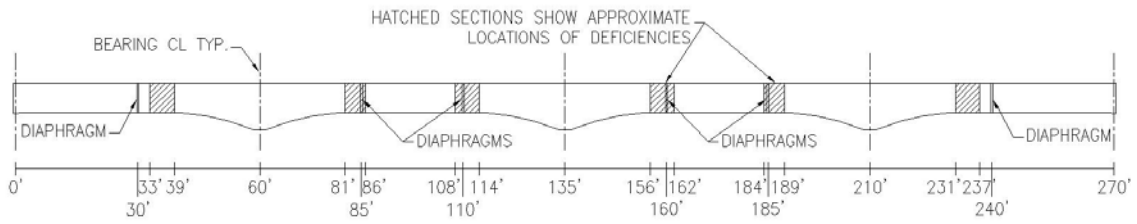


**Figure 5-1:** Elevation View of the Locations of the Letohatchee Bridge Deficiencies

Table 5-1, which is a reproduction of Table 3-6, shows the exact locations and magnitudes of the deficiencies and the strength increase needed.

**Table 5-1:** Negative Moment Deficiencies for Posting Trucks at Critical Locations

	Distance from end bearing CL (ft)	Distance from nearest interior support (ft)	$M_u$ (k-ft)	$\phi M_n$ (k-ft)	Difference in moment (k-ft)	Strength increase needed (%)
Region 1	33	27	-189	-226	38	----
	34	26	-229	-226	-2	1
	35	25	-269	-226	-43	19
	36	24	-309	-226	-83	37
	37	23	-350	-226	-124	55
	38	22	-396	-357	-39	11
	39	21	-443	-487	43	----
Region 2	81	21	-431	-487	55	----
	82	22	-386	-357	-29	8
	83	23	-341	-226	-114	50
	84	24	-300	-226	-73	32
	85	25	-261	-226	-34	15
	86	26	-223	-226	4	----
Region 3	108	27	-198	-226	28	----
	109	26	-228	-226	-1	1
	110	25	-265	-226	-39	17
	111	24	-304	-226	-78	34
	112	23	-344	-226	-118	52
	113	22	-389	-357	-33	9
	114	21	-434	-487	53	----

Figure 5-1 and Table 5-1 are specifically for an exterior girder. The exterior girder was found to be more critical than the interior girder. For the interior girder, the critical location still occurred at 37 ft from the bearing centerline, but the magnitude of the deficiency was slightly smaller, and the range over which it occurred was also smaller. Because the exterior girder and the interior girder were so similar, the amount and length of FRP recommended for the exterior girder was also used for the interior girder.

For the 60-foot exterior span, the deficiency ranges from about 33 to 39 ft from the centerline of the girder's end bearing. The diaphragm for this span is located at 30 ft. Even though the diaphragm is not located in the range of the deficiency, the FRP would

need to be extended past this location for adequate anchorage, and the diaphragm would obstruct its path. Holes could be drilled through the diaphragm to allow passage of the FRP, but this would add considerable construction time and therefore greatly increase labor and traffic-control costs.

For the 75-ft interior spans, the deficiencies occur from about 81 to 86 ft and 108 to 114 ft from the centerline of the girder's end bearing. The diaphragms for this span occur at 85 and 110 ft from the reference point, which results in both diaphragms actually being in the range of the deficiencies.

Because the diaphragms are found at the locations of where the FRP is needed, applying the EB FRP to the underside of the slab is not a feasible option. The FRP should not be terminated in regions of high moment demand due to possible debonding at the plate end. Because the diaphragms would force the FRP plates to be terminated in these regions, the EB type of application is not the most attractive option for the Letohatchee bridge.

NSM was also investigated to determine if it would be a viable FRP strengthening technique for this specific bridge. As stated by several researchers, the NSM type of application is very effective and practical for flexural strengthening of continuous concrete members in negative-moment regions (El-Hacha and Rizkalla 2004; De Lorenzis and Nanni 2002; Hassan and Rizkalla 2003). The NSM strip can be placed inside the concrete, and the concrete surface can remain flush with the surrounding concrete, which mitigates any adverse effects due to the environment or due to vehicular traffic. Therefore, the NSM FRP can be installed from above, which greatly decreases the costs and complexities associated with controlling traffic on the interstate highway that

passes beneath the bridge. Because the Letohatchee bridge is a continuous structure that needs negative-moment strengthening, the NSM type of application was chosen for this bridge.

## **5.2 FRP Amount Needed**

Based on the analysis of the FRP-debonding models presented in Chapter 4, the models by ACI 440 (2008), Standards Australia (2008), and Seracino et al. (2007a) were selected to determine the amount of FRP needed for the Letohatchee bridge. As shown in Table 5-1, the critical location for the exterior girder occurs in Region 1 at approximately 37 ft. The factored moment at this location is 350 kip-ft. By dividing the factored moment by the reduction factor  $\phi$ , which was assumed to be 0.9, the required nominal moment strength was calculated. For this critical location, the required nominal moment capacity is 389 kip-ft, which was used to determine the amount of FRP needed for the Letohatchee bridge.

To calculate the available nominal moment capacity for the Letohatchee bridge, the cross-sectional dimensions, the amount and location of the flexural steel, and the concrete, steel, and FRP material properties need to be known. These values are shown in Table 5-2.

**Table 5-2:** Dimensions and Material Properties for Capacity Calculations

Concrete	$b_w$	16.75 in.
	$h$	43.375 in.
Steel	$A_s$	1.92 in. <sup>2</sup>
	$d$	40.19 in.
	$E_s$	29000 ksi
	$f_y$	40 ksi
FRP	FRP thickness (#2- thin)	0.079 in.
	FRP thickness (#3- thick)	0.177 in.
	FRP width	0.63 in.
	$d_f$	43.06 in.
	$E_f$	18000 ksi
	$f_{fu}^*$ (thin strip)	300 ksi
	$f_{fu}^*$ (thick strip)	285 ksi

The FRP values shown in Table 5-2 are specifically for a product manufactured by Hughes Brothers called Aslan 500 CFRP Tape (Hughes Brothers 2009). This product consists of a precured strip with unidirectional carbon fibers formed through the pultrusion process and shaped into rectangular plates. For this product, there are two sizes of NSM FRP available. Hereafter, these sizes will be referred to as the “thin” strip and the “thick” strip. The thin strip is 2-mm (0.079-in.) thick and 16-mm (0.63-in.) wide and has a tensile strength of 2068 MPa (300 ksi). The thick strip is 4.5-mm (0.177-in.) thick and 16-mm (0.63-in.) wide and has a tensile strength of 1965 MPa (285 ksi). The concrete and steel values in Table 5-2 are for an exterior girder at the critical cross section, which is located at 37 ft from the centerline of the girder’s end bearing. The concrete compressive strength was assumed to be 3000 psi for the Letohatchee bridge; however, for the capacity calculations, the concrete strength was varied from 3000 to 8000 psi.

ACI 440 recommends a groove size as shown in Figure 5-2.

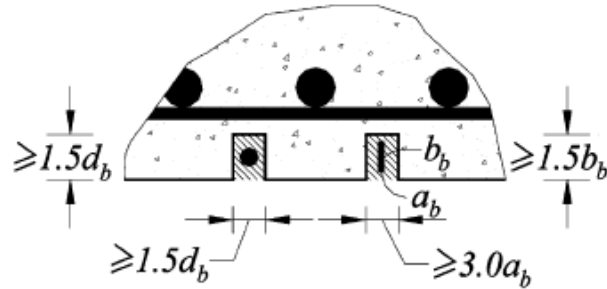


**Figure 5-2:** Recommended Groove Dimensions (ACI 440 2008)

For rectangular plates, the groove width should be at least 3.0 times the plate thickness,  $a_b$ , and the groove depth should be at least 1.5 times the plate depth,  $b_b$  (ACI 440 2008). Hughes Brothers (2009) recommends that the ACI 440 guidelines be followed for the groove dimensions. For the thin plates, a groove dimension of 0.24 in. wide by 0.95 in. deep is recommended. For the thick plates, a groove dimension of 0.53 in. wide by 0.95 in. deep is recommended.

To determine the amount of FRP needed, each of the three models was employed using different numbers of thin and thick strips and different concrete compressive strength values. From these analyses, it was determined that the bridge needed anywhere from four to six thin strips or three to five thick strips; therefore, the graphs shown in this section are limited to these amounts of FRP. To try to accurately match the concrete properties in the Letohatchee bridge, the concrete compressive strength values were limited to the range of 3000 to 8000 psi.

In this chapter, each model's design (characteristic) values were used instead of the mean values; therefore, the prescribed reduction factors and safety factors were applied to the strength calculations.

### 5.2.1 ACI 440 (2008)

Using the ACI 440 model, the strengthened nominal moment capacities for the Letohatchee bridge were predicted for different amounts of FRP and different concrete compressive strengths. Figure 5-3 indicates these capacities.

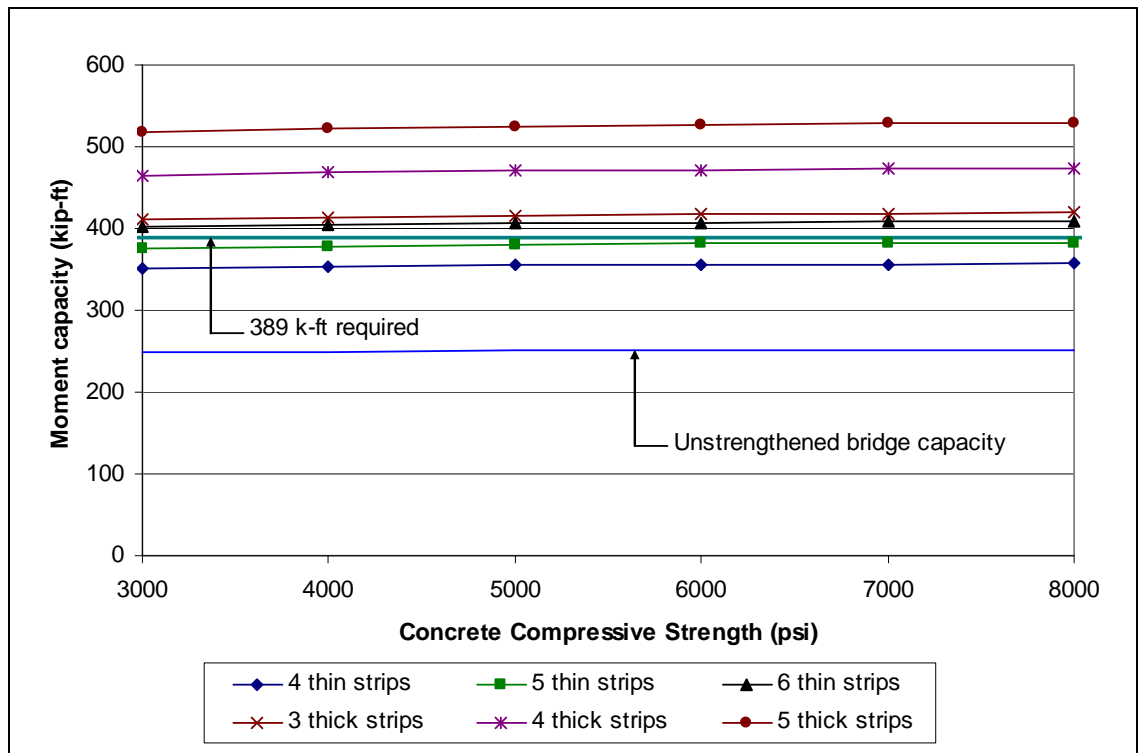


**Figure 5-3:** Letohatchee Bridge Capacities using the Model by ACI 440 (2008)

As shown in the figure, the ACI 440 model is not sensitive to the concrete compressive strength. The lines have a very small slope, which is similar to the slope for the unstrengthened bridge, and the moment capacity does not increase very much from 3000 to 8000 psi. In fact, the concrete compressive strength does not affect the FRP contribution to the capacity directly; it only affects the reinforced concrete contribution, which causes the lines in the graph to be almost horizontal.

Because the ACI 440 model limits the FRP strain to a fixed percentage of the rupture strain, all of the FRP strain values for each strip size are the same. The FRP strain value for the thin strips is 0.0099 in./in., which is 60% of the rupture strain of the thin strip. The FRP strain value for the thick strips is 0.0094 in./in., which is 60% of the FRP rupture strain of the thick strip. The concrete strain values using the ACI 440 model ranged from 0.0007 to 0.0014 in./in. Because these values were so low, a concrete crushing failure was not imminent. The ACI 440 model predicted an IC-debonding failure for all of the combinations of FRP strips and concrete compressive strengths. Appendix B shows some sample calculations with all of the intermediate values used in the calculations.

In Figure 5-3, the nominal flexural strength required by the Letohatchee bridge is shown as a line at 389 kip-ft. None of the data points for the four thin strips or the five thin strips lies above the line, and all of the data points for the six thin strips lie above this line. For the thick strips, all of the data points for all amounts of FRP and all concrete strengths are above the line.

According to the ACI 440 model, the most efficient selection of strips would be either six thin FRP strips or three thick FRP strips. As long as the concrete strength is between 3000 and 8000 psi, it has no effect on the number of strips chosen for this bridge.

According to Hughes Brothers, for the Aslan 500 CFRP Tape, the thick strips cost about 1.5 times more than the thin strips. Therefore, using three thick strips instead of six thin strips is more cost-effective, not only in material costs but also in labor costs.



### 5.2.2 Standards Australia (2008)

Using the model by Standards Australia, the strengthened nominal moment capacities for the Letohatchee bridge were predicted for different amounts of FRP and different concrete compressive strengths. Figure 5-4 indicates these capacities.

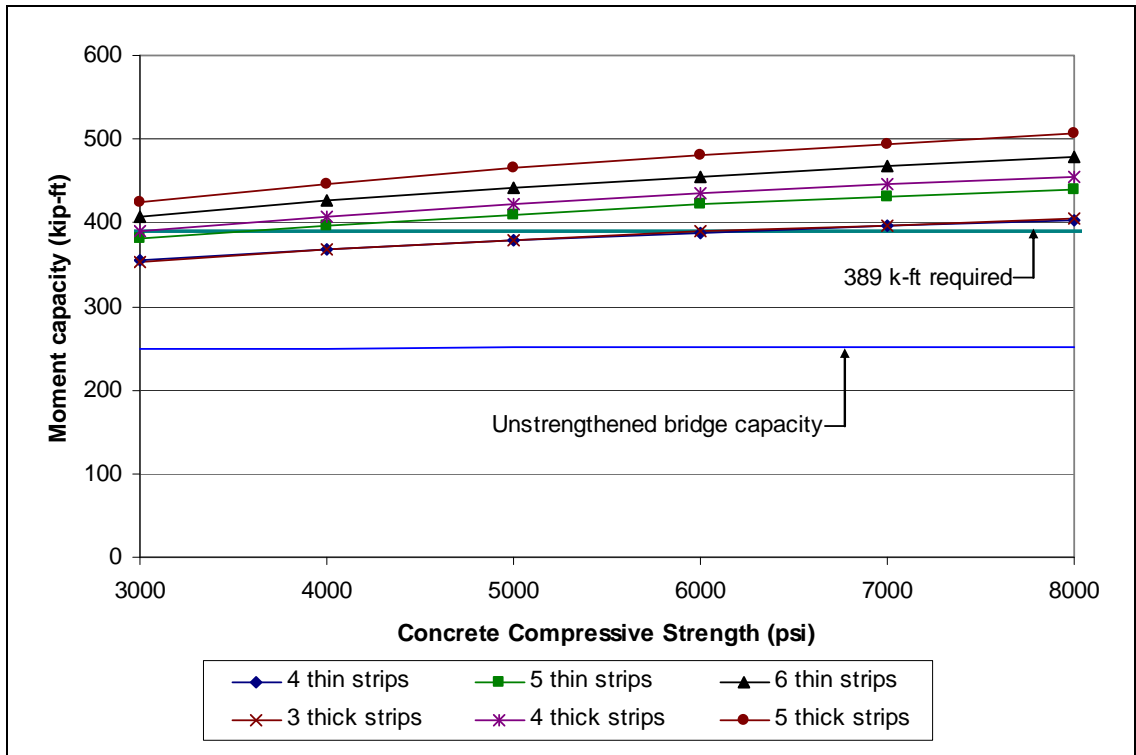


**Figure 5-4:** Letohatchee Bridge Capacities using the Model by Standards Australia (2008)

As shown in Figure 5-4, this model is somewhat sensitive to the concrete compressive strength. Some of the lines shown have a slope that actually crosses the line at 389 kip-ft, which is the required capacity for the Letohatchee bridge. For 3000-psi concrete, six thin strips are needed; for 4000- to 6000-psi concrete, five thin strips are needed; and for 7000- to 8000-psi concrete, four thin strips are needed. For the thick

strips, four are needed if the concrete strength is between 3000 and 5000 psi, and three are needed if the concrete strength is between 6000 and 8000 psi.

Table 5-3 shows the FRP strain values for thin and thick strips using the Standards Australia model.

**Table 5-3:** FRP Strain Values for the Letohatchee Bridge using the Model by Standards Australia (2008)

$f'_c$ (psi)	Thin FRP Strip		Thick FRP Strip	
	$\epsilon_f$ (in./in.)	$\epsilon_f / \epsilon_{f,rupt}$	$\epsilon_f$ (in./in.)	$\epsilon_f / \epsilon_{f,rupt}$
3000	0.0087	52%	0.0053	34%
4000	0.0096	57%	0.0058	37%
5000	0.0103	62%	0.0063	40%
6000	0.0109	66%	0.0067	42%
7000	0.0115	69%	0.0070	44%
8000	0.0120	72%	0.0074	46%

Table 5-3 shows how the FRP strain values varied for different concrete compressive strengths. The FRP strain values were not dependent upon the number of FRP strips. As shown in the table, the FRP strain values for the thin strips ranged from 52 to 72% of the rupture strain of the thin strips. For the thick strips, the FRP strain values ranged from 34 to 46% of the rupture strain of the thick strips. The concrete strain values were not very high and did not change much; they varied from 0.0006 to 0.0012 in./in. This model predicted an IC-debonding failure for all of the combinations of FRP strips and concrete compressive strengths

### 5.2.3 Seracino et al. (2007a)

Using the model by Seracino et al., the strengthened nominal moment capacities for the Letohatchee bridge were predicted for different amounts of FRP and different concrete compressive strengths. Figure 5-5 indicates these capacities.

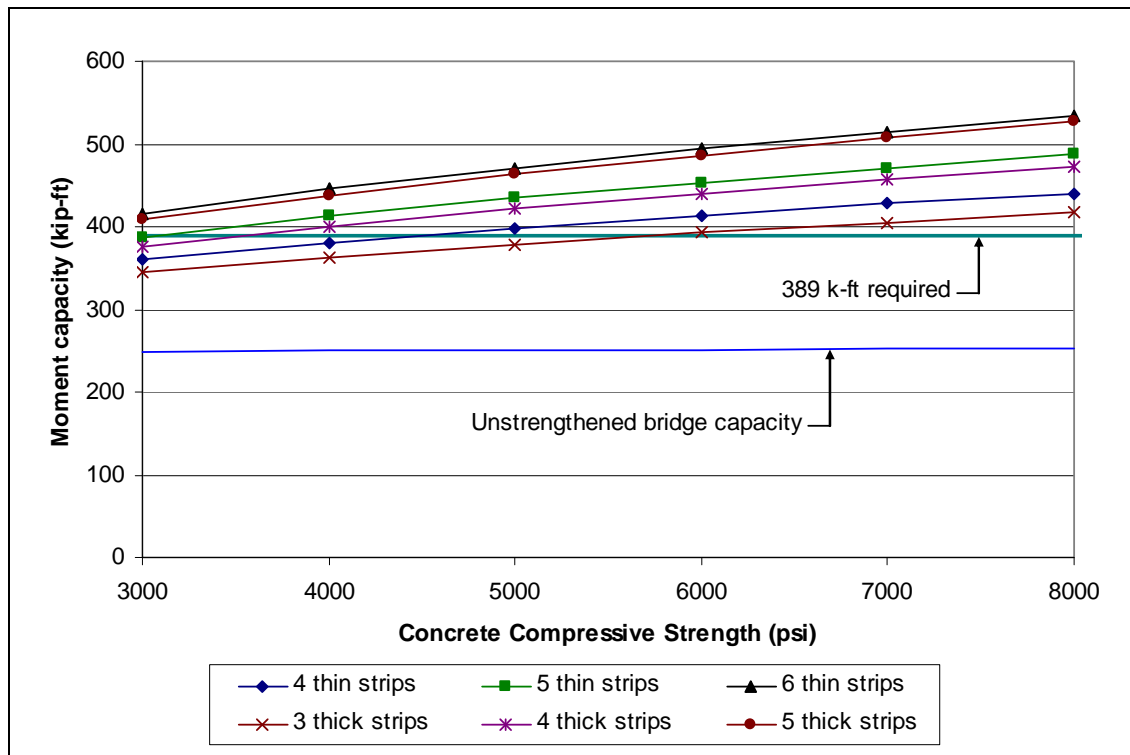


**Figure 5-5:** Letohatchee Bridge Capacities using the Model by Seracino et al. (2007a)

As shown in Figure 5-5, this model is also sensitive to the concrete compressive strength. The lines shown have a slope that actually crosses the line at 389 kip-ft, which is the required capacity for the Letohatchee bridge. For 3000-psi concrete, six thin strips are needed; for 4000-psi concrete, five thin strips are needed; and for 5000- to 8000-psi concrete, four thin strips are needed. For the thick strips, five are needed if the concrete

strength is 3000 psi, four are needed if the concrete strength is between 4000 and 5000 psi, and three are needed if the concrete strength is between 6000 and 8000 psi.

Table 5-4 shows the FRP strain values for thin and thick strips using the Seracino et al. model.

**Table 5-4:** FRP Strain Values for the Letohatchee Bridge using the Model by Seracino et al. (2007a)

$f'_c$ (psi)	Thin FRP Strip		Thick FRP Strip	
	$\epsilon_f$ (in./in.)	$\epsilon_f / \epsilon_{f,rupt}$	$\epsilon_f$ (in./in.)	$\epsilon_f / \epsilon_{f,rupt}$
3000	0.0092	55%	0.0049	31%
4000	0.0106	64%	0.0056	35%
5000	0.0118	71%	0.0063	40%
6000	0.0130	78%	0.0069	43%
7000	0.0140	84%	0.0074	47%
8000	0.0142	85%	0.0079	50%

Table 5-4 shows how the FRP strain values varied for different concrete compressive strengths. The FRP strain values were not dependent upon the number of FRP strips. As shown in the table, the FRP strain values for the thin strips ranged from 55 to 85% of the rupture strain of the thin strips. For the thick strips, the FRP strain values ranged from 31 to 50% of the rupture strain of the thick strips. The concrete strain values were not very high and did not change much; they varied from 0.0007 to 0.0013 in./in. This model predicted an IC-debonding failure for all of the combinations of FRP strips and concrete compressive strengths

### 5.2.4 Summary of Models

The results of the three design models were combined into one graph to determine the amount of FRP needed to attain a strengthened nominal moment capacity of 389 kip-ft for the Letohatchee bridge. This graph, which is dependent upon the concrete compressive strength, is shown in Figure 5-6 for thin FRP strips.

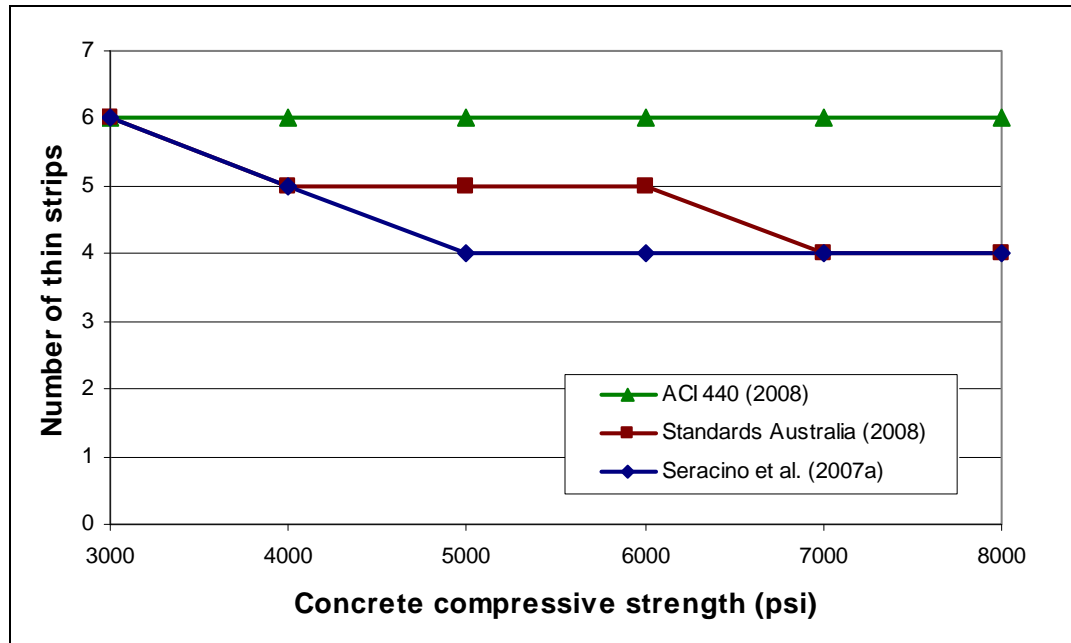


**Figure 5-6:** Required Amounts of Thin FRP Strips for each Model

Figure 5-7 shows the graph of the required amount of thick FRP strips needed to attain a strengthened nominal moment capacity of 389 kip-ft.

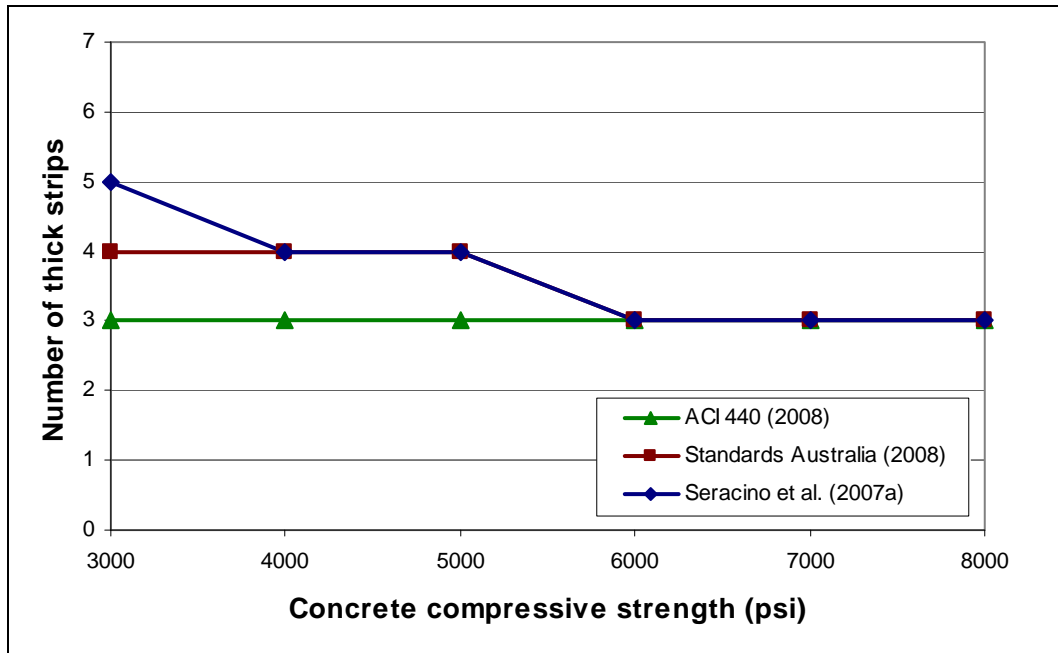


**Figure 5-7:** Required Amounts of Thick FRP Strips for each Model

As shown in Figures 5-6 and 5-7, the amount of FRP required decreases as the concrete compressive strength increases for two of the models. The results of the ACI 440 model, however, are not very sensitive to the concrete compressive strength. Because the ACI 440 model is the most conservative model for the thin FRP, as shown in Figure 5-6, six strips would be the most conservative number of strips to use for any concrete compressive strength from 3000 to 8000 psi; however, for the thick FRP, it would be very advantageous to know the concrete strength. Without any knowledge of the strength of the concrete, it would be conservative to use five thick strips, but by taking representative concrete core samples from the Letohatchee bridge, a reduction in the number of strips may be possible. Because the deck and the girders are assumed to have been cast monolithically and because the bond between the FRP and the concrete is important, the core samples should be taken from the bridge deck. To ensure that the core

samples are representative of the proposed FRP locations, the samples should be taken at different locations across the roadway surface and along the length of the girder. If the concrete strength is between 4000 and 6000 psi, then four thick strips can be used. If the concrete strength is between 6000 and 8000 psi, then only three thick strips need to be used.

For borderline cases, such as for concrete strengths between 3000 and 4000 psi and between 5000 and 6000 psi, calculations could be made to determine the number of thick strips that are needed.

### **5.3 FRP Length and Termination Points**

The models mentioned in the previous section are based on prevention of IC debonding. To prevent PE debonding, however, the issue is not the number of strips that are needed but the distance the strips need to be extended. Some code recommendations state that the FRP should be extended to a point of contraflexure (ACI 440 2008, Standards Australia 2008). In a continuous bridge girder that is subjected to a moving set of loads, there is no fixed point of contraflexure. Rather, the location of contraflexure moves within a range bounded by the positive moment envelope and the negative moment envelope, as discussed in Chapter 3. Because it is recommended that the strips be terminated at a point of contraflexure and no fixed point of contraflexure exists in a continuous bridge girder, this recommendation cannot be satisfied.

A similar approach to prevent PE debonding is to terminate the FRP strip on the compression face of a continuous beam, which means that the strip needs to be extended past the last possible point of contraflexure as opposed to terminating it directly at the

point (Standards Australia 2008). This second approach is slightly different than the first approach. A possible reason for this difference could be that the first approach tries to limit both the negative moment and the curvature at the termination point, and the second approach only tries to limit the negative moment at the termination point. To find the locations where the deck surface is in compression, the negative-moment envelope was examined to find the locations where no negative moment is possible under the design loads. The negative-moment envelope is shown in the factored demand and factored resistance graph, which was shown in Chapter 3 and is shown again in Figure 5-8.

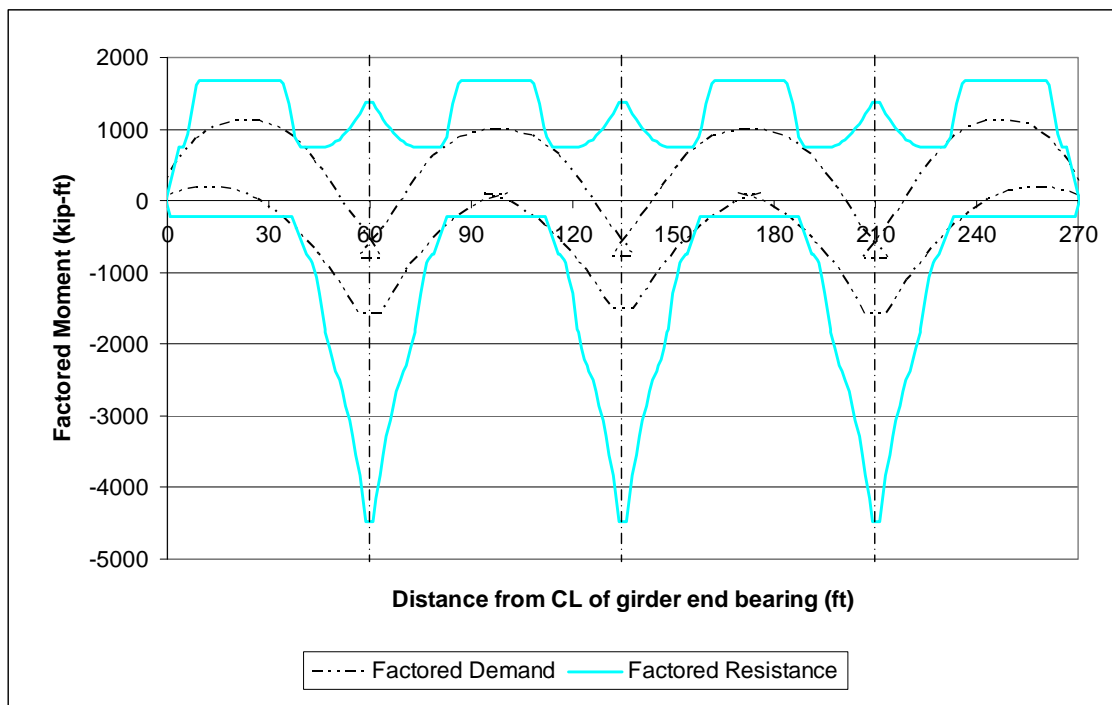


**Figure 5-8:** Factored Demand Envelope and Factored Resistance

As shown in Figure 5-8, the factored negative-moment demand envelope is not always negative. At four different locations, it crosses over into the positive side. In these regions, the top of the beam is always in compression and the bottom is always in



tension; therefore, these four regions are where the FRP strips could be terminated. The following locations are the specific distances from the centerline of the girder's end bearing where the negative-moment envelope is zero: 27.1, 93.6, 100.9, 169.1, 176.4, and 242.9 ft. For easier installation, the start distances will be rounded down to the nearest half-foot, and the end distances will be rounded up to the nearest half-foot.

To prevent PE debonding, it is recommended that the FRP strips extend over the deficient regions shown in Table 5-1 and then be terminated in one of the four regions where the negative-moment envelope is positive. Figure 5-9 shows the recommended lengths of the FRP for the Letohatchee bridge relative to the centerline of the girder's end.

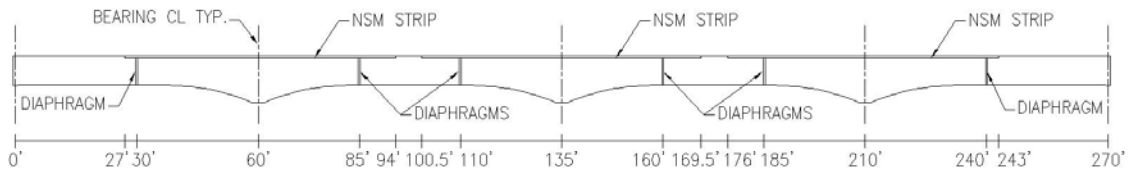


**Figure 5-9:** Elevation View of the Recommended FRP Lengths for the Letohatchee Bridge (not to scale)

An alternative to the recommended lengths shown in Figure 5-9 is to have one 216-ft continuous strip from the 27-ft mark to the 243-ft mark. A possible drawback for this approach might be constructability issues associated with the installation of 216-ft long strips of FRP.

#### 5.4 FRP Spacing Recommendations

The spacing of the FRP was determined by using the various models shown in the “FRP Spacing Recommendations for NSM Strips” section of Chapter 2. By assuming a groove side of 1/4 inch by 7/8 inch, which was recommended by Hughes Brothers for their Aslan 500 CFRP Tape, the following table was created:

**Table 5-5:** FRP Spacing Recommendations for Letohatchee Bridge

	Minimum clear spacing of strips (in.)	Minimum side cover distance (in.)
ACI Committee 440 (2008)	1.8	3.5
Hassan and Rizkalla (2004)	1.3	2.5
Kang et al. (2005)	1.6	1.6
Rashid, Oehlers, and Seracino (2008)	2.1	2.2
Vasquez (2008)	0.6	----

For the model by Hassan and Rizkalla, the FRP bar diameter was conservatively taken to be equal to the FRP depth. As shown in Table 5-5, the greatest of the clear spacing limits is 2.1 in., and the greatest of the side cover limits is 3.5 in. Because the Letohatchee bridge needs negative-moment strengthening, the entire slab width can be used for FRP placement, so there should be no spacing problems. Figure 5-10 shows a cross section with a possible spacing configuration for six strips per girder. Figure 5-11 shows a cross section with a possible spacing configuration for three strips per girder.

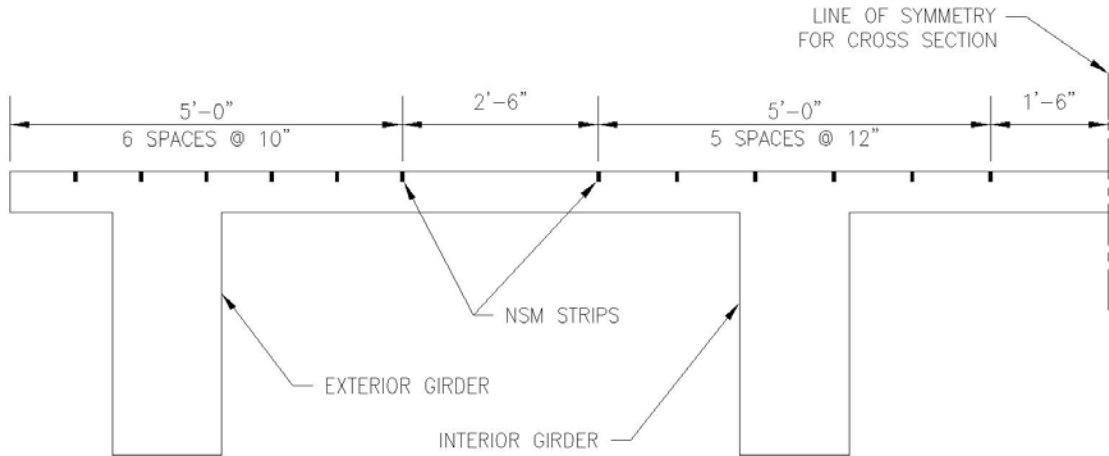


**Figure 5-10:** Cross Section of a Possible Spacing Configuration for Six NSM Strips per Girder

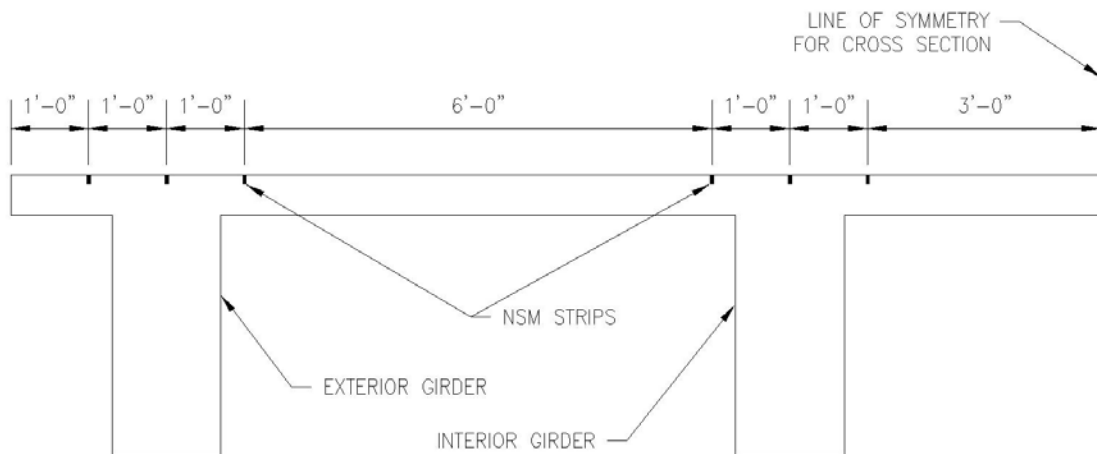


**Figure 5-11:** Cross Section of a Possible Spacing Configuration for Three NSM Strips per Girder

As shown in Figures 5-10 and 5-11, the smallest spacing for these configurations is 10 in., and the largest value from Table 5-5 is 3.5 in.; therefore, spacing should not be a problem for the Letohatchee bridge. As shown in Figures 5-10 and 5-11, the FRP is

spaced more closely directly over the girder to control flexural cracking, which tends to have increased crack widths over the girder (ACI 318 2008). In Section 10.6.6 of ACI 318 (2008), it is recommended to add additional flexural reinforcement to the outer portions of the flange when the effective flange width is greater than one-tenth of the span. Because the Letohatchee bridge already has flexural reinforcement at these locations, no additional FRP reinforcement is needed in these outer regions of the flange.

### **5.5 Summary of Proposed Design**

It is recommended that NSM carbon fiber-reinforced polymer (CFRP) strips be used for negative-moment strengthening of the Letohatchee bridge. Concrete core samples need to be taken from the bridge to determine the concrete compressive strength. If these core samples are not taken, then twenty-four thin NSM FRP strips, six strips per girder, should be spaced out across the roadway surface, as shown in Figure 5-10. An alternative would be to use five thick NSM FRP strips per girder, totaling twenty thick strips.

If the concrete strength is known, then fewer thick strips could be used. If the strength is between 4000 and 6000 psi, then four thick strips per girder can be used. If the strength is between 6000 and 8000 psi, then three thick strips per girder can be used.

The FRP strips should extend over the following distance ranges, measured relative to the centerline of the girder end bearing: from 27 to 94 ft; from 100.5 to 169.5 ft; and from 176 to 243 ft. The corresponding strip lengths are 67, 69, and 67 ft, respectively.

It is also recommended that a survey be done on the bridge deck to verify the locations and depths of the flexural steel reinforcement. If the steel bars are located too close to the surface, then there may be some interaction between the steel and the FRP.

### 5.6 Further Testing

More testing should be performed to verify the accuracy and level of safety of the models. The testing program should include specimens that fail due to IC debonding to determine if the models can predict when and if an IC-debonding failure will occur. The steel and FRP reinforcement ratios of the test specimens should attempt to match the pre-existing steel and added FRP reinforcement ratios of the Letohatchee bridge to try to accurately replicate the flexural response expected in the bridge, which would result in a more efficient bridge strengthening scheme. Table 5-6 shows the flexural reinforcement ratios for the critical regions of the Letohatchee bridge.

**Table 5-6:** Reinforcement Ratios for the Letohatchee Bridge

$\rho_s$	$\rho_f$	$\rho_f^*$	$\rho_f^* / \rho_s$
0.29%	0.030%	0.018%	0.064

In Table 5-6,  $\rho_s$  is the steel reinforcement ratio;  $\rho_f$  is the FRP reinforcement ratio;  $\rho_f^*$  is the normalized FRP reinforcement ratio; and  $\rho_f^* / \rho_s$  is the relative strengthening ratio. The steel reinforcement ratio, the FRP reinforcement ratio, and the normalized FRP reinforcement ratio can be calculated using the following equations:

$$\rho_s = \frac{A_s}{bd} \quad \text{Equation 5-1}$$

$$\rho_f = \frac{A_f}{bd} \quad \text{Equation 5-2}$$

$$\rho_f^* = \rho_f \left( \frac{E_f}{E_s} \right) \quad \text{Equation 5-3}$$

where  $A_s$  is the area of steel reinforcement;  $b$  is the width of the compression face of the member;  $d$  is the distance from the extreme compression fiber to the centroid of the tension reinforcement;  $A_f$  is the area of FRP reinforcement;  $E_f$  is the FRP modulus of elasticity; and  $E_s$  is the steel modulus of elasticity.

The reinforcement ratios for some of the experimental tests from the literature, which were introduced in Chapter 2 and then compared to the models in Chapter 4, are shown in Table 5-7.

**Table 5-7: Reinforcement Ratios for the Experimental Tests from the Literature**

Test Series	Specimen ID	$\rho_s$	$\rho_f$	$\rho_f^*$	$\rho_f^* / \rho_s$
El-Hacha and Rizkalla (2004)	B1	0.34%	0.10%	0.058%	0.17
	B2	0.34%	0.085%	0.060%	0.17
	B3	0.34%	0.080%	0.060%	0.17
	B4	0.34%	0.27%	0.060%	0.17
Jung et al. (2005)	NSM-PL-15	0.39%	0.039%	0.032%	0.082
	NSM-PL-25	0.39%	0.065%	0.054%	0.14
	CRD-NSM	0.39%	0.12%	0.072%	0.18
Tajsten and Nordin (2007)	NSMR 1	0.33%	0.17%	0.12%	0.36
	NSMR 2	0.33%	0.17%	0.12%	0.36
Yost et al. (2007)	6-1Fa	1.72%	0.16%	0.11%	0.064
	6-1Fb	1.72%	0.16%	0.11%	0.064
	6-2Fa	1.72%	0.32%	0.22%	0.13
	6-2Fb	1.72%	0.32%	0.22%	0.13
	9-1Fa	1.11%	0.11%	0.073%	0.066
	9-1Fb	1.11%	0.11%	0.073%	0.066
	9-2Fa	1.11%	0.22%	0.15%	0.13
	9-2Fb	1.11%	0.22%	0.15%	0.13
	12-1Fa	0.83%	0.081%	0.055%	0.066
	12-1Fb	0.83%	0.081%	0.055%	0.066
	12-2Fa	0.83%	0.16%	0.11%	0.13
	12-2Fb	0.83%	0.16%	0.11%	0.13
Liu, Oehlers, and Seracino (2006)	NS F1	0.72%	0.40%	0.35%	0.48
	NS F2	0.72%	0.12%	0.11%	0.15
	NS F3	0.72%	0.061%	0.053%	0.074
	NS F4	0.72%	0.14%	0.10%	0.14
	NB F2	1.09%	0.18%	0.16%	0.15
	NB F3	1.09%	0.40%	0.28%	0.26
Teng et al. (2006)	B2900	0.56%	0.079%	0.057%	0.10

In Table 5-7, the specimen ID is the label that was given for the specimens by the original researchers. The test series shown were chosen because all of them included NSM tests. As shown in the table, the steel reinforcement ratio ranges from 0.33 to 1.72%, and the FRP reinforcement ratio ranges from 0.039 to 0.40%; the Letohatchee bridge values for the steel and FRP reinforcement ratios are 0.29% and 0.030%, respectively.

The normalized FRP reinforcement ratio was used to compare the relative amount of FRP force in beams strengthened with different FRP stiffnesses. This value for the

experimental tests ranges from 0.032 to 0.35%; the value for the Letohatchee bridge is 0.018%.

The relative strengthening ratio was used to compare the amount of strengthening relative to the original strength of the beam. This value for the experimental tests ranges from 0.064 to 0.48; the value for the Letohatchee bridge is 0.064.

When compared to the steel reinforcement ratio, the FRP reinforcement ratio, the normalized FRP reinforcement ratio, and the relative strengthening ratio, the Letohatchee bridge falls at or beyond the boundary of the FRP-strengthened specimens tested in the past.

For the proposed testing program, a range of reinforcing amounts of both steel and FRP should be investigated that encompasses the reinforcement ratios of the Letohatchee bridge. A range of concrete strengths should also be investigated so as to generate results that will be applicable to a range of potential bridge strengthening projects. A proposed testing program was developed and is shown in Chapter 6.



## **Chapter 6: Proposed Laboratory Testing Program**

### **6.1 Overall Objectives and Scope of Testing Program**

In Chapter 5, the steel and FRP reinforcement ratios for past published experimental tests, which were introduced in Chapter 2, were compared to the ratios for the Letohatchee bridge. The reinforcement ratios for the tests were found to be larger than the ratios for the bridge; therefore, the results from the tests are not directly applicable to the Letohatchee bridge. Also, none of the NSM test specimens were cracked prior to FRP strengthening. To be able to use laboratory test results that can be directly applied to the bridge, a laboratory testing program was proposed. Because the proposed strengthening scheme that was presented in Chapter 5 employed NSM strips, only NSM will be evaluated in the testing program. The proposed testing program has four main objectives:

1. Develop a relationship between the test specimens and the Letohatchee bridge to more effectively and more efficiently propose an NSM FRP-strengthening scheme for the bridge.
2. Study the IC-debonding behavior to better quantify when and if it will occur and to verify the existing IC-debonding models.
3. Study the effects of the concrete compressive strength, amount of steel reinforcement, amount of NSM reinforcement, and cross-sectional shape on the strengthened moment capacity.

4. Evaluate the effectiveness of the NSM in a strengthening type of situation by cracking the unstrengthened specimens before applying the FRP.

To achieve the first objective, specimens were designed to match the Letohatchee bridge girders in a couple of different ways. The mechanical reinforcement ratio, the concrete cover distance, and the flange thickness will all be about the same. Also, the concrete compressive strength will be varied from 3000 to 7000 psi.

To achieve the second objective, each of the three NSM IC-debonding models from the previous chapter – ACI 440 (2008), Standards Australia (2008), and Seracino et al. (2007a) – were used to predict the strengthened moment capacities of the specimens. These predictions will then be evaluated using the experimental results in order to determine the most accurate model for the test specimens, to suggest modifications to the models, or to generate a more effective model.

To achieve the third objective, each of the four test series will be used to assess one or more of the key variables listed. In Test Series 1, the amount of steel will be studied. In Test Series 2, the cross-sectional shape will be studied. In Test Series 3 and 4, the concrete compressive strength will be studied. In each of the test series, the amount of FRP will be varied as well.

To achieve the fourth objective, the unstrengthened specimens will be loaded until the concrete cracks. After cracking, the specimens will be strengthened with NSM and loaded again until failure. Very few of the previously reported beam tests included specimens that were cracked prior to strengthening with FRP. More testing is needed to evaluate the effectiveness of FRP in strengthening situations, particularly because

reinforced concrete bridge girders in need of strengthening are usually cracked under existing service loads.

Four different test series are proposed in this laboratory testing program. In all of the test series, thin NSM FRP strips are used. Thin strips are used instead of thick strips to try to match the FRP reinforcement ratio of the proposed strengthening scheme of the Letohatchee bridge. Because the volume of concrete is so small for the proposed test specimens relative to the Letohatchee bridge girders, a smaller amount of FRP is needed; therefore, thin strips were chosen over thick strips.

For all of the test series, the specimens are designed to be loaded in a simply-supported configuration in symmetric four-point bending, with the two concentrated loads located 3 ft apart. The flanges for the specimens will be at the bottom of the cross section as the beams are subjected to positive moment. This setup is opposite to the Letohatchee bridge. The flange for the bridge is at the top of the cross section as the critical section is subjected to negative moment. Figure 6-1 shows the proposed test setup for the typical specimen.

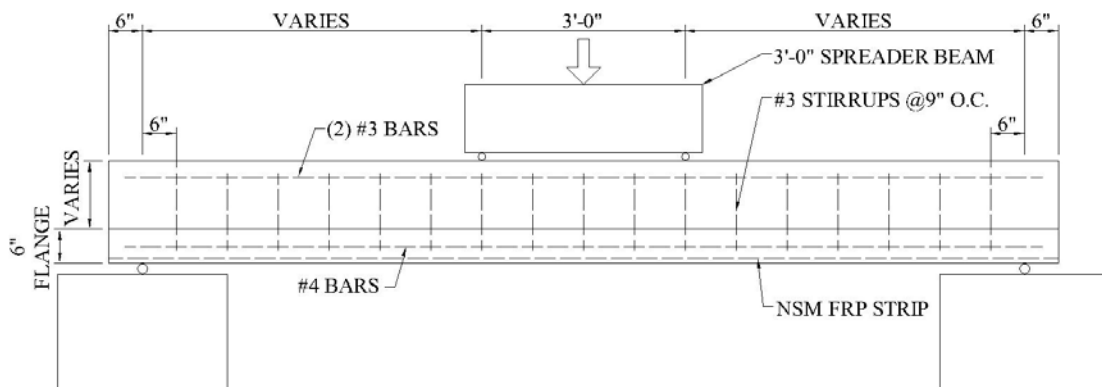


**Figure 6-1:** Elevation View of the Proposed Test Setup for a Typical Specimen

The specimen identification system used throughout this chapter is summarized in

Figure 6-2.

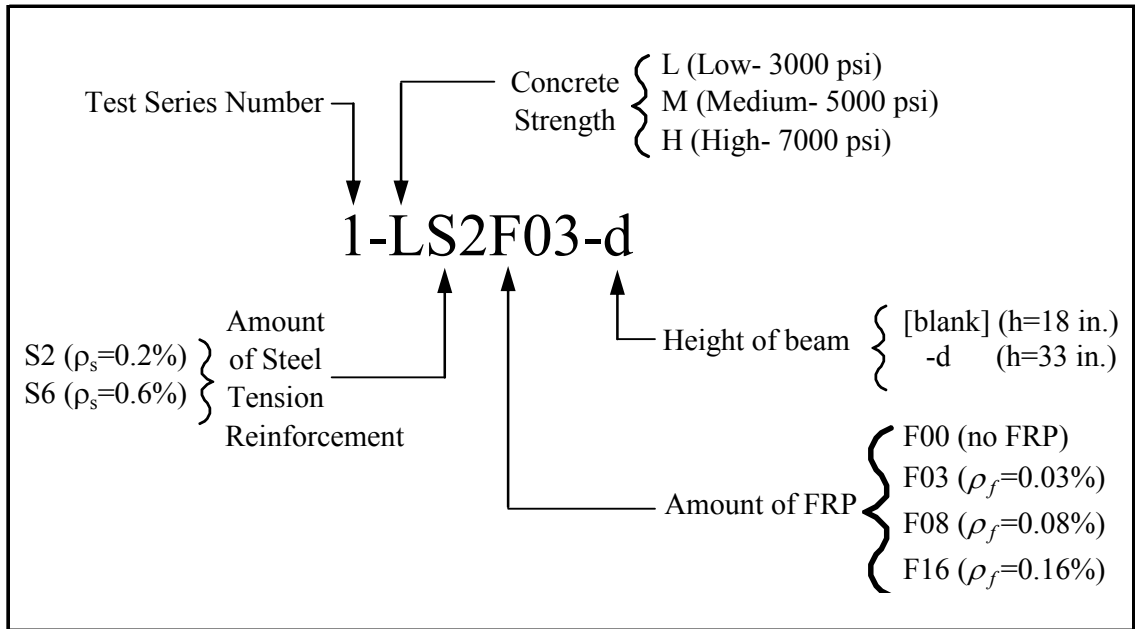


**Figure 6-2:** Specimen Identification System

The main goal in choosing the steel and FRP properties is to match the properties and appropriately scale the flexural behavior of the critical region of the Letohatchee bridge. For the test specimens, a yield stress of 50 ksi is selected for the steel. The Letohatchee bridge is assumed to have 40 ksi steel, but achieving an actual yield stress that low is not likely in modern reinforcement. Previous work at Auburn University (Reed 2003), has indicated that a yield strength of 50 ksi is likely for commercially available ASTM A 615 Grade 40 reinforcing steel. The FRP properties used in the test specimens are the same as the FRP properties used in the proposed strengthening scheme in Chapter 5. Table 6-1 shows a summary of some of the assumed steel and FRP properties.

**Table 6-1:** Properties and Dimensions of Steel and FRP for Proposed Testing Program

Steel	$f_y$	50 ksi
	$E_s$	29000 ksi
FRP*	$f_{fu}$	300 ksi
	$E_f$	18000 ksi
	FRP width	0.63 in
	FRP thickness	0.079 in

\*Aslan 500 CFRP Tape (Hughes Brothers 2009)

The intended failure mode for all but one of the specimens in the four test series is IC debonding; the other specimen is predicted to fail due to crushing of the concrete. The FRP is extended to the end of the specimen to prevent PE debonding.

**6.2 Test Procedure**

The proposed testing procedure is the same for all of the specimens except the unstrengthened comparison specimens (referred to as “control” specimens) for each series. The first step is to place the concrete in the forms so that the flange is on top. After the concrete has cured and reached the desired compressive strength, the beam needs to be inverted so that the flange is on the bottom. Once the beam is correctly oriented, it can be loaded until the concrete cracks.

For the specimens that will be left unstrengthened, the load can be applied again until the beam fails, but this testing should not occur until the companion beams have been strengthened and are ready for testing. For the FRP-strengthened specimens, the load should be removed once sufficient cracking has occurred, and the beam should be inverted again so that the flange is on top. The specimen should then be fully supported along its length, thereby ensuring that there are minimal flexural deformations due to

self-weight along the length during strengthening. By minimizing the flexural deformations at the time of strengthening, the specimen closely reflects the conditions in the actual bridge, and it also simplifies the analysis. The groove for the FRP can then be cut using a diamond-blade concrete saw. The groove size, as recommended by Hughes Brothers, should be 1/4-in. wide by 7/8-in. deep. Once the groove is cut, it needs to be thoroughly cleaned using a vacuum, compressed air, or both. Next, a structural adhesive recommended by Hughes Brothers, such as the Hilti HIT-RE 500, can be injected into the groove while ensuring that there are no entrapped air voids. The FRP strip is then placed in the groove, and the excess epoxy is removed.

According to Hilti's product information (Hilti 2009), it takes a minimum of twelve hours for the epoxy to fully cure for a base material temperature of 68 degrees Fahrenheit. To ensure that the epoxy curing duration is not a factor in the test, however, it is recommended that the epoxy be allowed to cure for at least seven days. After this time has elapsed, the beam can be flipped over onto its flange, and the specimen can be loaded until failure.

During loading, the vertical beam deflections, as well as the concrete, steel, and FRP strains, should be measured and recorded at critical locations. The steel strain gauges should be placed at several locations along the length of the specimens, especially at midspan, at the load points, and at the stirrup locations inside the maximum moment region. These are the probable locations for flexural cracks. The FRP strain gauges should be placed at the cracked sections. The specimens will be cracked prior to installation of FRP, so placing the FRP strain gauges at cracked locations can be done with certainty. The strains at the flexural cracks are desired because the behavior at

cracked sections is being investigated. The strains at cracked sections are larger than the strains between two cracks, and knowing the strains at the cracked sections will produce more accurate results. The applied load should also be recorded for the duration of the test.

### **6.3 Test Series 1**

Eight different specimens are proposed for Test Series 1. Four of the specimens have a mechanical reinforcement ratio ( $\omega_s$ ) similar to the Letohatchee bridge; the other four specimens have a mechanical reinforcement ratio that is three times as large. The amount of steel was tripled to observe the effects of the amount of steel on the strengthened moment capacity. For each set of four specimens, one beam is left unstrengthened and used as a control beam; the other three beams in each set are strengthened with one, three, and six thin FRP strips, respectively.

#### **6.3.1 Objectives of Test Series**

The main objectives of Test Series 1 are to study the effects of the amount of steel and the amount of FRP on the strengthened moment capacity and to determine the most accurate IC-debonding model for the test results. By analyzing the effects of the amounts of flexural steel and FRP together, the effects on the strengthened moment capacity of the amount of FRP relative to the amount of flexural steel can also be analyzed.

#### **6.3.2 Description of Test Specimens**

For the specimens in this test series, a concrete compressive strength of 3000 psi is used because it matches the assumed value of the Letohatchee bridge's concrete. The

specimens in this test series were sized so that all of the concrete for the specimens could come from the same batch, thereby maintaining concrete properties throughout the test series. The amount of steel was also chosen to try to match the Letohatchee bridge. For the Letohatchee bridge, the mechanical reinforcement ratio,  $\omega_s$ , is 3.80%. This ratio was the target value for four of the specimens in this test series. Two #4 bars are used in the first four specimens, giving them a mechanical reinforcement ratio of 3.56%. The flexural steel reinforcement ratio for the Letohatchee bridge is 0.29%, and the flexural steel reinforcement ratio for these specimens is about 0.2%. For the second set of four specimens, the amount of steel was tripled. Six #4 bars are used in the second set, giving them a mechanical reinforcement ratio of 10.7% and a flexural steel reinforcement ratio of about 0.6%. Figure 6-3 shows both of the cross sections used in Test Series 1.

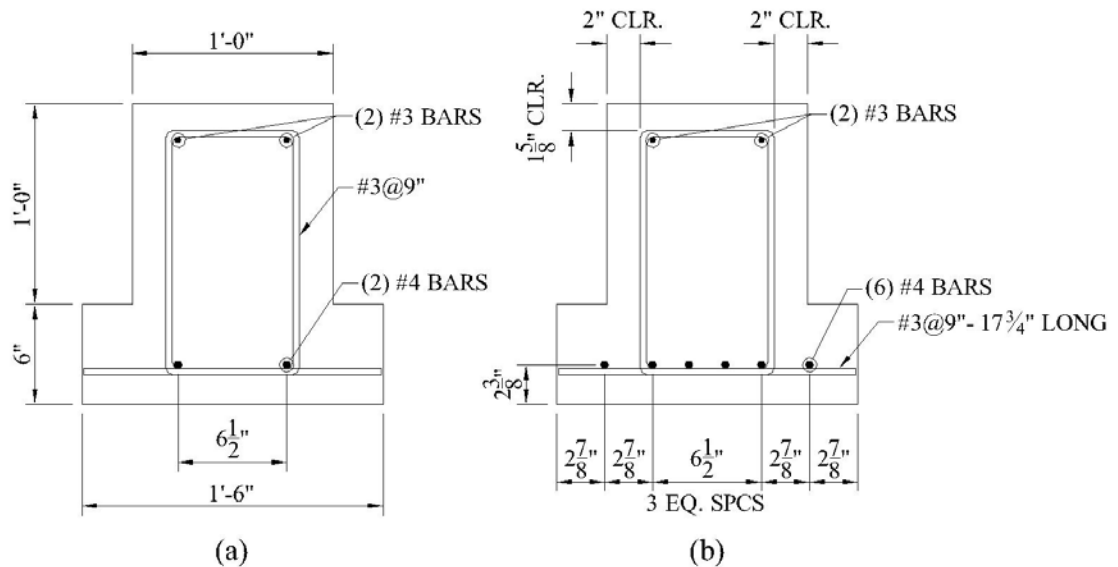


**Figure 6-3:** (a) Cross Section for Specimens with  $\rho_s$  of 0.2% (b) Cross Section for Specimens with  $\rho_s$  of 0.6%



Figure 6-3 shows the specimens before the FRP is applied. For each cross section, there are one, three, and six thin FRP strips applied, respectively. Also, one beam per cross section is left unstrengthened and is used as a control beam. The specimen names and cross sections for Test Series 1 are shown in Figure 6-4.

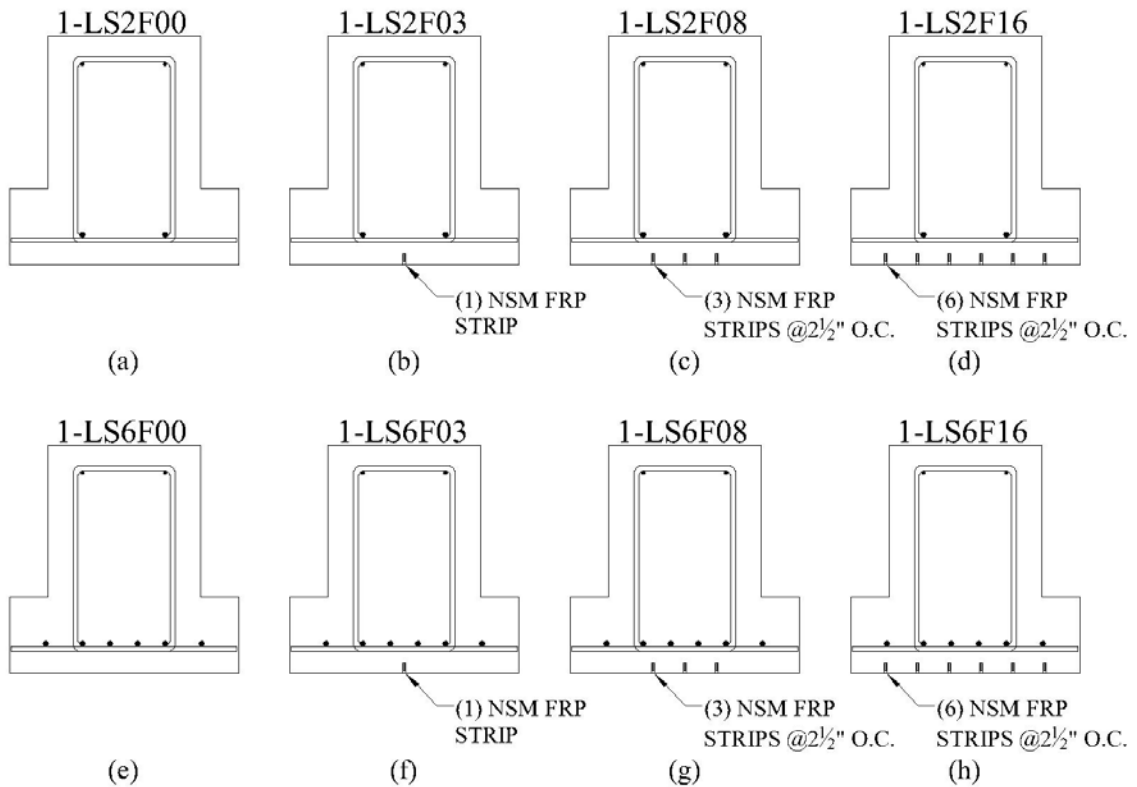


**Figure 6-4:** Specimen Names and Cross Sections for Test Series 1

As shown in Figure 6-4, the lateral spacing of the NSM strips is 2 1/2 in. The spacing was held constant to prevent any possible effects from the FRP spacing being included in the tests; however, if noticeable distress is observed in the concrete surrounding the NSM strips in specimen 1-LS6F16, then the spacing of the FRP relative to the flexural steel could be a concern. To determine the length of the beams, the shear

span-to-depth ratio was studied. Because the Letohatchee bridge is subjected to moving loads and has variable-depth girders, its shear span-to-depth ratio is not clear; however, the shear span-to-depth ratio was estimated to be about 1 to 2. To minimize the influence of shear on the flexural behavior, the test specimens were designed to have a shear span-to-depth ratio of approximately 4. Because the effective depth of the specimens is 15 5/8 in., the required shear span was calculated to be about 5 ft. By doubling the shear span, adding 3 ft for the spreader beam, and adding 6 in. on both ends of the girder for extra bearing, the total length of each specimen is 14 ft.

### **6.3.3 Anticipated Behavior and Failure Modes**

The cracking moments, yield moments, and nominal moment capacities were all calculated for the unstrengthened beams. The cracking moment calculations were based on Section 9.5.2.3 of ACI 318-08, except that a transformed section was used for the reinforced concrete instead of a gross section. The yield moment and nominal moment capacity calculations were based on a cracked-section analysis. To calculate the nominal moment capacity, the equivalent rectangular concrete stress distribution as stated in Section 10.2.7 of ACI 318-08 was assumed. The FRP-strengthened moment capacities and the stresses and strains for the steel, FRP, and concrete were calculated using three different models that address IC debonding: ACI 440 (2008), Seracino et al. (2007a), and Standards Australia (2008).

### 6.3.3.1 Unstrengthened Specimens

Table 6-2 shows the computed cracking moments, yield moments, and nominal moment strengths for the unstrengthened specimens 1-LS2F00 and 1-LS6F00. These values are also valid for the other specimens in Test Series 1 before the FRP is applied.

**Table 6-2:** Unstrengthened Moments for Specimens in Test Series 1

Specimen	$M_{cr}$ (kip-ft)	$M_y$ (kip-ft)	$M_n$ (kip-ft)
1-LS2 series	30.4	24.5	25.5
1-LS6 series	31.8	70.6	73.2

As shown in Table 6-2, the cracking moment,  $M_{cr}$ , is greater than both the yield moment,  $M_y$ , and the nominal moment,  $M_n$ , for specimens in the 1-LS2 series. This unusual behavior is most likely because the required minimum amount of flexural steel is greater than the actual amount of steel. For these specimens, the minimum amount of flexural steel required by ACI and AASHTO is 0.75 and 0.89 in.<sup>2</sup>, respectively; for these specimens, 0.40 in.<sup>2</sup> is provided. For specimens in the 1-LS6 series, the amount required is 0.75 and 0.98 in.<sup>2</sup>, respectively; for these specimens, 1.20 in.<sup>2</sup> are provided. For the Letohatchee bridge, only 1.92 in.<sup>2</sup> of flexural steel are provided, and ACI and AASHTO require 3.37 and 6.25 in.<sup>2</sup>, respectively. A possible reason for the large discrepancy between the two organizations might be because the AASHTO requirement is dependent upon the cracking moment, and the Letohatchee bridge has a very large cracking moment relative to the nominal moment capacity because of its wide flange.

### **6.3.3.2 Strengthened Specimens**

Using the three models previously mentioned, the strengthened moment capacities at which IC debonding occurs were predicted for the FRP-strengthened specimens. For these models, the mean values were used to try to accurately predict the FRP-strengthened beam behavior; therefore, no reduction factors were used. The capacities were also calculated for non-anchorage failures, such as rupture of the FRP or crushing of the concrete, to show the relative size of the IC-debonding capacities compared to the capacities for the non-anchorage failures. Table 6-3 shows the predicted nominal moment capacities, stresses and strains for the steel and FRP, concrete strains, and failure modes.

**Table 6-3:** Predicted Strengthened Capacities, Stresses, Strains, and Failure Modes

Specimen ID	Model used for predictions	$M_n$ (k-ft)	$\epsilon_s$	$f_s$ (ksi)	$\epsilon_{frp}$	$f_{frp}$ (ksi)	$\epsilon_c$	Failure mode
1-LS2F03	M1 (ACI)	39.9	0.0102	50	0.0117	210	0.0012	IC
	M2 (Seracino)	38.9	0.0095	50	0.0109	196	0.0012	IC
	M3 (SA)	38.0	0.0089	50	0.0102	184	0.0011	IC
	non-anch. failure	46.3	0.0145	50	0.0167	<b>300</b>	0.0017	R
1-LS2F08	M1 (ACI)	68.6	0.0101	50	0.0117	210	0.0017	IC
	M2 (Seracino)	65.8	0.0094	50	0.0109	196	0.0016	IC
	M3 (SA)	63.3	0.0089	50	0.0102	184	0.0015	IC
	non-anch. failure	86.8	0.0144	50	0.0167	<b>300</b>	0.0027	R
1-LS2F16	M1 (ACI)	109.9	0.0100	50	0.0117	210	0.0025	IC
	M2 (Seracino)	104.6	0.0094	50	0.0109	196	0.0023	IC
	M3 (SA)	99.9	0.0088	50	0.0102	184	0.0021	IC
	non-anch. failure	118.4	0.0111	50	0.0130	233	<b>0.003</b>	CC
1-LS6F03	M1 (ACI)	87.2	0.0101	50	0.0117	210	0.0022	IC
	M2 (Seracino)	86.3	0.0094	50	0.0109	196	0.0021	IC
	M3 (SA)	85.4	0.0088	50	0.0102	184	0.0020	IC
	non-anch. failure	92.4	0.0140	50	0.0162	292	<b>0.003</b>	CC
1-LS6F08	M1 (ACI)	113.8	0.0100	50	0.0117	210	0.0028	IC
	M2 (Seracino)	111.3	0.0093	50	0.0109	196	0.0026	IC
	M3 (SA)	109.1	0.0088	50	0.0102	184	0.0024	IC
	non-anch. failure	115.9	0.0106	50	0.0124	223	<b>0.003</b>	CC
1-LS6F16	M1 (ACI)	-----	-----	-----	-----	-----	-----	CC
	M2 (Seracino)	-----	-----	-----	-----	-----	-----	CC
	M3 (SA)	-----	-----	-----	-----	-----	-----	CC
	non-anch. failure	139.1	0.0083	50	0.0097	175	<b>0.003</b>	CC

Notes: M1- ACI 440 (2008)  
M2- Seracino et al. (2007a)  
M3- Standards Australia (2008)  
CC- crushing of the concrete  
IC- intermediate-crack debonding  
R- rupture of the FRP

In Table 6-3,  $M_n$  is the nominal moment;  $\epsilon_s$  is the steel strain;  $f_s$  is the steel stress;  $\epsilon_{frp}$  is the FRP strain;  $f_{frp}$  is the FRP stress; and  $\epsilon_c$  is the concrete strain. For all of the specimens, the steel reaches its yield stress of 50 ksi, and the strengthened capacity is greater than the unstrengthened capacity, which is shown in Table 6-2.

For five of the six strengthened specimens, the models predict an IC-debonding failure; however, for specimen 1-LS6F16, all three models predict a concrete crushing

failure. Because the stresses and strains are already shown for the non-anchorage failure, the values are not repeated for the models.

As shown in Table 6-3, the concrete strains become higher as more FRP strips are added. Similarly, as the amount of steel increases, the concrete strains increase. Consequently, the specimen with the most FRP and the most internal steel resulted in a concrete crushing failure prediction.

According to the IC-debonding models, the FRP stress and strain appear to be independent of both the amount of steel and the amount of FRP on the beams. As more steel and more FRP strips are added, the IC-debonding strain in the FRP remains constant for all three IC-debonding models. One of the main objectives of this test series is to investigate whether the IC-debonding behavior is actually independent of the amount of flexural reinforcement (steel or FRP).

#### **6.4 Test Series 2**

Three different specimens are proposed for Test Series 2: 2-LS2F00, 2-LS2F00-d, and 2-LS2F03-d. Specimen 2-LS2F00 is identical to specimen 1-LS2F00, the control beam from Test Series 1 that had a mechanical reinforcement ratio similar to the Letohatchee bridge. Specimen 2-LS2F00-d has an effective depth of about twice that of the first specimen. It also has twice the amount of steel so that the mechanical reinforcement ratio remains about the same. Specimen 2-LS2F03-d has the deeper cross section and is strengthened with two thin NSM strips.

Specimen 2-LS2F00 was included to provide a reference point to the specimens in Test Series 1. By duplicating the control beam from Test Series 1, the capacities can be

adjusted for any changes in the concrete compressive strength between the two test series, and a more accurate comparison can be made between the beams in Test Series 1 and the deeper beams in Test Series 2. All of the specimens in Test Series 2 should be cast from the same batch of concrete.

#### **6.4.1 Objectives of Test Series**

The main objectives of Test Series 2 are to study the effects of the cross-sectional shape, specifically the depth of the section, and the amount of FRP on the strengthened moment capacity and to determine the most accurate IC-debonding model for the test results.

#### **6.4.2 Description of Specimens**

As in Test Series 1, the specimens in Test Series 2 have a concrete compressive strength of 3000 psi. The steel reinforcement ratio for the deeper beams was held constant at about 0.2% by doubling the amount of steel from two to four #4 bars. Figure 6-5 shows both of the cross sections used in Test Series 2.

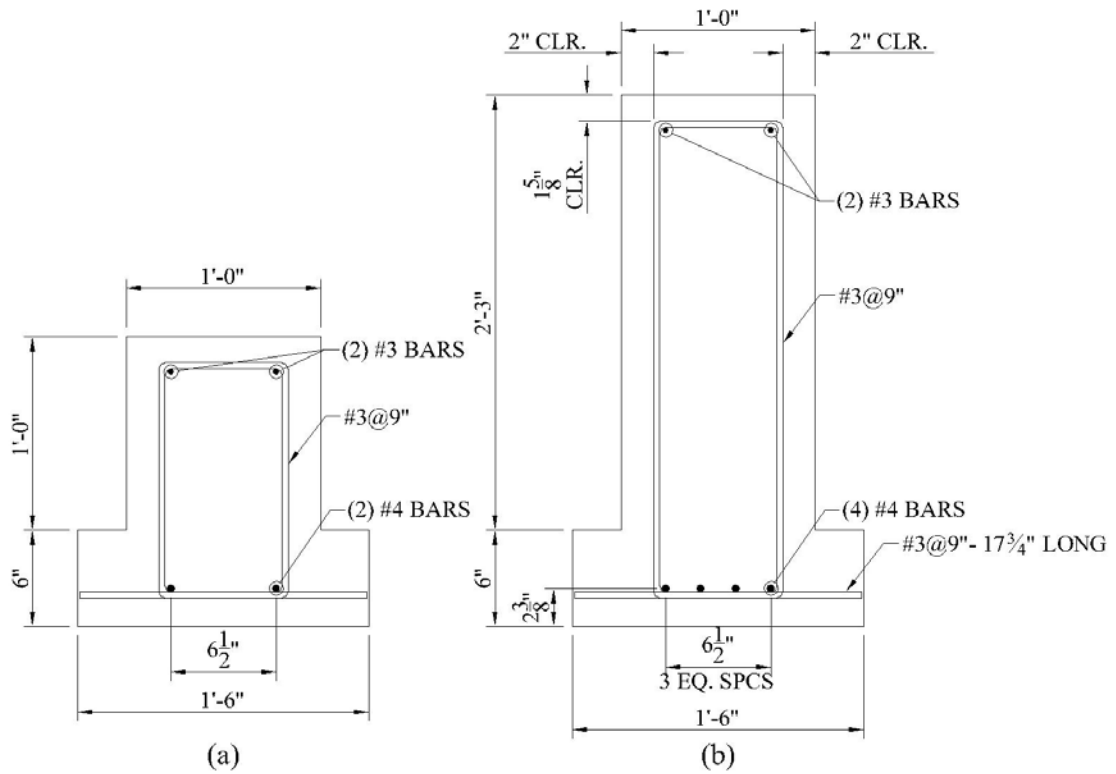


**Figure 6-5:** (a) Cross Section of Specimen 2-LS2F00 (b) Cross Section for Deeper Specimens

For the two specimens represented by the cross section in Figure 6-5b, one beam is left unstrengthened and is used as a control beam, and the other is strengthened with two thin NSM strips. The specimen names and cross sections for Test Series 2 are shown in Figure 6-6.



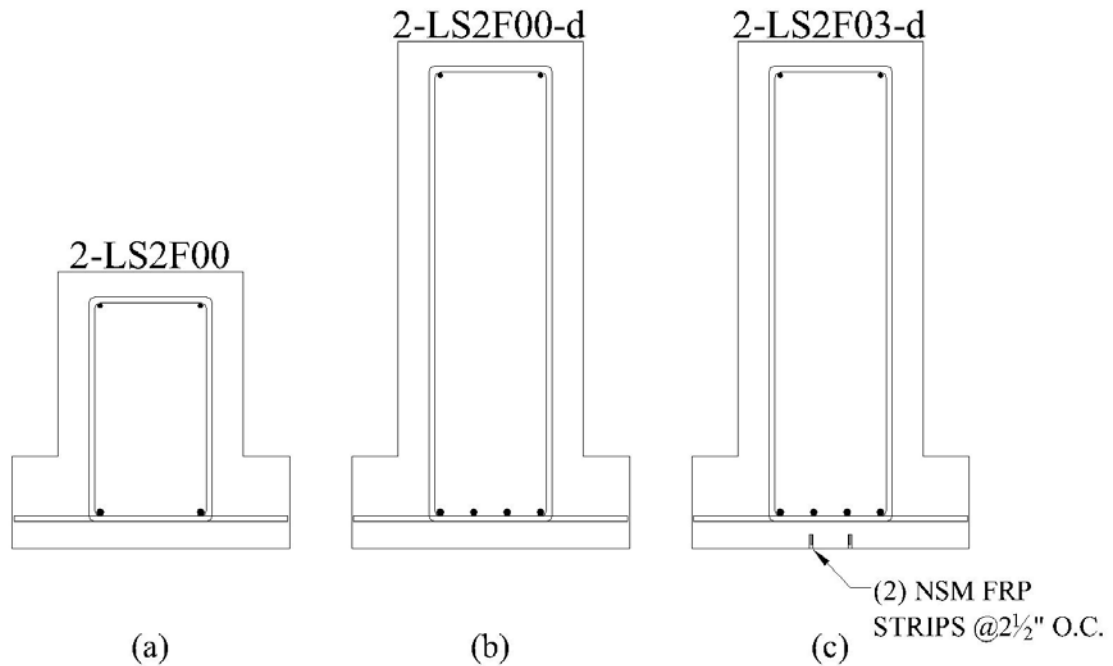


**Figure 6-6:** Specimen Names and Cross Sections for Test Series 2

As in Test Series 1, the shear span-to-depth ratio was studied to determine the lengths of the beams for Test Series 2. For specimen 2-LS2F00, which is exactly like specimen 1-LS2F00, 5 ft will be used for its shear span, and 14 ft will be used for its length. The other two specimens have an effective depth of 30 5/8 in. By using a shear span-to-depth ratio of approximately 4 again, the shear span was calculated to be about 10 ft, which makes the total length of the specimens 24 ft.

Only three specimens were proposed for Test Series 2 because of practical considerations. The volume of concrete that a concrete truck can transport is about 9 yd<sup>3</sup>. The volume of concrete for the three specimens in this test series is about 6.5 yd<sup>3</sup>. Adding another deep beam to the test series would have exceeded the limit of the concrete truck.

Because it was a priority to have all of the concrete be from the same batch for this test series, only three specimens are proposed.

### 6.4.3 Anticipated Behavior and Failure Modes

The cracking moments, yield moments, and nominal moment capacities were all calculated for the unstrengthened beams as described above for Test Series 1. Likewise, the FRP-strengthened moment capacities and the stresses and strains for the steel, FRP, and concrete were calculated using three different models: ACI 440 (2008), Seracino et al. (2007a), and Standards Australia (2008).

#### 6.4.3.1 Unstrengthened Specimens

Table 6-4 shows the cracking moments, yield moments, and nominal moment capacities for the unstrengthened specimens 2-LS2F00 and 2-LS2F00-d. The values for specimen 2-LS2F00-d are also valid for specimen 2-LS2F03-d before the FRP is applied.

**Table 6-4:** Unstrengthened Moments for Specimens in Test Series 2

Specimen	$M_{cr}$ (kip-ft)	$M_y$ (kip-ft)	$M_n$ (kip-ft)
2-LS2F00	30.4	24.5	25.5
2-LS2F00-d 2-LS2F03-d	97.3	95.9	99.9

The values for specimen 2-LS2F00 are the same as the values from Table 6-2 for the 1-LS2 series because they are exactly the same. Once again, the cracking moment is shown to be greater than both the yield moment and the nominal moment. For specimens 2-LS2F00-d and 2-LS2F03-d, the cracking moment is greater than the yield moment but less than the nominal moment. For these two specimens, the required minimum amount

of steel is 1.47 and 1.46 in.<sup>2</sup> using the ACI and AASHTO methods, respectively. For these specimens, only 0.80 in.<sup>2</sup> is provided, which results in large cracking moments in relation to nominal moment capacities.

#### 6.4.3.2 Strengthened Specimens

Using the three models previously mentioned, the strengthened moment capacity at which IC debonding occurs was predicted for the FRP-strengthened specimen. For these models, the mean values were used to try to accurately predict the FRP-strengthened beam behavior; therefore, no reduction factors were used. The capacity was also calculated for non-anchorage failures, such as rupture of the FRP or crushing of the concrete, to show the relative size of the IC-debonding capacities compared to the capacity for the non-anchorage failures. Table 6-5 shows the predicted nominal moment capacities, stresses and strains for the steel and FRP, concrete strains, and failure modes.

**Table 6-5:** Predicted Strengthened Capacities, Stresses, Strains, and Failure Modes

Specimen ID	Model used for predictions	$M_n$ (k-ft)	$\epsilon_s$	$f_s$ (ksi)	$\epsilon_{frp}$	$f_{frp}$ (ksi)	$\epsilon_c$	Failure mode
2-LS2F03-d	M1 (ACI)	153.0	0.0108	50	0.0117	210	0.0013	IC
	M2 (Seracino)	149.4	0.0101	50	0.0109	196	0.0012	IC
	M3 (SA)	146.2	0.0095	50	0.0102	184	0.0012	IC
	non-anch. failure	176.7	0.0155	50	0.0167	<b>300</b>	0.0018	R

Notes: M1- ACI 440 (2008)  
M2- Seracino et al. (2007a)  
M3- Standards Australia (2008)  
IC- intermediate-crack debonding  
R- rupture of the FRP

For the strengthened specimen shown in Table 6-5, the steel reaches its yield stress of 50 ksi. Also, the strengthened capacity is greater than the unstrengthened capacity from Table 6-4 by about 50 kip-ft, which results in a strengthened capacity

about 50% greater than the unstrengthened capacity. For this specimen, all of the models predict an IC-debonding failure will occur before a non-anchorage failure.

### **6.5 Test Series 3**

Four different specimens are proposed for Test Series 3: 3-MS2F00, 3-MS2F03, 3-MS2F08, and 3-MS2F16. These specimens all have the same cross section initially, but three of the specimens are strengthened with one, three, and six thin FRP strips, respectively. These four specimens are very similar to the first set of specimens in Test Series 1, except the specimens in Test Series 3 have a proposed concrete compressive strength of 5000 psi.

#### **6.5.1 Objectives of Test Series**

The main objectives of Test Series 3 are to study the effects of the concrete compressive strength and the amount of FRP on the strengthened moment capacity and to determine the most accurate IC-debonding model for the test results.

#### **6.5.2 Description of Specimens**

The specimens in Test Series 3 all have the same cross section initially. This cross section is shown in Figure 6-7.

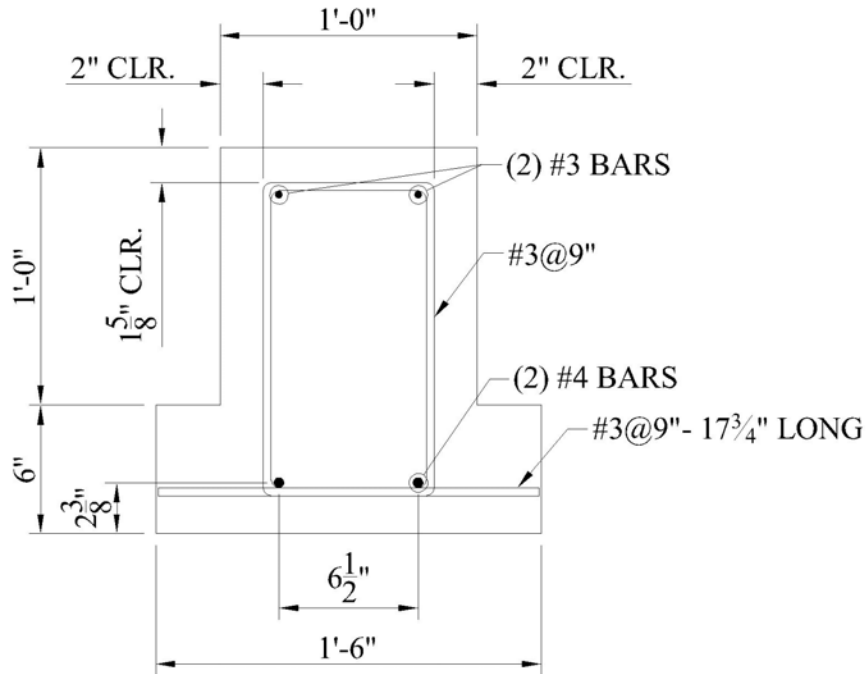


**Figure 6-7:** Cross Section of Specimens in Test Series 3

Three of the specimens will be strengthened with one, three, and six thin FRP strips, respectively. The specimen names and cross sections for Test Series 3 are shown in Figure 6-8.

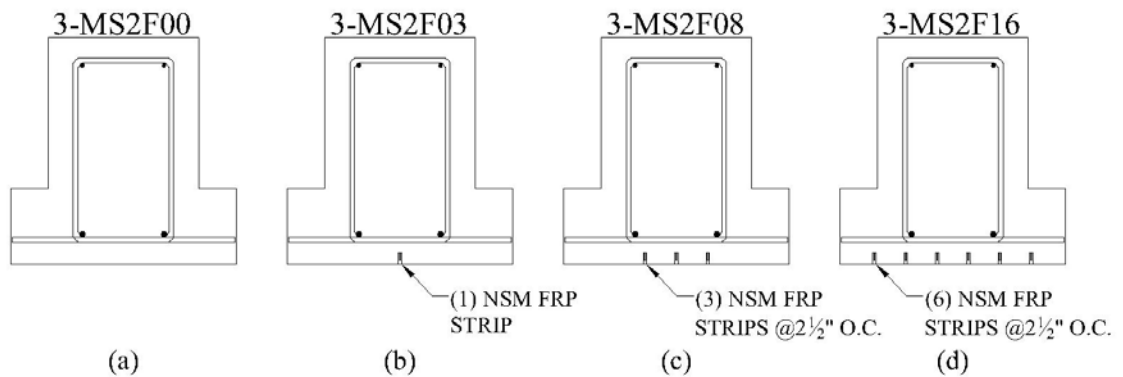


**Figure 6-8:** Specimen Names and Cross Sections for Test Series 3

Because the specimens in this test series have the same cross-sectional dimensions as the specimens in Test Series 1, the same shear span of 5 ft and the same beam length of 14 ft will be used. Once again, the number and size of the specimens was dependent upon the volume of concrete that could be transported in one batch.

### 6.5.3 Anticipated Behavior and Failure Modes

The cracking moments, yield moments, and nominal moment capacities were all calculated for the unstrengthened beams as described above for Test Series 1. Likewise, the FRP-strengthened moment capacities and the stresses and strains for the steel, FRP, and concrete were calculated using three different models: ACI 440 (2008), Seracino et al. (2007a), and Standards Australia (2008).

#### 6.5.3.1 Unstrengthened Specimens

Table 6-6 shows the cracking moment, yield moment, and nominal moment capacities for the unstrengthened specimen. The values shown are also valid for the strengthened specimens before the FRP is applied.

**Table 6-6:** Unstrengthened Moments for Specimens in Test Series 3

Specimen	$M_{cr}$ (kip-ft)	$M_y$ (kip-ft)	$M_n$ (kip-ft)
all specimens	39.0	24.6	25.7

For these specimens, the required minimum amount of steel is 0.80 and 1.14 in.<sup>2</sup> using the ACI and AASHTO methods, respectively, and only 0.40 in.<sup>2</sup> is provided. As in Test Series 1, the lack of steel causes the cracking moment to be greater than the unstrengthened nominal moment capacity.

### 6.5.3.2 Strengthened Specimens

Using the three models previously mentioned, the strengthened moment capacities at which IC debonding occurs were predicted for the FRP-strengthened specimens. For these models, the mean values were used to try to accurately predict the FRP-strengthened beam behavior; therefore, no reduction factors were used. The capacities were also calculated for non-anchorage failures, such as rupture of the FRP or crushing of the concrete, to show the relative size of the IC-debonding capacities compared to the capacities for the non-anchorage failures. Table 6-7 shows the predicted nominal moment capacities, stresses and strains for the steel and FRP, concrete strains, and failure modes.

**Table 6-7:** Predicted Strengthened Capacities, Stresses, Strains, and Failure Modes

Specimen ID	Model used for predictions	$M_n$ (k-ft)	$\epsilon_s$	$f_s$ (ksi)	$\epsilon_{frp}$	$f_{frp}$ (ksi)	$\epsilon_c$	Failure mode
3-MS2F03	M1 (ACI)	40.3	0.0102	50	0.0117	210	0.0009	IC
	M2 (Seracino)	43.4	0.0123	50	0.0141	253	0.0011	IC
	M3 (SA)	40.9	0.0106	50	0.0121	218	0.0010	IC
	non-anch. failure	46.8	0.0146	50	0.0167	<b>300</b>	0.0012	R
3-MS2F08	M1 (ACI)	69.6	0.0102	50	0.0117	210	0.0013	IC
	M2 (Seracino)	78.8	0.0123	50	0.0141	253	0.0015	IC
	M3 (SA)	71.4	0.0106	50	0.0121	218	0.0013	IC
	non-anch. failure	88.6	0.0145	50	0.0167	<b>300</b>	0.0018	R
3-MS2F16	M1 (ACI)	112.8	0.0101	50	0.0117	210	0.0017	IC
	M2 (Seracino)	130.5	0.0122	50	0.0141	253	0.0021	IC
	M3 (SA)	116.1	0.0105	50	0.0121	218	0.0018	IC
	non-anch. failure	149.1	0.0144	50	0.0167	<b>300</b>	0.0027	R

Notes: M1- ACI 440 (2008)  
M2- Seracino et al. (2007a)  
M3- Standards Australia (2008)  
IC- intermediate-crack debonding  
R- rupture of the FRP

For all of the strengthened specimens shown in Table 6-7, the steel reaches its yield stress of 50 ksi, and the strengthened capacity is greater than the unstrengthened

capacity from Table 6-6. For this specimen, all of the models predict an IC-debonding failure will occur before an FRP rupture failure.

For Test Series 1 and 2, all of the models produced very similar results, with the ACI 440 (2008) model producing the largest strengthened capacity; however, in Test Series 3, the Seracino et al. (2007a) model produced the largest strengthened capacity, which is most likely a result of the increased concrete compressive strength of Test Series 3. The ACI 440 model is not highly sensitive to the concrete compressive strength, and the Seracino et al. model is the most sensitive to it.

## **6.6 Test Series 4**

Four different specimens are proposed for Test Series 4: 4-HS2F00, 4-HS2F03, 4-HS2F08, and 4-HS2F16. These specimens all have the same cross section initially, but three of the specimens are strengthened with one, three, and six thin FRP strips, respectively. These four specimens are very similar to the first set of specimens in Test Series 1 and all of the specimens in Test Series 3, except the specimens in Test Series 4 have a proposed concrete compressive strength of 7000 psi.

### **6.6.1 Objectives of Test Series**

The main objectives of Test Series 4 are to study the effects of the concrete compressive strength and the amount of FRP on the strengthened moment capacity and to determine the most accurate IC-debonding model for the test results.



### 6.6.2 Description of Specimens

The specimens in Test Series 4 all have the same cross section initially. This cross section is shown in Figure 6-9.

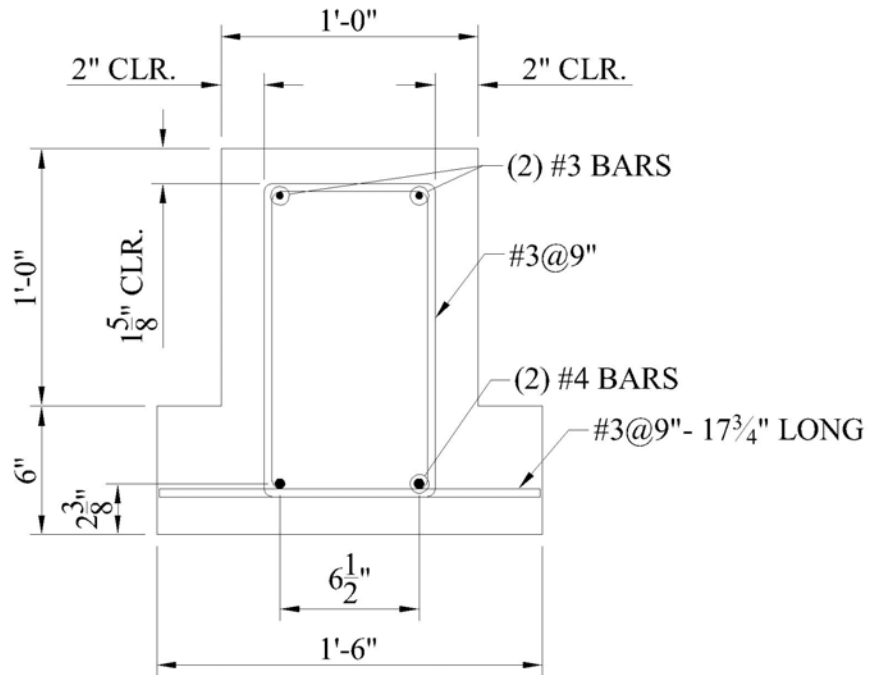


**Figure 6-9:** Cross Section of Specimens in Test Series 4

Three of the specimens will be strengthened with one, three, and six thin FRP strips, respectively. The specimen names and cross sections for Test Series 4 are shown in Figure 6-10.

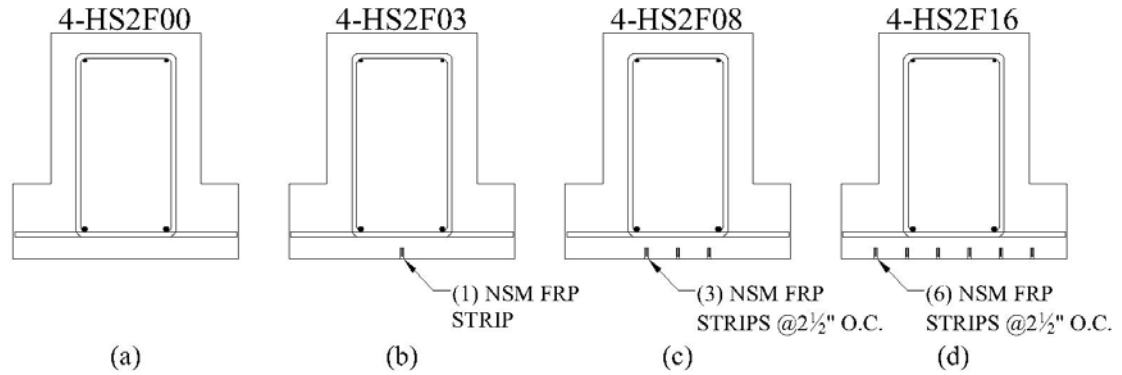


**Figure 6-10:** Specimen Names and Cross Sections for Test Series 4

Because the specimens in this test series have the same cross-sectional dimensions as the specimens in Test Series 1 and Test Series 3, the same shear span of 5 ft and the same beam length of 14 ft will be used. Like the other test series, the number and size of the specimens was dependent upon the volume of concrete that could be transported in one batch.

### 6.6.3 Anticipated Behavior and Failure Modes

The cracking moments, yield moments, and nominal moment capacities were all calculated for the unstrengthened beams as described above for Test Series 1. Likewise, the FRP-strengthened moment capacities and the stresses and strains for the steel, FRP, and concrete were calculated using three different models: ACI 440 (2008), Seracino et al. (2007a), and Standards Australia (2008).

### 6.6.3.1 Unstrengthened Specimens

Table 6-8 shows the cracking moment, yield moment, and nominal moment capacities for the unstrengthened specimen. The values shown are also valid for the strengthened specimens before the FRP is applied.

**Table 6-8:** Unstrengthened Moments for Specimens in Test Series 4

Specimen	$M_{cr}$ (kip-ft)	$M_y$ (kip-ft)	$M_n$ (kip-ft)
all specimens	46.0	24.8	25.8

For these specimens, the required minimum amount of steel is 0.94 and 1.34 in.<sup>2</sup> using the ACI and AASHTO methods, respectively, and only 0.40 in.<sup>2</sup> is provided. As in Test Series 1 and Test Series 3, the lack of steel causes the cracking moment to be greater than the unstrengthened nominal moment.

### 6.6.3.2 Strengthened Specimens

Using the three models previously mentioned, the strengthened moment capacities at which IC debonding occurs were predicted for the FRP-strengthened specimens. For these models, the mean values were used to try to accurately predict the FRP-strengthened beam behavior; therefore, no reduction factors were used. The capacities were also calculated for non-anchorage failures, such as rupture of the FRP or crushing of the concrete, to show the relative size of the IC-debonding capacities compared to the capacities for the non-anchorage failures. Table 6-9 shows the predicted nominal moment capacities, stresses and strains for the steel and FRP, concrete strains, and failure modes.

**Table 6-9:** Predicted Strengthened Capacities, Stresses, Strains, and Failure Modes

Specimen ID	Model used for predictions	$M_n$ (k-ft)	$\epsilon_s$	$f_s$ (ksi)	$\epsilon_{frp}$	$f_{frp}$ (ksi)	$\epsilon_c$	Failure mode
4-HS2F03	M1 (ACI)	40.5	0.0102	50	0.0117	210	0.0008	IC
	M2 (Seracino)	47.0	0.0146	50	0.0166	300	0.0010	IC
	M3 (SA)	42.9	0.0119	50	0.0135	244	0.0009	IC
	non-anch. failure	47.0	0.0146	50	0.0167	<b>300</b>	0.0010	R
4-HS2F08	M1 (ACI)	70.1	0.0102	50	0.0117	210	0.0010	IC
	M2 (Seracino)	89.2	0.0145	50	0.0166	300	0.0014	IC
	M3 (SA)	77.3	0.0118	50	0.0135	244	0.0012	IC
	non-anch. failure	89.3	0.0146	50	0.0167	<b>300</b>	0.0014	R
4-HS2F16	M1 (ACI)	113.9	0.0101	50	0.0117	210	0.0014	IC
	M2 (Seracino)	151.3	0.0145	50	0.0166	300	0.0020	IC
	M3 (SA)	128.0	0.0118	50	0.0135	244	0.0016	IC
	non-anch. failure	151.4	0.0145	50	0.0167	<b>300</b>	0.0020	R

Notes: M1- ACI 440 (2008)  
M2- Seracino et al. (2007a)  
M3- Standards Australia (2008)  
IC- intermediate-crack debonding  
R- rupture of the FRP

For all of the strengthened specimens shown in Table 6-9, the steel reaches its yield stress of 50 ksi, and the strengthened capacity is greater than the unstrengthened capacity from Table 6-8. For this specimen, all of the models predict an IC-debonding failure will occur before an FRP rupture failure. As in Test Series 3, the Seracino et al. (2007a) model produced the largest strengthened capacities, which were significantly greater than the strengthened capacities predicted by the ACI 440 (2008) model. Once again, the Seracino et al. model is the most sensitive to the concrete compressive strength, while the ACI 440 model is the least sensitive to it.

## **Chapter 7: Summary and Conclusions**

### **7.1 Summary**

The Letohatchee bridge has been identified as being deficient under certain types of truck loadings. For this bridge, there are currently load restrictions on some vehicles due to deficiencies in the negative-moment regions of the girders. To remove the load restrictions, different FRP-strengthening techniques were investigated. Because the deficiencies occurred in the negative-moment regions of the continuous bridge girders, near-surface mounted (NSM) FRP strips, as opposed to externally-bonded (EB) FRP strips, are proposed for the strengthening of the Letohatchee bridge.

As reported in this thesis, the Letohatchee bridge was specifically investigated to determine the amount of strengthening that is needed. NSM behavior was then examined to determine the amount of strengthening that it can provide.

The Bridge Rating and Analysis of Structural Systems (BRASS™) program was used to determine the flexural demands on the Letohatchee bridge. These moments were then factored using the operating load combination. Once the demand was known, the bridge's capacity was calculated. The capacity was reduced by a reduction factor and compared to the demand to determine the exact locations and magnitudes of the deficiencies. The locations of the deficiencies for the exterior and interior girders were the same. Because the deficiencies in the exterior girder were found to be more critical

than the deficiencies in the interior girder, the exterior girder was used for the design of the strengthening scheme.

Various models and code recommendations that are used to predict FRP-strengthened moment capacities were investigated. Two types of debonding models were analyzed: plate-end (PE) debonding and intermediate-crack (IC) debonding. The IC-debonding models consisted of models for EB and models for NSM. For the PE-debonding models, the focus was solely on NSM. Using previous experimental results, the various models were compared to each other to determine the most accurate models for the given tests.

Once the more accurate models were determined, a strengthening scheme was designed for the Letohatchee bridge using these models. In the proposed strengthening scheme, the amount and spacing of the NSM were chosen for different concrete compressive strengths.

The steel and FRP reinforcement ratios for the Letohatchee bridge were compared to the ratios for previous experimental tests. The reinforcement ratios for the bridge were found to be lower than the ratios for the experimental tests. Also, none of the NSM test specimens were cracked prior to FRP strengthening. To be able to use laboratory test results that can be directly applied to the bridge, a laboratory testing program was developed. Because the proposed strengthening scheme employed NSM strips, only NSM was studied in the testing program. The proposed testing program has four main objectives. The first objective is to develop a relationship between the proposed test specimens and the Letohatchee bridge to more effectively and more efficiently propose an NSM FRP-strengthening scheme for the bridge. The second objective is to study the

IC-debonding behavior to better quantify when and if it will occur and to verify the existing IC-debonding models. The third objective is to study the effects of the concrete compressive strength, amount of steel reinforcement, amount of FRP reinforcement, and cross-sectional shape on the strengthened moment capacity. The fourth objective is to evaluate the effectiveness of the FRP in a strengthening type of situation by cracking the unstrengthened specimens before applying the FRP.

Four different test series are proposed to achieve these objectives. In the first test series, the amount of tension steel and the amount of FRP are varied to determine the corresponding effects on the strengthened moment capacity. In the second test series, the overall height of the specimens is increased while holding the reinforcement ratio constant to evaluate whether a size effect is present. In the third and fourth test series, the concrete compressive strength is increased to 5000 and 7000 psi, respectively, to establish whether the concrete strength has a significant effect on the IC-debonding behavior.

## **7.2 Conclusions**

Several conclusions are reported in this section for the various FRP-debonding models and the Letohatchee bridge and its strengthening scheme.

### **7.2.1 Debonding Models**

After using the existing experimental tests to determine the accuracy of the debonding models, several conclusions were reached:

1. None of the PE-debonding models correlated with the existing NSM tests.

2. For the IC-debonding models for EB FRP, the *fib* 9.3 (2001) model and the Seracino, Raizal Saifulnaz, and Oehlers (2007) model were not very accurate. The other four models – ACI 440 (2008), Standards Australia (2008), Rosenboom (2006), and Said and Wu (2008) – were all relatively accurate.
3. For the IC-debonding models for NSM FRP, the *fib* 9.3 (2001) model and the Said and Wu (2008) model were overly conservative and not very accurate. The other three models – Seracino et al. (2007a), Standards Australia (2008), and ACI 440 (2008) – were all relatively accurate.

### **7.2.2 Letohatchee Bridge**

Because three of the IC-debonding models were relatively accurate for the existing NSM tests, they were all used to determine the amount of NSM needed for the Letohatchee bridge. The following conclusions were reached for the Letohatchee bridge and its strengthening scheme:

1. The Letohatchee bridge's deficiencies occur in three main regions of the bridge. The FRP strips should extend over the following distance ranges, measured relative to the centerline of the girder end bearing: from 27 to 94 feet; from 100.5 to 169.5 feet; and from 176 to 243 feet. The lengths of the strips are 67, 69, and 67 feet, respectively.
2. If no concrete cores are taken from the bridge, then either twenty-four total thin NSM strips, six strips per girder, or twenty total thick NSM strips, five strips per girder, should be used.



3. If the concrete strength is determined to be between 4000 and 6000 psi, then sixteen total thick strips, four strips per girder, can be used.
4. If the concrete strength is determined to be between 6000 and 8000 psi, then twelve total thick strips, three strips per girder, can be used.
5. If thin strips are chosen, then twenty-four total strips, six strips per girder, should be used for any concrete strengths of 3000 psi or greater.
6. Spacing the strips fairly evenly across the cross section should effectively control service-level cracking while minimizing debonding interaction between the strips.

### **7.3 Recommendations**

For the Letohatchee bridge, concrete core samples should be extracted and tested to determine the compressive strength of the concrete. Once the concrete strength is known, a more efficient FRP-strengthening scheme can be implemented if thick strips are used.

In this study, debonding models were compared to previous test results to determine the accuracy of the models. Based on the results of this study, however, more testing on NSM is needed to verify the validity of the models and code recommendations. Flexural tests, as opposed to push-pull tests, are specifically needed to better simulate the actual conditions of the unstrengthened members. Another way to simulate the actual conditions is to crack the test specimens before the FRP is applied. The most direct approach, however, would be to have testing of full-scale strengthened bridge girders. Full-scale testing would be ideal for determining the effectiveness of the FRP systems. In-place testing of the strengthened Letohatchee bridge will provide valuable data about

the service-level performance of full-size members, but failure testing of an in-service bridge is not feasible.

## References

- AASHTO. 2006. *AASHTO LRFD Bridge Design Specifications: Customary U.S. Units*. 3<sup>rd</sup> ed. Washington, D.C.: American Association of State Highway and Transportation Officials (AASHTO).
- AASHTO. 1996. *AASHTO Standard Specifications for Highway Bridges*. 16<sup>th</sup> ed. Washington, D.C.: American Association of State Highway and Transportation Officials (AASHTO).
- ACI Committee 318. 2008. Building Code Requirements for Structural Concrete (ACI 318-08) and Commentary. Farmington Hills, Michigan: American Concrete Institute (ACI).
- ACI Committee 440. 2008. Guide for the Design and Construction of Externally Bonded FRP System for Strengthening Concrete Structures (ACI 440.2R-08). Farmington Hills, Michigan: American Concrete Institute (ACI).
- Blaschko, M. 2003. Bond Behaviour of CFRP Strips Glued into Slits. In *6<sup>th</sup> International Symposium on FRP Reinforcement for Concrete Structures (FRPRCS-6)*, ed. K. H. Tan. Singapore: World Scientific, 205-214.
- Carmichael, Benjamin M., and Robert W. Barnes. 2005. *Repair of the Uphapee Creek Bridge with FRP Laminates*. Final Report RP-930-466-2, Auburn, Alabama: Auburn University Highway Research Center.

- CEB. 1990. CEB-FIP Model Code 1990: Design Code. Lausanne, Switzerland: Euro-International Committee for Structural Concrete (CEB).
- De Lorenzis, Laura, and Antonio Nanni. 2002. Bond between Near-Surface Mounted Fiber-Reinforced Polymer Rods and Concrete in Structural Strengthening. *ACI Structural Journal* 99, no. 2: 123-132.
- El-Hacha, Raafat, and Sami H. Rizkalla. 2004. Near-Surface-Mounted Fiber-Reinforced Polymer Reinforcements for Flexural Strengthening of Concrete Structures. *ACI Structural Journal* 101, no. 5: 717-726.
- Fanning, Paul J., and Oliver Kelly. 2001. Ultimate Response of RC Beams Strengthened with CFRP Plates. *Journal of Composites for Construction* 5, no. 2: 122-127.
- fib Task Group 9.3. 2001. Externally bonded FRP reinforcement for RC structures (Bulletin 14). Lausanne, Switzerland: International Federation for Structural Concrete (*fib*).
- Google Maps. 2009. <http://maps.google.com> (accessed February 25, 2009).
- Hassan, Tarek, and Sami Rizkalla. 2003. Investigation of Bond in Concrete Structures Strengthened with Near Surface Mounted Carbon Fiber Reinforced Polymer Strips. *Journal of Composites for Construction* 7, no. 3: 248-257.
- Hassan, Tarek K., and Sami H. Rizkalla. 2004. Bond Mechanism of Near-Surface-Mounted Fiber-Reinforced Polymer Bars for Flexural Strengthening of Concrete Structures. *ACI Structural Journal* 101, no. 6: 830-839.
- Hilti. 2009. <http://www.hilti.com> (accessed May 6, 2009).
- Hughes Brothers. 2009. <http://hughesbros.com> (accessed March 24, 2009).

- Jung, W.-T., Y.-H. Park, J.-S. Park, J.-Y. Kang, and Y.-J. You. 2005. Experimental Investigation on Flexural Behavior of RC Beams Strengthened by NSM CFRP Reinforcements. In *7<sup>th</sup> International Symposium: Fiber-Reinforced Polymer (FRP) Reinforcement for Concrete Structures*, eds. Carol K. Shield, John P. Busel, Stephanie L. Walkup, and Doug D. Gremel. Farmington Hills, Michigan: American Concrete Institute, 795-806.
- Kang, J.-Y., Y.-H. Park, J.-S. Park, Y.-J. You, and W.-T. Jung. 2005. Analytical Evaluation of RC Beams Strengthened with Near Surface Mounted CFRP Laminates. In *7<sup>th</sup> International Symposium: Fiber-Reinforced Polymer (FRP) Reinforcement for Concrete Structures*, eds. Carol K. Shield, John P. Busel, Stephanie L. Walkup, and Doug D. Gremel. Farmington Hills, Michigan: American Concrete Institute, 779-794.
- Liu, I. S. T., D. J. Oehlers, and R. Seracino. 2006. Tests on the Ductility of Reinforced Concrete Beams Retrofitted with FRP and Steel Near-Surface Mounted Plates. *Journal of Composites for Construction* 10, no. 2: 106-114.
- Mattock, A., and N. Hawkins. 1972. Shear Transfer in Reinforced Concrete—Recent Research. *PCI Journal* 17, no. 2: 55-75.
- Oehlers, Deric John, Matthew Haskett, Chengqing Wu, and Rudolf Seracino. 2008. Embedding NSM FRP Plates for Improved IC Debonding Resistance. *Journal of Composites for Construction* 12, no. 6: 635-642.
- Rashid, R., D. J. Oehlers, and R. Seracino. 2008. IC Debonding of FRP NSM and EB Retrofitted Concrete: Plate and Cover Interaction Tests. *Journal of Composites for Construction* 12, no. 2: 160-167.

- Reed, Michael W., Robert W. Barnes, Anton K. Schindler, and Hwan-Woo Lee. 2005. Fiber-Reinforced Polymer Strengthening of Concrete Bridges that Remain Open to Traffic. *ACI Structural Journal* 102, no. 6: 823-831.
- Reed, Michael Wayne. 2003. Effects of Traffic Loads during FRP Strengthening of the War Memorial Bridge. Master's Thesis, Auburn University.
- Rosenboom, Owen Arthur. 2006. Behavior of FRP Repair/Strengthening Systems for Prestressed Concrete. Ph.D. diss., North Carolina State University.
- Said, Hemdan, and Zhishen Wu. 2008. Evaluating and Proposing Models of Predicting IC Debonding Failure. *Journal of Composites for Construction* 12, no. 3: 284-299.
- Sena Cruz, Jose Manuel de, and Joaquim Antonio Oliveira de Barros. 2004. Bond Between Near-Surface Mounted Carbon-Fiber-Reinforced Polymer Laminate Strips and Concrete. *Journal of Composites for Construction* 8, no. 6: 519-527.
- Sena Cruz, Jose M., Joaquim A. O. Barros, Ravindra Gettu, and Alvaro F. M. Azevedo. 2006. Bond Behavior of Near-Surface Mounted CFRP Laminate Strips under Monotonic and Cyclic Loading. *Journal of Composites for Construction* 10, no. 4: 295-303.
- Seracino, Rudolf, Nicola M. Jones, M. S. M. Ali, Mark W. Page, and Deric J. Oehlers. 2007a. Bond Strength of Near-Surface Mounted FRP Strip-to-Concrete Joints. *Journal of Composites for Construction* 11, no. 4: 401-409.
- Seracino, R., M. R. Raizal Saifulnaz, and D. J. Oehlers. 2007b. Generic Debonding Resistance of EB and NSM Plate-to-Concrete Joints. *Journal of Composites for Construction* 11, no. 1: 62-70.

- Standards Australia. 2008. Design handbook for RC structures retrofitted with FRP and metal plates: beams and slabs (HB 305-2008). Sydney, Australia: Standards Australia.
- Taljsten, Bjorn, and Hakan Nordin. 2007. Concrete Beams Strengthened with External Prestressing Using External Tendons and Near-Surface-Mounted Reinforcement (NSMR). In *SP-245CD Case Histories and Use of FRP for Prestressing Applications*, eds. Raafat El-Hacha and Sami H. Rizkalla. Farmington Hills, Michigan: American Concrete Institute, 143-164. CD-ROM.
- Teng, J. G., L. De Lorenzis, Bo Wang, Rong Li, T. N. Wong, and Lik Lam. 2006. Debonding Failures of RC Beams Strengthened with Near Surface Mounted CFRP Strips. *Journal of Composites for Construction* 10, no. 2: 92-105.
- Vasquez Rayo, Diego L. 2008. Plate-End Debonding of Longitudinal Near-Surface Mounted Fiber Reinforced Polymer Strips on Reinforced Concrete Flexural Members. Master's thesis, North Carolina State University.
- Wyoming Department of Transportation. 2009. BRASS™ program.  
<http://dot.state.wy.us/web/brass/index.html> (accessed April 21, 2009).
- Yalim, Baris, Ahmet Serhat Kalayci, and Amir Mirmiran. 2008. Performance of FRP-Strengthened RC Beams with Different Concrete Surface Profiles. *Journal of Composites for Construction* 12, no. 6: 626-634.
- Yost, Joseph Robert, Shawn P. Gross, David W. Dinehart, and Jason J. Mildenberg. 2007. Flexural Behavior of Concrete Beams Strengthened with Near-Surface-Mounted CFRP Strips. *ACI Structural Journal* 104, no. 4: 430-437.

## APPENDIX A: NOTATION

$A_s$	= area of nonprestressed steel reinforcement
$A_f$	= area of FRP reinforcement
$a_b$	= smaller cross-sectional dimension for rectangular FRP bars
$a_r$	= distance between the strip and the edge of the concrete member
$b$	= width of the compression face of the member
$b_b$	= larger cross-sectional dimension for rectangular FRP bars
$b_c$	= width of the concrete
$b_f$	= width of the FRP ( <i>fib</i> 9.3 2001)
$b_f$	= length of the failure surface parallel to the concrete surface (Seracino, Raizal Saifulnaz, and Oehlers 2007)
$b_L$	= width of the FRP strip
$b_p$	= width of the EB plate (Standards Australia)
$b_p$	= plate dimension parallel to the concrete surface (Seracino et al. 2007a)
$b_w$	= web width of the concrete member
$c$	= distance from the extreme compression fiber to the neutral axis
$C1$	= constant
$C2$	= constant
$C3$	= constant
$C_E$	= environmental reduction factor
CLR.	= clear
$d$	= distance from the extreme compression fiber to the centroid of the tension reinforcement
$d_b$	= FRP bar diameter
$d_f$	= effective depth of the FRP flexural reinforcement
$d_f$	= length of the failure surface perpendicular to the concrete surface (Seracino, Raizal Saifulnaz, and Oehlers 2007)
$d_{NSM-tp}$	= distance between the centroid of the specific NSM plate and the neutral axis of the cracked plated section
$d_p$	= plate dimension perpendicular to the concrete surface
$(EA)_p$	= axial rigidity of the FRP
$E_f$	= modulus of elasticity of the FRP
$(EI)_{cr.pl}$	= flexural rigidity of the cracked plated cross section adjacent to the plate end
$E_p$	= modulus of elasticity of the plate
$E_s$	= modulus of elasticity of steel



$f_c$	=	concrete cylinder compressive strength
$f'_c$	=	concrete compressive strength
$f_{cb}$	=	Brazilian or splitting tensile strength of the concrete
$f_{cbd}$	=	bond shear strength of concrete
$f_{cm}$	=	concrete's mean compressive strength
$F_{conc}$	=	force in the concrete
$f_{ct}$	=	tensile strength of the concrete
$f_{ctk}$	=	characteristic concrete tensile strength
$f_{ctm}$	=	concrete's mean tensile strength
$f_{fd}$	=	design stress of the FRP reinforcement
$f_{fe}$	=	effective stress in the FRP
$f_{frp}$	=	stress in the FRP
$F_{frp}$	=	force in the FRP
$f_{fu}$	=	design ultimate tensile strength of the FRP material
$f_{fu}^*$	=	ultimate tensile strength of the FRP as reported by the manufacturer
$f_{rupt}$	=	rupture stress of the FRP
$f_s$	=	stress in the nonprestressed steel reinforcement
$F_{steel}$	=	force in the steel
$F_{V,k}$	=	characteristic bond strength
$f_y$	=	yield strength of the nonprestressed steel reinforcement
$G_a$	=	shear modulus of the adhesive
$h$	=	overall height of the member
$I_1$	=	constant
$I_2$	=	constant
$I_3$	=	constant
$I_{eff}$	=	effective moment of inertia of the section
$K$	=	constant
$L$	=	bonded length of the FRP
$l_{df}$	=	development length of the FRP reinforcement
$l_o$	=	distance from the end of the beam to the start of the FRP strip
$L_{per}$	=	total length of the debonding failure surface
$l_v$	=	bond length
$M_{cr}$	=	cracking moment
$M_{db}$	=	debonding moment
$M_{exp}$	=	experimental moment
$M_n$	=	nominal moment
$\left[ (M_{PE})_{NSM-tfp} \right]_{ch}$	=	characteristic moment at the plate end that causes PE debonding for a tension-faced NSM plate
$\left[ (M_{PE})_{tfp} \right]_{ch}$	=	characteristic moment at the plate end that causes PE debonding for a tension-faced EB plate

$M_u$	=	ultimate moment
$M_y$	=	yield moment
$n$	=	FRP's modular ratio (Hassan and Rizkalla 2003)
$n$	=	number of FRP plies (ACI 440)
$nE_f t_f$	=	axial stiffness of FRP material per unit width
O.C.	=	on center
$P$	=	applied concentrated load
$P_{IC}$	=	IC debonding resistance
$(P_{IC})_{EB}$	=	mean value of the IC-debonding resistance for EB plates
$[(P_{IC})_{pp}]_{EB}$	=	IC-debonding resistance for an EB plate
$s$	=	shear span
$t_a$	=	thickness of the adhesive
$t_f$	=	FRP thickness
$t_{NSM-tfp}$	=	thickness of the tension-faced NSM plate
$t_p$	=	thickness of the EB plate
$t_{tfp}$	=	thickness of the tension-faced EB plate
TYP.	=	typical
$V_d$	=	design shear force
$x$	=	longitudinal coordinate starting from the cutoff point of the strip
$x_y$	=	distance from the support to the location of first yielding of the internal tensile reinforcement
$y_{eff}$	=	distance from the FRP strip to the neutral axis of the section
$z_m$	=	lever arm of the tensile reinforcement
$\alpha$	=	IC-debonding coefficient
$\alpha_1$	=	multiplier on $f'_c$ to determine the intensity of an equivalent rectangular stress distribution for concrete
$\alpha_{EB}$	=	IC-debonding coefficient
$\alpha_p$	=	IC-debonding coefficient
$\beta$	=	factor used to account for bond length
$\beta_1$	=	ratio of the depth of the equivalent rectangular stress block to the depth of the neutral axis
$\beta_p$	=	width factor
$\gamma_c$	=	material safety factor for the concrete
$\Delta M_d$	=	change in moment across the two cross sections
$\Delta M_{exp}$	=	change in experimental moment
$\Delta M_n$	=	change in nominal moment
$\Delta N_{fd}$	=	change in the FRP axial force between the two cross sections
$\Delta x$	=	distance between the two cross sections
$\varepsilon_{bi}$	=	strain level in the concrete substrate at the time of FRP installation
$\varepsilon_c$	=	strain in the concrete
$\varepsilon_{c,frp}$	=	strain in the concrete at the location of the FRP

$\epsilon_{cu}$	=	maximum usable strain of unconfined concrete, which is generally taken as 0.003
$\epsilon_{db}$	=	FRP debonding strain
$\epsilon_{f@y}$	=	tensile strain in the FRP at first yielding of the internal tensile steel at a moment of $M_y$
$\epsilon_{fd}$	=	debonding strain of the FRP
$\epsilon_{fe}$	=	effective strain level in the FRP reinforcement at failure
$\epsilon_{f,exp}$	=	experimental failure strain in the FRP
$\epsilon_{f,pred}$	=	predicted failure strain in the FRP
$\epsilon_{frp}$	=	strain in the FRP
$\epsilon_{f,rupt}$	=	rupture strain in the FRP
$\epsilon_{fu}$	=	design rupture strain of the FRP reinforcement
$\epsilon_{fu}^*$	=	ultimate rupture strain of the FRP reinforcement
$\epsilon_s$	=	strain in the steel reinforcement
$\phi$	=	strength reduction factor
$\rho_f$	=	FRP reinforcement ratio
$\rho_f^*$	=	normalized FRP reinforcement ratio
$\rho_f^* / \rho_s$	=	relative strengthening ratio
$\rho_s$	=	steel reinforcement ratio
$\sigma$	=	normal stress
$\sigma_1$	=	one of the principal normal stresses
$\sigma_2$	=	one of the principal normal stresses
$\sigma_3$	=	one of the principal normal stresses
$\Sigma F$	=	summation of forces
$\tau$	=	shear stress
$\tau_b$	=	average bond stress for NSM FRP bars (ACI 440)
$\tau_b$	=	shear stress at the FRP-concrete interface ( <i>fib</i> 9.3 2001)
$\tau_{cmax}$	=	limiting shear stress in the concrete
$\tau_i$	=	total concrete shear stress
$\tau_{max}$	=	maximum shear stress
$\tau_{K,k}$	=	characteristic shear strength of the adhesive
$\tau_{scmax}$	=	shear stress in the concrete due to stress concentrations at the toes of the flexural cracks
$\tau_{wmax}$	=	shear stress in the concrete due to the load
$\phi_f$	=	confinement ratio
$\psi_f$	=	FRP strength reduction factor

$\omega$  = defined in Equation 2-29 (Hassan and Rizkalla 2003)  
 $\omega_s$  = mechanical reinforcement ratio

## APPENDIX B: SAMPLE CALCULATIONS

**Table B-1:** Input for Sample Calculations for All Models

Concrete Properties			Steel Reinforcement Properties			FRP Properties			Reduction Factors		
$b_w$	=	16.75 in.	$A_s$	=	1.92 in. <sup>2</sup>	# grooves	=	6	$\kappa$	=	0.7
$h$	=	43.375 in.	$d$	=	40.19 in.	$t_f$	=	0.079 in.	$C_E$	=	0.85
$f'_c$	=	3000 psi	$E_s$	=	29000 ksi	$d_f$	=	0.63 in.	$\psi_f$	=	0.85
$\epsilon_{bi}$	=	0.0481%	$f_y$	=	40 ksi	$E_f$	=	18000 ksi			
						$f_{f,rupt}$	=	300 ksi			

**Table B-2:** Sample Calculations using each Model

Model	$P_{IC}$ (kips)	$f_{fu}$ (ksi)	$\epsilon_{frp}$ (%)	$\epsilon_{c,frp}$ (%)	$c^*$ (in.)	$\epsilon_s$ (%)	$\epsilon_c$ (%)	$f_s$ (ksi)	$\beta_1$	$\alpha_1$	$F_{frp}$ (kips)	$F_{steel}$ (kips)	$F_{conc}$ (kips)	$\Sigma F$ (kips)	$a$ (in.)	$M_n$ (k-ft)
1	N/A	179	0.99	1.04	4.95	0.96	0.14	40	0.72	0.73	53.3	76.8	130.1	0.0	3.54	402
2	7.8	157	0.87	0.92	5.06	0.85	0.12	40	0.71	0.69	46.8	76.8	123.6	0.0	3.59	407
3	8.2	165	0.92	0.97	5.01	0.89	0.13	40	0.71	0.70	49.3	76.8	126.1	0.0	3.56	415

Notes: Model 1- ACI 440 (2008)

Model 2- Seracino, Raizal Saifulnaz, and Oehlers (2007)

Model 3- Seracino et al. (2007a)

$\epsilon_{c,frp}$  is the strain in the concrete at the location of the FRP.

$F_{frp}$  is the force in the FRP;  $F_{steel}$  is the force in the steel; and  $F_{conc}$  is the force in the concrete.

$\Sigma F$  is the summation of the forces.

Model 1 uses all three reduction factors,  $\kappa$ ,  $C_E$ , and  $\psi_f$ . Models 2 and 3 only use the environmental reduction factor,  $C_E$ .

\*The value for  $c$  was guessed, calculated, and then iterated until the sum of the forces ( $\Sigma F$ ) was equal to 0.